

Flow in **POROUS ROCKS**

Energy and Environmental Applications

ANDREW W. WOODS



Flow in Porous Rocks

Energy and Environmental Applications

Driven by the increasing need for energy resources and by worsening environmental scenarios, techniques to exploit flows in porous rocks, such as fracking and CO₂ sequestration, are gaining international importance.

This book describes some of the challenges of modelling flow in natural rocks, which often have a complex, layered or heterogeneous structure, and whose properties are typically unknown in detail. Simplified physical models are introduced to help identify the challenges associated with the recovery of oil and gas from hydrocarbon reservoirs, the long-term geosequestration of CO₂, geothermal power production, and the processes which drive underground contaminant dispersal relevant for example in assessing the long-term storage of nuclear waste. The author approaches these problems by developing simplified mathematical models which help to identify the key dimensionless variables that control the processes. Analytical solutions for flows are provided where possible, and analogue laboratory experiments are presented to help illustrate and provide a different perspective on the flows.

Based on the author's extensive research and teaching experience, this book provides an important introduction to the different controls on flow in porous rocks, especially relevant to the energy industry. Incorporating end-of-chapter exercises, it is a key resource for academic researchers, energy industry professionals and graduate students.

Andrew W. Woods is the BP Professor and Head of the BP Institute in the University of Cambridge, and a Fellow of St Johns College, Cambridge. His research interests include theoretical and experimental modelling of flows in porous rocks, phase changes, turbulent plumes, volcanic systems and other natural flows in the environment and near surface of the Earth. Professor Woods has received several awards including the 1997 Italgas Prize for work on geothermal systems, the 1997 Marcello Carapezza Prize for work on volcanic systems, and the 2002 Wager Medal of the International Association of Volcanology and Chemistry of the Earth's Interior.

Flow in Porous Rocks

Energy and Environmental Applications

Andrew W. Woods

University of Cambridge



CAMBRIDGE
UNIVERSITY PRESS

CAMBRIDGE
UNIVERSITY PRESS

University Printing House, Cambridge CB2 8BS, United Kingdom

Cambridge University Press is part of the University of Cambridge.

It furthers the University's mission by disseminating knowledge in the pursuit of education, learning and research at the highest international levels of excellence.

www.cambridge.org

Information on this title: www.cambridge.org/9781107065857

© Andrew W. Woods 2015

This publication is in copyright. Subject to statutory exception and to the provisions of relevant collective licensing agreements, no reproduction of any part may take place without the written permission of Cambridge University Press.

First published 2015

Printed in the United Kingdom by TJ International Ltd. Padstow Cornwall

A catalogue record for this publication is available from the British Library

ISBN 978-1-107-06585-7 Hardback

Cambridge University Press has no responsibility for the persistence or accuracy of URLs for external or third-party internet websites referred to in this publication, and does not guarantee that any content on such websites is, or will remain, accurate or appropriate.

Contents

	<i>Preface</i>	<i>page ix</i>
1	Introduction	1
	1.1 The energy context	4
2	Porous rocks	11
	2.1 Turbidites	11
	2.2 Deltaic deposits	13
	2.3 Fluvial deposits	18
	2.4 Aeolian	20
	2.5 Compaction	21
	2.6 Carbonates	22
	2.7 Modelling flow in complex rocks	23
3	Flow in porous rocks	28
	3.1 Source–sink flows	29
	3.2 Sweep and flow in a two-layer system	32
	3.3 Sweep in a multi-layer system	34
	3.4 Lenses and trapping	35
	3.5 Wavy layers	39
	3.6 Seal layers	39
	3.7 Effects of multiple baffles and reduced vertical permeability	45
	3.8 Faults	47
	3.9 Cross-bedding	49
	3.10 Exercises	51
4	Accounting for uncertainty	52
	4.1 Sweep in the layered reservoir	53
	4.2 Boundary location and geological uncertainty	53
	4.3 Difference in spatial distribution of mean and variance	59
	4.4 Sensitivity to geological uncertainties	63
	4.5 Exercises	68

5	Dispersion in porous media	70
5.1	Molecular diffusion in a porous layer	71
5.2	Pore-scale mechanical dispersion	72
5.3	No-slip effects	75
5.4	Experimental laws for dispersion	77
5.5	Lenses of different permeability	80
5.6	Large-scale shear dispersion	84
5.7	Oscillatory flow	89
5.8	Exercises	91
6	Frontal instability	92
6.1	A model of the instability	92
6.2	Surface tension	97
6.3	Axisymmetric flow	99
6.4	Fluid annuli and droplet formation	100
6.5	Instability of reaction fronts	103
6.6	Instabilities in unconsolidated porous media	104
6.7	Fingering in fractures of variable width	106
6.8	Exercises	109
7	Two-phase flow	110
7.1	Wetting	110
7.2	Capillary entry pressure	112
7.3	Gas cap size and transition zones	114
7.4	Two-phase flow	116
7.5	The thin gap analogue	123
7.6	Capillary imbibition	124
7.7	Exercises	127
8	Fluid–rock interactions	128
8.1	Thermal energy conservation	129
8.2	Instability of a thermal front	132
8.3	Compositional reactions	133
8.4	Thermally controlled reactions	136
8.5	The partial dissolution reaction	137
8.6	The full dissolution reaction	140
8.7	Polymer floods	143
8.8	Polymer released from a dissolving encapsulant	143
8.9	Polymer activated by a thermal trigger	147
8.10	Polymer injection into a multi-layer formation	151
8.11	Exercises	154

9	Gravity-driven flow in porous media	156
9.1	Point release of buoyant fluid	162
9.2	The leaky boundary	166
9.3	Rapid injection and drain back: the dipole	169
9.4	Multiple fluids and stratified currents	170
9.5	Reacting fronts	173
9.6	Capillary trapping	176
9.7	Flow on a slope	178
9.8	Capillary trapping in a plume running upslope	179
9.9	Confined gravity-driven flows	181
9.10	Confined buoyancy-driven flow on a slope	184
9.11	Three-dimensional gravity currents	190
9.12	Exercises	194
10	Buoyancy effects on dispersion	196
10.1	Buoyancy effects on pore-scale mechanical dispersion	199
10.2	Convective plumes	202
10.3	Dispersal of a vertical plume by shale baffles	207
10.4	Dispersion by inclined baffles	210
10.5	Dispersion in a multi-layered horizontal system	213
10.6	Boundaries and buoyancy-driven dispersion through trapping	216
10.7	Exchange flows, mixing and controls on dissolution of CO ₂	219
10.8	Long-time buoyancy-driven dispersion	223
10.9	Exercises	226
11	Geothermal power and heat storage	227
11.1	Thermal fronts	229
11.2	Boiling fronts	230
11.3	Slow boiling	232
11.4	Fast boiling	233
11.5	Boiling gravity-driven flows	236
11.6	Double-advective plumes with reversing buoyancy	238
11.7	Gravity currents with thermal and compositional buoyancy	243
11.8	Scale precipitation and its impact on buoyancy-driven flow	246
11.9	Aquifer thermal energy storage	249
11.10	One-dimensional injection and production of hot water	251
11.11	Heat loss to lenses of low permeability	252
11.12	Heat loss to the surrounding formation	255
11.13	Mixing of the injected and formation fluids on extraction	257
11.14	Exercises	260
12	Compressibility and gas flows	262
12.1	Idealised one-dimensional gas production	264

12.2	Well selection	268
12.3	Radial flow and fracking	270
12.4	Multiple-layer formations	273
12.5	Shale gas	275
12.6	Exercises	278
13	Epilogue	279
	<i>References</i>	281
	<i>Index</i>	285
	<i>Colour plate section found in between pages 150 to 151</i>	

Preface

This book originated with a series of lectures related to the production of oil and gas from layered permeable rocks, which were focused on the challenge of the areal sweep of oil from injection to production wells, through complex, heterogeneous rock. Over the past few years, these lectures have been combined with some of my ongoing research into various fluid mechanical aspects of (i) power generation from geothermal systems through recovery of heat; (ii) scale formation in porous rocks; problems of (iii) carbon sequestration; and (iv) the dispersion of radioactive contaminants from geological nuclear waste repositories, to form a graduate-level course related to the fluid mechanics of energy systems in porous rocks.

The book explores the physical processes which influence oil and gas production, CO₂ sequestration and geothermal energy production. It draws together a series of simplified physical models of the many complex processes relating to flow in porous media to provide insight into the different phenomena, and where possible results from laboratory experiments are used to illustrate the processes, as well as quantitative scalings which identify the dominant controls on the flows and help build up insight into the processes.

After a brief discussion of the importance of oil and gas resources for global energy supply, this book reviews the topology of various porous rocks and presents simplified models for pressure-driven flow through a variety of complex rock architectures. It then briefly discusses how such models may help quantify the impact of the uncertainty in the rock properties and structure in making predictions. We then discuss the processes of dispersion and mixing in pressure driven flows, both produced by the pore-scale flow and larger scale flows around lenses or layers of low or high permeability. Saffman–Taylor instability is discussed and generalised to problems of reaction, temperature change and erosion of loose sand. After a discussion of two-phase flow, and the Buckley–Leverett shock formation process, there is a chapter discussing reactions in rocks, including both compositional and thermally driven reactions; these ideas are generalised to discuss the injection of polymers and their gelling within a porous rock as may be desirable to modify properties of a reservoir. The book then turns to buoyancy-driven flows and introduces gravity currents, including effects of capillary

trapping and leakage relevant for CO₂ sequestration. We then discuss the role of buoyancy in promoting mixing and dispersion, especially with complex rock structure, relevant for enhanced oil recovery through gas injection or CO₂ sequestration. Water injection into hot rocks to recover geothermal energy is then discussed, and the phenomena of boiling for steam generation, as well as the water flooding patterns which may be produced when the buoyancy depends on temperature and composition, are presented and explored. Finally, we present some models of compressible flow, which provide insight into gas production from layered and low permeability gas/shale-gas fields.

There are many texts on flow in porous media, including the comprehensive treatise by Bear (1972), on modelling flow in porous media, the fascinating book on reactions and flow in porous media by Phillips (1991), the work of Dagan on dispersion in porous media and the book *Enhanced Oil Recovery* by Lake (1991). The objective of this book is to complement these earlier works, focusing on the physical processes, with simple laboratory models supported by simplified mathematical models. The work draws from the well-established modelling of pressure-driven flow in layered and heterogeneous porous rocks, including the resulting processes of dispersion, interfacial instability, and two-phase flow dynamics, to explore problems of buoyancy-driven flows in porous media and the dispersion of flows in complex layered strata. There is an underlying theme of energy related applications throughout the text.

I have been extremely fortunate to work with many colleagues and students whose quest for knowledge and application to their research has driven forward much of the work reported in this volume, largely during my time in the BP Institute in Cambridge. This includes in particular Silvana Cardoso, Adrian Farcas, Will Rayward-Smith, Jason Furtney, Peter Dudfield, Thierry Menand, Mats Nigam, Gennaro Del Ioio and Karen Otto, who has kindly assisted with figures in Chapters 5, 6 and 9. I am also very grateful to Colm Caulfield for carefully checking the contents, as well as to Gil Arnaud, Alex Evans and Adrian Farcas. In addition, I have been very fortunate to work with numerous colleagues from industry who have shared their challenges and experience of real energy systems in helping to frame many of the problems set out in this work, including in particular Pete Smith, Andy Leonard, Ian Collins, Tony Espie, Simon Norris and Bryan Lovell.

I am first and foremost indebted to my family for their generous encouragement, patience and support in the writing of this book, and also the research reported herein, especially my wife Sharon.

1 Introduction

The energy of the mind is the essence of life

Aristotle

In this book we explore flow processes in permeable rocks which are important for the energy industry and the environment. As well as the oil and gas industry, flows in porous rocks are key for geothermal energy production, CO₂ sequestration, interseasonal heat storage and the geological disposal of nuclear waste. The motivation for the book stems from the flourishing interest in energy systems and the use of such energy, much of which relies on fluids. As well as being the raw material, for example oil and gas, fluids can transport the energy, as occurs in geothermal systems and in some cases the product of energy consumption, namely CO₂, can be sequestered in the ground to reduce atmospheric emissions from burning fossil fuels. Flow in permeable rocks impacts the nuclear industry, with the challenges of geological disposal of radioactive waste and especially the potential for dispersal of such waste through the subsurface. Contamination of groundwater systems can also arise from spillages for example of non-aqueous phase petroleum liquids (NAPLs).

There are many classic texts on flow in porous media, and the recovery of oil, including those by Muskat (1937), Bear (1972), Phillips (1991) and Lake (1991). However, recently, there has been a resurgence of interest in a number of new fundamental physical problems relating to flow in porous media. These arise for a number of factors. First, it is becoming increasingly challenging to recover the remaining oil and gas reserves. The challenges arise as operators work in more extreme environments as they search for increasingly high temperature and high pressure deep reservoirs of viscous oil; shale gas is being recovered from very low permeability rocks; very heavy oil is being recovered from tar sands; and operators are exploring in difficult deep water and arctic environments. However, developing effective secondary and tertiary recovery of oil from existing fields through injection of water and chemicals is also likely to be key to enabling the continued effective recovery of hydrocarbons from existing fields, especially as global energy consumption rises and oil demand approaches the global production capacity. Furthermore, although there have been spectacular advances in geophysical imaging of reservoirs using seismic waves, the remote and harsh

environments of new oil provinces leads to increased cost of exploration wells and other data-acquisition systems. This emphasises the importance of developing models of flow in permeable rock which can help inform decisions by reflecting uncertainty in the architecture of and potential production from oil fields.

Other challenges for flow in permeable rocks are associated with the emerging science of CO₂ sequestration, where there is interest in the fate of CO₂ injected into the subsurface, both on the short timescale of injection, and on the longer timescale of hundreds to thousands of years when buoyancy forces dominate the flow. Related to this, there are important questions about the dispersal of contaminants in the subsurface, especially concerning potential geological waste repositories designed for the long-term storage of radioactive waste. Knowledge of flow patterns and contaminant dispersal by these flows can be key for risk assessment.

Flows in porous media are also of importance for the renewable energy industry, including the challenge of geothermal heat production from the circulation of fluids through hot, permeable rock. Here, we explore the transport and dispersal of heat, both as a liquid and a vapour, following liquid injection into the system. We also study the role of convection on the fate of liquid injected for geothermal energy recovery. These issues are strongly coupled with challenges of aquifer thermal energy storage.

The objective of this book is to introduce simplified quantitative models, in some cases supported by experiment, to help to understand some of the different fluid mechanical processes which arise in porous rocks. Many of the flows described above are so complex and ill-constrained by data about the specific geological formations that it is very difficult to simulate the flows in detail. In many cases, the detailed structure of the rock, at the scale of the layers and other heterogeneities in the formation, is unavailable and so only relatively coarse, averaged models are available to describe the flow. These models are often informed by the structure of analogue rocks visible at the surface. Many of the parameters relating to the rock structure can only be constrained probabilistically, owing to the difficulty and expense of measuring such properties far below the surface. The idealised modelling approach proposed herein, which focuses on quantifying specific physical flow processes, enables discussion and illustration of the impact of geological uncertainties on the flow. Indeed, in Chapter 4, with a series of very simple models, we outline some of the challenges related to assessing uncertainty and the ultimate use of models to help inform decisions.

The book has been arranged in a series of themes to reflect some of the above challenges. First, we start with a simplified introduction to the complexity and diversity of geological formations which constitute the rocks involved in oil and gas recovery, CO₂ sequestration and geothermal heat recovery. This leads to the challenge of developing models of the effective large-scale flow properties within a formation as these tend to be strongly controlled by individual geological layers and the interaction between these layers. We illustrate how the geological complexity of a reservoir can impact the effectiveness of the displacement of fluid through the reservoir by the injection of

water. We then explore how the predictions of simplified models depend on the geological parameterisation and how the sensitivity of models to these parameters might be determined, identifying that the boundary conditions are key. In Chapter 5, we turn to a discussion of dispersion by pressure-driven flow in porous media. This topic has been very thoroughly studied, and there have been many substantial books describing the processes from the pore scale to the scale of the macroscopic heterogeneities in the formation. The present physically based account is designed to illustrate some of the different phenomena, and to develop simplified scaling rules to assess the likely magnitude of the dispersion in some idealised systems. We then describe the classical process of viscous instability, whereby less viscous fluid develops a fingering pattern through a more viscous fluid rather than displacing the more viscous fluid with a planar front; this presents a fundamental challenge for oil recovery, and we illustrate how the associated instability pervades many fluid–fluid displacement problems in porous rock, including a fascinating erosional instability when liquid is injected into unconsolidated sand. In Chapter 7, we introduce immiscible flow in porous media, and describe how, in a two-phase flow, there is an asymmetry between the resistance experienced by the wetting and non-wetting phases. This leads to prediction of the classical Buckley–Leverett shock front, across which there is a jump in the saturation of the wetting fluid in the pore space, across an advancing wetting front in which the upstream pore space may be largely occupied with, for example, water to a flow downstream which is dominated by the non-wetting phase, for example oil. There are again many excellent texts which explore two- and three-phase flow dynamics in porous media in detail (Bear, 1972; Lake, 1991). We focus much of the continuing discussion in the present book on the dynamics of fronts and fluid–fluid interfaces. We first explore the dynamics of thermal fronts and reaction fronts as building blocks to describe the dynamics of gelling polymer fronts. Such fronts are likely to have a growing importance in enhanced recovery, and we illustrate some of the effects of using gels in layered geological strata. In Chapter 9, we turn to buoyancy-driven flows, and explore how buoyancy forces tend to localise interface instabilities into a single gravity dominated flow. We then develop various models of buoyancy-driven flows to illustrate the processes associated with CO₂ sequestration, including capillary retention and leakage across layer boundaries. In Chapter 10, we discuss the possible influence of heterogeneity in the geological structure of a formation in dispersing such buoyancy-driven flows, a process which is key for CO₂ dispersal and possible hydrogen gas release from geological waste repositories. In Chapter 11, we turn to the transport of thermal energy, and illustrate how injection of liquid into superheated rock can lead to vaporisation, while the injection into warm rock can lead to heating and a change in the buoyancy of the flow, producing a range of complex patterns of water flood with associated changes in the efficiency of heat recovery from the system. In Chapter 12, we return to hydrocarbon production, but focus on the dynamics of gas production, for which the compressibility of the system is key. We illustrate how important cross-layer flows between high and low permeability

rock can be for enhancing the production of gas, and discuss the analogous benefits of fracturing the formation normal to the well in very low permeability systems.

Before launching into the fluid mechanics of these different processes, it is of interest to describe present energy resource production. This provides context for the very substantial challenge of maintaining present rates of energy supply, and the need for new technology in the oil and gas industry in order to continue to develop hydrocarbons at scale, while also building up the technology base and infrastructure for renewable energy and CO₂ sequestration.

1.1 The energy context

Interest in energy resources arises from concerns about security of energy supply and its maintenance over the next few decades; abatement of carbon emissions from those sources which are hydrocarbon based; the challenge of supplying a material fraction of the energy base from renewable resources; and the more efficient usage of energy, so the output in productivity per unit of fuel is increased. Although projections of energy consumption depend on many interrelated factors the historical data shown in Figure 1.1 indicate that there has been a nearly linear increase in global energy supply over the past four decades, with the last decade occurring in a post-Kyoto Protocol world (Figure 1.1). It is not unreasonable to assert that over the next few decades there is likely to be further growth in demand. Feeding this demand requires the development of new energy sources. Energy supplies today are largely sourced from hydrocarbons, as seen in Figure 1.1. Over 80% of global energy is derived from fossil fuels and the remaining sources are dominated by nuclear and hydroelectric.

Before considering the challenges and opportunities for continued hydrocarbon production, and the need for managing the associated CO₂ emissions it is worth reflecting on the other sources of energy.

Nuclear energy is a viable alternative to hydrocarbons, and can provide a nearly carbon-free energy source. However, there are challenges for the global growth of nuclear power, including the large upfront cost and timescale to bring new nuclear online, and the environmental concerns relating to accidents. In addition, there is a long-term challenge of the storage of the waste. Many countries have adopted a strategy of using a geological repository, whereby the waste will be stored in a low permeability part of the subsurface. As part of these plans, there is considerable research effort underway to explore the possible interaction of such waste with subsurface flow processes over the very long time comparable to several half lives of the radioactive material.

Hydroelectric power generation already makes a substantial contribution to global energy supply and, for example, in South America and China contributes a significant

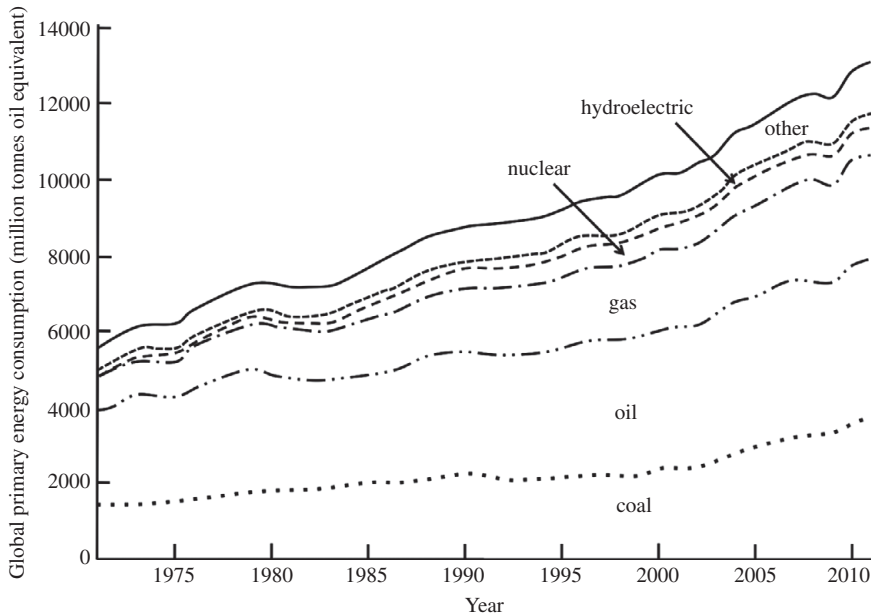


Figure 1.1 Breakdown of the global primary energy supply by fuel type. From 1970 to 2010 there is a near linear rise in total consumption with time, with oil, coal and gas accounting for over 85% of the total supply. Data from BP Statistical Review of Energy (2013). ‘Other’ which includes wind, solar and biomass is gradually increasing.

amount of energy, in part through large river-dam systems. Other renewable energy sources, such as wind and solar, presently only account for a relatively small fraction of the whole energy supply. However, this is a rapidly growing sector of the energy industry and installed capacity is increasing (Figure 1.1) although this is likely a multi-decadal process. A further challenge for such sources of power is associated with possible storage, to level out the somewhat intermittent supply. Here, battery technology or other storage systems can play an important role, and we consider some challenges of aquifer thermal energy storage systems in Chapter 11. Geothermal energy could also play a very significant role. At a large scale, there are several high temperature systems, with the Geysers in northern California and Larderello in Tuscany, Italy, being two examples with potential electrical power generating capacity of order 1000 MW, and very many lower temperature systems providing thermal energy for direct use in heating. Biofuel technology has made enormous progress, and there are major plants generating bioethanol as a transport fuel, with, for example, Brazil fuelling a substantial fraction of its car fleet through bioethanol from sugar cane. Tidal and wave power is less well developed, but at EMEC, offshore Orkney (www.pelamiswave.com) there are new installations being developed with the Pelamis wave system and submarine tidal turbines, although they are a relatively minor part of the global energy supply. With all these renewable energy sources, cost is a key factor in order that they are competitive.

Given the present mix of energy supply, and the associated infrastructure which is built around this energy supply, it is likely that we will continue to produce and use hydrocarbons over several decades, even if it was straightforward to replace the supply with alternative sources of power. One of the key drivers for renewable energy is associated with carbon emissions produced by burning fossil fuels. Although an aspiration would be to move all supply to renewable energy sources, the time required for this to become a material reality on a global scale may be decades. There are two important ways of reducing emissions associated with the likely use of fossil fuels during this period while the renewable energy supply grows. First, there could be a switch from coal to gas for power generation. Coal is a very substantial part of the energy supply but when used for power generation it produces nearly 1.5–2.0 times the CO₂ emissions per kilowatt hour of electric power that is produced by natural gas. Switching from coal- to gas-fired power stations could therefore have an enormous impact on CO₂ emissions, as has happened recently in the United States. Second, CO₂ produced at power stations, and other large consumers of fossil fuels, can be captured and geosequestered underground into deep saline aquifers. This would reduce the continued supply of CO₂ to the atmosphere, although incurring a substantial cost in infrastructure.

However, underpinning the above arguments is the assertion that the supply of hydrocarbons is readily maintained. The continued supply of hydrocarbons, and especially liquid hydrocarbons, at present production rates is not straightforward and will rely heavily on new technology. Hydrocarbon reserves can be categorised into different groups, called conventional and unconventional. Conventional resources describe reservoirs with good quality rock and fluid oil, which can be recovered using techniques available today.

In typical oil fields, initial approval to develop the field may be based on an aspiration to extract 30–40% of the oil, while the technical limit, based on the effect of capillary retention, for example, may indicate that up to 80% may be recovered. The effects of layering, heterogeneities and compartmentalisation of the field can lead to significant challenges in recovering this secondary oil, as described in Chapter 3. However, it is possible to produce considerably more of the resource. There are examples in the North Sea where over 70% of the initial oil in place has been produced, including the Fortes field. In achieving high recovery rates, much technology has been developed and applied relating to (i) lower cost and horizontal drilling technology, to enable a larger surface area of the well to be located within oil-bearing horizons; (ii) seismic imaging of oil fields before and during their production which can enable improved three-dimensional characterisation of the reservoir and identification of regions of the reservoir in which there has been little flow, which may be targets for infill drilling, (iii) use of surfactants and polymers in water injected into the field to enhance the recovery of the residual oil. All of these techniques can benefit from knowledge of the dynamics of flow in permeable rock, and this forms the first major set of topics of the book, including discussion of the effects of the macroscopic and microscopic structure of the

rock formation on the flow, and the intermingling or dispersion of an injected fluid through the original reservoir fluid (Chapters 3–7).

Challenges in the development of oil from new oil fields are often associated with their being located in more remote or hostile environments: new fields may be deeper in the ground, under deeper bodies of water and in many potential reservoirs, the oil may be very viscous, contained in low permeability rocks or loose-packed sand requiring considerable post-extraction processing. Data about the detailed structure of these remote fields may be limited up to the point of development, owing to the cost and inaccessibility, and this introduces risk, which increases the cost and impacts the likelihood of their successful development. The early sections of this volume are concerned with describing some of the difficulties of oil recovery, especially relating to water flooding. In large part, this is a result of the complex structure of these reservoir rocks and the difficulty of driving liquids through the different geological layers in a formation; it also depends on the pore-scale structure and the capillary forces which ultimately retain a fraction of the oil within the pores.

Data available in the BP Statistical Review of Energy and information available from the IEA suggests that up to the present day, the world has used about 1000 billion barrels of oil. However, there are very substantial resources remaining. As well as the significant volume of conventional resources which are still to be developed, which exceeds that already produced, there are enormous volumes of non-conventional resources for which new approaches are required to produce the hydrocarbons. One fascinating example of a so-called non-conventional resource is shale gas: here, gas is bound within extremely low permeability rock. By fracturing the rock in the subsurface, around a well, a fraction of the gas can be released, and with sufficient fracture area, this leads to economic rates of recovery of the gas. This has transformed the US gas market, supplying nearly 40% of US gas requirements, and illustrates the power of technology in opening up new resources.

Some of the major non-conventional oil resources include heavy oil and bitumen deposits in the Canadian and Venezuelan tar sands, where estimates suggest that about another 1 billion barrels of oil may exist. Oil shales are rocks containing high levels (tens of per cent) of organic material which were deposited in shallow seas in anoxic conditions, but which have not been buried to sufficient depth within the Earth to pyrolyse. By heating these resources to temperatures of 400–500°C, the bitumen can be converted into hydrocarbons; technology for this is at a very early stage of development, but the Green River Basin in Colorado, USA, may contain 500–1000 billion barrels of oil. Perhaps one of the most intriguing unconventional resources are the methane hydrates, which consist of ice type structures within which methane is trapped. These hydrates are stable at the pressure and temperature conditions found in shallow marine sediments and the permafrost. The resources of such hydrates are thought to be very substantial, of the same order as conventional hydrocarbons, but there remain major challenges in the extraction technology before these become

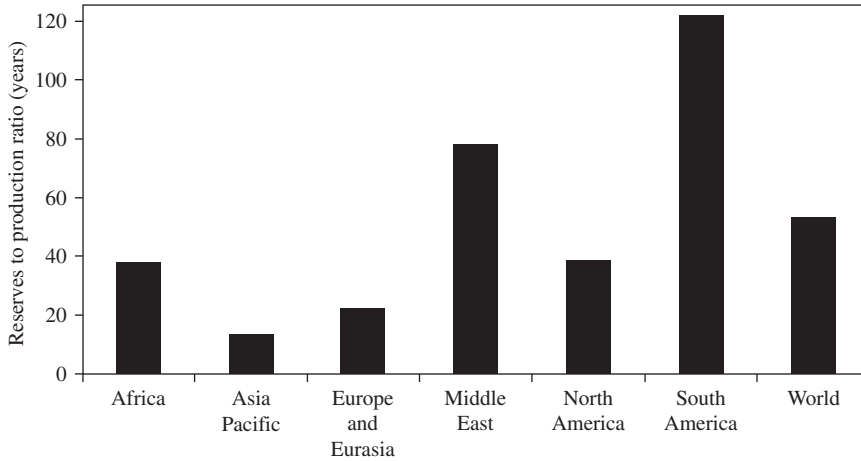


Figure 1.2 Illustration of the reserves to production ratio of oil in different parts of the world, illustrating the number of years of remaining proved resource based on present day production rates. Data from BP Statistical Review of Energy 2013. The total global resources are much larger than the proved reserves shown here.

material energy resources. In particular, the dissociation of the gas and the ice requires latent heat, and this typically leads to freezing of the surrounding permeable layer, thereby suppressing flow of the methane. Also, in some areas, the methane hydrates play a key geotechnical role in supporting the geological strata, and if they dissociate, then slope instability may ensue.

In the short term, the major source of oil production is likely to be that which still remains in existing oil fields, with exploration focusing on the habitat of the oil within the reservoir after the initial phases of oil recovery. Much of the resource is located in the Middle East, where there are some very large reservoirs in carbonate rocks. There are also very significant ongoing oil production developments around the globe, including deep-water offshore West Africa, the Brazilian offshore deposits, the North Sea and the Gulf of Mexico, as well as northern Canada and Alaska. The potential resource base around the globe is often characterised by the reserves to production ratio, where reserves represent those resources which can be recovered economically using known technology. Figure 1.2 illustrates that many of the oil-producing centres round the globe have many decades of future production based on present rates.

As well as the many challenges of oil recovery through water flooding and related techniques, there are a number of related problems in the emerging technology of carbon sequestration. Carbon sequestration is the process of capturing CO_2 from combustion of hydrocarbons and injecting it into subsurface aquifers to reduce the emissions of CO_2 directly into the atmosphere (Figure 1.3). There are still numerous challenges for its implementation and in particular the establishment of a viable economic framework to grow an industry able to inject large volumes of CO_2 into the subsurface. Also the

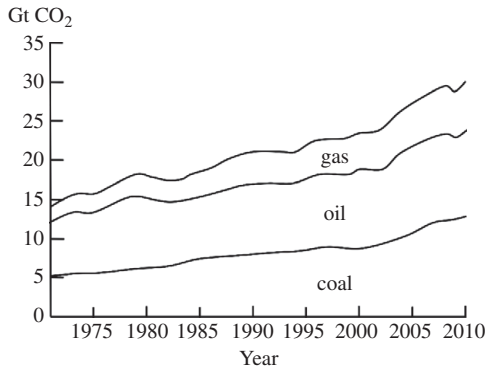


Figure 1.3 Illustration of the source of greenhouse gas emissions associated with use of primary energy. Data from BP Statistical Review of Energy, 2013. The increasing use of coal has led to an increase in coal-related emissions.

assessment of the risk that a significant fraction of sequestered CO₂ may escape from the storage reservoir back to the surface or to subsurface potable aquifers, with the associated problems of cross-contamination is critical. We address some of the technical challenges of modelling and monitoring the fate of the CO₂ during and after injection. Again, fluid mechanics lies at the heart of this process, with the motion of CO₂ often being dominated by buoyancy forces as the plumes ascend through the geological strata or spread horizontally along the strata (Chapters 9 and 10). Some of the processes which control the dispersal of CO₂ in the subsurface are also in operation in the dispersal of plumes of dense non-aqueous phase liquid (DNAPL) following a spillage, and in the migration of plumes of buoyant hydrogen gas which may be emitted from geological waste repositories, and we consider the implications of buoyancy-driven flow for these applications as well (Chapter 10).

Geothermal power involves the recovery of thermal energy from the subsurface, often by pumping cold water into the rock and recovering hot water. Again this is a fluid mechanical process, but involves the migration of thermal fronts, and often mineralisation fronts, as the injected water heats up and in supercritical systems boils. There are significant reserves globally, although at present those which provide substantial sources of energy tend to be strongly coupled to geologically active regions, such as Iceland and New Zealand. In superheated geothermal systems, such as the Geysers in Santa Rosa, northern California and the Lardarello field in Tuscany, cold water is injected into the system to generate additional steam through heating from the rock. This leads to some fascinating phase change problems, which we explore in Chapter 11. There is also interest in using aquifers for interseasonal thermal energy storage, for improving power station efficiency and also for levelling load from intermittent renewable energy sources such as wind. We consider some challenges associated with this in terms of the fluid dynamics of injection and production of water to transport thermal energy.

In Chapter 12, we discuss flow in gas fields, initially considering conventional gas, but then extending the models to account for shale gas. In gas fields, often the pressure is allowed to fall as gas is produced. This can lead to a gradual waning of the flow over time which may introduce other challenges, such as suppression of the gas production if water flows into the production wells from the formation, increasing the backpressure in the field. We examine how gas flows through layered strata, in which the flow path from deep in the reservoir to the well is typically dominated by the flow through high permeability pathways, while the main source of the gas may be in the low permeability matrix surrounding these high permeability channels. The models are also useful in building understanding of the production of gas from very low permeability rocks which are fractured during development, and can be developed to account for the release of adsorbed gas as the formation is decompressed; this is relevant for the production of shale-gas reservoirs.

2 Porous rocks

Oil and gas reservoirs are composed of permeable rock, often arranged in layers. Although there are many different types of formation which can become oil-bearing rocks, the dominant requirements are a source of hydrocarbon in the source rock, a reservoir rock and a seal. A classic source rock may be seen in Kimmeridge Bay on the South Coast of England (Figure 2.1), in which organic material from a shallow marine environment is buried in an anoxic environment and then, as it is compressed and heated over geological times, pyrolyses to form oil and gas. This then migrates upwards through the geological strata and accumulates in permeable rock provided there is a seal or caprock which arrests further ascent. Depending on the geological environment and history of the formation, the reservoir rock may be composed of many superposed layers of sandstone, clay and shales or carbonate rocks including limestone and chalk. There has been an enormous effort over the past century in the geological community to describe the processes by which such sedimentary rocks form and the post-depositional processes which ultimately shape the geological strata. The excellent texts by Allen (1992) and Nichols (2009) introduce many of the concepts and processes involved, and we defer to the geological literature for details of this. Our purpose is to review, in a simplified fashion, some of the dominant topologies of permeable rocks, to help motivate some of the modelling in later sections of the book, but also to emphasise the complexity of the geology in controlling the boundary conditions for flow in porous rocks. The presentation is designed to be illustrative and not in any way exhaustive.

2.1 Turbidites

Deep-sea turbidite deposits tend to be extensive sheet-like structures which form from the rapid discharge of a large volume of sediment from high up on the continental shelf. The turbidite flow runs down the shelf and then spreads out on the deep abyssal plain, where it gradually sediments, producing a fan-type deposit. On geological timescales, there will be multiple discharge events leading to the accumulation of many turbidite fan-like deposits. Although each layer may be metres to tens of metres thick, the overall



Figure 2.1 Photograph of the Kimmeridge source rock in the cliffs on the beach at Kimmeridge Bay, Dorset. The photograph also shows the active gathering station on top of the cliffs, at which oil from a deeper reservoir directly below is being produced at the surface. Photo courtesy of D. van Sommeren. A black and white version of this figure will appear in some formats. For the colour version, please refer to the plate section.

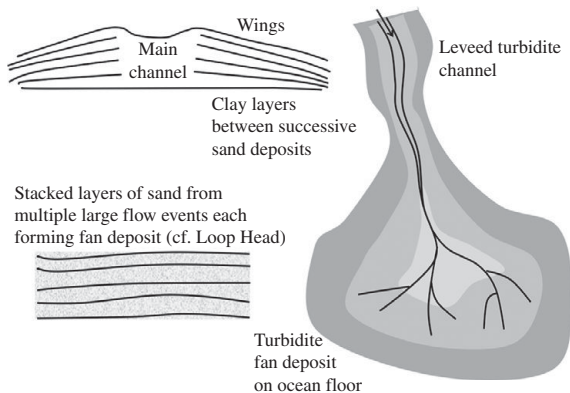


Figure 2.2 Schematic of the channel and wing structure of a turbidite and of the distal fan deposit, where multiple flows may stack over time. These features may be seen in Figure 2.3.

deposit may be many tens or hundreds of metres thick. There may be some channelling of the deposits from successive flows, leading to the characteristic channel and wing structure often seen in turbidites (Figure 2.2). The channel contains sands from multiple events, as the flow from successive events follows similar pathways. Larger sized events may lead to the flow overspilling the channel to form the wing deposits and between successive discharges there may be gradual accumulation of finer grained material. This produces thin clay or shale deposits between successive turbidite flows. The clay layers may often be eroded in the channel leading to formation of a massive sandy channel deposit, whereas they remain in the wings, dividing the successive flows. This leads to a complex reservoir geometry in which the channel is well-connected,

whereas the wings are vertically stratified and may even be independent owing to the low permeability clay layers. If a turbidite layer forms an oil reservoir, there may be a considerable challenge in displacing oil from the wings of the deposit, whereas the channel may form very good reservoir rock.

Further from the source, the distal end of the turbidite deposits, most distant from the source, typically consist of layer upon layer of fan-like deposits, sometimes separated by thin clay or other fine-grained sediment layers, which can act as a hydraulic seal between the layers. Owing to post-emplacement processes, the seal may become fractured and permeable. The formation may therefore approximate a two-dimensional sheet-like structure, leading to relatively simple topology of the permeable rock. One tremendous turbidite outcrop may be found in Western Ireland, at Kilbaha Bay and the nearby Loop Head formation (Figure 2.3). The first two panels show a series of turbidite layers, with evidence of a channel feature in the centre and wings to the sides which are separated by layers of shale and clay ranging from a few millimetres to many centimetres thickness. An image of the coastline reveals the extensive layered fan deposit which forms the Loop Head Cliffs. Here a large number of sand sheets, each a few metres in thickness are stacked above each other, separated by thin shale layers of much smaller permeability. Note also the significant fold at the right-hand end of the cliffs.

Flows over the continental shelf may channellised, and may erode some of the underlying strata to form submarine canyons. As successive events generate sediment flows, this may lead to meandering channels being superposed, and can lead to complex topology of the final deposits. Successive deposits may have common boundaries, enabling hydraulic communication for fluids migrating through the rocks which are subsequently formed.

2.2 Deltaic deposits

Moving up the continental shelf, another important type of reservoir arises in estuarine or deltaic environments where there are sand bars and channels, which are typically layered sandy formations, again of high permeability, and often separated by finer grained sediment layers. Figure 2.4 illustrates a picture of a distributary channel in a deltaic setting at Tullig Point in County Clare, Western Ireland. The scale is about 20 m high by 100 m across, and this photograph illustrates a complex, layered system, which would again represent a high quality reservoir rock owing to the high content of coarse-grained sand.

Estuarine deposits may develop as complex deltas which involve many smaller streams, with bars of sand and finer sediment of complex topology separating the streams; this can ultimately produce rocks with regions of high and low permeability,

(a)



(b)



(c)



Figure 2.3 (a) Kilbaha Bay, County Clare, Western Ireland. A multilayered turbidite deposit illustrating how the sand layers are separated by smaller grain-size shale rock which acts as a seal between layers. (b) Cliffs on the coast near Kilbaha Bay, illustrating the laterally extensive stacked turbidite deposits, interspersed with thin layers of seal rock. (c) Loop Head Cliffs, County Clare, Western Ireland, showing a series of laterally extensive distal turbidite fan deposits. Note the fold in the layers at the right-hand side of the photograph.



Figure 2.4 Tullig Point, County Clare, Western Ireland. A distributary channel illustrating the highly layered nature of a deltaic environment. A black and white version of this figure will appear in some formats. For the colour version, please refer to the plate section.

with preferred orientations which are related to the original estuarine flow environment. Shallow, near-shore deposits may include tidal sand bars, storm deposits and other structures, which lead to large-scale anisotropy in the ultimate rocks, and hence in the permeability field, as we explore in Chapter 3. Another fine example of a near-shore deposit are the cliffs at West Bay in Bridport, Dorset (Figure 2.5). Here, there is a laterally extensive formation, which is nearly 100 m high and consists of many horizontal and laterally extensive layers, each a few metres thick. This formation, known as the Bridport Sandstone dips below the surface towards the east, and at Poole Harbour, the Bridport formation is saturated with oil, 900 m below the surface, supplying oil to a major onshore oil field, the Wytch Farm reservoir. As may be seen in this exposed section, the rock consists of a series of layers 1–10 m thick, with a cemented, lower permeability layer between these units, perhaps up to 1 m thick. Modelling flow in this formation requires description of the flow within layers and also between the layers. In the context of a subsurface reservoir, this is challenging since only the relatively coarse-scale features of the rock, on lengthscales typically in excess of 10 m can be measured from surface geophysical techniques, such as seismic-imaging techniques.

In contrast to the sandy relatively good quality formations in deltaic and turbidite sediments, shallow marine deposits can be much finer grained and highly layered, leading to much less favourable rock for hydrocarbon resources. They may also include localised storm deposits which are composed of somewhat coarser sediment and can therefore provide a high permeability conduit through the system. Sedimentary rocks produced in a range of depositional settings can also include cross-bedding or cross-

(a)



(b)



(c)



Figure 2.5 Photograph of the Bridport Sandstone, Dorset, UK. (a) Panoramic view of the cliffs and (b) a close-up showing the complexity of the layering, with each layer being in the range of 2–5 m thick; (c) close-up of a single layer in the sequence bound above and below by cemented horizons. Photograph courtesy of D. van Sommeren. A black and white version of this figure will appear in some formats. For the colour version, please refer to the plate section.

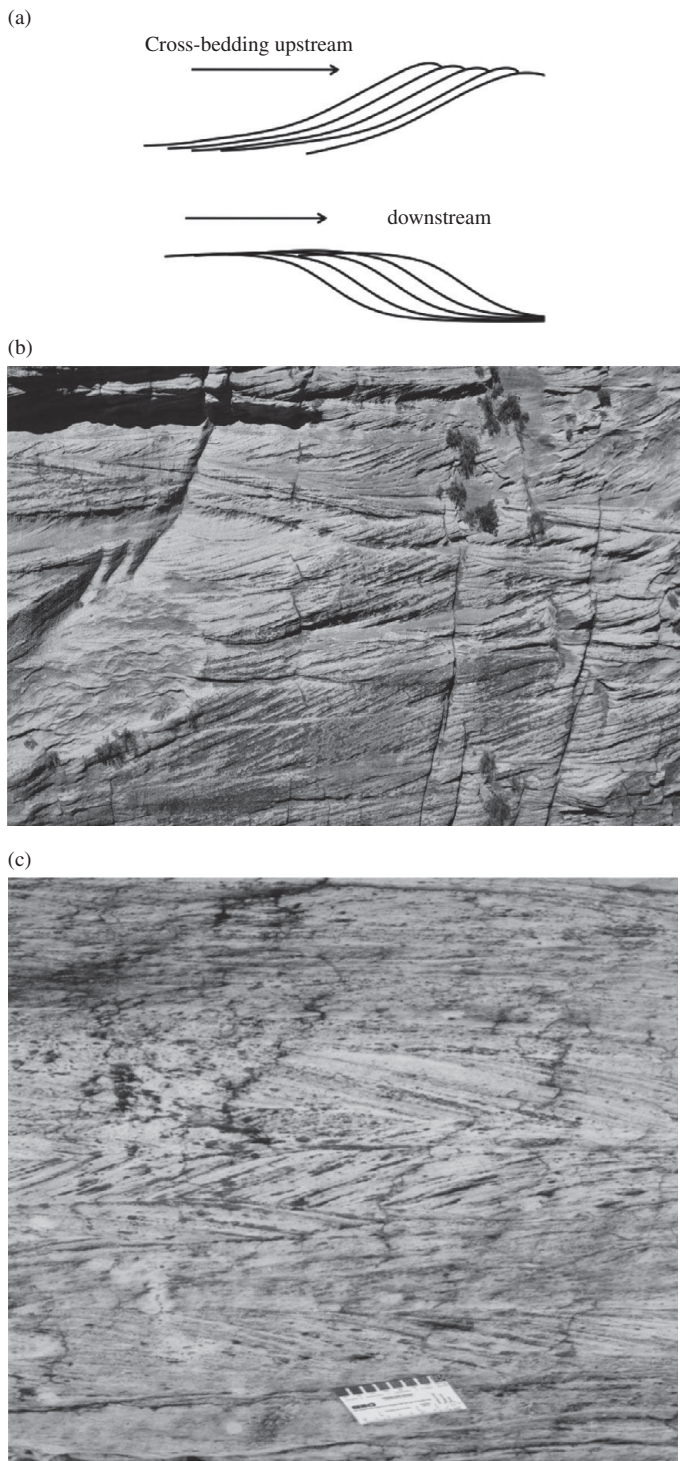


Figure 2.6 (a) Cartoon of cross-bed formation owing to deposition migrating upstream or downstream. Illustration of cross-bedding on walls of (b) Glen Canyon, USA, and (c) in the Tabernas Basin, Spain. The bedding has a very fine scale and variable direction relative to the strata leading to potentially complex flow trajectories through the formation. A black and white version of this figure will appear in some formats. For the colour version, please refer to the plate section.

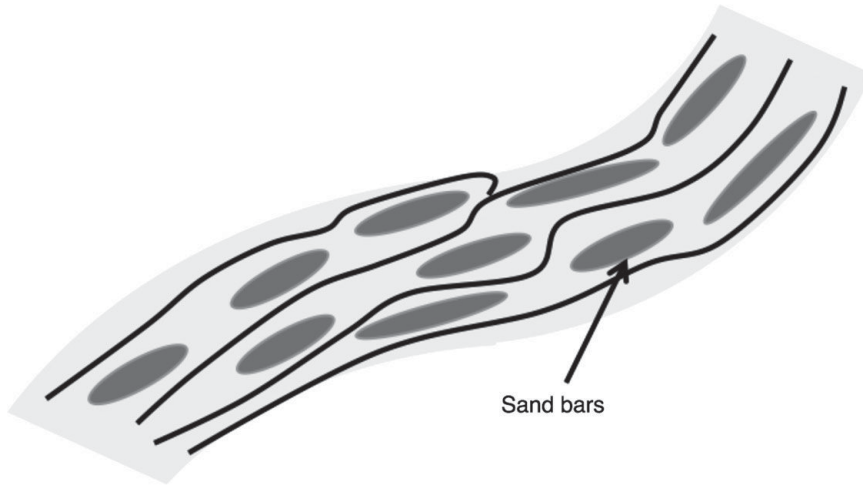


Figure 2.7 Illustration of braided stream, with diverse patterns and structures of deposition in the stream owing to formation of sand bars.

lamination, and this may be critical for the subsequent flow of liquids through the porous rock. Figure 2.6 shows some cross-bedded deposits for illustration.

2.3 Fluvial deposits

Upstream of the coastline, fluvial deposits can be very complex, with river beds transporting a wide range of sediment particle sizes downstream and, in some cases, eroding the underlying substrate. The rocks forming from such deposits may be of high permeability in places, but may also be very variable spatially owing to the complexity of river deposition processes. Often there is cross-bedding in the deposit, in which the layers of sediment build up on the downstream or upstream side of the formation, so that the local layering is not parallel to the direction of the overall deposit. Also, as a river flow varies seasonally, sand bars and braided river systems may evolve, and the grain size carried by the flow may also change, leading to a very intricate and heterogeneous rock structure with lenses of high or low permeability embedded throughout the rock (Figure 2.7). Such structures can have an enormous influence on the flow patterns and the dispersal or spreading of flow through the rock, as we explore in Chapters 5 and 10. An image of a fluvial deposit from the Dingle Peninsula in Western Ireland is shown in Figure 2.8a,b, illustrating cross-bedding and in the lower panel a fault which runs orthogonal to the bedding direction. Some sedimentary deposits are very complex and involve layers of larger pebble-sized rocks interspersed with finer grain deposits as shown in Figure 2.8c.

(a)



(b)



(c)



Figure 2.8 (a,b) Photographs of a fluvial deposit, Dingle Peninsula, Ireland, illustrating the intricate pattern of cross-bedding, and the local variability in grain sizes and layer permeability. The lower panel illustrates a fault running orthogonal to the bedding direction. (c) Photograph of very heterogeneous layering in a sedimentary deposit at Point Lobos, California, showing pebble laden deposits, of order centimetres in size, interleaved with fine sandy deposits. A black and white version of this figure will appear in some formats. For the colour version, please refer to the plate section.

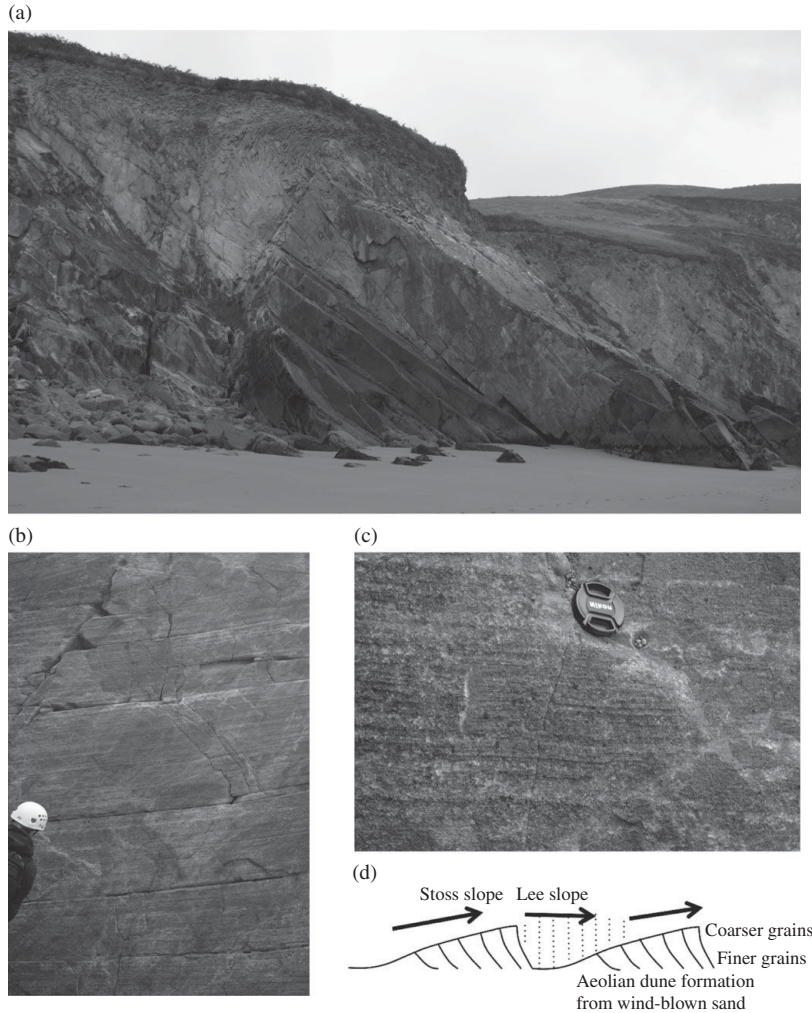


Figure 2.9 (a–c) Photograph of an aeolian deposit in the Dingle Peninsula, Western Ireland, illustrating (a) the lee side of the slope, with multiple parallel layers and (b,c) close-ups of the layering showing the highly stratified nature of the layering on both metre and centimetre scales. (d) Schematic to illustrate the formation process of aeolian dune formation, with successive layers forming as the dune migrates. A black and white version of this figure will appear in some formats. For the colour version, please refer to the plate section.

2.4 Aeolian

Aeolian deposits result from wind-blown sand which often forms dunes. Typically, the deposits are formed of grains with similar size and include a series of parallel layers, associated with the seasonal avalanching and deposition on the lee side of the dune.

Figure 2.9 illustrates an image of an aeolian deposit, showing the very anisotropic structure of the formation, which tends to favour flow down the lee side of the dune parallel to the layers. As the grains avalanche down the lee side of the slope, the grains become progressively finer grained, so that the pore size and permeability progressively decrease towards the base of the dune (see next chapter). This leads to a very stratified permeability structure, both across the layers and also along the layers. The lower panel shows the layers in the deposit running from left (top of deposit) to the right (base of deposit). Each layer has some changes in depth along the formation.

2.5 Compaction

Post-depositional processes can also be critical for the evolution of sedimentary rocks. The sediment layers are typically compressed as they are buried and the water within the sediment is driven out owing to the stress imposed by the overlying rocks. This process, known as compaction, can lead to deformation of the sediment if the vertical permeability structure is non-uniform and leads to accumulation of water-rich and hence buoyant layers below low permeability seal layers (Figure 2.10). In addition, regional stresses resulting from the relative motion of different parts of the surface can lead to folding and faulting of the strata. This can add further complexity to the topology of an oil-bearing rock.

Folding and faulting can also lead to compartmentalisation of a reservoir if a fault cuts through a permeable layer allowing relative movement along the fault of the geological strata on each side of the fault. Such compartmentalisation can lead to small pockets of permeable rock which have poor or no communication with neighbouring compartments. If the faults become impermeable through subsequent mineral precipitation then wells may be required in each compartment in order to produce the fluids within.

Figure 2.10a illustrates a small sand-injection structure which has been exposed on a horizontal surface. Also shown is a deformation structure, of scale 0.5 m in height and 1 m in length (Figure 2.10b), in which a layer of sediment has been distorted following formation. Fluid migrating through such a rock would follow the tortuous pathway along the fold, within each of the flow-units in the formation. This would decrease the effective permeability of the rock and lead to a different pattern of flow streamlines than may be envisaged in a uniform homogeneous sand. Figure 2.10c illustrates the presence of a large fold in one layer 15–20 m thick in a deposit in the Tabernas Basin in Spain. This fold involves a series of the individual depositional layers in the rock. Modelling flow in such a structure is difficult, owing to the range of lengthscales required in a model; also, detecting the precise shape of such structures is likely to be difficult from remote observation again leading to imprecision in the ability to model flow through such a system.

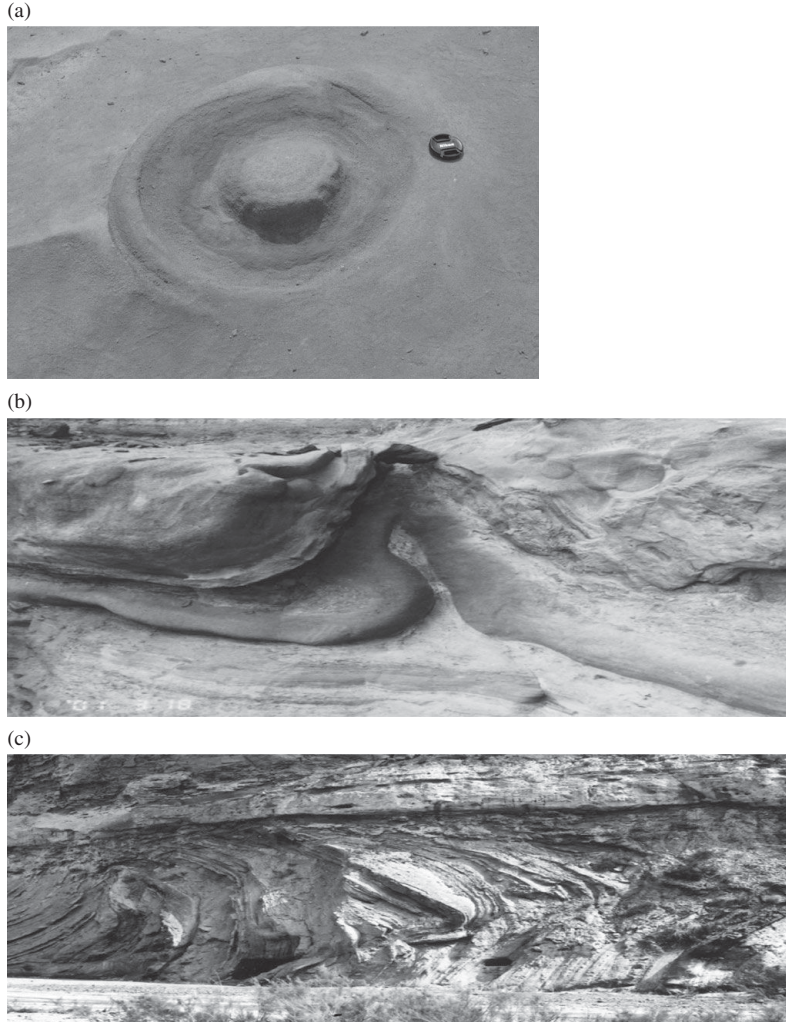


Figure 2.10 Photograph of (a) a small sand-injection structure breaking through on overlying layer of sediment; (b) a side view of a small-scale deformation structure in the formation, with a vertical scale of about 50 cm and length 1 m; (c) an illustration of the folding of sediment layers following deposition in a turbidite deposit in Tabernas Basin, southern Spain. Here the scale is about 15–20 m. A black and white version of this figure will appear in some formats. For the colour version, please refer to the plate section.

2.6 Carbonates

Carbonate reservoirs are built up in shallow, hot, marine environments and can be very complex structures. Reservoirs include oolitic limestone, mudstones and also reef

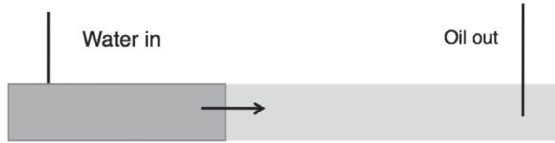
deposits. Ooids are small near-spherical particles of carbonate which precipitate from the supersaturated marine waters. These particles gradually grow as they move towards shore, and may build dune structures, ultimately forming oolitic limestone. This is a very permeable rock with a well-defined grain size. In contrast, mud flats are composed of very small particles and so are highly impermeable, although they may include fragments of shells or other larger particles. These can lead to local layers of high permeability which may provide dominant pathways through the system, causing water floods to short-circuit through the rock. Also, biota can lead to horizons of high permeability within these layers and such layers can act as high permeability lenses or conduits, which can again divert fluids injected into such rocks (Chapter 3).

2.7 Modelling flow in complex rocks

The above brief tour through some reservoir rocks has identified, in a simplified fashion, the complexity and variability in the structure of permeable rocks which are host to oil fields and geothermal reservoirs, and possible sites for CO₂ sequestration or geological waste repositories. Given that such reservoirs are in the subsurface, it is not possible to map out all of the detailed structure of the geological strata in order to build a model, although different well-logging and seismic techniques can lead to a reasonably detailed picture of the system on scales of 10–20 m. Ideally, one might then develop effective flow models of the geological strata which are sufficiently flexible to accommodate the uncertainty in the detailed structure of the formation. However, this is a non-trivial task, especially when processes which operate at very small scales, such as capillarity, can influence the predictions at large scale.

For example, a simple, yet surprisingly complex, modelling question is to assess the potential fraction of the oil in place which may be recovered from a reservoir, given a particular extraction strategy. Suppose we consider one of the turbidite layers at the Loop Head cliffs and adopt a strategy of producing oil from the layer by injecting water into one well and extracting oil at a second well as it is displaced by the injected water. With time, we envisage that the water front migrates to the production well and eventually breaks through. Following water breakthrough, the effectiveness of the water flood is reduced as the water begins to short-circuit through the reservoir (Figure 2.11) and the rate of growth of the region of the reservoir flooded with water decreases.

In order to predict the potential production from a reservoir, first, one might calculate the volume of oil in the system which can be produced at a production well through the injection of water (Figure 2.11). To this end, one needs to estimate the average porosity of the rock, ϕ , and the volume of the reservoir which is likely to be swept by the water. This depends on the location of the boundaries relative to the wells and the distribution of pressure and hence pressure gradients which develop in the reservoir. The fraction of



Time evolution

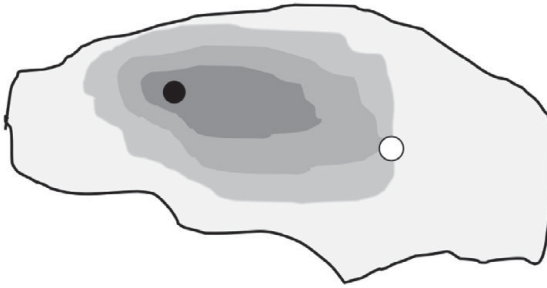


Figure 2.11 Schematic of the flow involved in oil production from a laterally extensive layer by water flooding. The water progressively sweeps the oil towards the production well.

the reservoir from which one can reasonably expect to displace the oil may also depend on the geological complexity of the system, in terms of layers, baffles, compartments, folds, as seen in the figures above. A part of this estimation process also relates to the volume of water which can be injected into the reservoir on an economic timescale. Finally, we require parameterisations of the processes at smaller scales. For example, the fraction of oil which can be displaced from the system depends on the details of the displacement of oil by water within each pore; the key to this is to determine the fraction of the oil which is retained in pore spaces by capillary forces, overcoming the viscous stresses exerted by the passing water.

Combining all these calculations leads to an estimate of the fraction of the total oil which can be recovered. This typically represents about 5–10% of the rock volume, and 10–50% of the pore space. Indeed, to date many of the oil fields in the North Sea have recovered only 35–40% of the oil in place. Recovery of additional oil is more challenging and requires an understanding of the distribution of oil in the field, a model of the geological structure in sufficient detail to drill infill wells appropriately and perhaps the use of some chemical systems, such as surfactants or polymers, to reduce the short-circuiting of water through the field to the producing well. In order to determine these values with more precision, more detailed models can be developed to quantify the different physical and chemical processes. However, even with more detailed models, there still remains uncertainty about the description of the topology of the reservoir, including the location of the boundaries, and the details of the total pore space and its distribution within these boundaries. Quantification of such uncertainty

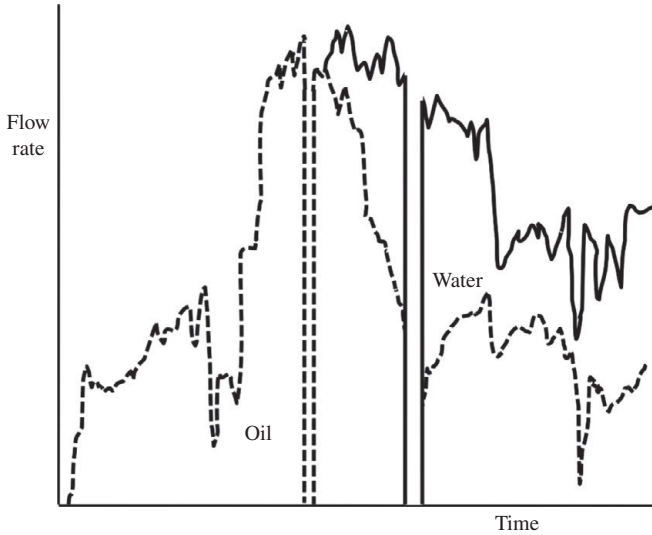


Figure 2.12 Time series of data illustrating the production of oil (dashed line) and then water and oil as a function of time during the water flooding of a North Sea reservoir. The water flux is given by the difference between the solid and dashed lines. The gaps in the data denote intervals of no production and serve to illustrate the complexity of water flooding and oil production, especially at offshore platforms. The long-term trend is a gradual evolution to less oil and more water production, with the overall flow rate decreasing after reaching the maximum. However, large short-term fluctuations arise in addition to the long-term trend.

is critical in establishing the possible range of recovery factors for the reservoir and identifies the limitations in the precision of any model of the system.

To help illustrate this discussion, in Figure 2.12, we present a typical example of oil and water production data from an oil field in the North Sea, offshore UK, over a period of about 1 year. In this field, the flow was largely controlled by one injection and one production well. It is seen that during the first quarter of the time shown on the plot, the oil rate was low, but then increased to a maximum, coincident with the successful deployment of water injection. However, soon after this, water arrived at the production well, with the difference between the solid and dashed line denoting the water flux. As a result, the oil–water ratio and the oil rate gradually decreased with time. The data illustrate the complexity of real operations, in which the total flow rate and oil–water ratio varies with time over a wide range of scales; some of this is associated with operational issues, while some is associated with the complexity of the flow system.

In order to model and quantify the different effects, we might build a hierarchy of models to account for the different elements which influence the process. As with much physical modelling, we examine the lengthscales in the problem, and then build models appropriate for each lengthscale (Figure 2.13).

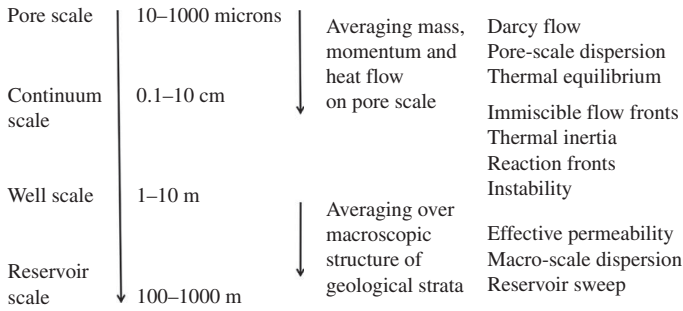


Figure 2.13 Illustration of the range of lengthscales involved in flow in porous rocks.

In modelling the flow between wells, spaced several hundred metres apart, it is difficult to include all the details of the flow at the finest scale (even if they were known). On the larger scale of individual layers in the geological strata, there are differences in the properties of each layer, and this can lead to differences in the flow rate and flow pattern in the different layers. As a consequence, if water is injected with uniform pressure into a series of layers in the reservoir, some layers may be swept of oil, with water breaking through to production well, long before others.

Guided by this discussion, and Figure 2.13, in Chapter 3 we introduce the governing equations for single-phase flow in a porous layer, modelled over a scale sufficiently large that there are well-defined continuum properties, and we then explore a series of problems to quantify pressure-driven flow in heterogeneous rocks, including the effects of multiple layers, lenses of high or low permeability, cross-bedding, seal rock and faults as expected from the different geological strata described in this chapter. In Chapter 4 we then assess how one might use such models, in combination with parameterisations of the uncertainty of the physical properties of the rock, to help establish the mean and range of flow behaviour expected in the system, and how such models may help inform engineering decisions.

In the remainder of the book, we then build from the simplified model of flow in heterogeneous rocks, to account for a number of additional physical processes which can influence the flow and transport of fluids. These include modelling dispersion at pore scale and on the larger scale of the geological heterogeneities. We also introduce models to describe interface instability when a less viscous fluid displaces a more viscous fluid. We assess the role of interfacial tension and wetting in controlling the structure of immiscible flows which arise when one fluid, for example water, displaces a second fluid, for example oil. Having considered these processes in the context of pressure-driven flows, we then turn the discussion to buoyancy-driven flows. We assess some of the effects of heterogeneities in permeable rocks in dispersing buoyancy-driven flows, as relevant for CO₂ sequestration. In Chapter 11, we consider heat transport through porous media, and explore the possible consequences of thermal inertia in controlling

buoyancy-driven flows, as arise in both oil fields and geothermal systems. Finally, in Chapter 12 we turn to compressible flows, relevant for gas production.

Guided by the complexity of the geology, which leads to considerable uncertainty in model predictions, the focus in this book is on developing a very simplified picture of the flows to build intuition about the different processes. Where possible we use simplified analytic solutions to illustrate the phenomena and complement more conventional numerical models of these complex flow processes. Inevitably, only a fraction of possible flow geometries and flow processes are explored in this volume, but the aim is to provide an introduction to a range of flow problems which illustrate the complexity but also fascination of flow in porous rocks. Indeed, many examples are guided by the geometry of laterally extensive, relatively thin layers of permeable rock, as described in this chapter, for which the flow is dominantly two dimensional.

3 Flow in porous rocks

Flow through porous rocks occurs in the connected pore space, with volume fraction or porosity ϕ . The interstitial speed of the flow corresponds to the actual speed of the fluid particles, and is denoted v_i in direction x_i . Owing to the variations of porosity with position in the rock, it is convenient to work with the volume transport. On a suitable lengthscale, L , larger than the grain size, but over which the porosity has a well-defined value, the volume flow in each direction u_i can be defined in terms of the interstitial speed in that direction, averaged over an area $A = L^2$,

$$u_i = \frac{1}{A} \int \phi v_i dA \quad (3.1)$$

The conservation of mass may then be written in terms of the Darcy or transport velocity \mathbf{u} in the form

$$\phi \frac{\partial \rho}{\partial t} + \nabla \cdot (\rho \mathbf{u}) = 0 \quad (3.2)$$

assuming the matrix is incompressible. With incompressible fluid this reduces to the simpler form

$$\nabla \cdot \mathbf{u} = 0 \quad (3.3)$$

Coupled with the mass conservation, we require an equation of motion. For many porous flow problems, the flow typically has a very low Reynolds number, and so for an isotropic medium we can relate the applied pressure gradient with the averaged viscous stress in the fluid, according to Darcy's law which has the form

$$\mathbf{u} = -\frac{k}{\mu} \nabla p \quad (3.4)$$

where k is called the permeability, a function of the size and shape of the grains, and the structure and packing of the porous medium composed of the grains or other pathways through the matrix. k has units of length² and in many permeable rocks has values of order 0.001–1.0 Darcy, where 1.0 Darcy = 10^{-12} m².

The assumption of low Reynolds number can be checked by writing the Reynolds number, $\rho v d / \mu$, where the density ρ has value 1000 kg/m³ and the viscosity μ has

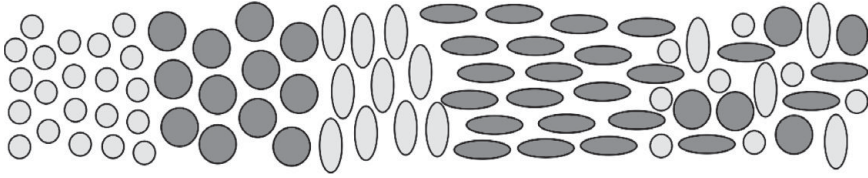


Figure 3.1 Illustration of different grain packing structures in a permeable matrix, leading to different forms of anisotropic permeability.

value of about $0.001 \text{ kg/m}^2/\text{s}$ for water. With grain size $d \sim 0.001\text{--}0.0001 \text{ m}$, and flow speeds v of 1 m/year , the Reynolds number is about 0.01 .

In an idealised system, composed of close packed glass ballotini, the permeability typically follows the Kozeny–Carman relation

$$k = \frac{\phi^3 d^2}{180(1 - \phi)^2} \quad (3.5)$$

where ϕ is the porosity. In general, however, with irregular shaped grains, the permeability requires measurement. The model for flow in porous rocks is usually more complex owing to the non-isotropic nature of many porous rocks. For example, the grains may be asymmetric, or there may be some clay or other particles in the mixture which result in preferred directions for flow (Figure 3.1). Indeed, after sediment is deposited, it is typically of high water content. As it gradually compacts and reduces its water content, as a result of the continually growing overburden of subsequent sediment, the grains may deform or preferentially align, leading to anisotropic permeability.

We can generalise Darcy's law to the form

$$u_i = -\frac{1}{\mu} K_{ij} \frac{\partial p}{\partial x_j} \quad (3.6)$$

where K_{ij} is the permeability tensor. With anisotropic media, the flow is no longer necessarily parallel to the pressure gradient and we consider this in the discussion of cross-bedding later in this chapter.

3.1 Source–sink flows

In many permeable rocks, the geological strata are highly layered (Chapter 2), and so many flows occur within the layers. If the distance between the injector and producer wells far exceeds the depth of the layer, then this leads to a flow which fills the depth of the layer and hence is effectively two dimensional. Numerous solutions for flows in such a planar two-dimensional geometry exist, especially in the case of steady flow of one fluid. Indeed, the flow can be expressed in terms of a streamfunction ψ and a potential ϕ_f (not to be confused with the porosity), where the potential is related to the pressure by the relation $p = -\mu\phi_f/k$, according to the relations

$$\mathbf{u} = \left(\frac{\partial \psi}{\partial y}, -\frac{\partial \psi}{\partial x} \right) = \left(\frac{\partial \phi_f}{\partial x}, \frac{\partial \phi_f}{\partial y} \right) \quad (3.7)$$

There are many books detailing techniques from the theory of complex variables to solve for such two-dimensional flows, with a variety of boundary conditions, for example by using the hodograph transform (e.g. Muskat, 1937; Bear, 1972) for two-dimensional flow. We do not plan to expand on such approaches herein, except to note that the solution for a source of strength m takes the form

$$\mathbf{u} = \frac{m}{2\pi r^2}(x, y) \quad \text{with} \quad \phi_f = \frac{m}{2\pi} \ln(r) \quad \text{where} \quad r^2 = x^2 + y^2 \quad (3.8)$$

A useful extension of this solution describes the flow from a source at position \mathbf{r}_1 towards a sink at the origin, with the flow confined within a circular impermeable boundary of radius R centred at the origin

$$\phi_f = \frac{m}{2\pi} \left[\ln |\mathbf{r} - \mathbf{r}_1| + \ln \left| \mathbf{r} - \frac{R^2}{r_1^2} \mathbf{r}_1 \right| - \ln |\mathbf{r}| \right] \quad (3.9)$$

In this solution, to ensure that there is no flow across the boundary $r=R$, we have introduced the image source outside the boundary at position $\frac{R^2}{r_1} \mathbf{r}_1$. Owing to linearity, a number of solutions of this form can be superposed, for example to represent a multiple source and sink flow within a finite domain. The closed form solution is also useful for estimating the swept volume of a reservoir after a finite time, in the case that a reservoir is developed using vertical wells, and in the case that the injection fluid is of comparable viscosity to the formation fluid. To this end, we integrate along each streamline to find the location of the leading edge of the injected fluid after a given time.

In Figure 3.2, we illustrate the potential, ϕ_f , for the flow associated with a source–sink pair located at $x=50$ and $x=-50$ in a circular domain of radius 100. We can calculate the path followed by a ring of particles released from the injection well at time $t=0$ at a number of successive times by using the velocity field associated with this source–sink pair. The position of the particles at each time are calculated numerically using the analytical expression for the flow field in the cases that the source and sink are located at $x=9$ and -9 with the domain of radius 10 (Figure 3.3). It is seen that the swept area develops a tear drop shape as the flow advances through the porous medium. Eventually the fluid reaches the sink and some injection fluid is then extracted, reducing the sweep of the remaining porous layer.

In some situations, reservoirs are developed using horizontal wells; these are drilled using a drill bit which can establish an angle with the drilled hole, and thereby change direction of the hole. In that case, we can model the flow with line sources and sinks. If the spacing between such horizontal sources and sinks is comparable to the length of the wells, or if the flow domain is essentially a long channelised system, with channel width much smaller than the spacing between the wells, then the flow may be approximated, to leading order, as having one horizontal dimension. If the reservoir

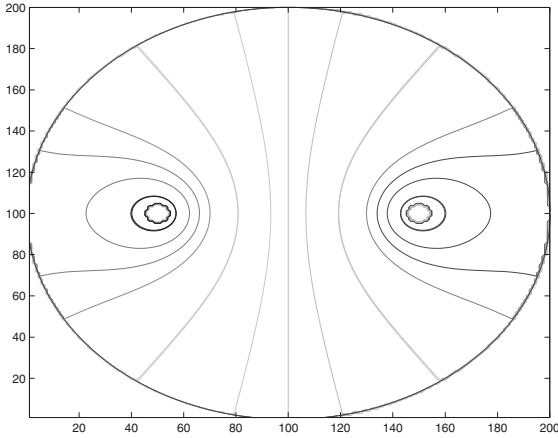


Figure 3.2 Potential field for a source–sink flow confined within a circular boundary. Source and sink are located along a common diameter, each midway between the centre and the circumference of the model reservoir. A black and white version of the figure will appear in some formats. For the colour version, please refer to the plate section.

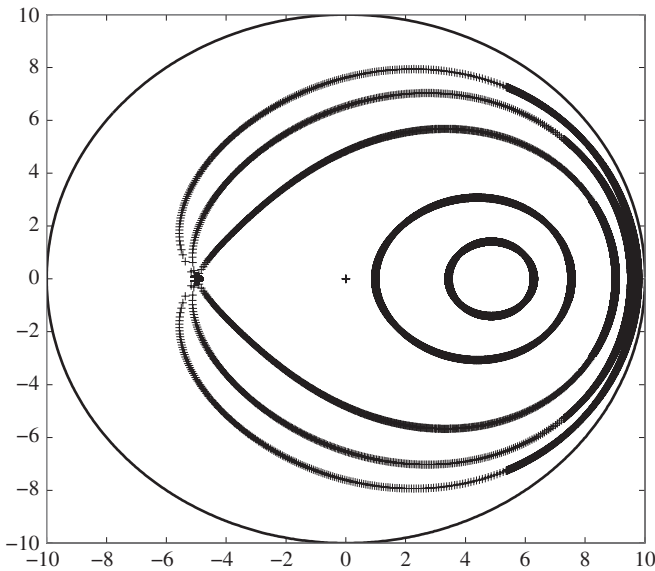


Figure 3.3 Illustration of the migration of a pulse of tracer released into the flow at the injection well as it is carried by the flow towards the producing well. Flow has the potential field shown in Figure 3.2. Curves correspond to the position of the tracer at different times following release. The shape of the outer domain is circular. The area within the tracer provides a simplified picture of the area of the reservoir from which the oil has been swept (although effects of fractional flow will be added to this picture in Chapter 7).

has vertical variations in the permeability associated with isolated shale or clay layers, this can lead to a vertical structure in the flow, depending on whether these baffles lead to hydraulic isolation or reduced hydraulic coupling of different layers in the reservoir. We now consider some of these effects.

3.2 Sweep and flow in a two-layer system

As a simple example of the use of Darcy's law we can consider flow in a confined layered permeable rock, including the case in which the flow is parallel to the strata and perpendicular to the strata (Figure 3.4a,b).

In the case of flow in series (Figure 3.4a), driven by a pressure decrease across the medium from pressure P_A to P_C we apply Darcy's law to the first section of the medium, $0 < x < L$, with permeability k_1 and the second section, $L < x < 2L$, with permeability k_2 to find that in order that the flow is uniform the pressure P_B is given by the algebraic mean of the two pressures at the end of the sample,

$$P_B = \frac{k_1 P_A + k_2 P_C}{k_1 + k_2} \quad (3.10)$$

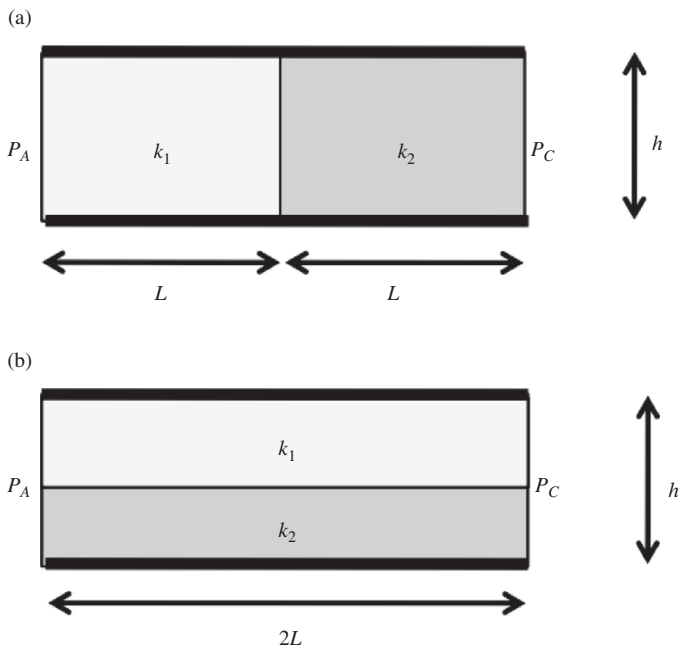


Figure 3.4 (a) Flow perpendicular to the strata; (b) flow parallel to the strata.

and thereby we find the flow has the corresponding uniform Darcy flow throughout the sample,

$$u = \frac{2k_1k_2}{(k_1 + k_2)} \frac{(P_A - P_C)}{2\mu L} \quad (3.11)$$

In the case in which the samples are arranged in parallel, as shown in Figure 3.4b, then, assuming the samples are in good contact all along the boundary, the pressure in both layers will be the same at each position along the boundary. This leads to the result that the vertically averaged Darcy flow is given by

$$u = \left(\frac{k_1 + k_2}{2} \right) \frac{(P_A - P_C)}{2\mu L} \quad (3.12)$$

It follows that the effective permeability of the layers when arranged in parallel is greater than with the layers in series, except for the case $k_1 = k_2$ when they are identical. This leads to the interesting question of how to maximize the flux of original formation fluid at the production well through injection of a second fluid. The case of flow in parallel leads to a greater flux at early times; this is because the flow speed in the high permeability layer is larger than that in the low permeability layer, and so this layer is swept of original fluid very rapidly. Once this layer is swept, however, the flux of original formation fluid through the layers in series becomes greater; as a consequence, all the original fluid is swept from the system with the layers in series before the low permeability layer is swept in the case in which the layers are in parallel (Figure 3.5a).

The value of the production typically decays exponentially with time according to models of economics in which value is discounted with time. This leads to a net present value of some future production at time t given by

$$V(t) = V_o \exp(-\lambda t) \quad (3.13)$$

where V_o is the present value of that production, and λ is related to the discount rate in that $1/\lambda$ is the time for the value to decrease by a factor e . In order to evaluate the net present value of a scheme, we therefore integrate into the future the product of the value and the production rate (Figure 3.5b). Depending on the discount rate, this may imply the rapid early production associated with flow in parallel is most valuable, or that the later, higher flux in the production associated with the layers in series is more valuable.

In the case of flow in parallel, once the higher permeability layer is all swept, then some of the injection fluid is produced. In the analogous situation of oil recovery, this would correspond to water and oil being co-produced. This adds a second challenge which is the need for separation of the produced water from the oil and then disposal of the produced water which can be costly owing to the need to filter/clean this water. In some reservoirs, the effect of such short-circuiting of the reservoir, as for the parallel flow model, driven by the injection of liquid leads to the water production rate being over ten times the oil production rate. Ultimately, the ability to process the

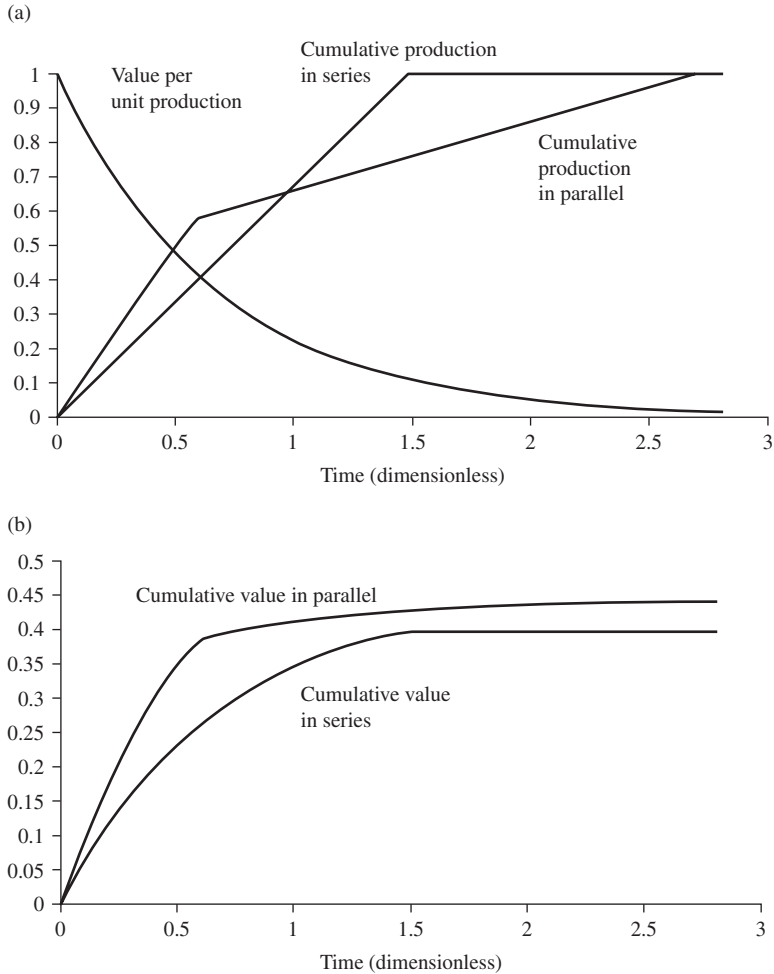


Figure 3.5 Example calculation comparing (a) the cumulative production and (b) the cumulative value with time from a system with the layers in parallel and the layers in series. In this specific case, the discount rate is sufficiently rapid that the cumulative value for the parallel arrangement exceeds that for the series arrangement.

produced water economically may become a rate-limiting factor in the late-life economics of a well and hence on the overall fraction of the original oil in place which can be recovered. However, in Chapter 8, we illustrate the potential for the use of polymers in reducing this problem by the process of flow diversion.

3.3 Sweep in a multi-layer system

Although the above example is very helpful in identifying some of the challenges of producing oil, many rocks are composed of multiple sedimentary layers with different

permeability and hence different flow speeds and rates of sweep. In a laterally extensive system, in which there are wells placed a large distance apart relative to the thickness of the layers, then if we assume that the wells open into each of the layers, that the layers are independent, and that the two liquid phases have the same viscosity, μ , then the pressure will vary at a similar rate through each layer. As a result the net flow will be given by

$$Q_{total} = \frac{\sum h_i k_i}{\mu} \frac{\partial p}{\partial x} \quad (3.14)$$

while the flow in layer i is

$$Q_i = \frac{h_i k_i}{\sum h_i k_i} Q_{total} \quad (3.15a)$$

with k_i and h_i the permeability and thickness of layer i . The time of flight in layer i , given by the travel time over the well–well distance L , has value

$$t_i = h_i L \phi / Q_i \quad (3.15b)$$

The effect of the variable time of flight is that in different layers the injected fluid (water) arrives at the production well at different times. This leads to a gradual evolution of the flow rate of original fluid (oil) at the production well. For example, we have calculated the flux through a simplified model of a 20-layer rock (cf. the Loop Head turbidite, Figure 2.3b), in which there is a range of permeabilities as shown in Figure 3.6a. This leads to a variation in the fraction of the flow in each layer, and hence the travel time of the fluid through each layer (Figure 3.6b). In turn, the fractional flow of injected fluid increases with time as the injected fluid in each layer arrives at the production well (Figure 3.6c). The time to sweep the lowest permeability layers may be much longer than that required to sweep the highest permeability layers, and this leads to some of the difficulty in recovering oil from a layered reservoir.

3.4 Lenses and trapping

As well as the effects of layering impeding efforts to recover all of the original fluid in the formation, lenses of low or high permeability in the formation can lead to the flow bypassing large regions of the rock, and thereby limiting the efficiency of the sweep. For example, if there is a laterally extensive lens of permeability k_2 and thickness d embedded in a layer of sediment of permeability k_1 and thickness H , perhaps as a result of dune formation or reworking of sand and silt in a tidal zone during the formation of the rock, then as fluid migrates through the rock it may be diverted into the lens if it has higher permeability than the formation, or otherwise will be diverted around a lens of low permeability (cf. Figure 3.7).

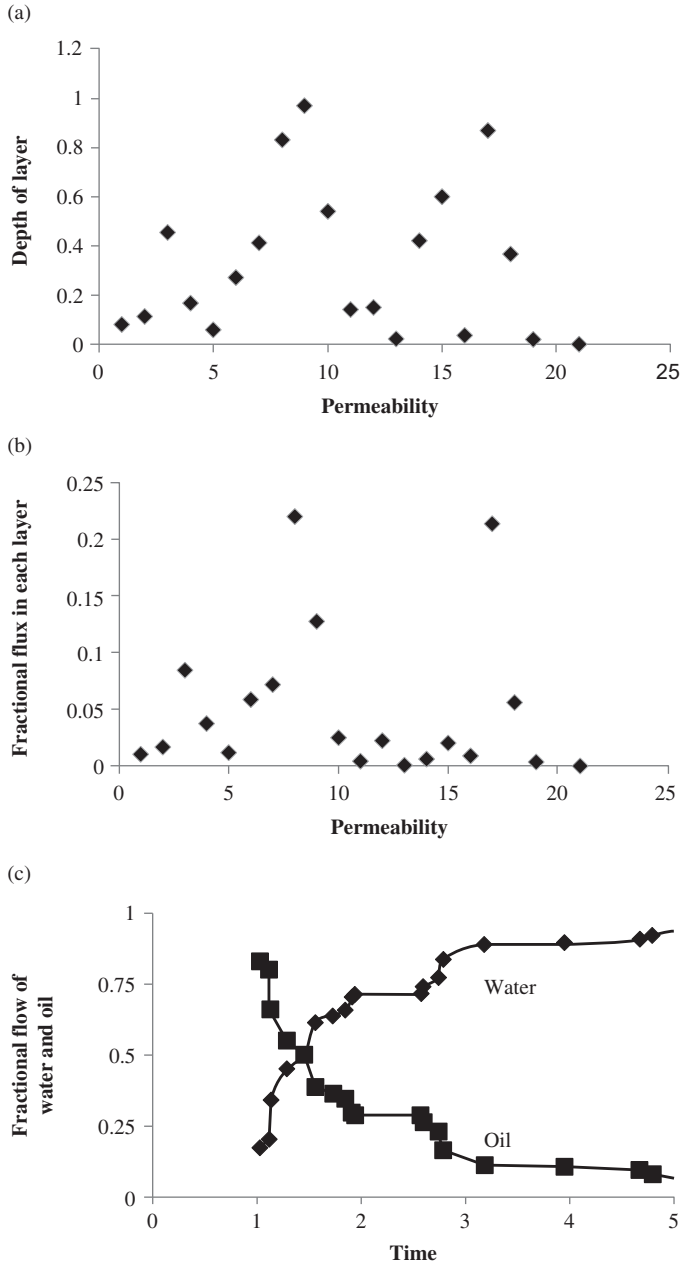


Figure 3.6 (a) Variation of the thickness and permeability in a model 20-layer reservoir; each dot corresponds to one layer. (b) Fraction of the flow in each layer as a function of the permeability of the layer, where the thickness of each layer is shown in (a). (c) The fraction of the total flux composed of the injection fluid, as a function of time. The progressive sweep of water through the high permeability layers leads to successive watering out of the layers, and an increase in the water production rate.

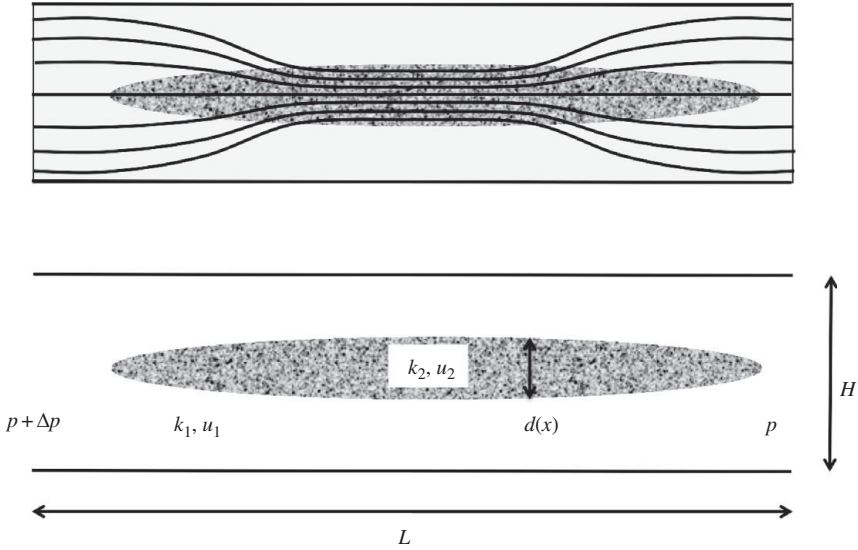


Figure 3.7 Flow diversion into a lens of high permeability

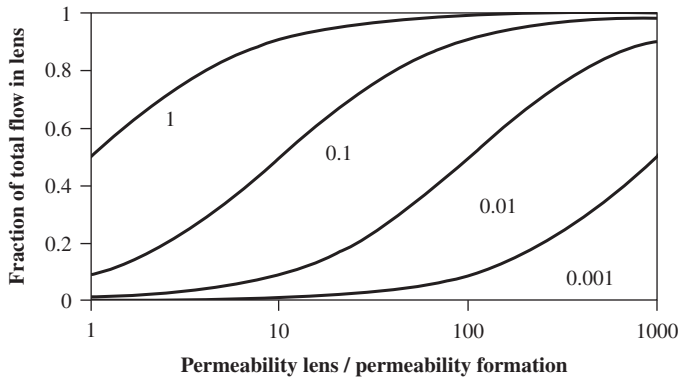


Figure 3.8 Fraction of the flow which bypasses the formation through a high permeability lens, as a function of the permeability ratio and thickness of the lens as a fraction of the total layer depth, d/H , shown by the numbers on the curves.

Providing the lens is much longer than the width H , then in the region of the lens the pressure gradient is approximately the same inside and outside the lens, so a flow in the along layer direction will be partitioned into a fraction in the lens F and a fraction outside the lens, $1 - F$, in the proportion

$$\frac{F}{(1 - F)} = \frac{k_2 d}{k_1 (H - d)} \tag{3.16}$$

with the total flow Q in the formation being given by

$$Q = -\frac{1}{\mu} [k_1 (H - d) + k_2 d] \frac{dp}{dx} = -\frac{H \bar{k}}{\mu} \frac{dp}{dx} \tag{3.17}$$

Globally the flux through the formation has value

$$Q = \frac{H \Delta p}{\mu \int_0^L \frac{dx}{\bar{k}}} \quad (3.18)$$

in terms of the pressure drop across the layer, Δp . We can then find the local speed in the lens, $u_2(d)$, which is a function of the thickness of the lens, $d(x)$, and also the speed outside the lens, $u_1(d)$, in terms of the total flux and the permeability ratio, with values given by

$$u_2(d) = \frac{k_2}{k_2 d + k_1(H - d)} Q \quad \text{and} \quad u_1(d) = \frac{k_1}{k_2 d + k_1(H - d)} Q \quad (3.19)$$

It is interesting to note that the flux ratio may be as large as 10:1 even if the lens is only 1 m thick in a layer of thickness 100 m, provided the permeability ratio is 1:1000. This may be realistic with relatively large grains in the lens, and smaller grains, mixed with clay in the remainder of the formation. In this case, most of the formation is bypassed, and 90% of the flow passes through the thin high permeability streak. The remaining fluid in the formation will then require a much longer time to be displaced than may be estimated based on the layer thickness and the flux. Indeed, without the lens, for the same pressure gradient, the flux would be reduced to about 0.1 of the value with the lens.

One of the key features of this flow is the range of travel times of fluid particles from one end of the porous layer to the other, which, in turn, depends on the time spent in the lens of high permeability. In the simple parallel flow model, with a symmetric lens, located in the centre of the aquifer, then for a total flux, Q , we can label the streamfunction which passes through the boundary between the lens and the surrounding medium when the thickness of the lens is d as $\psi(d)$. In travelling from the point $x = 0$ upstream to a point $x = L$ downstream, the time a particle spends within the lens travelling along this specific streamline, $\psi(d)$ say, is given by

$$t_2(d) = \phi \int_{x_1(d)}^{x_2(d)} \frac{dx}{u_2} \quad (3.20)$$

where the lens has thickness d at points x_1 and x_2 . It also spends a time

$$t_1(d) = \phi \int_0^{x_1(d)} \frac{dx}{u_1} + \phi \int_{x_2(d)}^L \frac{dx}{u_1} \quad (3.21)$$

outside the lens, in the regions upstream and downstream of the lens. The total travel time is then given by $t_1(d) + t_2(d)$ in travelling from $x = 0$ to $x = L$, assuming the lens thickness increases monotonically to a maximum and then decreases back to zero.

If we follow streamlines which cross the lens at different times, the travel time also changes as more or less time is spent in the lens. This has a key effect in controlling the shape of a pulse of tracer injected into the formation, and hence in dispersing the pulse; we explore this further in Chapter 5.

3.5 Wavy layers

In some rocks, the boundary between successive layers may be wavy or sinuous owing to the depositional environment; for example, in shallow marine settings where wave and tidal action combine to generate sand bars. In this case, the effective permeability of the formation and the fraction of the formation which may be swept by the flow will depend on the spatial distribution of the different layers. In Figure 3.9a, we show an image of a shallow marine sediment, illustrating a wavy horizon within the strata. A simple model of a wavy interface between the two layers of rock, with depth

$$d(x) = H(0.5 + a \sin(2n\pi x/L)) \quad (3.22a)$$

of one layer and $H - d(x)$ of the other layer, leads to the integral expression for the effective permeability in a region $0 < x < L$ which is host to n waves in the interface

$$\bar{k} = \frac{L}{H} \left[\int_0^L \frac{dx}{k_1 d(x) + k_2 (H - d(x))} \right]^{-1} \quad (3.22b)$$

In this model, we assume the upper and lower boundary of the domain is sealed. For such a sinuous interface, centred in the middle of the domain (Figure 3.9b), the effective permeability then depends on the amplitude of the wavy interface, aH (Eq. 3.22a) and the permeability contrast between the layers, k_2/k_1 as shown in Figure 3.10. With a permeability ratio of 1:10 and a wave amplitude $a = 0.25$ of the total layer thickness, the permeability is a fraction 0.502 of the maximum permeability, k_1 , whereas with two parallel layers, and no sinuous interface, the permeability is a fraction 0.55 of the maximum. Such reductions in the effective permeability, resulting from the regions where there is a thicker zone of low permeability rock, can lead to reduced flow rates and production as compared to the parallel-sided two-layer model. In Chapter 10, we return to wavy horizons in the context of buoyancy-driven flow, and explore how they can lead to trapping of gas or CO_2 .

3.6 Seal layers

In the examples described above concerning layered rocks, we have assumed the layers are in good pressure communication, and then illustrated the associated flow patterns. However, if there is a low permeability seal layer, with permeability k_b , between successive layers of reservoir rock, of permeability k_u and k_l , then this can limit the flow between successive layers in the formation and pressure gradients may develop between the layers. In turn, such low permeability layers may limit the vertical extent of the sweep of fluid through a reservoir. In order to illustrate the effect, we can consider

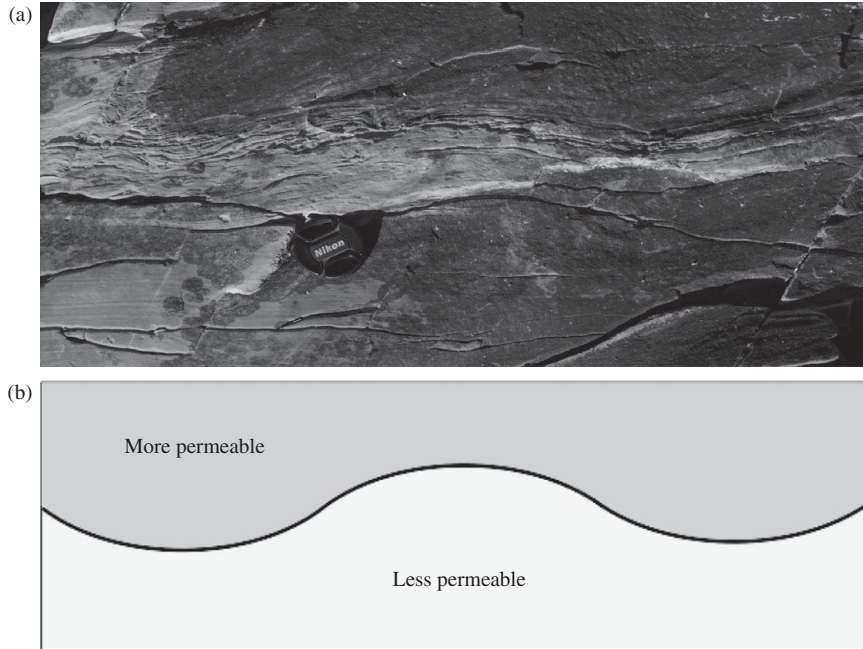


Figure 3.9 (a) Illustration of a wavy horizon in a shallow marine sediment in the Dingle Peninsula, South West Ireland; (b) cartoon of a sinuous interface used in the modelling of effective permeability. A black and white version of this figure will appear in some formats. For the colour version, please refer to the plate section.

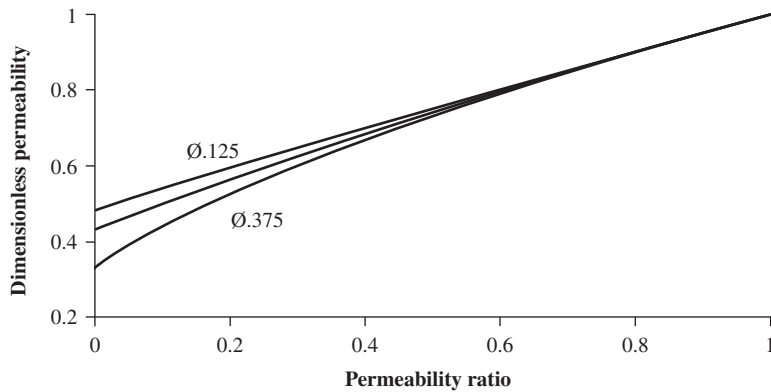


Figure 3.10 Calculation of the dimensionless permeability of layers with sinuous interfaces, for the case in which the amplitude of the wavy interface a/H is 0.125, 0.25 and 0.375, with the two outer values labelled on the graph. Values are shown for different values of the permeability ratio. The permeability is scaled relative to the value of the more permeable layer.

the two-dimensional flow in the case in which a two-layer reservoir has an injection well and producing well located within the same layer, a distance L apart, and a thin low permeability layer, of thickness b , separating this from a second permeable layer. We assume for simplicity that the outer boundary of each of these layers is imperme-

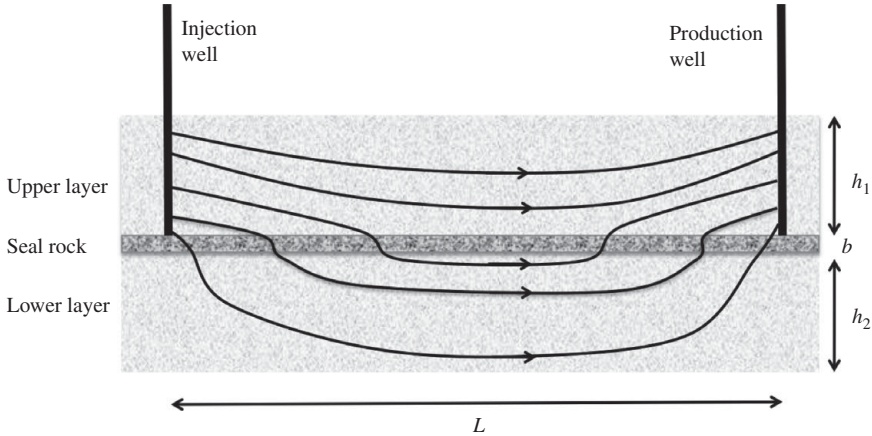


Figure 3.11 Flow from an injector to a producer through a two-layer permeable rock in which the layers are separated by a low permeability seal layer. The flow migrates across the low permeability seal layer into the lower high permeability layer, leading to an increase in the effective thickness of the flow domain which is being swept.

able. We can then explore the fraction of the flow which migrates through neighbouring permeable layers as a function of the permeability and thickness of the seal rock, and the permeability and thickness of the two permeable layers (Figure 3.11). As may be typical, we assume that the interwell spacing is large compared to the vertical extent of the layers, so that there is a large surface area connecting the two layers.

To solve for the flow in such a long, thin reservoir, we observe that to leading order the flow will be parallel to the line joining the wells, but that there will be a slow leakage flow between the two layers associated with the pressure mismatch between the layers. Near the injector well this will drive the flow into the second layer, while near the producer well this will drive the flow back into the primary layer in which the wells supply and extract the flow (Figure 3.11). Given the separation of the scales between the along-layer and cross-layer flow, we will develop an approximate solution, by expanding in terms of the small aspect ratio of the layers. First, however, it is worth noting the two limiting physical balances in the problem. If $k_b/b \ll k_u/L$, then the resistance to flow through the seal rock is small compared to the resistance to flow through layer 1 from the injector to the producer. In this limit, there will be near pressure equilibrium between the layers, and a substantial volume swept through the lower layer, with the total flux scaling as $(k_u h_u + k_l h_l) \Delta P / L \mu$, where k_u and k_l are the upper and lower layer permeabilities and h_u and h_l the upper and lower layer depths. In the other limit, $k_b/b \gg k_u/L$ then the resistance to flow across the layers is large compared to the resistance to flow from the injector to producer, and so the flow will largely be limited to the upper layer in which the fluids are injected, so that the flux will tend to the value $k_u h_u \Delta P / \mu L$.

We now develop an asymptotic expansion to capture the details of the transition from one of these regimes to the other. It is convenient to work with dimensionless

equations, and so we scale the spatial coordinates (x, y) in terms of the length and thickness, (L, h_u) , of the primary layer containing the wells, to define dimensionless coordinates (\hat{x}, \hat{y}) . We also assume that the pressure relative to the background P is scaled relative to the pressure difference between the injector and producer well, ΔP , so that the dimensionless pressure is given by $\hat{p} = P\Delta P$. Finally we use subscripts $i = u, l$ to denote the property of the primary layer, $i = u$ and secondary layer $i = l$. (Note the ‘adventurous’ reader could extend the approach to explore the flow in a multi-layer system.) The reference velocity is $U = k_u\Delta P/\mu L$ and the dimensionless velocities are then $\hat{u}_i = u_i/U$. Darcy’s law requires that in layer i

$$\hat{u}_i = -\frac{k_i}{k_u}\nabla\hat{p}_i \quad (3.23)$$

and combining this with the equation for continuity, we find

$$\epsilon^2\frac{\partial^2\hat{p}_i}{\partial\hat{x}^2} + \frac{\partial^2\hat{p}_i}{\partial\hat{y}^2} = 0 \quad (3.24)$$

where $\epsilon = H/L$.

The boundary conditions for the problem require that the dimensionless pressure at the two ends of the upper layer, $\hat{x} = 0$ and $\hat{x} = 1$, are given by

$$\hat{p}_u(0) = 1 \quad \text{and} \quad \hat{p}_u(1) = 0 \quad (3.25)$$

In this calculation, we aim to find the dimensionless horizontal speed of the flow in the upper layer at both $\hat{x} = 0, 1$. The quantity

$$\left.\frac{\partial\hat{p}_u}{\partial\hat{x}}\right|_{\hat{x}=0} - 1 \quad (3.26)$$

denotes the dimensionless increase in the flow speed, relative to the single layer case, owing to any flow through the lower permeable layer.

In the lower, secondary layer we require

$$\frac{\partial\hat{p}_l}{\partial\hat{x}} = 0 \quad \text{at} \quad \hat{x} = 0, 1 \quad (3.27)$$

since there is no flux in that layer through the end boundaries of the domain, $\hat{x} = 0, 1$. In addition, there is no flow through the upper and lower horizontal boundaries of the two-layer domain, which we assume to be impermeable. This leads to the constraint

$$\frac{\partial\hat{p}_u}{\partial\hat{y}} = 0 \quad \text{at} \quad \hat{y} = 1 \quad \text{and} \quad \frac{\partial\hat{p}_l}{\partial\hat{y}} = 0 \quad \text{at} \quad \hat{y} = -H_2 \quad (3.28)$$

where $H_2 = h_l/h_u$. Finally at the interface between the two layers, we require that the flux normal to the boundary is continuous, and given by the flux across the low permeability seal layer

$$\frac{\partial \hat{p}_u}{\partial \hat{y}} = K \frac{\partial \hat{p}_l}{\partial \hat{y}} = \omega (\hat{p}_u - \hat{p}_l) \quad (3.29)$$

where $\omega = \frac{h_u k_b}{kb}$ and we assume the seal layer has depth $b \ll h_u, h_l$ and permeability $k_b \ll k_u$.

To proceed we introduce a power series expansion for the pressure in each layer,

$$\hat{p}_i = \hat{p}_i^o(\hat{x}, \hat{y}) + \epsilon^2 \hat{p}_i^1(\hat{x}, \hat{y}) + \dots \quad (3.30)$$

and, in developing the solution, we determine a consistency condition for the boundary condition (3.29).

The leading order solution for the flow involves two functions $\hat{p}_i^o(\hat{x}, \hat{y})$, one for each of the layers. On inspection it is seen that there is no dependence on the vertical coordinate \hat{y} owing to the boundary condition along the upper and lower impermeable boundaries of the domain. This implies there is a near uniform horizontal flow in each layer at each position \hat{x} , which can slowly change owing to the leakage between the layers. In order to determine the functions $\hat{p}_i^o(\hat{x})$ we are required to solve the $O(\epsilon^2)$ problem relating to the flux across the boundary; in solving this we also require that the flux associated with the cross-layer flow changes slowly along each layer, for consistency, so that the flow remains approximately parallel.

The second terms in the perturbation expansion for each layer satisfy the differential equations for $i = u, l$

$$\frac{\partial^2 \hat{p}_i^1}{\partial \hat{y}^2} = -\frac{\partial^2 \hat{p}_i^o}{\partial \hat{x}^2} \quad (3.31)$$

and these equations have solutions

$$\hat{p}_u^1(\hat{x}, \hat{y}) = -\frac{\partial^2 \hat{p}_u^o}{\partial \hat{x}^2} \left[\frac{\hat{y}^2}{2} - \hat{y} \right] + f_u(\hat{x}) \quad (3.32a)$$

$$\hat{p}_l^1(\hat{x}, \hat{y}) = -\frac{\partial^2 \hat{p}_l^o}{\partial \hat{x}^2} \left[\frac{\hat{y}^2}{2} + H_2 \hat{y} \right] + f_l(\hat{x}) \quad (3.32b)$$

Here $f_u(\hat{x})$ and $f_l(\hat{x})$ are unknown functions which can be determined by higher order terms in the expansion. The vertical structure of the solutions (3.32a,b) has been selected to satisfy the boundary conditions at the top, $\hat{y} = 1$, and bottom, $\hat{y} = -H_2$, impermeable boundaries. At the interface between the two layers, $\hat{y} = 0$ we then have

$$\epsilon^2 \frac{\partial^2 \hat{p}_u^o}{\partial \hat{x}^2} = -\epsilon^2 K H_2 \frac{\partial^2 \hat{p}_l^o}{\partial \hat{x}^2} = \omega [\hat{p}_u^o - \hat{p}_l^o] \quad (3.33)$$

In the case $\epsilon \ll \omega$, we require $\hat{p}_u^o \sim \hat{p}_l^o$ so that the flux in the upper and lower layers are similar; the analysis then breaks down in detail near the points $\hat{x} = 0$ and $\hat{x} = 1$ since there is a narrow boundary layer across which there is flow from the upper layer to the lower layer. In the case $\epsilon \gg \omega$, we require $\hat{p}_u^o = 1 - x$ and $\hat{p}_l^o = 0$ so the flow in the lower

layer is small compared to the upper layer and there is little enhancement of the flow. In the intermediate regime, $\omega \sim O(\epsilon^2)$, we define

$$\Omega = \frac{\omega}{\epsilon^2} \quad (3.34)$$

and seek solutions for \hat{p}_u and \hat{p}_l which emerge from combining equations (3.32) and (3.33) and solving

$$\left(\frac{\partial^2}{\partial \hat{x}^2} - \Omega \right) \left(KH_2 \frac{\partial^2}{\partial \hat{x}^2} - \Omega \right) \hat{p}_u^o = \Omega^2 \hat{p}_u^o \quad (3.35)$$

This has solutions

$$\hat{p}_u^o(\hat{x}) = a_u \exp(\Gamma \hat{x}) + b_u \exp(-\Gamma \hat{x}) + c_u \hat{x} + d_u \quad (3.36)$$

where

$$\Gamma = \left[\Omega \left(\frac{1 + H_2 K}{H_2 K} \right) \right]^{1/2} \quad (3.37)$$

and the coefficients a_i, \dots, d_i emerge by applying the boundary conditions for each layer. After some algebra, we find that

$$a_1 = \frac{1}{2(1 - \exp(\Gamma)) - \frac{\Gamma}{H_2 K}(1 + \exp(\Gamma))} \quad ; \quad b_1 = -\exp(\Gamma)a_1 \quad ; \quad (3.38a)$$

$$c_1 = \Gamma \left(\frac{1 + \exp(\Gamma)}{H_2 K} \right) a_1 \quad ; \quad d_1 = 1 - a_1(1 - \exp(\Gamma)) \quad (3.38b)$$

so the dimensionless speed at $\hat{x} = 0, 1$ in the upper layer is given by $-\frac{\partial \hat{p}_u^o}{\partial \hat{x}}|_{\hat{x}=0}$ and leads to the expression for the flux

$$\hat{Q} = -\frac{[\Gamma(1 + H_2 K)(1 + \exp(\Gamma))]}{[2KH_2(1 - \exp(\Gamma)) - \Gamma(1 + \exp(\Gamma))]} \quad (3.38c)$$

It may be shown that this reduces to the limits

$$\hat{Q} = 1 \quad \text{as} \quad \Omega \rightarrow 0 \quad (3.39a)$$

$$\hat{Q} \rightarrow (1 + KH_2) \quad \text{as} \quad \Omega \rightarrow \infty \quad (3.39b)$$

provided KH_2 remains finite. These correspond to either no flow in the lower layer or fully coupled flow in the lower layer, in which the pressure gradient in each layer is essentially the same, depending on whether the permeability of the seal rock is small, and hence allows no communication between the layers, or the layers are in good communication and the seal rock has no influence on the flow. The more general flow solution for \hat{Q} , which lies between these two limits, is shown in Figure 3.12 and depends in detail on the value of Ω and $H_2 K$.

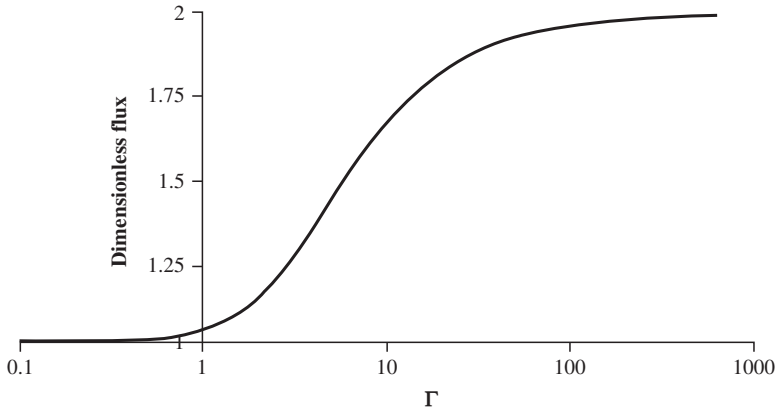


Figure 3.12 Dimensionless flow as the permeability of the seal rock increases, as parameterised by Γ . The leakage flux through the seal rock increases the total flow by sweeping some of the lower layer. Here we take $KH_2 = 1$ so in the limit of good pressure communication the flux is double that in a single layer.

In practice, it would be very difficult to determine the permeability of such a seal layer, since it may be fractured, or spatially variable in thickness or laterally discontinuous owing to erosion by subsequent geological flows. If we could generate a probability distribution for the likely range of permeability of this seal rock, then we can determine the expected enhancement of the flux owing to the leakage into the lower layer as a function of this probability distribution using the above relation for the net flux (see Chapter 4).

3.7 Effects of multiple baffles and reduced vertical permeability

The above model calculations have identified the impact of weakly permeable baffles in isolating the horizontal flow in different parts of a permeable rock. A more direct effect of such baffles is to reduce the effective permeability normal to the direction of the baffles for a pressure-driven flow. With a pressure-driven flow normal to the orientation of a series of permeable baffles, the flow is diverted around the baffles and so has a considerably greater flow path which leads to a greater pressure drop. The cartoon (Figure 3.13) illustrates a possible example of such a convoluted flow. In the case that the openings in individual layers of baffles are of width d and that these openings are a distance of order L apart, and the vertical spacing between successive layers of baffles is h where $L \gg h \gg d$, we can approximate the pressure loss through the system as follows, assuming two-dimensional flow.

The pressure loss in moving through such a system can be estimated by considering the pressure loss as the flow migrates through the gaps between the baffles, of width d ,

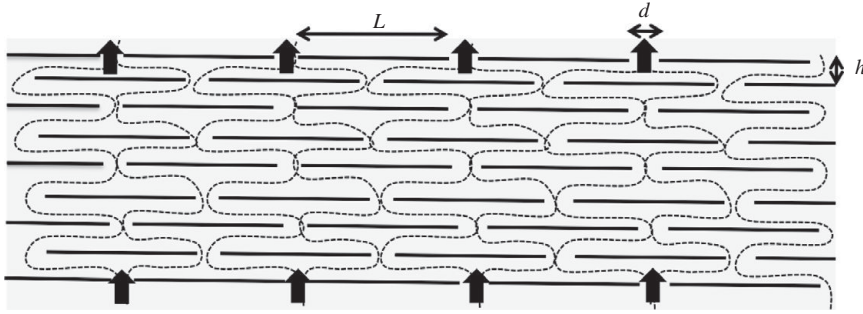


Figure 3.13 Convoluted flow around a series of fractured baffles.

using results from point sources and point sinks, and the pressure loss as the flow migrates a distance $L/2$ from one inter-baffle opening to the next by using the results for pressure loss in a parallel-sided channel. The pressure loss as a sink flow, in a half-space, with flux Q , contracts from the inter-layer width h to one half the gap width $d/2$, and then as a source flow expands from a radius comparable to one half the gap width d to a radius comparable to the inter-layer distance h , scales as

$$\Delta p_1 = \frac{Q\mu}{\pi k} \ln \left(\frac{2h}{d} \right) \quad (3.40)$$

The pressure drop as the flow $Q/2$ migrates parallel to the baffles, a distance $L/2$, through a layer of thickness h , prior to passing through the next gap follows the scaling

$$\Delta p_2 = \frac{\mu QL}{4kh} \quad (3.41)$$

The approximate pressure drop associated with the flux Q , which extends over a length L , as it moves vertically a distance h is the sum of these two pressure losses. We can compare this to the pressure loss in a purely vertical flow, in the absence of baffles,

$$\Delta p = \frac{\mu Qh}{Lk} \quad (3.42)$$

and this leads to the ratio K of the effective permeability of the baffled system, compared to the original system, as given by

$$K = \left(\frac{h}{L} \right) \left[\frac{L}{4h} + \frac{1}{\pi} \ln \left(\frac{2h}{d} \right) \right]^{-1} \quad (3.43)$$

The value of K is shown in Figure 3.14 as a function of $h/L \ll 1$ for two values of $h/d \gg 1$. In the case that $d \sim h$, the effect of the pressure loss through the baffles becomes small, and it is the excursion of the flow along the baffles, between successive openings in the baffles, which accounts for the main loss of pressure (Eq. (3.41)). In the case that the gaps between the baffles are very narrow, $d \ll h$, the pressure loss in passing through each layer (Eq. (3.40)) may, in contrast, have the dominant effect in reducing the effective permeability.

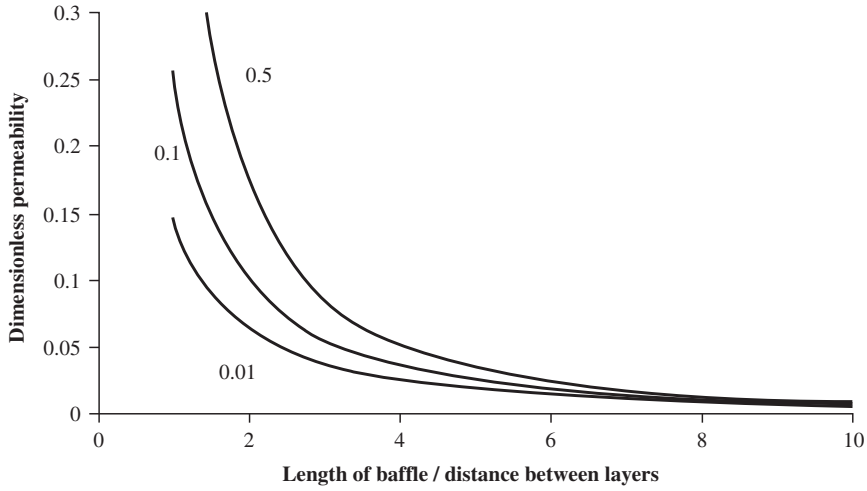


Figure 3.14 Variation of the effective dimensionless permeability of a baffled porous rock as a function of the ratio of the spacing between successive rows of the baffles and the length of the baffles, h/L (Figure 3.13) for the three values $d/h = 0.01, 0.1$ and 0.5 corresponding to the width of the gap between successive baffles through which the flow passes, compared to the spacing between successive rows of baffles.

We return to this picture of a baffled permeable rock in Chapter 10, where we explore the effect of such baffles on buoyancy-driven flow rather than the uniform pressure-driven flow considered herein. In that case, the baffles can have a very different effect on the flow, and we show the above effective permeabilities do not describe the flow in that case.

3.8 Faults

Another heterogeneity which arises in permeable rock are faults, across which there may be some offset of the geological strata. Faults may be permeable if they remain open following formation, or in some cases, the geothermal circulation which develops following their formation can lead to cement precipitation and closure of the fault suppressing the flow across and along the fault. We envisage that the vertical offset across a fault reduces the vertical extent of the flow path from the layer thickness H to the smaller value $h \ll H$, and that in the fault, of thickness b there is a layer of permeability $k_f \ll k$ where k is the permeability of the formation. The pressure decrease across the fault, in a region $-H < x < H$ upstream to downstream of the fault, may then be approximated, in a very simple way by combining the pressure fall across a one-quarter sink, followed by the loss across the fault, and then across a one-quarter source, as suggested in Figure 3.15.

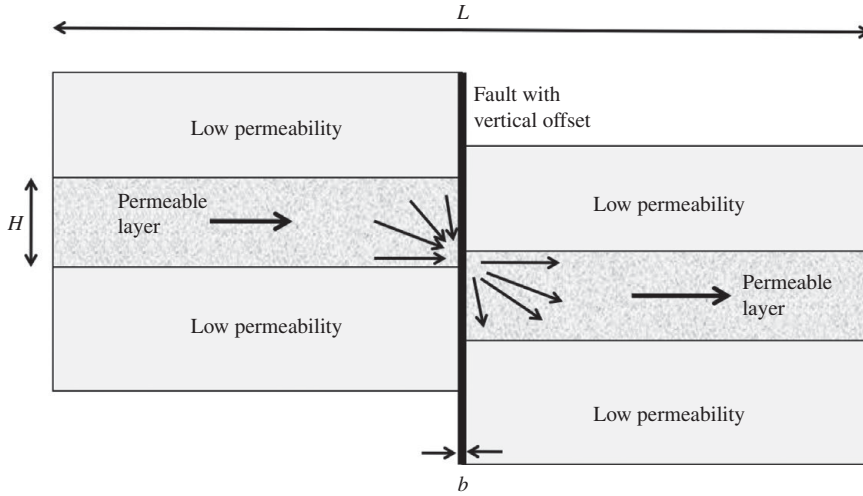


Figure 3.15 Schematic of the flow through an offset fault, indicating the convergence and then divergence of the flow which produces a large pressure drop and hence decreases the effective permeability of the formation.

This leads to a pressure decrease across each of the one-quarter sinks which scales as

$$\Delta p_s \approx \frac{2\mu Q \ln\left(\frac{H}{h}\right)}{\pi k} \quad (3.44)$$

combined with the pressure loss across the fault, which is

$$\Delta p_f \approx \frac{Q\mu b}{hk_b} \quad (3.45)$$

If we compare this to the case of a uniform aquifer with no fault, the pressure loss in the region $-H < x < H$ is $2Q\mu/k$ leading to a dimensionless permeability in the region $-H < x < H$ around the fault of order

$$\frac{k_{eff}}{k} \approx \left(\frac{1}{\pi} \ln\left(\frac{H}{h}\right) + \frac{kb}{2k_b h} \right)^{-1} \quad (3.46)$$

In turn, based on our earlier results for layers in series, if there are a source and sink well which are a distance L apart, and which drive flow through the region with the fault, then, for a one-dimensional flow, the effective well–well permeability, k_w , will take the value

$$k_w = \left(\frac{Lk_{eff}}{2Hk + (L - 2H)k_{eff}} \right) \quad (3.47)$$

in terms of k_{eff} given by Eq. (3.46). Since k_{eff} may be as small as $0.01k$ if $H/L \sim 0.1$, the fault may lead to an effective reduction of the well–well permeability by a factor of order 10, leading to a substantial reduction in flow rate.

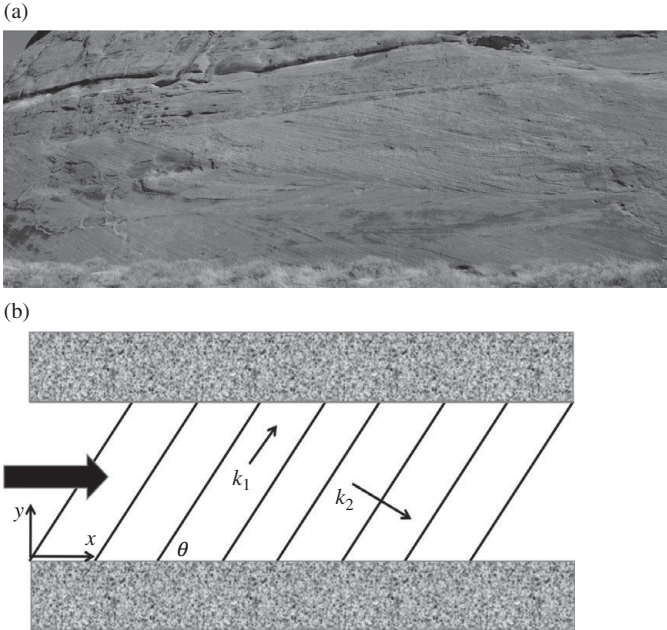


Figure 3.16 (a) Photograph of cross-bedding in Glen Canyon, USA. The horizontal scale of the figure is about 10 m and (b) schematic diagram of cross-bedded deposit, with angle θ between the orientation of the bedding and the impermeable bounding rock, as used in the model prediction of cross-flow. A black and white version of this figure will appear in some formats. For the colour version, please refer to the plate section.

3.9 Cross-bedding

One of the important features of many fluvial deposits, and the boundaries between some aeolian deposits is the presence of cross-bedding, whereby the depositional layers are inclined at an angle to the main depositional direction (Figures 2.6, 2.8, 3.16). Typically, the permeability is greater in the direction parallel to the deposition, and so in this case, the flow may tend to flow at an angle to the direction of the main geological strata. However, if the lateral boundaries of the cross-bedded deposit are impermeable, then the flow will migrate parallel to the boundaries rather than along the direction of maximum permeability (Figure 3.16). We now model this flow. Let us consider the bedding planes to have angle θ to the direction of flow, and the permeability of the rock to be k_1 in that direction and $k_2 < k_1$ in the cross-bed direction.

If there is a pressure gradient G_x in the direction, x , of the formation, then this has a component $G_x \cos \theta$ in the direction of the bedding plane, and $G_x \sin \theta$ in the direction normal to this. These two pressure gradient components lead to a flow in the x direction

$$u_x(G_x) = \frac{1}{\mu} \left(k_1 G_x \cos^2 \theta + k_2 G_x \sin^2 \theta \right) \quad (3.48)$$

and in the y direction normal to the lateral boundaries, given by

$$v_x(G_x) = \frac{1}{\mu} (k_1 G_x \sin \theta \cos \theta - k_2 G_x \cos \theta \sin \theta) \quad (3.49)$$

In order that there is no flow normal to the boundaries of the domain, a pressure gradient, G_y , will develop normal to the boundaries to suppress the flow (3.49) normal to the boundaries produced by the along-layer pressure gradient G_x . The pressure gradient, G_y , leads to a flow normal to the boundaries

$$v_y(G_y) = \frac{1}{\mu} \left(k_1 G_y \sin^2 \theta + k_2 G_y \cos^2 \theta \right) \quad (3.50)$$

and a flow along the layer

$$u_y(G_y) = \frac{1}{\mu} (k_1 G_y \sin \theta \cos \theta - k_2 G_y \cos \theta \sin \theta) \quad (3.51)$$

If we impose the condition of no flow normal to the boundaries,

$$v_x(G_x) + v_y(G_y) = 0 \quad (3.52)$$

we find a relation between G_y and G_x so that the net flow along the layer, $u_x(G_x) + u_y(G_y)$ is given by

$$u = \frac{G_x}{\mu} \left(\frac{k_1 k_2}{k_1 \sin^2 \theta + k_2 \cos^2 \theta} \right) \quad (3.53)$$

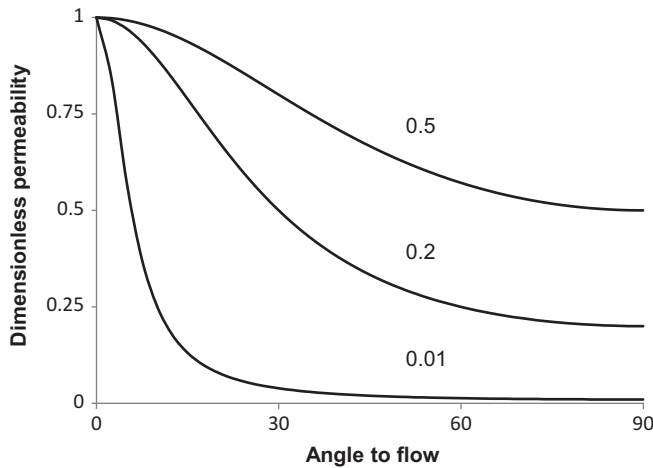


Figure 3.17 Graph illustrating the reduction in the effective (dimensionless) permeability as a function of the angle of the cross-bedding and the ratio of the minimum to maximum permeability of the cross-bedded deposit with values of 0.01, 0.2 and 0.5, as shown.

leading to the prediction that the effective permeability as a function of the angle of inclination of the bedding

$$k_{eff} = \left(\frac{k_1 k_2}{k_1 \sin^2 \theta + k_2 \cos^2 \theta} \right) \quad (3.54)$$

Figure 3.17 illustrates the reduction in the permeability associated with such anisotropy, as a function of the permeability ratio k_2/k_1 and the angle of the beds, θ , to the x direction.

3.10 Exercises

1. Calculate the effective permeability of a two-layer rock, of thickness H and length $L (\gg H)$ bounded above and below by impermeable boundaries in which one layer has thickness $d(x) = Hx/L$ and permeability k_1 and the other layer has thickness $H - d(x)$ and permeability k_2 , for $0 \leq x \leq L$. This illustrates the effect of the pinching out of one layer by another.
2. Calculate the minimum travel time between a source and a sink located at the points $(a, 0)$ and $(-a, 0)$ within a circular impermeable boundary centred at the origin and of radius R , when there is a two-dimensional volume flux of fluid, Q , supplied to the source. This illustrates the control on the water breakthrough time of the location of the source–sink relative to the boundary of the domain.
3. For a two-dimensional domain, find the velocity potential, ϕ_f and streamfunction ψ in the case that there is a uniform flow $(u, v) = (U, 0)$ far upstream, $x \rightarrow -\infty$, and a point source which supplies two-dimensional flux Q at the origin. Calculate how far upstream, $x < 0$, the flow from the source advances before being arrested by the oncoming flow. Show that far downstream, $x \rightarrow \infty$, the flux issuing from the source is located in the region $-Q/2U < y < Q/2U$.
4. A two-dimensional reservoir consists of two layers of permeable rock, each of thickness H and lateral extent $L \gg H$, and of permeability k . The layers are separated by an impermeable layer of shale, at $y = 0$, of thickness $b \ll H$ and permeability $k_b \ll k$, and the exterior of the flow domain, on the four surfaces $y = H + b/2$, $y = -H - b/2$, $x = 0$ and $x = L$ are impermeable. A line source located in the region $b/2 < y < H + b/2$ at $x = 0$ has a pressure $p + \Delta p$ while a sink, located at $x = L$ and $-H - b/2 < y < -b/2$ has pressure p . Find the flow from the source to the sink, and hence calculate the effective permeability. This illustrates the impact of a seal layer in reducing the flow between a source and a sink located on either side of the seal, in an otherwise uniform permeable rock.

4 Accounting for uncertainty

As mentioned in Chapter 2, it is difficult to describe the full detail of the subsurface rocks, especially in terms of the layer thicknesses, cross-bedding, seal layers, and the presence and permeability of faults and fractures, yet such details can be key for modelling the effective flow properties, as illustrated with the simplified models of Chapter 3. The difficulty arises from the remoteness of subsurface geological strata, the spatial resolution of the methods to image the system remotely, and ultimately the computational challenge even if all the data were available. Well data provide a highly resolved vertical sample of the full reservoir, but provide very limited spatial information. Geophysical techniques, such as seismic imaging, provide a fully three-dimensional image of the system, but can only distinguish features on scales typically of order 10 m or greater. This contrasts with the possible cm to m scale heterogeneities in rock fabric which can impact the flow and sweep patterns, as described in Chapters 2 and 3.

To test the sensitivity of models to the unknown properties of the system, such as seal layers, lenses and heterogeneities within the strata, one can parameterise the properties and test the sensitivity of model predictions to uncertainties in the parameters. In developing the models, and exploring the sensitivity of the model predictions, it is important to identify the key uncertainties in a problem, so that the range of possible outputs from a model reflects the uncertainty. In assessing a particular model prediction, one can then quantify the expected outcome and the variance of the outcome relative to the mean. In general in fluid flow problems, the boundary conditions are critical and this was reflected in some of the models in Chapter 3 concerning systems with seal rock, faults and multiple layers. Uncertainty analysis should therefore reflect the uncertainty in the position of the boundaries amongst other properties. We now consider a number of simple porous flow problems to illustrate the possible variance in model predictions associated with parameterisation of permeabilities and boundary locations. We then explore one approach to determine the sensitivity of model predictions based on the uncertainty in the precise values of the parameters governing the problem. The approach outlined in this chapter is simplified, but serves to highlight the role of simplified models in assessing uncertainty in complex physical processes. For more formal accounts of uncertainty analysis, and the challenge of accounting for the

unknown details of heterogeneities, amongst many papers, there are fascinating contributions by Chiles and Delfiner (1999), Gerritson and Durlofsky (2005) and Naff *et al.* (1998).

4.1 Sweep in the layered reservoir

A very simple example to illustrate the variance in model outputs concerns the flow and sweep in a quasi-one-dimensional model of a permeable rock composed of 20 parallel layers of equal thickness, each connected to a producer and injector well. We assume that there is the same pressure difference applied across each layer, and that the fluid within each layer is displaced by a uniform flood front and that the speed in the different layers varies with the permeability of that layer. We assume that the permeability of each layer is known to lie within two limits, and that each value between these limits is equally likely. We have calculated the time at which the injection fluid first arrives at the production well, which occurs in the highest permeability layer, and we have calculated the fraction of the area of the reservoir which is swept when one reservoir volume of fluid has been injected into the system. These metrics are somewhat arbitrary but provide two complementary measures relating to the sweep efficiency and volume of water injected into the system.

For the calculations, we generated 10 000 realisations of the permeability of the different layers, and we have then plotted the breakthrough time and the fraction swept for each realisation to determine the likely range of values these properties may take in this simple model. Figure 4.1 illustrates the results of the calculations in the case that the permeability ranges by (a) a factor of 10 from 0.1 to 1.0, and (b) a factor of 2 from 0.5 to 1.0. It is seen that with a factor of 10 variability in the permeability the fraction swept after one reservoir volume is injected ranges from about 0.7 to 0.9, and the range of water breakthrough times varies from about 0.4 to 0.8 of the time required to inject one reservoir volume of fluid. With a factor 2 variability in the permeability, the fraction swept varies from 0.85 to 0.95 while the time for water breakthrough ranges from about 0.65 to 0.9 of the time to inject one reservoir volume. However, such variations in the effective properties of the rock are entirely reasonable, and may be motivated for example by the effect of the heterogeneities considered in Chapter 3.

4.2 Boundary location and geological uncertainty

A fundamental problem concerns the location of the wells within a reservoir in order to maximise the recovery of the original fluid in place. Although the details of this problem require knowledge of fractional flow, interface instability and the role of reservoir heterogeneity on the flow, some of the basic principles emerge by consideration of a

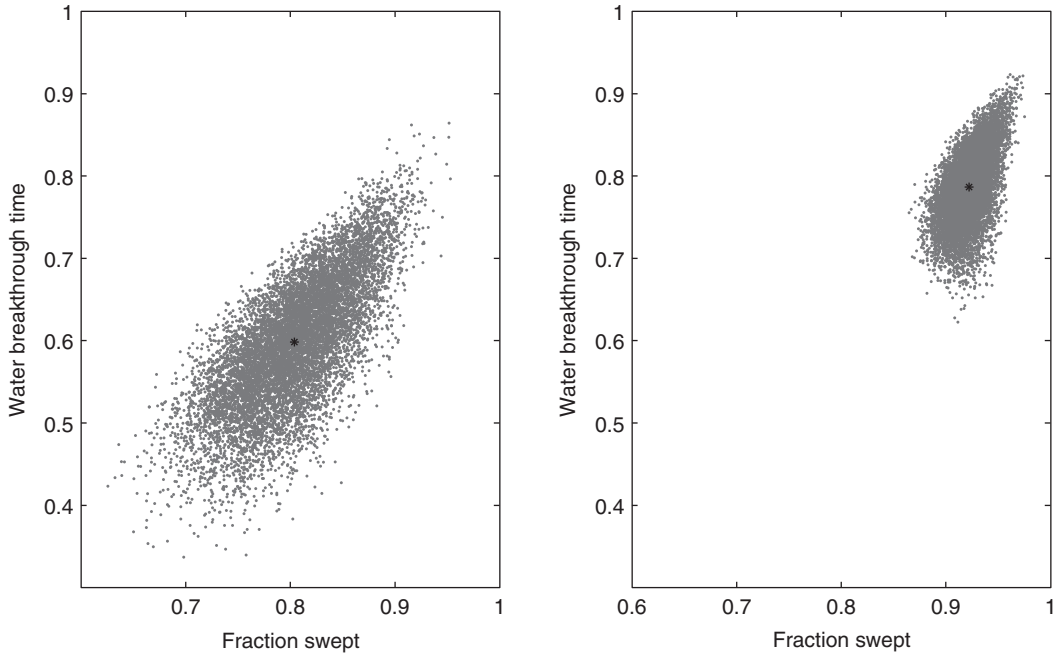


Figure 4.1 Variation of the water breakthrough time and the fraction of the original fluid swept from the reservoir after injecting one pore volume for a series of realisations of the values of the permeability in the five-layer porous rock. Permeabilities are sampled from a uniform distribution ranging from 0.1–1.0 and 0.5–1.0 for the left- and right-hand panels.

much simpler problem. Essentially, as a well-posed challenge, we aim to determine how to locate the wells to maximise the volume of original reservoir fluid which is produced when one reservoir volume of water is injected into the system.

Although we can carry out numerical calculations given an arbitrary shape of the reservoir boundary, for the present purposes, we assume the reservoir is circular, and we position the wells symmetrically about the origin. We can then use the source–sink potential theory described in Chapter 3 to model the flow, and use this to calculate the volume of original fluid recovered from the system as a function of the volume of injected water. The results can be parameterised in terms of the volume of injected fluid and the distance between the wells. As may be anticipated, for a given injected volume, the swept volume progressively increases as the well spacing increases, since there is more fluid between the wells which requires displacement by the flow. The calculations could be more complex, by adding heterogeneity to the structure of the formation (Chapter 3), and including a more complete model of the motion of an immiscible fluid–fluid displacement (see Chapters 6, 7). However, already we have identified from the idealised fluid mechanics that the wells should be placed on the boundary of the reservoir and this in itself introduces a challenge. The problem is that while this may be possible in principle, in practice, one does not know the location of the reservoir boundary with very great precision. The sand may thin out near the distal end of a flow,

and the grains may become finer, leading to lower permeabilities. As a result, the calculations are likely to be sensitive to the rock properties near the boundary of the domain.

In order to develop a quantitative approach to selecting a well location, one can try to develop a probability distribution as to the likelihood that for a given well spacing, the wells lie within the reservoir. Such a probability distribution might be based on seismic imaging of the reservoir combined with analysis of outcrops of analogue systems and well data. Such a probability distribution is likely to indicate that as the well spacing increases beyond some value, then the probability that the wells lie within the good quality rock in the reservoir decreases. One might then combine the fluid mechanical prediction of the volume of reservoir fluid which is produced from the extraction well as a result of the injection of one reservoir volume of water at the injection well (see Figure 4.3), with the probability analysis, to estimate the location of the wells at which there will be the highest expected production of reservoir fluid. The problem highlights the criticality of the boundary conditions.

Figure 4.2 illustrates the position of the leading edge of the injected liquid as a function of time, until reaching the time when the injected volume of fluid matches the

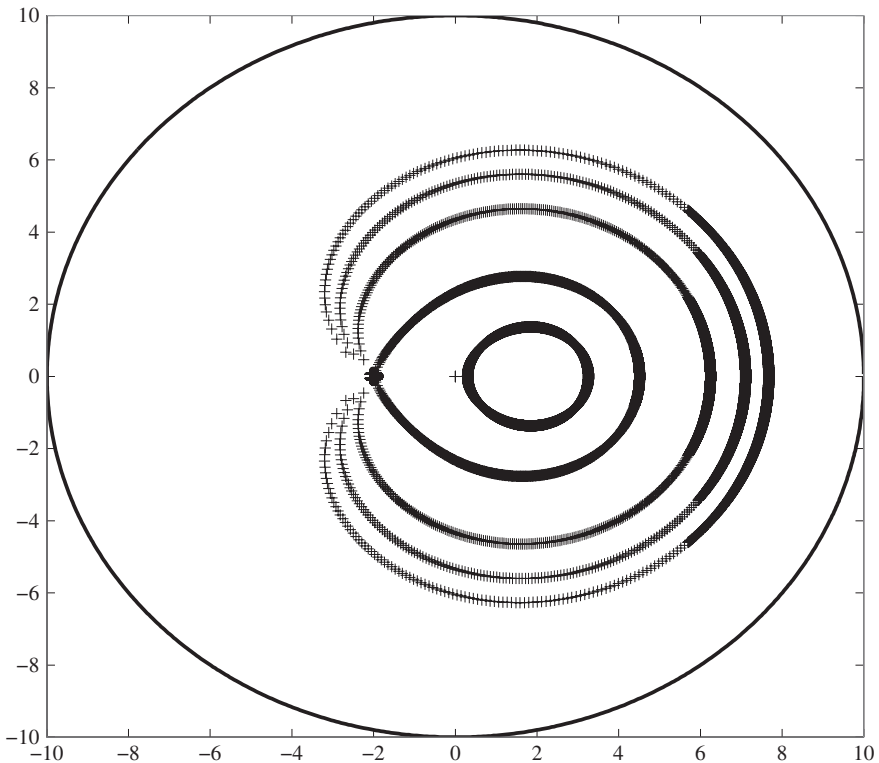


Figure 4.2 Sweep pattern for a typical flood within a circular reservoir, illustrating the location of the leading edge of the injected fluid at a series of times up to the time when one reservoir volume has been injected. In this figure the distance between the wells is a fraction 0.4 of the radius of the circle bounding the reservoir.

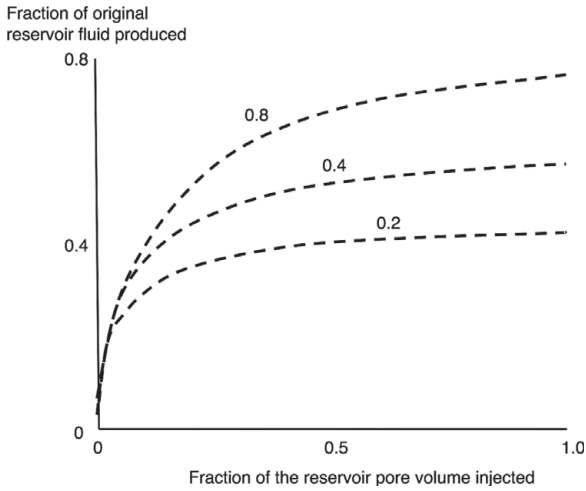


Figure 4.3 Illustration of the fraction of oil swept from a reservoir which has a circular shape, of radius 10, and is bounded by impermeable rock at the boundary, as a function of the spacing between the wells (different curves) ranging from a fraction 0.2 to 0.4 to 0.8 of the radius, with the wells located symmetrically about the origin, and also as a function of the fraction of the reservoir volume which has been injected into the injection well, as shown on the x -axis. With one pore volume injected, the typical fraction of the original fluid which is extracted from the reservoir lies between 40 and 80%, and depends on the time at which the injected fluid reaches the production well.

volume of the reservoir pore space for a typical source–sink flow. Once the injected liquid breaks through to the production well, the fraction of the extracted fluid which was originally in the reservoir decreases (Figure 4.3). If the wells are located closer together, the fraction of the original fluid which is extracted decreases, as less of the reservoir is swept.

Figure 4.4 illustrates how the fraction of the original fluid in the reservoir which is produced after one reservoir volume of fluid has been injected, the swept volume varies as a function of the well spacing. In this figure, we also show an example of how the probability that the wells lie within the reservoir varies as a function of the well spacing. For each well spacing the product of the probability with the swept volume gives the expected recovery. Using this we can determine well spacing, L^* , which would maximise the expected recovery. However, the selection of this spacing, L^* , is highly dependent on the probability distribution relating to the location of the reservoir boundary. Such a strategy is therefore extremely sensitive to any missing information about the location of the reservoir boundary. Different geo-experts are likely to draw different conclusions about the range of values which the missing information may take, and hence they would generate different probability curves. If information about the possible range of values that the probability distribution could take could be generated, then the sensitivity of L^* to the uncertainty in the probability distribution could be quantified.

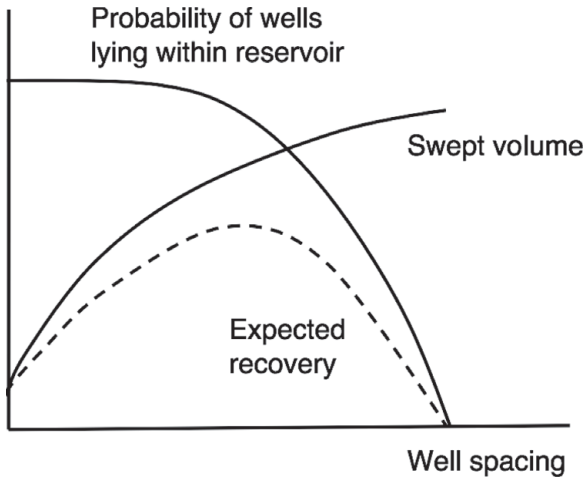


Figure 4.4 Expected recovery of oil after injecting one reservoir pore volume of fluid into the system, as based on the estimated probability distribution for the likelihood that wells with a given spacing will lie in the reservoir.

One approach may be to select a number of geo-experts to generate independently a probability distribution about the likelihood that the wells lie within the reservoir. The distributions should agree near the centre of the reservoir, when there is little separation of the wells, and when the wells are far apart, in which case they will fall outside the reservoir. However, near the actual boundary region, there may be considerable difference in the probability distributions produced by different experts, as shown in Figure 4.5a, where example probability distributions generated by three different geo-experts are shown (in principle one could use as many independent geo-experts as are available). The different estimates of the probability can be used to generate different expected recovery curves (Figure 4.5a). The average and variance of the production can then be assessed based on these three production curves. The variance helps to identify where there is most uncertainty about the produced volume as a function of the well placement (Figure 4.5b). Strategies which lead to a large variance based on the different probability distributions might be rejected, since these strategies are most sensitive to the lack of information, while strategies which have a smaller range of model prediction, are less sensitive to the lack of information. Figure 4.6 illustrates the relationship between the expected value of the fraction of original fluid which would be produced and the variance: as one moves along the curve from the origin, the well spacing increases (cf. Figure 4.5b).

In selecting the optimal well placement for development, one may introduce a utility function, U , to describe the value of a particular well placement L ,

$$U = U(E(L), V(L)) \quad (4.1)$$

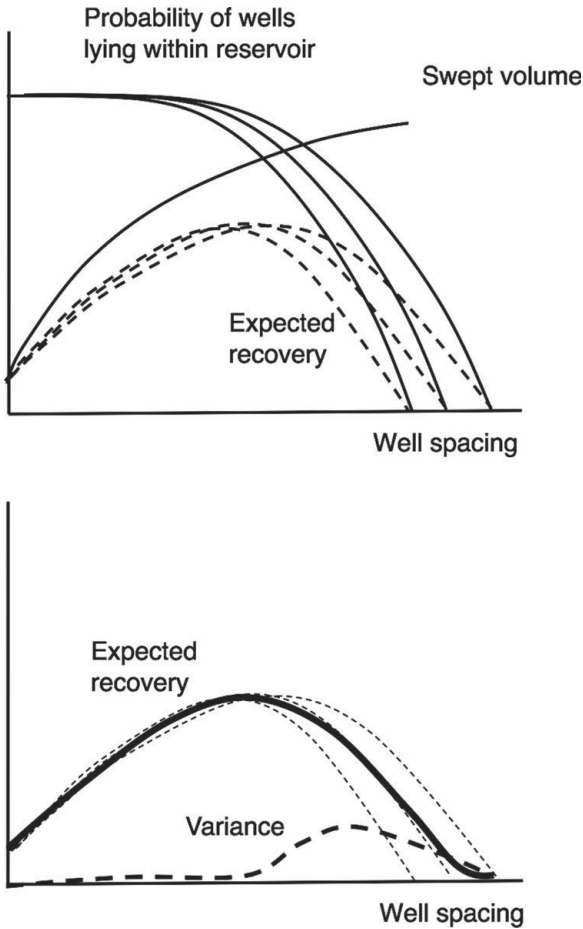


Figure 4.5 (a) Model prediction of recovery for three different probability distributions of the likelihood that the wells lie within the reservoir (see Figure 4.4). (b) The average of these expected recovery curves has a maximum near the point where the difference between the curves is significant, as measured by the variance in the expected recovery. In economic terms, such variance has a cost, and so the optimal solution will correspond to a closer well spacing than given by the maximum expected recovery.

where the value depends on both the expected recovery, $E(L)$, and the variance of this expected recovery, $V(L)$, which corresponds to a cost. The precise form of the utility function depends on commercial imperatives, but one might anticipate that $dU/dE > 0$ and $dU/dV < 0$.

For the above problem, one can plot contours of U in the (E, V) plane, and these are shown in Figure 4.6 as faint dotted lines, using the example that U is a linear function of E and V for simplicity.

For small well spacings, Figure 4.6 shows that E and V are both small, and that increasing L initially leads to an increase in E and subsequently an increase in V as

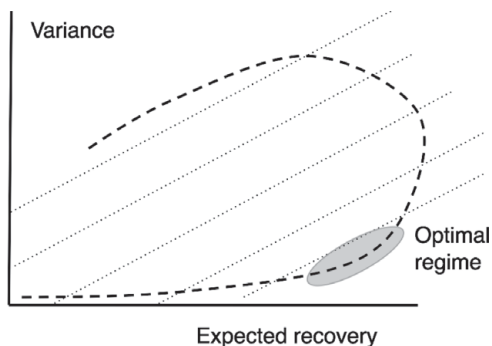


Figure 4.6 Illustrative example of contours of the value or utility of a particular drilling strategy (thin black lines) in which the utility increases linearly with expected return and decreases linearly with the variance of the return. The dashed line maps out the values of E (return) and V (variance) as a function of the implicit variable, L , the well spacing for the model shown in Figure 4.5. The shaded zone may correspond to the optimal strategy.

the expected location of the boundary of the reservoir is approached (cf. Figure 4.5b). For larger values of L , the variance remains high, but the expected recovery decreases as the likelihood that the wells have missed the reservoir increases. The shaded zone represents the optimal choice for L , which differs from that leading to the maximum expected recovery.

In summary, although highly simplified, this problem has identified how the uncertainty of the boundary locations may be key for specific engineering decisions. Optimisation of a development strategy may then depend on developing models to highlight the importance of the uncertainty in the boundary location. Such information may then be used to inform the possible value of acquiring new data or the selection of an optimal strategy for production based on the existing limited data.

4.3 Difference in spatial distribution of mean and variance

In using model predictions to assess optimal recovery strategies, it is important to account for the variability in the possible recovery given the uncertainty in the geological properties of the formation (e.g. Figure 4.1). As the complexity of a problem increases, this becomes increasingly difficult, since there are progressively more parameters which control the solution. Often Monte Carlo methods are used to sample a wide range of the possible parameter space to determine the different possible outcomes in a flow problem. However, in using the data from such calculations, it is important to account for both the expected value of a given metric and also the variance of this metric as different properties are varied, especially in problems with spatial

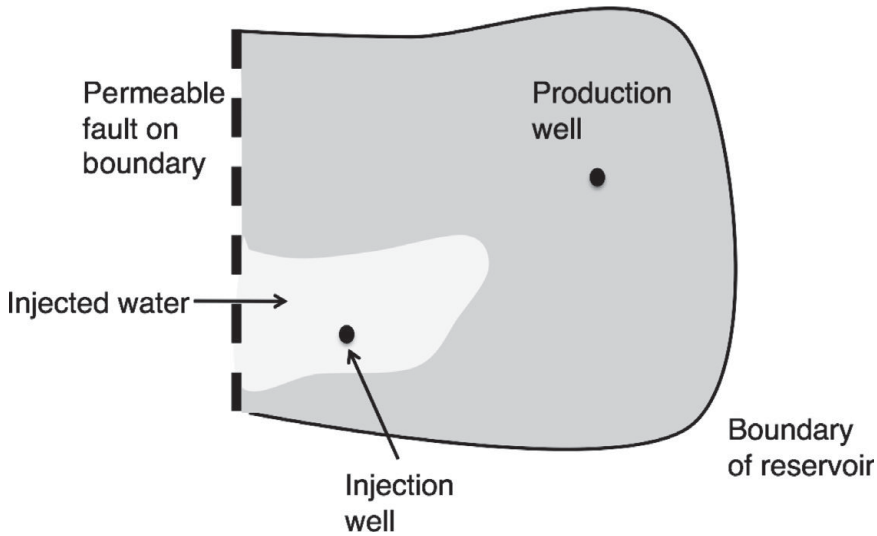


Figure 4.7 Illustration of the flow which may arise when an injection well is located near a leaky boundary so that some of the injected water leaks off from the reservoir, while the remainder flows to the production well.

variability. This issue is important, since the non-linear nature of many flow problems, associated with the boundary conditions, results in different spatial distributions of the expected value of a given metric and the variance of this metric. This can again be important in informing the selection of optimal strategies. As a simple example, we consider the two-dimensional problem of locating an injection well in a field in which there is already a production well, but in which there is a bounding fault of uncertain permeability (Figure 4.7; following Furtney and Woods, 2014).

For a given value of the permeability of the fault, one can carry out a systematic series of calculations in which the position of the well is varied throughout the reservoir. One can then determine the fraction of the injected fluid which drives original reservoir fluid through the fault, compared to the fraction which leads to production of the original fluid out of the extraction well. As a simple metric we can consider the fractional volume of the reservoir which is produced once one reservoir volume of fluid has been injected into the well.

In Figure 4.8, we show contours of this fractional recovery for four values of the fault permeability, k_e , based on a series of calculations in which the wells were placed at a regular series of positions within the reservoir. We denote these fractional recovery values for a given value of k_e and well position (x, y) as $F(x, y, k_e)$. The figure shows that with a low fault permeability, the maximum fractional production occurs when the injection well is placed near the fault. However, as the fault permeability increases, there is more leakage from the reservoir, and the maximum fractional production requires the injection to move into the reservoir, away from this boundary,

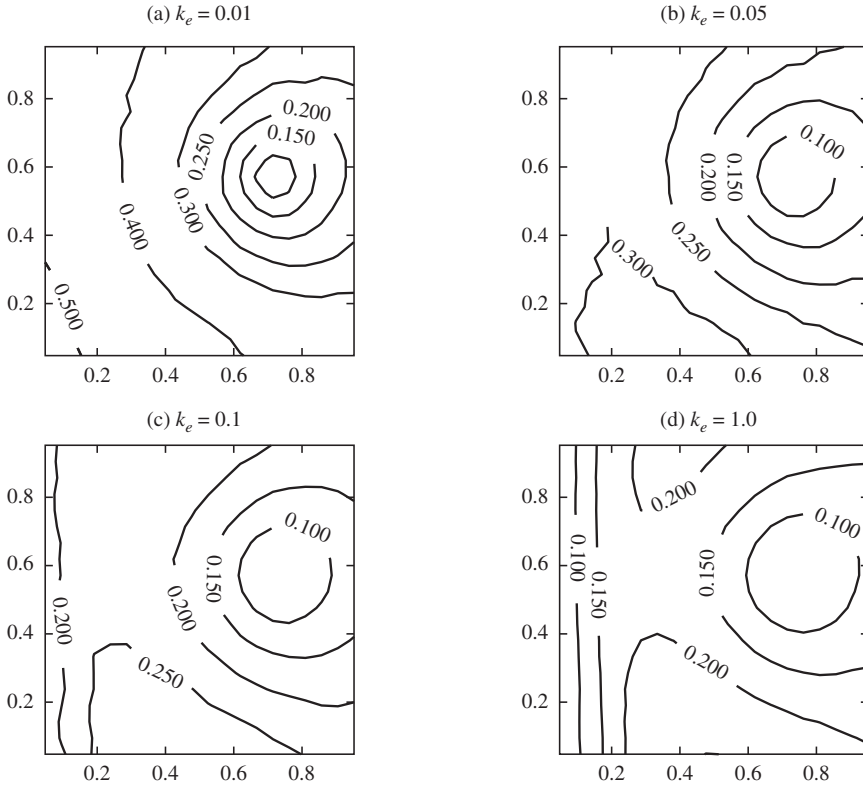


Figure 4.8 Illustration of the contours of the expected fraction of fluid which is recovered after flooding with one pore volume in an ideal square reservoir, as a function of the location of the production well. In the calculations, the location of the injection well is given and the permeability of the boundary fault is fixed in each panel, with the four panels corresponding to increasing permeability of the fault which is located on the y -axis. Figure courtesy of J. Furtney (as described in Furtney and Woods, 2014).

while not being too close to the production well to avoid the short-circuiting of the injection fluid directly into the production well.

If one can generate a probability distribution $p(k_e)$ to assess the likely permeability of the fault, k_e , perhaps informed by field observations, well tests and studies of analogue geological systems, then for each location of the injection well, we can compute the expected value and the variance of the fractional volume which may be produced: this is achieved by calculating the recovery when a well is placed at that point for a range of values of fault permeability and then using the probability distribution to weight each of these calculations. At each point (x, y) , the expected recovery $E(x, y)$ is then given by

$$E(x, y) = \int_{k_{min}}^{k_{max}} p(k_e) F(x, y, k_e) dk_e \quad (4.2)$$

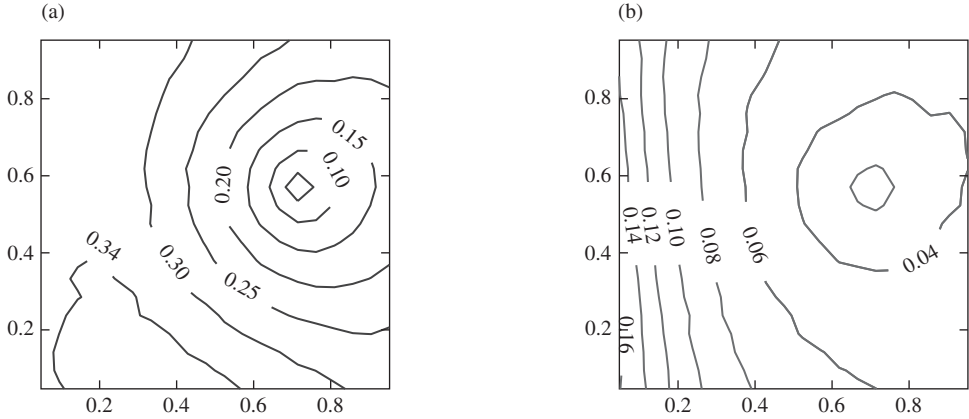


Figure 4.9 Illustration of (a) the expected fraction of the original fluid in place which may be recovered from the reservoir as a function of the location of the well. The values are calculated by taking the average of the fraction of the original reservoir fluid which may be recovered by injecting one reservoir volume of fluid, where the averaging is carried out over the range of possible values of the permeability of the fault located on the y -axis. Each calculation is weighted according to the probability distribution for that value of the permeability. (b) The square root of the variance of the fraction of the original reservoir fluid which may be recovered for wells located at each position in the reservoir, based on calculations used to estimate the mean (panel a). These values are based on a specific probability distribution for the permeability of the fault at the edge of the reservoir. Figure courtesy of J. Furtney (as described in Furtney and Woods, 2014).

and the variance $V(x, y)$ is given by

$$V(x, y) = \int_{k_{min}}^{k_{max}} [F(x, y, k_e) - E(x, y)]^2 p(k_e) dk_e \quad (4.3)$$

By calculating E and V at a series of possible well locations distributed throughout the field, we can produce a contour plot of the expected fractional sweep and the standard deviation of this sweep as a function of the location of the injection well, as illustrated in Figure 4.9 using a specific model for the probability $p(k_e)$.

The contour plots of E and $V^{\frac{1}{2}}$ are shown side by side in Figure 4.9, and we see that the two quantities have different spatial distributions. This is a result of the non-linear variations of the flow as the boundary condition (i.e. the permeability) on the fault is changed. In practice, in order to use the information contained in the calculations of the expected value and the variance, a utility function $U(E, V)$ is required as in Section 4.2, so that the cost of the uncertainty associated with each possible well location can be priced and combined with the value of the expected recovery. Since the two properties have different spatial distributions, as shown in Figure 4.9, this will, in general, lead to a selection of a well location which differs from that corresponding to the maximum expected recovery, since, in general, that choice would involve a larger uncertainty and hence cost of the associated risk.

4.4 Sensitivity to geological uncertainties

In general in geological formations, precise values for the permeability and other properties may not be available, and so calculations are made using estimates of the properties. It is then useful to assess the possible sensitivity in the predictions to the estimates used for the different properties, such as the permeability. As described in the above examples, this may be achieved with a series of calculations for different realisations of the properties, and then, by combining these calculations with probability distributions for the properties one can gain some understanding of the variance in the model predictions. However, although in principle this approach is rational, in practice, the number of parameters in many problems are prohibitively large, and so it is not possible to carry out sufficient numerical calculations, sampling the different probability distributions, to gain an accurate statistical picture of the uncertainty. In order to move forward, if the critical parameters to which the model predictions are most sensitive can be identified, then this helps to focus the numerical parameter studies on a small subset of parameters, thereby enabling a large number of calculations to be made relating to the major uncertainties in a flow process.

However, identification of the parameters upon which model predictions are most sensitive is not always straightforward. Even with the simplified models, as developed in this book, there may be several parameters, or dimensionless groups, which influence the model predictions. One strategy to help identify the parameters upon which the model predictions are most sensitive is to differentiate the model predictions with respect to each parameter, and determine which parameters have the largest gradients and hence sensitivity, at least in a linearised sense.

This process is in general rather complex, given that the flow is the solution of a series of partial differential equations, in which the coefficients of different terms represent the parameters relative to which we want to test the sensitivity of the model predictions. By evaluating the derivative of the model predictions with respect to the estimates of the rock properties one could in principle optimise particular metrics of the flow, such as the swept volume, but in general this is a numerically intensive operation.

From a physical perspective, the model predictions are likely to be more sensitive to those properties of the formation through which the majority of the fluid passes, and less sensitive to those parts of the system which are bypassed by the flow. This intuitive picture can be formalised in some simple flow problems. For example, in the case of a source–sink flow, our aspiration may be to determine the effective permeability of the formation for flow between an injection and production well, given a pressure difference applied across the wells.

We may also wish to explore the sensitivity of the flux from an injection to a production well to the possible variability in the permeability of a formation. For example,

if for simplicity we consider a two-dimensional flow, in the (x, y) plane, then we can represent the permeability in parametric form

$$k = k(x, y, q_i) \quad (4.4)$$

where $q_i, i = 1, \dots, n$ are n parameters which prescribe the permeability field. This may represent for example the n grid cells being used in a numerical calculation, or n parameters used to define a spatially continuous permeability field. Using Darcy's law

$$u_i = -\frac{k}{\mu} \frac{\partial p}{\partial x_i} \quad (4.5)$$

and the equation for continuity

$$\frac{\partial u_i}{\partial x_i} = 0 \quad (4.6)$$

where the summation notation is assumed, one can then show that the integral over the flow domain

$$\int_S u_i \frac{\partial p}{\partial x_i} dS = \int_{C_I + C_P} n_i u_i p dl = -\Delta p Q \quad (4.7)$$

where the line integral is calculated around the injection and production wells, C_I and C_P , and the surface integral is evaluated over the two-dimensional flow domain S . This provides a useful expression for the flux Q , and if we choose a reference value for $k(x, y, q_i)$ we can find the reference flux Q and reference velocity and pressure fields, u_o and p_o say.

If we now consider a small change, δq_k to parameter q_k , then the change in the permeability field is given by

$$\delta k = \frac{\partial k}{\partial q_k} \delta q_k \quad (4.8)$$

where we assume $\delta q_k \ll q_k$. This leads to a corresponding change to the velocity and pressure

$$\delta u = -\delta k \frac{\partial p_o}{\partial x} - \epsilon k_o \frac{\partial p_1}{\partial x} \quad (4.9)$$

$$\delta p = \epsilon p_1 \quad (4.10)$$

where, by linearity, we expect $\epsilon \ll 1$ to be proportional to $\frac{\delta q_k}{q_k} \ll 1$. For fixed pressure at the injection and production wells, this perturbation leads to a change in the flow rate given by Eq. (4.7), after substituting in the perturbations,

$$\frac{\partial Q}{\partial q_k} \delta q_k = \frac{1}{\Delta p} \int_S \left[2\epsilon \frac{\partial p_o}{\partial x_i} k_o \frac{\partial p_1}{\partial x_i} + \frac{\partial p_o}{\partial x_i} \delta k \frac{\partial p_o}{\partial x_i} \right] dS \quad (4.11)$$

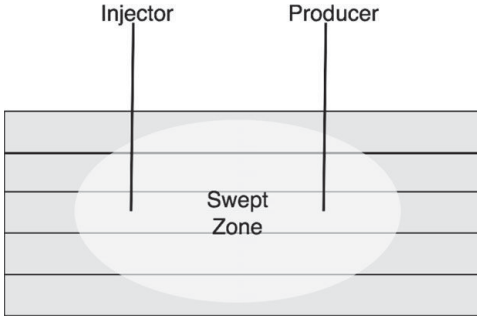


Figure 4.10 Cartoon of the injector–producer flow problem in a layered permeable rock for which the sensitivity of the flux to variations in the permeability of the layers is calculated. In order to assess the sensitivity, the distance of the wells from the interface between the layers is varied as seen in the Figures 4.11 and 4.12.

The first term on the right-hand side of this integral equals zero, since the pressure perturbation at the injector and producer are zero, and this term may be rewritten as

$$\int_s 2 \frac{\partial p_o}{\partial x_i} k_o \frac{\partial p_1}{\partial x_i} dS = \int_s 2 u_{oi} \frac{\partial p_1}{\partial x_i} dS = 2 \int_{C_1+C_2} n_j u_{oj} p_1 dl = 0 \quad (4.12)$$

where we have used the fact that the flow field is incompressible (Eq. (4.6)).

This leads to an expression for the derivative of the flow rate with respect to the parameter q_i

$$\frac{\partial Q}{\partial q_k} = \frac{1}{\Delta p} \int_s \frac{\partial p_o}{\partial x_i} \left(\frac{\partial k}{\partial q_k} \right) \frac{\partial p_o}{\partial x_i} ds \quad (4.13)$$

This integral depends only on the gradient of the permeability field with respect to the parameter q_k , and the reference pressure field, p_o , associated with the flow through rock based on the reference model for the permeability, $k(x, y, q_k)$.

In many cases, there is a correlation scale for the properties of a formation; as a simple example, one may parameterise the flow properties of an n -layer turbidite formation (cf. Figure 2.3) on a layer by layer basis, while a fluvial deposit may also require parameterisation of the permeability in localised lenses of high or low permeability within each layer. In the case of a turbidite in which the parameter q_k may correspond to the value of the permeability k_k in the k^{th} geological layer of the formation, where index $k = 1, \dots, n$, then the sensitivity of the flow to the permeability of the k^{th} layer

$$\frac{\partial Q}{\partial k_k} = \frac{1}{\Delta p} \int_{s_k} \frac{\partial p_o}{\partial x_i} \frac{\partial p_o}{\partial x_i} ds \quad (4.14)$$

where s_k is the area of the k^{th} layer, and p_o is the pressure solution for the flow based on the reference permeability field. In this case, the sensitivity of the volume flux to the permeability of each layer is readily calculated using the reference pressure field,

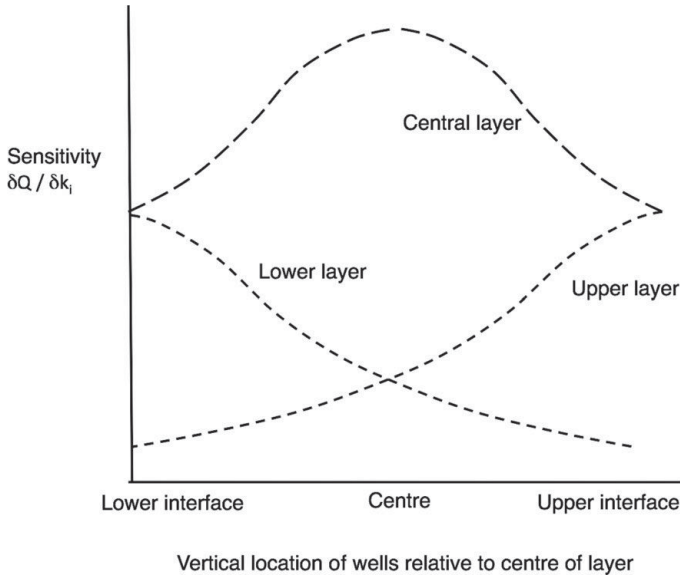


Figure 4.11 Variation of the sensitivity of the flux to the permeability of the central three layers, as the location of the wells within the central layer migrates from the lower boundary to the upper boundary. The figure shows how the sensitivity to the permeability of the neighbouring layers depends on the location of the wells relative to the boundary between the layers.

and in this way those parts of the domain which influence the flux most strongly can be identified.

As a simple application of this result we consider a source–sink flow in a layered turbidite reservoir in which the permeability of each layer is approximately the same, but may vary between layers, as each layer corresponds to a specific geological flow event (e.g. the Loop Head rock described in Chapter 2) (Figure 4.10). If the source and sink well are placed in a specific layer, then we can calculate the pressure field throughout the flow domain, taking the reference permeability to be a constant, equal in each layer. Using this reference solution for the flow and pressure distribution, we can then calculate the integrals given by Eq. (4.14) for each of the layers to determine the sensitivity of the flow solution to the value of permeability used in that layer. Since the reference permeability is taken as being a constant, Eq. (4.14) shows the sensitivity of the model prediction to the permeability in each layer varies in proportion to the square of the flow speed averaged over that layer. If we label the layers in the turbidite as being $i = -n, \dots, n$ where the wells lie within layer $i = 0$, then we can calculate how sensitive the estimate for the flux is to variations of the permeability in each layer.

In making such calculations, one requires information about the location of the wells relative to the interface between layer $i = -1$ and layer $i = 0$, and between layers $i = 0$ and layer $i = 1$. In practice, even if the well has been drilled into layer $i = 0$, the vertical position within this layer may be uncertain. This has an important impact on our uncer-

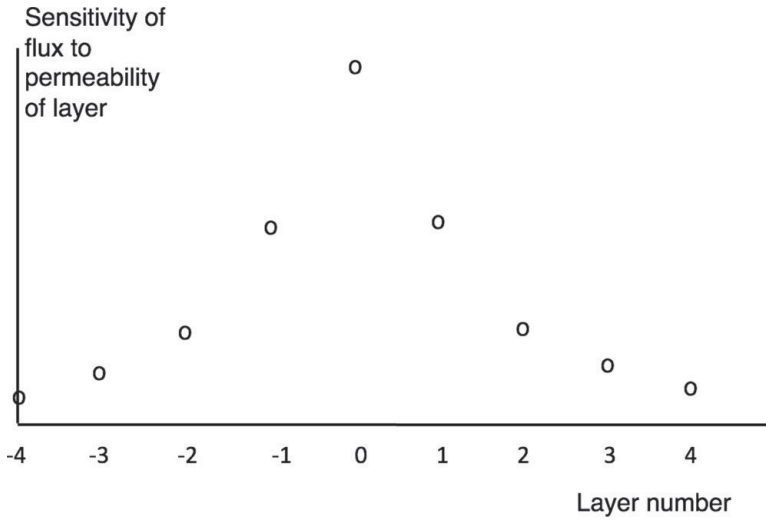


Figure 4.12 Example of the sensitivity of the flux to the permeability of each layer, in a layered reservoir containing 9 layers, with the same mean permeability for each layer. The sensitivity of each layer is the average value assuming that there is an equal probability that the wells lie anywhere within the central layer $i=0$ (see Figure 4.11). The figure shows that the value of the permeability in the central layer containing the well is the most sensitive, and that the sensitivity of the flux to the permeability in the neighbouring layers decays with distance from the central layer. Further calculations show that the rate of decay depends on the well spacing relative to the thickness of the layers.

tainty assessment. To illustrate this point, we calculate the integral (4.14) with respect to variations of the permeability in layers $i = -1, 0$ and 1 for a range of realisations of the positions of the wells, starting with a calculation in which they are assumed to lie close to the boundary with the layer $i = -1$ and exploring how the sensitivity changes as the position of the wells moves up through layer $i = 0$, so that eventually the wells lie just below the interface with layer $i = 1$. The sensitivity is normalised with respect to the maximum value, which arises for variations of the permeability in the layer $i = 0$ when the wells are assumed to lie in the centre of the layer (Figure 4.11). In Figure 4.11, we show the sensitivity of the flux to the permeability of each of the layers $i = 1$ (upper layer), $i = 0$ (central layer) and $i = -1$ (lower layer), as a function of the vertical location of the wells within layer $i = 0$. When the wells lie at the interface between two layers ($i = 0$ and $i = 1$) or ($i = 0$ and $i = -1$), the sensitivity to the permeability value in each layer near the wells is the same. However, the sensitivity to the permeability of $i = 1$ or $i = -1$ decreases if the location of the wells migrates away from the interface and into the central layer $i = 0$, while the sensitivity to the permeability of the central layer, $i = 0$ increases.

Further calculations show that the sensitivity of the flux to the permeability of the layers further from that containing the wells falls off with distance (Figure 4.12), and

the rate of decrease of the sensitivity depends on the well spacing relative to the thickness of the layers. With relatively thin layers, there is a significant flux through several layers and the sensitivity decays slowly, whereas with relatively thick layers, most of the flow is carried by the central layer and the sensitivity decays rapidly away from the central layer.

In the limiting case that the fluctuations in the permeability are parameterised as being small, but non-zero, relative to the mean permeability, it is possible to use Eq. (4.14) to estimate the variance of the flux, relative to the mean flux, as a function of the variance of the distribution of permeability in each layer, assuming that the variation in permeability of each layer is independent. For example, if we assume that the variance in the permeability is the same in each layer, then the variance of the flux, $V(Q)$ is given in terms of the variance of the permeability of each layer, σ by the relation

$$V(Q) = \sigma \sum_{k=1, \dots, n} \left[\frac{\partial Q}{\partial k_k} \right]^2 \quad (4.15)$$

Such models, although linear, are valuable in helping to determine the relative sensitivity of model predictions to assumptions about different reservoir properties. In many cases, production data can be used to invert for the reservoir properties; the above model can be combined with such data to identify that the best resolved information about the field properties lies in the region near to and between the wells.

In concluding this chapter, we note that in order to develop a non-linear picture of such uncertainties, non-linear numerical calculations are required; that is much more numerically intensive than the linearised approach herein. However, the linearised analysis of the very simplified models illustrates the importance of the location of the boundaries in such calculations, and may identify the parameters to which the flow predictions are most sensitive. This may provide key input in determining the ordering of parameters which should be varied when a series of non-linear calculations are made to assess the uncertainty, since, when constrained by numerical computation time, it may be most valuable to explore variations with respect to the most sensitive parameters. A comparison of such non-linear calculations with the linearised model may be found in Evans *et al.* (2014).

4.5 Exercises

1. In a reservoir embedded in a long, thin channel, of cross-sectional area A , the flow is primarily along channel and the permeability decreases as $k \exp(-\lambda x)$ with distance x along the channel. If an injector well is placed at $x = 0$, find how the production rate varies for a given pressure difference from the injector to producer if the producer is to be placed a distance L down the channel from the injector. You may assume that

when $L = 1/\lambda$, the flow speed $u = 1$. If the value of the oil decays into the future with exponential rate β determine an expression for the value of the oil produced at the point that the water breaks through into the production well. You may assume the oil and water have the same mobility, and there is no mixing between phases. If λ is uncertain to within a factor of 20%, find the possible range in the cumulative (net present) value of the production calculated up to the time at which water breaks through into the production well. Make calculations for a range of values of L , and for the cases $\beta = 0.5$ and $\beta = 2$. (This latter part of the question may require numerical solution.)

5 Dispersion in porous media

The motion of fluid through a permeable matrix can follow complex pathways and this can lead to intermingling and mixing of fluid as it migrates through the porous medium. There are several different mechanisms which lead to mixing, and we shall explore these in this chapter. Dispersion can have important implications in many contexts. In enhanced oil recovery, water is injected into the formation, and knowledge of the spatial distribution of the water is key, especially if chemicals such as polymers are added to the injected water to assist the flow. In groundwater remediation problems, such as associated with cleanup of LNAPL and DNAPL (light and dense non-aqueous petroleum liquids), which result from spillages of fuel and industrial chemicals, knowledge of the distribution of the contaminant in the ground is key to inform cleanup strategies (see Chapter 10). Models of dispersion are also of relevance in predicting the possible long-term distribution of radioactive contaminants in the subsurface if geological storage facilities are breached. On shorter timescales, understanding dispersion is key for interpreting tracer tests, which are used by both the oil industry and the geothermal industry to infer transport properties in the subsurface. Dispersion is important in modelling reactions which occur in porous rocks as a result of chemical disequilibrium between the injected fluid and the formation fluid or the formation itself.

Owing to the importance of dispersion for numerous problems in groundwater transport and enhanced oil recovery, there is a large literature on the topic. The recent contribution by Bear and Cheng (2010) provides a comprehensive review of large part of such modelling approaches, and the discussion of Phillips (1991, 2009) provides a simple physical picture of the various processes. Other important works include the review by Berkowitz *et al.* (2010) and earlier papers by Koch and Brady (1985), Young and Jones (1991), Saffman (1959) and Bear (1972), as well as the works of Dagan (1989). One important paper summarising field observations is by Gelhar, Welty and Rehfeldt (1991) illustrating the variability of dispersion coefficients from 59 different aquifers.

In this chapter, which is designed to provide an introduction to the physical processes of dispersion, we develop some simple models to illustrate various effects. Pore-scale mechanical dispersion arises because neighbouring streamlines become decorrelated as the flow passes around solid grains in the matrix, and follow different pathways

(Section 5.2). This spreading of the flow front is a mechanical dispersion process, dependent on the decorrelation of different fluid particles at junctions in the porous layer. There is also larger scale mechanical dispersion which arises if the formation is heterogeneous, with regions of high and low permeability causing the flow speed to vary in space. This results in a range of fluid travel times on different streamlines and hence leads to decorrelation on a larger scale. If there are extended regions of shear in the flow, then as discrete clouds of tracer become stretched out, there will be an increased surface area normal to the flow direction across which the tracer may diffuse into the surrounding fluid. This process, known as Taylor dispersion, can also produce very substantial dispersion of a cloud of tracer. In porous layers, there are additional effects, such as the no-slip condition on pore walls and dead-end pores, which can lead to anomalous dispersion characterised by clouds of tracer spreading at rates different from the normal diffusive-type spreading, in which the scale of the cloud grows in proportion to $t^{1/2}$. Finally, we discuss the effects of oscillatory or time-dependent flows which can lead to dispersion even in the absence of a mean flow.

In this chapter, the focus is on pressure-driven flows and the transport of a passive scalar by the flow. One aspect we identify is that the structure of the rock has an important control on the dispersion, since it causes intermingling of the different fluids owing to spatial variations in the permeability. Some of the principles which emerge from such macroscopic dispersion may also be used to help interpret more complex transport processes in porous media. These include the transport of thermal energy, which we consider in Chapters 8 and 11, the transport of chemical phases which react with the matrix, again considered in Chapters 8 and 11, and the evolution of the saturation of one fluid phase as it migrates through a second fluid phase within a porous medium, as considered in Chapter 7. However, the force balance driving the flow can also have a critical impact on the dispersion associated with the heterogeneity of the formation. Although the present chapter focuses on pressure-driven flows, in Chapter 10 we discuss some dispersion effects particular to buoyancy-driven flows; there we identify some different flow patterns and phenomena which can lead to buoyancy-driven dispersion of a passive tracer and indeed, one fluid within a second.

5.1 Molecular diffusion in a porous layer

In a porous layer, molecular diffusion tends to be suppressed relative to that in an unconstrained fluid owing to the presence of the matrix walls which only allow diffusion parallel to the boundaries. As a result, if the direction of a pore channel has angle θ relative to a concentration gradient, the diffusive flux will act on a fraction $\cos \theta$ of the gradient and the component of this flux in the direction of the gradient will then be proportional to $\phi \cos^2 \theta$, where the ϕ denotes the fraction of the rock consisting of

pores. If this directional effect is averaged over all the pore channels in a representative volume, and the pore channels are oriented in random directions, then the average of the geometrical factor, known as the inverse of the tortuosity, $1/\tau$, should be used in evaluating the molecular transport, since there will be no bias in the transport direction. Typically the tortuosity has a value of order 10, resulting in an effective reduction of the molecular diffusion by a factor of order 10. For example, many salts in solution have a diffusion coefficient D_m of order 10^{-9} m²/s and so the effective molecular diffusion in a porous layer is of order 10^{-10} m²/s.

In a fractured rock, bounded above and below by impermeable strata, the situation may be more complex, especially if there are two preferred directions of the fractures, with different fracture density or aperture in the two preferred directions. For example, if the effective aperture area, per unit cross-sectional area, in direction θ to the along-layer direction is ϕ_1 while it is ϕ_2 in the direction $\pi/2 - \theta$, then there will be a net flux associated with a gradient, $\frac{\partial c}{\partial x}$, along the layer, of magnitude

$$D_m(\phi_1 \cos^2 \theta + \phi_2 \sin^2 \theta) \frac{\partial c}{\partial x} \quad (5.1)$$

However, owing to the asymmetry, there will also be a net cross-layer flux,

$$D_m(\phi_1 - \phi_2) \cos \theta \sin \theta \frac{\partial c}{\partial x} \quad (5.2)$$

and this will induce a cross-layer gradient $\frac{\partial c}{\partial y}$ which will exactly cancel this flux. As with the permeability of cross-bedded strata we considered in Chapter 3, this cross-layer gradient will then lead to a flux in the along-layer direction, which, when added to the original flux, will result in a net along-layer flux

$$D_m \left(\frac{\phi_1 \phi_2}{\phi_1 \sin^2 \theta + \phi_2 \cos^2 \theta} \right) \frac{\partial c}{\partial x} \quad (5.3)$$

5.2 Pore-scale mechanical dispersion

As fluid migrates through a porous rock, the fluid particles continually change direction as they reach junctions with the grains and move round the grains. This leads to a random-walk-type process in which individual particles gradually spread owing to the decorrelation of fluid trajectories at the grain–grain junctions. To illustrate the phenomenon, in Figure 5.1 we show how a patch of red-dyed fluid spreads out as it moves in a uniform downward flow through a bead pack. In the experiment, the beads are 1 mm in size, and the cell is 15 cm across and 1 cm deep. Note that although the patch of dye spreads a considerable distance in the flow direction, produced by the

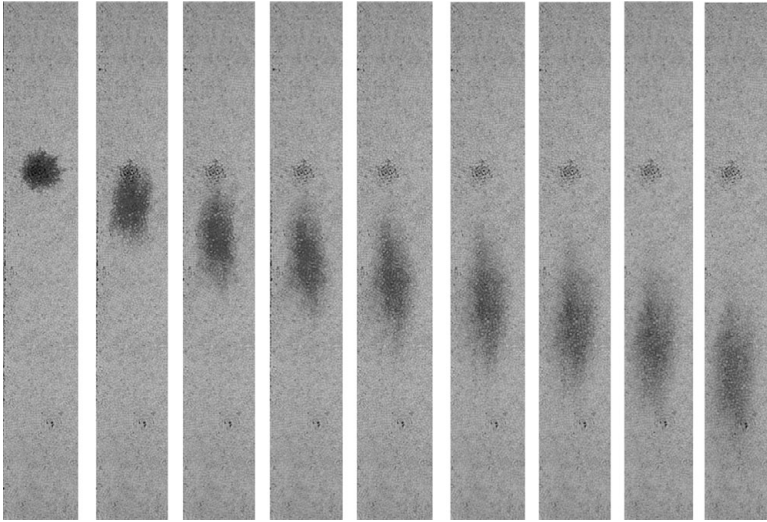


Figure 5.1 Illustration of the longitudinal and transverse dispersion of a parcel of dye as fluid migrates through a porous layer. The flow is from top to bottom, and the dye streak is seen to spread much more rapidly in the along-flow longitudinal direction than the cross-flow transverse direction. Photograph courtesy of C. Otto. A black and white version of this figure will appear in some formats. For the colour version, please refer to the plate section.

longitudinal dispersion, it does not spread very far in the cross-flow direction, associated with the transverse dispersion.

We first illustrate a simple model which enables quantification of the mechanical dispersion. We then assess additional processes which can modify the mixing and lead to different parameterisations of the dispersion. As noted, there are many classic works on this topic, and this chapter primarily serves as an introduction to some of the key points, as well as being a building block for some flow problems considered later in this volume.

First we consider the migration of a single particle through a porous layer, denoting the position at time t , $x(a, t)$ in terms of the initial position a at time $t = 0$ according to the relation

$$x(a, t) = \int_0^t v(a, t) dt + a \quad (5.4)$$

where v is the interstitial velocity, $v = u/\phi$. If we consider a large number of such particles, migrating through a porous layer (Figure 5.2), then, given the fluctuations in the precise structure of the medium, we can take an ensemble average to define the motion of the centre of mass of the cloud of particles

$$\overline{x(a, t)} - a = \int_0^t \overline{v(x, t)} dt = \overline{v(a)} t \quad (5.5)$$

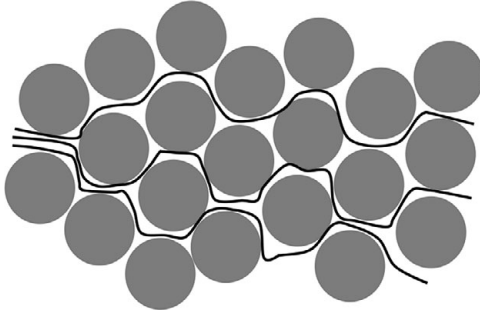


Figure 5.2 Illustration of the migration of different fluid particles through a porous layer, indicating the decorrelation of the fluid particles with distance downstream as they pass successive junctions between particles in the formation.

and the location of a specific particle relative to this centre of mass is then given by

$$x(a, t) - \overline{x(a, t)} = \int_0^t [v(a, t) - \overline{v(a)}] dt \quad (5.6)$$

where $v(x, t)$ denotes the interstitial velocity and $\overline{v(a)}$ is the ensemble average interstitial velocity. The rate of change of the ensemble average of the square of the variation in position from the centre of mass is then given by

$$\frac{1}{2} \frac{d}{dt} \overline{(x(a, t) - \overline{x(a, t)})^2} = \int_0^t \overline{dt' [v(a, t) - \overline{v(a)}][v(a, t') - \overline{v(a)}]} \quad (5.7)$$

The integral on the right-hand side of Eq. (5.7) represents the velocity correlation in time. As a simplifying approach, we assume that fluid particles decorrelate at the grain junctions, then neglecting no-slip effects and side branches, as a simple picture, the decorrelation time scales with the travel time across the grains δ/\bar{v} where δ is the typical grain size and \bar{v} the average interstitial velocity. Hence to leading order, if we approximate the correlation integral with the value $\lambda\delta\bar{v}/2$ where λ is a constant which depends in detail on the geometry of the porous media, we find that

$$\overline{[x(a, t) - \overline{x(a, t)}]^2} = \lambda\bar{v}\delta t \quad (5.8)$$

This implies particles become dispersed as a random-walk-type process owing to the tortuous path they follow through the medium. The dispersive flux which leads to spreading of gradient, ∇c , of the concentration field c therefore has the form

$$J = \phi\lambda\bar{v}\delta\nabla c \quad (5.9)$$

We note that the cross-flow transverse dispersion λ_T is typically 1–2 orders of magnitude smaller than that of the longitudinal dispersion λ_L (see Section 5.4). Note this is a simplified picture since in some cases the correlation may not decrease as rapidly with distance (see Phillips, 2009).

The above discussion is somewhat simplified in that we have neglected effects of the no-slip condition on the surface of particles, the effects of dead ends or side branches, and the effects of there being a structure associated with fractures or finite layers of impermeable clay or shale which we refer to as baffles, which lead to a non-random geometry and anisotropic dispersion. We have also assumed that on the timescale of the flow within the pore spaces, the molecular diffusion is small, so that the dispersion is mechanical and uninfluenced by molecular mixing. This is valid provided the pore-scale diffusion time is much longer than the travel time across the pore, $\delta^2/D \gg \delta/u$. With a flow speed 10^{-5} m/s, this requires grains larger than 10^{-5} m, which is typically the case, although with slower flows, molecular diffusion on scales < 0.1 mm may begin to become significant.

5.3 No-slip effects

The effects of the no-slip condition can lead to a delay in the spreading of the tail of a patch of dye as it is carried through the formation. Saffman (1959) described this anomalous dispersion which can lead to a skewed tail in the distribution of the tracer, and Bear and Cheng (2010) discuss the generalisation of this approach in the case of anisotropic and heterogeneous media. In order to illustrate the effect, it is useful to consider a simplified model of the geometry of the porous layer. We adopt a model in which the porous layer consists of a series of channels or tubes, connected at junctions, and in which the flow migrates along the channels as a parallel flow, and then mixes in the junctions to redistribute itself uniformly into the next channel (cf. Young and Jones, 1991). In this case, if the velocity in a two-dimensional channel (for example a local fracture) has the form

$$u(y) = \frac{6u_o}{h^2}(yh - y^2) \quad (5.10)$$

where y is the distance from one wall of the channel, $y = 0$ to the other, $y = h$, then the mean flow speed is u_o . If the channel is of length L and is initially filled with fluid A but then displaced by fluid B, the volume of fluid A remaining in the channel decreases with time (see Figure 5.3). At long times, owing to the no-slip condition, Eq. (5.10) reveals that there will be a small layer adjacent to each wall containing fluid A. Since the speed very near the wall varies approximately linearly with distance from the wall, then the point which was originally at $x = 0$ and at a height $y \ll h$ above the wall $y = 0$ will have migrated to the end of the channel, $x = L$, after a time t given by the relation

$$y \approx \frac{hL}{6u_o t} \quad (5.11)$$

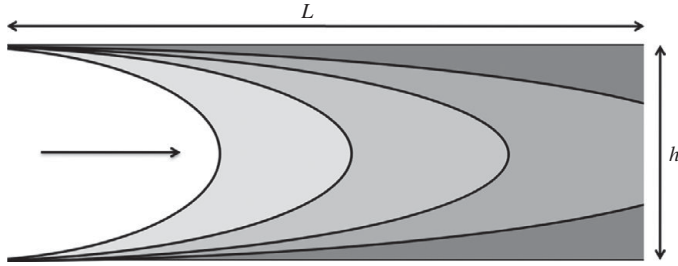


Figure 5.3 Effect of the no-slip condition on the dispersion in a channel. The curves denote the position of the fluid interface at successive times, showing that at long times, a small approximately triangular shaped region of original fluid remains beside the walls of the channel owing to the no-slip condition.

At long times, the volume of fluid A remaining in the channel is then given by the approximate relation

$$V(A, t) \approx \frac{L^2 h}{6u_o t} \quad (5.12)$$

given there are two walls at $y = 0, h$ and hence two zones of trapped particles. All the points in these two remaining zones of fluid have approximate speed $-u_o$ relative to the centre of mass.

As mentioned above, the fluid velocity remains correlated while the fluid remains in the channel, but becomes decorrelated after each junction, and so the fraction of the original particles in the channel whose velocity remains correlated after time t is given by

$$C(t) \approx \frac{L}{6u_o t} \quad (5.13)$$

and the correlation velocity is $-u_o$ approximately. Using this ensemble average, we can evaluate an integral of the form Eq. (5.7) at long times, $t \gg L/6u_o$, and this leads to the result that

$$\frac{d}{dt} \overline{[x(a, t) - \overline{x(a, t)}]^2} = \frac{Lu_o}{3} \ln(t) \quad (5.14)$$

and so

$$\overline{[x(a, t) - \overline{x(a, t)}]^2} = \frac{Lu_o}{3} (t \ln(t) - t) \sim \frac{Lu_o}{3} t \ln(t) \quad (5.15)$$

This illustrates the anomalous spreading of a moving slug of concentration owing to the no-slip condition on the walls of the flow channels. However, this effect only persists for times less than the cross-channel diffusion time, d^2/D , beyond which time, tracer in the fluid layer near the wall will tend to mix into the fluid in the centre of the channel.

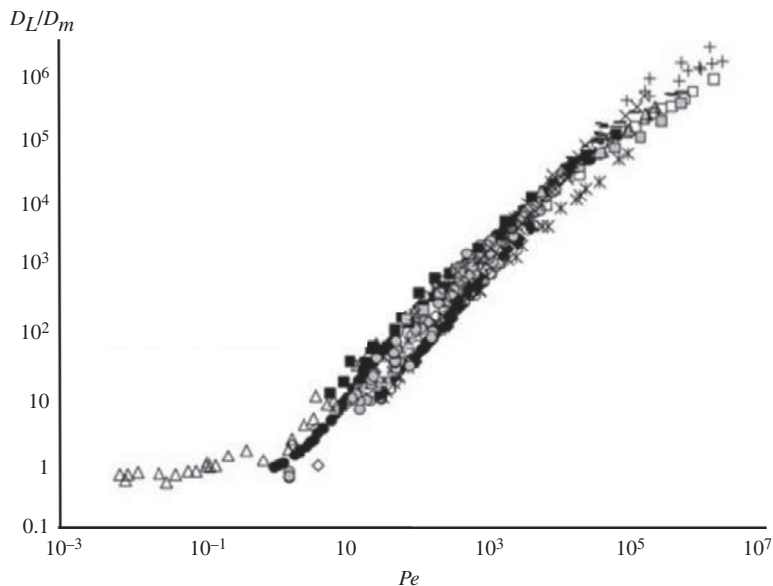


Figure 5.4 Experimental data on the longitudinal dispersion coefficient in a porous layer as a function of the Peclet number, defined in terms of the molecular diffusivity, D_m , the grain size, δ , and the Darcy speed, u as $Pe = u\delta/D_m$. The data points have been collated from a wide series of references in the literature, as compiled by Delgado (2007). The relationship becomes dominated by mechanical dispersive transport for Pe in excess of about 10–100. Reprinted from *Chemical Engineering Research and Design*, Vol. 85, J.M.P.Q. Delgado, Longitudinal and Transverse Dispersion in Porous Media, 1245–1252. Copyright (2007) with permission from Elsevier.

5.4 Experimental laws for dispersion

The above discussion illustrates the potential complexity in making theoretical predictions for the pore-scale dispersivity. The mechanical dispersion model above (Section 5.2) predicts a dispersivity which is a linear function of the Pe (Peclet) number, given by $u\delta/D_m$ where u is the speed, δ the pore size and D_m the molecular diffusivity (Section 6.1). However, the effects of the no-slip condition, dead ends and other factors may lead to a non-linear dependence on the Peclet number. Experimental evidence from many laboratory tests suggests that the dispersion coefficient is primarily a function of the Peclet number, with the mechanical dispersion being the dominant process. One rather comprehensive compilation of data by Delgado (2007) provides some detailed empirical models for the dispersion, including the effect of the Schmidt number (D_m/ν) as well as the Peclet number (see Figures 5.4 and 5.5). However, a model which is useful for aqueous systems suggests that the longitudinal dispersion can be approximated as

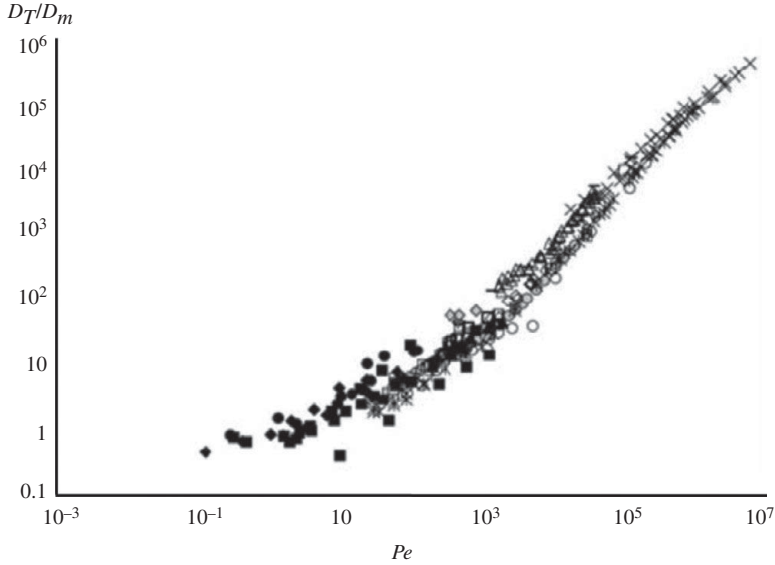


Figure 5.5 Experimental data on the transverse dispersion coefficient in a porous layer as a function of the Peclet number, defined in terms of the molecular diffusivity, D_m , the grain size, δ , and the Darcy speed, u as $Pe = u\delta/D_m$. The data points have been collated from a wide series of references in the literature, as compiled by Delgado (2007). The relationship becomes dominated by mechanical dispersive transport for Pe in excess of about 10–100. Reprinted from *Chemical Engineering Research and Design*, Vol. 85, J.M.P.Q. Delgado, Longitudinal and Transverse Dispersion in Porous Media, 1245–1252. Copyright (2007), with permission from Elsevier.

$$D_L \approx D_m \left(\frac{1}{\tau} + (1.8 \pm 0.4)Pe \right) \quad \text{for } 300 < Pe < 10^5 \quad (5.16a)$$

and

$$D_L \approx D_m \left(\frac{1}{\tau} + 0.5Pe^{1.2} \right) \quad \text{for } 5 < Pe < 300 \quad (5.16b)$$

while the transverse dispersion, in the direction orthogonal to the flow, can be described by

$$D_T \approx D_m \left(\frac{1}{\tau} + 0.025Pe \right) \quad \text{for } 300 < Pe < 10^5 \quad (5.17a)$$

and

$$D_T \approx D_m \left(\frac{1}{\tau} + 0.025Pe^{1.1} \right) \quad \text{for } 5 < Pe < 300 \quad (5.17b)$$

This parameterisation concurs with the scalings which emerged from the numerical study of Bijeljic *et al.* (2004) using a pore-network model of sandstone cores to model the pore geometry.

The above correlations show that the dispersive transport typically dominates the diffusive transport provided the Peclet number exceeds a value of about 10–100.

Given the parameterisations of the transport, and noting its simplifications, we can write down an effective equation for conservation of an inert tracer which does not interact with the rock formation

$$\phi \frac{\partial c}{\partial t} + \mathbf{u} \cdot \nabla c = \phi \nabla [D_{eff} \nabla c] \quad (5.18)$$

In this equation, the second term on the left-hand side denotes the advective transport through the medium associated with the flow, while the term on the right-hand side represents the diffusive and dispersive transport. As shown in the correlations above, the transverse dispersivity is typically much smaller than the longitudinal dispersivity and so D_{eff} should be written as a tensor. Note also that the advection speed of inert tracer of concentration c is given by u/ϕ , the interstitial speed, as illustrated by this equation, where the speed $u = |\mathbf{u}|$.

According to (5.18), if fluid in the region $x < 0$ has concentration $c = c_o$ and fluid in the region $x > 0$ has concentration $c = 0$ at $t = 0$, then the concentration evolves according to the solution

$$c(x, t) = c_o \left(1 - \operatorname{erf} \left[\frac{x - ut}{2(D_{eff}t)^{1/2}} \right] \right) \quad (5.19)$$

for flow in the positive x direction with net Darcy speed u where ϕ is the porosity.

There are more complex models which account for the adsorption of the tracer onto the formation and solutions for flow in fractures (e.g. van Genuchten and Wierenga, 1976; Freeze and Cherry, 1979; Sudicky and Frind, 1982). We do not aim to replicate all this material herein, but observe that there is a significant literature in this topic.

However, at this point, it is relevant to note that in the field, the larger scale heterogeneities of the system can lead to additional dispersion, as we discuss below with a description of dispersivity in localised lenses of different permeability within the formation. In the case that the heterogeneity of the formation is correlated a significant distance in the along-flow direction, transverse mixing across streamlines may also become important and we also discuss this below. We will see that some of macroscopic dispersion processes can lead to a scale dependence of the dispersion, which is consistent with some observations in real aquifers. For example Gelhar *et al.* (1991) critically reviewed data from 59 field sites, in which the dispersivity was measured over different scales and found considerable scatter, but also suggestion of a general relation between the value of the longitudinal dispersivity and the scale of observation. They also presented data on transverse dispersivity in both the horizontal and vertical direction, which again had considerable scatter and was typically 1–2 orders of magnitude smaller than the longitudinal dispersivity (Figure 5.6). In their compilation of the data, they defined the dispersion coefficients in terms of A_{Lv} and A_{Tv} where v is the seepage or interstitial velocity, u/ϕ where u is the Darcy velocity. The plot in

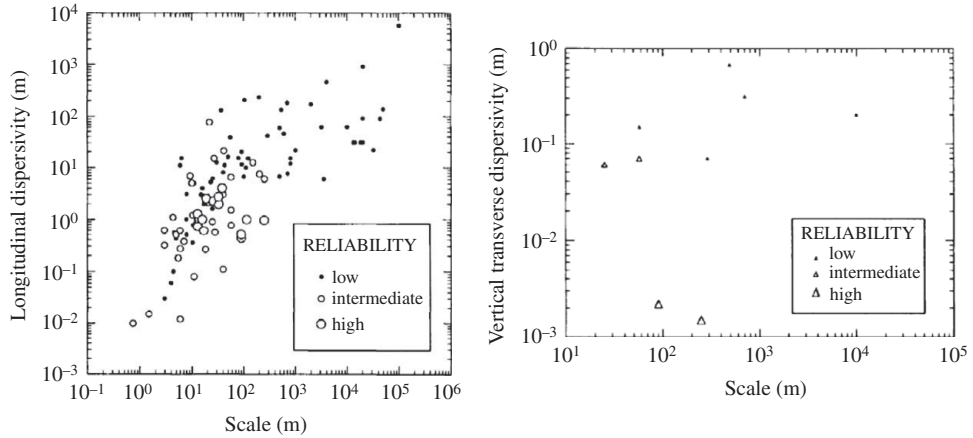


Figure 5.6 Field data on dispersivity as a function of scale from 59 field sites, as reviewed by Gelhar *et al.* (1991). The quality of the data was assessed as indicated on the figure. The data show a trend of increasing dispersion coefficient as a function of scale, and illustrate the challenge of modelling the large-scale dispersion and its variability. After Gelhar *et al.* (1991).

Figure 5.6 shows the values A_L and A_T . With typical flow speeds in the subsurface of 10^{-7} – 10^{-5} m/s these values correspond to dispersivities with values in the range 10^{-8} – 10^{-4} m depending on the scale of the process and the scatter, although Gelhar *et al.* (1991) emphasise the reliability of the smaller values in this range.

5.5 Lenses of different permeability

The presence of localised lenses of different permeability, such as often occurs in fluvial deposits (Chapter 2) also leads to mechanical dispersal of the flow. As an example, we focus on the case of a localised lens of different permeability and develop a simplified picture for the macroscopic dispersion associated with the different travel time of fluid through the lens compared to the background flow (Section 3.4; Figures 5.7–5.9). Different approaches have been adopted in the literature to examine the impact of such a lens, including models of random walks and drift flux (Eames and Bush, 1999). If we consider the fraction of the flow which is diverted into a lens of different permeability, and the travel time of this diverted fluid through the lens, we can estimate the evolution in time of the correlation in the fluctuations of the velocity field relative to the mean flow (cf. Eq. 5.7). We can then use this to assess the effective mechanical dispersivity. In proceeding with this strategy, it is useful to consider the flow through a cylindrical shaped lens; this approach can be extended to consider flow through different shaped inclusions, for example an elongated lens, within the permeable rock. In each case, we

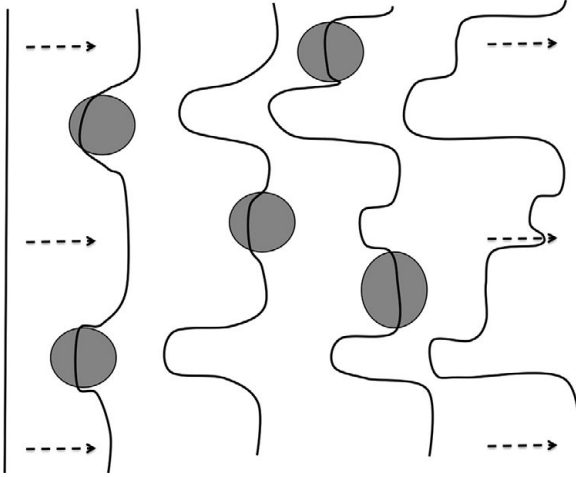


Figure 5.7 Illustration of the gradual distortion of a material surface passing through a series of local regions of high permeability.

can assess the fraction of the flow which is diverted into the lens and the travel time of the fluid through the lens, and thereby develop a scaling for the dispersion.

We consider a uniform flow in the x direction far upstream, u , in a rock of permeability k_o which contains a cylindrical lens of radius a , and permeability k_c whose axis is oriented normal to the flow. We seek a solution for the pressure equation (see Chapter 3)

$$\nabla^2 p = 0 \quad (5.20a)$$

where $u = -\frac{k}{\mu} \nabla p$ such that at the boundary of the cylinder the pressure is continuous $[p]_{\pm} = 0$ and the velocity normal to the boundary is continuous $\left[\frac{k}{\mu} \frac{\partial p}{\partial r}\right]_{\pm} = 0$. This has solution

$$p = -\frac{\mu u}{k_o} \left(1 + \frac{a^2(k_o - k_c)}{r^2(k_o + k_c)}\right) r \cos \theta \quad \text{for } r > a$$

and

$$p = -\frac{2u\mu}{(k_c + k_o)} r \cos \theta \quad \text{for } r < a \quad (5.20b)$$

which illustrates that the flow within the cylindrical region has uniform speed with a maximum value $2u$ when $k_c \gg k_o$ while the minimum speed in the cylinder is approximately $2uk_c/k_o \rightarrow 0$ as $k_c/k_o \rightarrow 0$.

From this solution, we can infer that with a uniform flow in a layer of vertical extent $H \gg a$ (in the direction normal to the flow and the axis of the cylinder), and with a very permeable lens, $k_c \gg k_o$, of size a , the fluid within a region $4a$ wide upstream of the cylinder is diverted into the cylinder. In the cylinder this fluid has an approximate speed

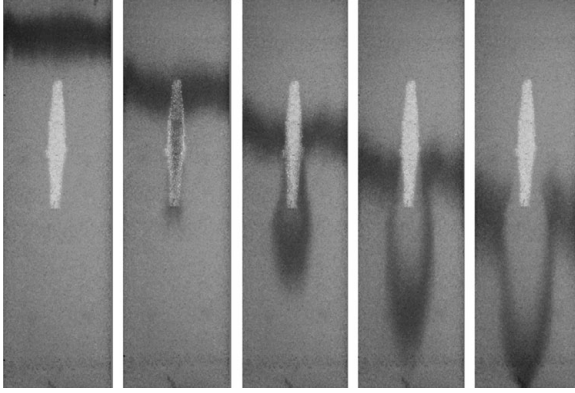


Figure 5.8 Experiment in which fluid is injected from the top and travels down through a thin bead pack which includes a high permeability lens. The lens may be identified as the bright elliptical region in the centre of the porous layer. The figure illustrates the migration and distortion of an initially horizontal line of red dye as it moves through the high permeability lens. The flow short-circuits into the lens, and then emerges downstream leading to considerable dispersion. Photographs courtesy of C. Otto. A black and white version of this figure will appear in some formats. For the colour version, please refer to the plate section.

u relative to the background speed. In this region, the travel time scales as a/u and so the tracer particles are displaced from the mean longitudinal position by an amount of order a . If we have a slug of tracer, initially distributed uniformly in the cross-flow direction, $0 < y < H$, and migrating along the porous layer with the flow (Figure 5.8), then the fraction of the tracer entering the cylinder is $4a/H$. If there is a volume fraction α of such lenses within the formation, then after time t , the number of lenses which will have been encountered is $n \sim \alpha H u t / \pi a^2$. The longitudinal dispersion coefficient associated with the sum of all the lenses, assuming they are sufficiently far apart to act independently, is given by one half the rate of change of the variance in longitudinal position (cf. Eq. 5.7), $\sigma^2(t)$ and this is equal to the sum of the displacements of the tracer by the individual lenses. So the net variance scales as

$$\sigma^2(t) = 2\lambda_h(a/H)(\alpha H u t / a^2)a^2 = 2\lambda_h\alpha a u t \quad (5.21)$$

where λ_h is a constant for the high permeability lens. This leads to the expression for longitudinal dispersion

$$D_L = \frac{1}{2t}\sigma^2(t) = \lambda_h\alpha u a \quad (5.22)$$

Eames and Bush in fact calculated that $\lambda_h = 2.59$. This model assumes that the cross-lens diffusive transport is slow compared to the travel time through the lens, so that there is little time for cross-streamline diffusion as the fluid migrates through the cylinder, $ua/D \gg 1$.

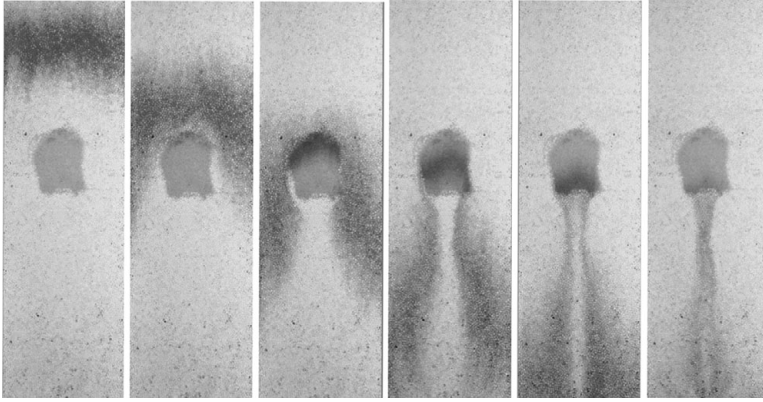


Figure 5.9 Experiment in which fluid is injected from the top and migrates down through a high permeability porous layer which includes a low permeability region, which may be identified as the darker zone in the centre of the cell. The figures show the migration and distortion of an initially horizontal line of red dye through the low permeability lens in a flow which is uniform far upstream and far downstream. The dye is retarded in the lens, and then emerges in a thin plume trailing behind the original red dye front. Photographs courtesy of C. Otto. A black and white version of this figure will appear in some formats. For the colour version, please refer to the plate section.

In the case of a lens of low permeability, the speed within the cylinder has very low values relative to the background (Figure 5.9), scaling as

$$u \sim 2uk_c/k_o \quad (5.23)$$

and so fluid from a region of width $4ak_c/k_o$ is diverted into the cylinder, and has residence time of order $k_o a/2uk_c$ within the cylinder. This leads to a net variance in the position of the fluid relative to that of the mean flow of order $k_o^2 a^2/k_c^2$ in passing one cylinder. The ensemble average variance then has value

$$\sigma^2(t) = 2\lambda_l(ak_c/Hk_o)(\alpha H u t/a^2)(k_o a/k_c)^2 = 2\lambda_l \alpha (k_o/k_c) a u t \quad (5.24)$$

with λ_l a constant, which Eames and Bush calculated to have value $8/3\pi$. In this case, the effective longitudinal dispersivity has value

$$D_L = \frac{1}{2t} \sigma^2(t) = \lambda_l \alpha a u \frac{k_o}{k_c} \quad (5.25)$$

again assuming the cross-streamline diffusion is small. This is greater than the high k_c result since the residence time of the tracer within the lens is greater, leading to a larger variance from the mean, even though a smaller fraction of the flow is diverted into the lens. The model may be generalised to account for lenses with a distribution of shapes and sizes.

Cross-streamline diffusion may become important in the limit that the travel time through the low permeability lens exceeds the diffusion time in the cross-lens direction,

$\frac{a^2}{D_T} < \frac{ak_a}{uk_c}$. In this case, the tracer will diffuse transversely from the low permeability lens into the main stream, substantially reducing the magnitude of the mechanical dispersion. Indeed, in the cross-layer diffusion time a^2/D_T , the background flow will spread a distance of order $(D_L t)^{1/2} \sim a(D_L/D_T)^{1/2}$ in the along-flow direction. This will be larger than the distance that the tracer moving through the lens has been delayed relative to the main flow, over this time, owing to the low permeability of the lens, $\approx a^2 u/D_T$, if $au < (D_L D_T)^{1/2}$.

Some anomalous dispersion effects have been described in terms of a random walk in which there are random waiting times at the nodes of the walk, between successive displacements (cf. Berkowitz and Scher, 1997, 2001). Such effects can lead to a skewness in the dispersal of tracer and more complex models for the dispersion.

5.6 Large-scale shear dispersion

The above models pertain to a representative volume of rock in which the heterogeneity is localised and leads to mechanical dispersion associated with the difference in the travel times between the local regions of different permeability and the main matrix. However, if the heterogeneities extend over longer scales, the transverse pore-scale dispersion may be key in controlling the macroscopic dispersion. To quantify these effects, we can build a model in which we adopt the above picture of dispersion on the pore scale; the larger scale processes are then dominated by the macroscopic structure of the heterogeneity of the formation combined with the cross-flow pore-scale dispersion. Here we consider pressure-driven flow, but in Chapter 10, we extend the analysis to consider the effects of buoyancy-driven flow.

Shear can lead to macroscopic spreading of a patch of tracer, producing an extensive interface between the tracer filled fluid and the original fluid (Figure 5.10). If the interface persists for a sufficiently long distance, coherent dispersive transport across this interface can then be very effective, since the interface may be much larger than the original front. With time, one may envisage that a balance becomes established between the along-stream shear and the cross-stream diffusion. This balance is known as shear dispersion, after G.I. Taylor (1953) who explored such dispersion in a Poiseuille flow in a tube.

In order to illustrate how the magnitude of shear dispersion in a porous layer can be calculated, we present a simplified two-dimensional problem in which there is a parallel flow migrating in the x direction through a stratified aquifer, of thickness w , $0 < z < w$, with the flow speed, $u(z)$ varying in the z direction, normal to the flow. We decompose the concentration and velocity fields into a mean component which only varies along the layer and a fluctuating component which varies across the layer, in the

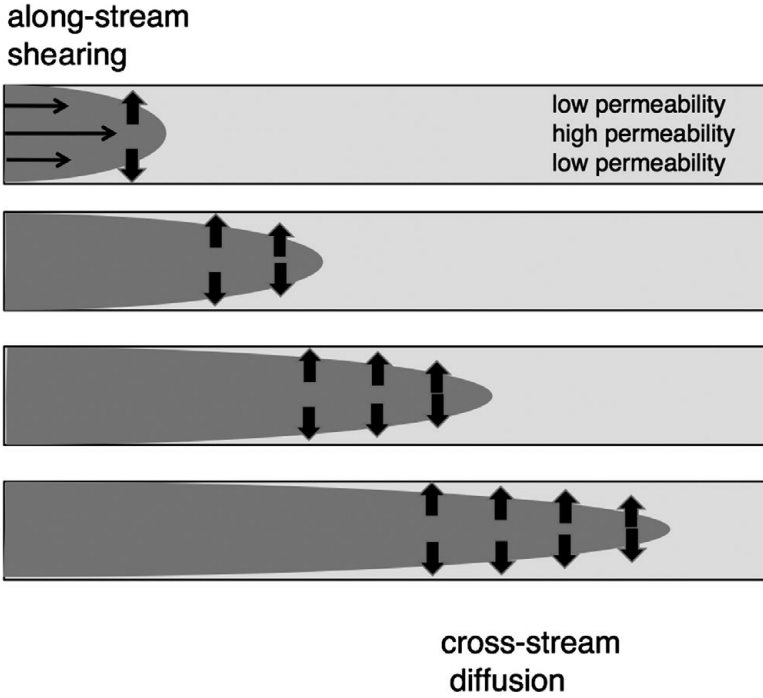


Figure 5.10 Illustration of the physical process of shear dispersion, which leads to cross-streamline diffusion of the tracer as the flow shears out the interface between tracer laden and tracer free fluid.

z direction, and impose zero flux of concentration normal to the boundary at $z = 0$ and $z = w$

$$c = \bar{c}(x) + \hat{c}(x, z) \quad \text{and} \quad u = \bar{u} + \hat{u}(z) \tag{5.26}$$

where

$$\bar{c}(x) = \frac{1}{w} \int_0^w dz c(x, z) \tag{5.27}$$

If we then write the transport equation for concentration in terms of \bar{c} and \hat{c} and \bar{u} and \hat{u} , we find the overall equation has the form

$$\phi \frac{\partial(\bar{c} + \hat{c})}{\partial t} + (\bar{u} + \hat{u}) \frac{\partial(\bar{c} + \hat{c})}{\partial x} = \phi \left[D_L \frac{\partial^2(\bar{c} + \hat{c})}{\partial x^2} + D_T \frac{\partial^2(\bar{c} + \hat{c})}{\partial z^2} \right] \tag{5.28}$$

and so the cross-channel average is

$$\phi \frac{\partial \bar{c}}{\partial t} + \bar{u} \frac{\partial \bar{c}}{\partial x} + \frac{1}{w} \int_0^w \hat{u} \frac{\partial \hat{c}}{\partial x} dz = \phi D_L \frac{\partial^2 \bar{c}}{\partial x^2} \quad (5.29)$$

The challenge in this equation is to determine the non-linear term associated with the fluctuations in concentration and velocity in the cross-channel direction (the last term on the left-hand side). We can make progress with this by noting that the shear along-channel spreads the mean gradient and this produces large concentration gradients cross-channel which are then dispersed in the transverse direction, leading to a net along-channel dispersive flux.

In this limiting regime, we expect the fluctuations to satisfy the relation

$$D_T \frac{\partial^2 \hat{c}}{\partial z^2} \sim \frac{\hat{u}}{\phi} \frac{\partial \bar{c}}{\partial x} \quad (5.30)$$

The detailed solution of this relation requires a parameterisation of the local transverse dispersion coefficient, and for simplicity we take this to be a constant, as is consistent with slow flow for which the molecular transport dominates in the transverse direction or in which the mean velocity is much larger than the fluctuations, so that there is little variation of Peclet number across the flow domain. In each case we can write

$$\hat{c} \sim \int_0^z dz' \int_0^{z'} dz'' \left(\frac{\hat{u}(z'')}{\phi D_T} \right) \frac{\partial \bar{c}}{\partial x} \quad (5.31)$$

We may then evaluate the integral using the knowledge of the velocity shear for a specific flow problem, and this enables us to calculate the non-linear transport. This leads to the relation

$$\frac{1}{w} \int_0^w \hat{u} \hat{c} dz \sim \frac{\beta \bar{u}^2 w^2}{\phi D_T} \frac{\partial \bar{c}}{\partial x} \quad (5.32)$$

where β is a constant of order unity, which depends on the details of the flow structure. It follows that the non-linear transport associated with the velocity and concentration fluctuations is diffusive in character, and we obtain the full transport equation

$$\phi \frac{\partial \bar{c}}{\partial t} + \bar{u} \frac{\partial \bar{c}}{\partial x} = \left(D_L + \frac{\beta u_o^2 w^2}{\phi^2 D_T} \right) \phi \frac{\partial^2 \bar{c}}{\partial x^2} \quad (5.33)$$

where u_o is a scale for the velocity fluctuations. Given that $D_L \approx 1.8\bar{u}d + D_m/\tau$ and $D_T \approx 0.025\bar{u}d + D_m/\tau$ (Section 5.4), with d the pore size and τ the tortuosity, then with high Peclet number, the two terms on the right-hand side can be written as

$$D_{eff} = \bar{u}d \left(1.8 + 40\beta \left(\frac{u_o^2}{\bar{u}^2} \right)^2 \left(\frac{w}{d} \right)^2 \right) \quad (5.34)$$

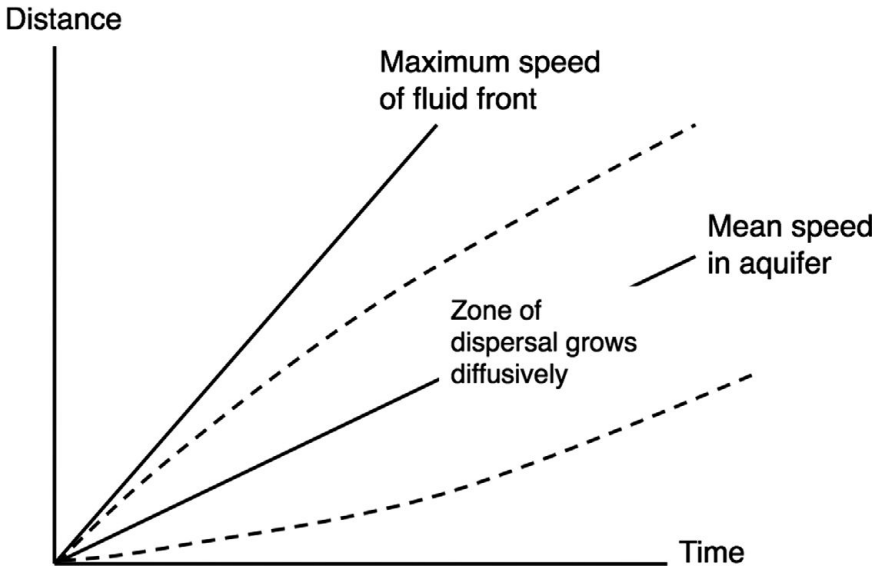


Figure 5.11 Schematic illustration of the effect of cross-flow dispersion in spreading a tracer about the location of the mean flow: cross-streamline diffusion occurs as a tracer becomes stretched by the shear flow, about this mean speed, and this diffusion limits the distance over which tracer can spread ahead and behind the characteristic which migrates with the mean speed.

Note, in building this model, we have assumed that the along-flow distance is sufficient to establish the cross-flow diffusion. This requires a domain of along-stream scale $L > uH^2/D_T$. If the domain is much shorter than this, then the velocity shear will generate mechanical dispersion, as described in the section on localised lenses.

In order to determine the importance of the macroscopic shear dispersion compared to the longitudinal dispersion we require an estimate of the second term in the bracket of Eq. (5.34). For a velocity fluctuation of order 0.1 of the mean, and a layer which has width w in excess of 10^3 – 10^4 times the pore scale, d , the shear dispersion will typically dominate the longitudinal dispersion as we illustrate in the detailed calculation below. Note that since the macrodispersion acts as a diffusive-type effect in this reduced model, one can show that the two terms which are balanced in Eq. (5.35) are indeed the long-time dominant terms in the equation for fluctuations about the mean.

In the above model, we have assumed that the perturbations to the background flow are small so that the local dispersion coefficient may be taken to be approximately constant. However, if the perturbations are comparable to the background flow, this can lead to anomalous dispersion effects if the local dispersion coefficient depends on the local speed, in a somewhat analogous fashion to that described for the no-slip condition (Section 5.3) in which there is a long tail in the dispersing flow associated with the slow release of the fluid from the low velocity zones.

As a simple example of the basic calculation we can consider the case of a linear shear flow, in the x direction

$$u = \bar{U} + U_o \left(\frac{z}{h} - 1/2 \right) \quad \text{for } 0 < z < h \quad (5.35)$$

along a porous layer of finite cross-flow extent, $0 < z < h$, with impermeable boundaries at $z = 0$ and $z = h$. The mean and perturbation flow is therefore given by

$$\bar{u} = \bar{U} \quad \text{and} \quad \hat{u} = U_o \left[\frac{z}{h} - \frac{1}{2} \right] \quad (5.36)$$

using Eq. (5.31), the perturbation concentration in the layer, is given by

$$\hat{c} = \frac{U_o}{\phi D_T} \left[\frac{z^3}{6h} - \frac{z^2}{4} \right] \frac{\partial \bar{c}}{\partial x} \quad (5.37)$$

and combining this with the perturbation velocity, we find that the dispersive transport is given by

$$\frac{1}{h} \int_0^h \hat{u} \hat{c} dz = - \frac{U_o^2 h^2}{120 \phi D_T} \frac{\partial \bar{c}}{\partial x} \quad (5.38)$$

where we assume that $\bar{U} \gg U_o$. In a porous layer of depth $h \sim 1$ m, with a flow speed of about 10^{-6} m/s, and with pore-scale dispersion for a typical tracer being of order 10^{-8} m²/s, it follows that the longitudinal shear dispersion associated with the macroscopic flow has value $\sim 10^{-5}$ m²/s, which far exceeds the pore-scale longitudinal dispersive transport.

The model described above, in which we work with the averaged properties in the formation, requires time for the cross-flow diffusion to act. Since the pore-scale diffusivity is so small, the flow will in fact shear out a distance

$$L = U_o \tau \quad (5.39)$$

over the time τ required to diffuse a distance h in the cross-flow direction as given by

$$\tau \sim \frac{h^2}{D_T} \sim 10^9 - 10^{10} \text{ s} \quad (5.40)$$

based on the typical flow values above, with $D_T \sim 10^{-9} - 10^{-10}$ m²/s. We therefore expect the tracer to homogenise across a layer of 1 m thickness over times of order 30–300 years, and the flow will migrate a distance 1–10 km. These times may be relatively short compared to times of interest in the transport of radionuclides or contaminants from DNAPL plumes in groundwater flows, and so may be key in long-term modelling of the dispersion of such flows: we note, however, that in modelling such flows effects of adsorption onto the porous matrix can have an impact on the transport patterns. In large oil fields, with production over 10–15 years, such effects may become important for the transport and dispersal of injected water and in some cases

treatment chemicals. However, on shorter times, even though tracer will be sheared and will diffuse in the cross-flow direction it may not homogenise across the layer. The description of the depth averaged properties of the flow is very useful for gaining a picture of the rate of spread of a cloud of tracer. It is important to note, however, that if the along-flow scale of the heterogeneity is much smaller, there may be more localised shearing of the tracer leading to mechanical dispersion as discussed for localised lenses of different permeability (Section 5.5).

A shear flow, as considered in this idealised example, might arise, in principle, in a porous layer in which the grains were deposited from a waning flow, and hence in which at each point in the deposit, the grain size would gradually fine upwards, leading to a gradual decrease in permeability, speed and also dispersivity. In such a formation, the macrodispersion associated with the large-scale shear in theory produces a transport flux which is inversely proportional to the transverse pore-scale dispersion, and scales with the square of the fluctuations in the mean speed.

5.7 Oscillatory flow

We have focused on dispersion in simple translational flows to this point. However, in various situations oscillatory flows develop and lead to dispersive mixing with the rate of mixing dependent on the Peclet number for the oscillatory flow. As a simple example, if we consider a rectilinear oscillatory flow for which the flow has frequency ω and oscillation amplitude a then we can in fact define a Peclet number based on the oscillation amplitude, $P_o = \omega a^2 / D_m$ as well as the Peclet number based on the pore scale, as used above, $Pe = \omega a d / D_m$. For the mechanical mixing limit we might envisage that the effective longitudinal dispersion has the form

$$D_L = \alpha D_m P_o f(a/d) \quad (5.41)$$

where α is a constant of order unity. Laboratory models of the mixing in bead packs with beads of sizes 0.5–1.0 mm, and oscillation amplitudes ranging from 0.5–5.0 cm, with frequencies of 0.1–1.0 Hz, using a saw-tooth profile for the oscillation, suggest that the dispersive mixing coefficient for this range of Peclet number, 10^3 – 10^5 , collapses to the form

$$D = 0.3 D_m P_o = 0.3 \omega a^2 \quad (5.42)$$

A laboratory experiment of this mixing is shown in Figure 5.12, in which panel a illustrates the growth of the intermediate zone between the lower (orange) and upper (blue) layers, and the black and white adjacent image illustrates the growth of the mixed zone. Figure 5.12b illustrates the collapse of a wide range of experimental data to this mixing law. Such oscillatory mixing may be important in situations in which there

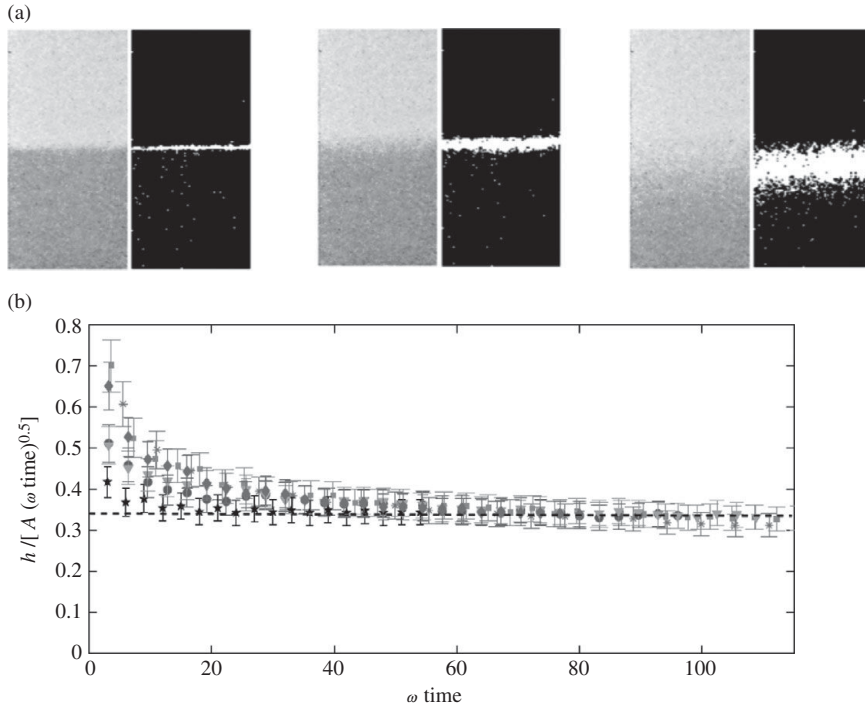


Figure 5.12 (a) Illustration of the mixing at an interface with an oscillatory flow, showing the broadening of the intermediate coloured zone between the lower and upper layer fluid, with successive oscillations, and a black–white image illustrating the growth of the region of intermediate concentration. (b) Estimate of the dispersion coefficient, as compared to laboratory data, by comparing the thickness of the mixed zone h with $a(\omega t)^{1/2}$. Figure courtesy of C. Otto. A black and white version of this figure will appear in some formats. For the colour version, please refer to the plate section.

are tidal oscillations or fluctuations in rainfall and aquifer recharge, causing mixing of different fluids within an aquifer even with no mean flow. In heterogeneous formations, the longitudinal mixing is much more effective in the high permeability layers in which there is a higher amplitude of oscillation. If there is also a density difference between the two bodies of fluid, this can induce a substantial transverse dispersion driven by the ensuing unstable density gradient across the layers (Otto *et al.*, 2014).

With unidirectional flow in a porous layer, the asymmetry between transverse and longitudinal dispersion causes much more dispersion in the along-flow direction (see Figure 5.1). However, if there is a forced flow which is intermittent in direction and time, then it may be possible to produce a more spatially uniform pattern of dispersion even with no net flux. If a chemical treatment is being injected into a porous layer, the use of such a spatially varying oscillation may enable more complete dispersion of the chemical within the medium. Otherwise, the chemical may become very effectively

dispersed in the flow direction, owing to the relatively large longitudinal dispersion, while remaining relatively localised in the transverse direction.

5.8 Exercises

1. Calculate the anomalous dispersion associated with the no-slip condition in a cylindrical tube–connector–tube type porous medium, in which you may assume perfect mixing in each of the connectors.
2. Calculate the distortion to a line $0 < y < H$ originally far upstream, $x \ll 0$, produced by a flow through a two-dimensional porous layer containing a lens of width $d(x) = d_o \sin(2\pi x/L)$ of permeability k_1 in the region $0 < x < L$, where the lens is embedded in a porous layer of width $H \gg d_o$ and of permeability $k_o \ll k_1$. If there are n such lenses per unit length in a laterally extensive layer of porous rock, such that the lenses do not overlap, calculate the dispersion associated with the lenses. You may use the result that $\frac{1}{2t} \left(\overline{[x(t) - \bar{x}(t)]^2} \right)$ equals the sum of the area of distortion of the line, relative to the uniform flow per unit time.
3. In the case of a radial flow with uniform flux such that $D_L \sim ud$ where u is the speed and d the pore size, show that the dispersive mixing at a fluid front may initially be significant but at long times, the dispersion becomes small relative to the advection, leading to a localised front on the scale of the flow.

6 Frontal instability

In Chapters 3 and 4 we presented a series of problems which relate to the displacement of one fluid by a second, and prediction of the sweep; these flows involve fronts. To date we have modelled fronts between miscible fluids, and we have treated the fronts as being planar in our theoretical discussion. However, in many problems associated with the extraction of natural resources there will also be immiscible fronts, or fronts across which there may be changes in the viscosity and density of the fluids. We now explore the stability of such fronts, and find that in numerous circumstances fronts in porous layers can become unstable. This is a classical problem, first described by Saffman and Taylor (1956) and there is a fascinating review by Homsy (1987). Since then there has been an enormous body of work on viscous fingering, and variants thereof, which arise with non-Newtonian fluids (e.g. Linder *et al.*, 2002), reacting fronts (Hinch and Bhatt, 1990), granular media and fronts with phase change (e.g. Riolfo *et al.*, 2012). Our aim in this chapter is to provide a basic understanding of viscous fingering, and consider its role in flow in porous media, especially for injection or extraction phenomena, but we mention analogous processes in non-consolidated media. In order to mitigate the instability when water is used to displace viscous oil, viscosifiers are added to the water to make it more viscous, and we discuss the implications of the instability for injection of a discrete slug of viscosified water into an oil field. In later chapters we consider the effect of reactions and the dissolution instability (Chapter 8) and the instability of a boiling front, relevant for geothermal systems (Chapter 11).

6.1 A model of the instability

Figure 6.1 shows a series of four photographs, at successive times in which fresh low viscosity water displaces a more viscous sugar solution in a bead pack which is 10 cm wide, 1 cm deep (into the page) and composed of beads of size 1 mm. The mechanism of instability can be understood by observing that the pressure gradient in the more viscous fluid downstream is greater than that in the less viscous fluid upstream. Thus, instead of displacing the high viscosity fluid downstream with a uniform flow, the

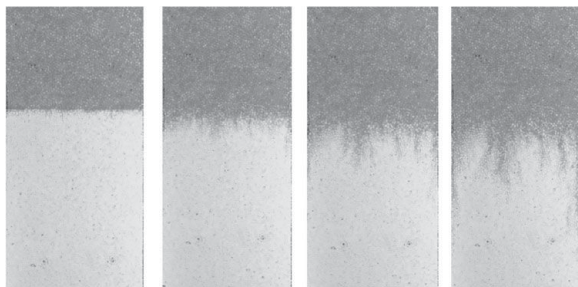


Figure 6.1 Development and evolution of miscible fingers in a porous bead pack as water displaces a more viscous sugar solution. The motion is in the downwards direction in the figure. Small fingers of the red water migrate through the sugar solution in an irregular pattern, developing a zone of intermingled fluid, which grows with time. There is little mixing of the phases during this experiment owing to the relatively long time for diffusion across the fingers compared to the time of the experiment. Figure courtesy of C. Otto. A black and white version of this figure will appear in some formats. For the colour version, please refer to the plate section.

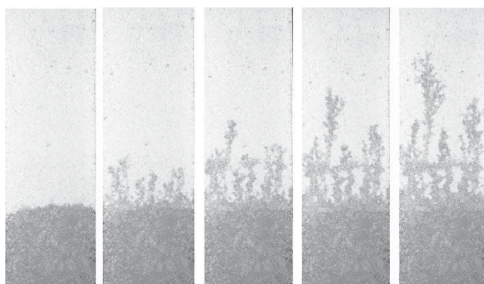


Figure 6.2 Viscous fingering produced as water (red) migrates upwards and displaces oil (clear) in a bead pack of width 10 cm. The intermingled zone grows with time. Figure courtesy of C. Otto. A black and white version of this figure will appear in some formats. For the colour version, please refer to the plate section.

lower viscosity fluid advancing from upstream drives the more viscous fluid sideways, generating channels or fingers into which the displacing fluid continually advances. This provides a path of much lower resistance, and much of the more viscous fluid is bypassed. In Figure 6.2, we illustrate viscous instability arising in an immiscible oil–water system in the same bead pack. The bead pack acts as a permeable layer, as red water migrates upwards to displace clear oil. In this case the fingers become more dispersed as they pass successive beads and break up into multiple fingers. Again the two-phase zone becomes progressively larger with time in the flow direction.

To model this instability we consider a uniform flow of one fluid displacing a second across an interface, and perturb the interface with a sinusoidal perturbation parallel to the interface. We then examine how the perturbations vary in time, to see if the interface is stable under displacement. The pressure is modelled in terms of a base pressure

gradient for rectilinear flow with a small perturbation pressure field associated with a sinusoidal distortion of the interface,

$$p(x, y, t) = p_m^0(x, t) + \epsilon p_m^1(x, y, t) \quad (6.1)$$

where $\epsilon \ll 1$.

The basic state has pressure gradient in each layer given by

$$\frac{dp_m^0}{dx} = -\mu_m u/k \quad (6.2)$$

where subscript m denotes the upstream displacing fluid $m=1$ or the downstream displaced fluid, $m=2$. We analyse the stability of a sinusoidal perturbation to the flat interface in the form

$$x = \frac{ut}{\phi} + \eta \exp(iny + \sigma t) \quad (6.3)$$

where σ is the growth rate of the perturbation and n the wavenumber (Figure 6.3). The pressure perturbation p_m^1 satisfies

$$\nabla^2 p_m^1 = 0 \quad (6.4)$$

with boundary conditions that (i) p is continuous across the interface (for miscible flow); (ii) the perturbation decays far from the interface since the instability is generated at the interface; and (iii) the fluid speed matches the interface speed at the interface. This leads to the solution

$$p_m^1 = \epsilon a_m \exp \left[iny - (-1)^m n \left(x - \frac{ut}{\phi} \right) + \sigma t \right] \quad (6.5)$$

for $m=1, 2$ and the boundary condition (iii)

$$\frac{\partial \eta}{\partial t} = -\epsilon \frac{k}{\phi \mu_m} \frac{\partial p_m^1}{\partial x} \quad (6.6)$$

requires that

$$\sigma \eta = -\epsilon \frac{k}{\phi \mu_1} n a_1 = \epsilon \frac{k}{\phi \mu_2} n a_2 \quad (6.7)$$

and the pressure continuity condition requires that

$$\epsilon a_1 - \frac{\mu_1 u \eta}{k} = \epsilon a_2 - \frac{\mu_2 u \eta}{k} \quad (6.8)$$

Eliminating a_1 and a_2 we find the dispersion relation for the growth rate of perturbations

$$\sigma = \frac{nu}{\phi} \left(\frac{\mu_2 - \mu_1}{\mu_1 + \mu_2} \right) \quad (6.9)$$

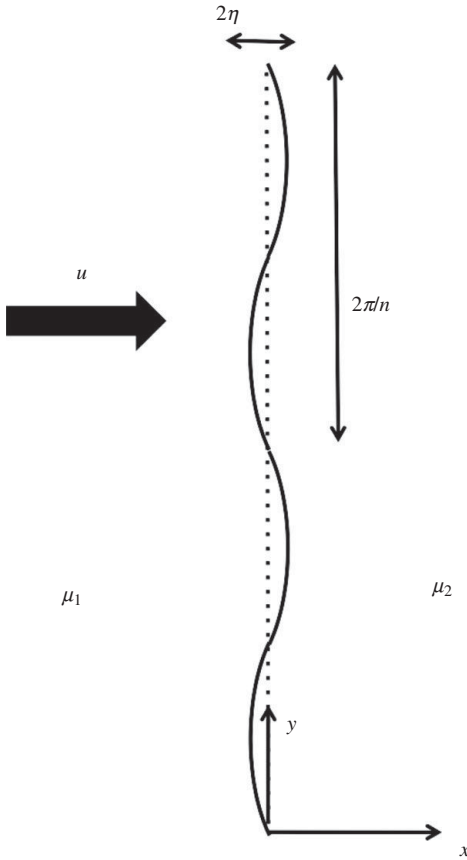


Figure 6.3 Cartoon illustrating the geometry for the Saffman–Taylor instability calculation.

We see that if a low viscosity fluid displaces a high viscosity fluid, $\mu_1 < \mu_2$, the perturbation to the interface grows. As the instability becomes non-linear, the low viscosity fluid can finger through the high viscosity fluid. According to this model, the most unstable wavelength for the instability is zero, as this corresponds to the shortest cross-flow displacement of the high viscosity fluid in order to allow a finger of low viscosity fluid to move forward. However, the short wavelength instability tends to be suppressed by several effects: first in miscible displacements, diffusion between the species will cancel out the difference in properties and tend to prevent very short wavelength perturbations from growing (cf. Homsy *et al.*, 1987). Second, in immiscible displacements, the surface tension will tend to stabilise the interface; the effect of surface tension is greatest for short wavelengths which have the greatest curvature and this leads to a minimum wavelength for instability (see below).

In the case that the fluids also have different density, then the instability will either be promoted or suppressed by gravity when the motion has a component parallel to

the gravitational acceleration. With the interface oriented at angle θ to the horizontal, with fluid 2 above fluid 1, the dispersion relation becomes modified to include the hydrostatic pressure gradient in the fluid, leading to the relation

$$\sigma = \frac{n}{\phi(\mu_2 + \mu_1)} [(\mu_2 - \mu_1)u + k(\rho_2 - \rho_1)g \cos \theta] \quad (6.10)$$

From this relation, it may be seen that a favourable viscosity gradient with high viscosity fluid displacing low viscosity fluid, $\mu_1 > \mu_2$ may stabilise a gravitationally unstable front with dense fluid above less dense fluid, $\rho_2 > \rho_1$, if the interface migrates sufficiently rapidly. Also, a viscously unstable interface may be stabilised by gravity if $\rho_2 < \rho_1$ and the interface migrates sufficiently slowly.

In Chapter 9, we turn to gravitationally driven flows, in which the difference in density of one fluid relative to a second controls the flow. However, we illustrate a photograph from a laboratory experiment showing a gravitational instability on a downward moving front, in which a layer of relatively dense red saline fluid displaces a layer of clear fresh liquid; with a sufficiently slow injection rate, the interface develops fingers which advance ahead of the main front, and leads to a dispersed interface (Figure 6.4: see Chapter 10). The process, while the instability is still of small amplitude, is directly analogous to the viscous instability on a moving front, as seen in the analysis above. In both cases, one assumes that the initial state involves a planar interface with an extensive zone of fluid on each side of this interface. In practice this can be established by setting up the system upside-down and then inverting the cell.

The analysis above was based on modelling flow in a porous medium. In order to explore some of these phenomena, it is convenient to use an analogue two-dimensional system, known as a Hele–Shaw cell. This consists of two parallel plates with a thin

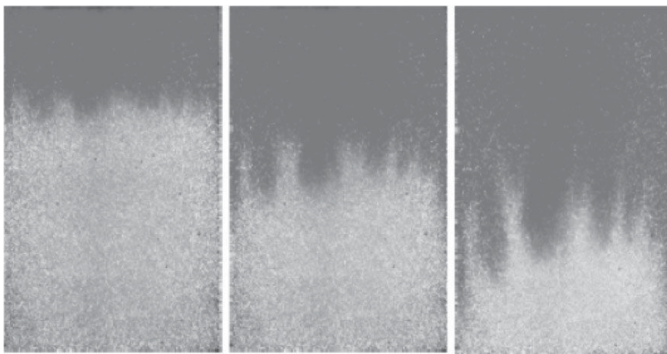


Figure 6.4 An example of gravitational instability as a layer of saline dense red liquid migrates downwards into a layer of less dense clear fresh water in a bead pack. A black and white version of this figure will appear in some formats. For the colour version, please refer to the plate section.

gap, b , so that the flow between the plates is of low Reynolds number, and for single phase flow develops a Poiseuille flow profile,

$$u(y) = \nabla p \frac{(y^2 - by)}{2\mu} \quad (6.11)$$

as a function of the cross-gap position y , $0 < y < b$, so that the mean flow between the plates is given by

$$u = - \frac{b^2}{12\mu} \nabla p \quad (6.12)$$

for a pressure gradient Δp . This corresponds to a porous medium with $\phi = 1$ and permeability $k = b^2/12$. Paterson (1985) has proposed that with a Hele–Shaw cell, the minimum wavelength of instability for a miscible displacement scales with the thickness of the cell in order that the viscous dissipation is minimised; with smaller wavelengths, the distortion associated with the flow leads to greater dissipation.

6.2 Surface tension

If we consider an immiscible displacement, we need to account for the effects of surface tension. In a Hele–Shaw cell, the surface tension has a constant component associated with the curvature normal to the plane of the plates, and a component parallel to the plane of the plates associated with the displacement and instability of the interface. In addition to the consideration of the interfacial tension between the two fluids, the wetting properties of the fluids on the walls of the Hele–Shaw cell, which are related to the difference in the fluid–fluid and each of the fluid–wall interfacial tensions, determines whether the fluid being displaced leaves a thin film on the walls of the cell, or if there is an advancing contact line. This effect, as well as the effect of the normal viscous stress at the interface, has been considered by several researchers in more complete models of the process, and leads to correction terms in modelling immiscible Hele–Shaw displacements (Schwartz, 1986; Reinelt, 1987; Maxworthy, 1989; Kim *et al.*, 2007). However, many of the general principles follow from a simplified analysis in which we model the cross-layer curvature of the interface as being constant, leading to a pressure drop across the interface $x = x(y, t)$ given by

$$\Delta p = T \left[\frac{2}{b} + \frac{\partial^2 x}{\partial y^2} \right] \quad (6.13)$$

The first term denotes the pressure drop from the curvature normal to the plates, a distance $2b$ apart. Substituting this expression into the pressure boundary condition

at the interface, as given above, the dispersion relation acquires an additional term, leading to the expression, for $\phi = 1$,

$$\left[\frac{\mu_1 + \mu_2}{k} \right] \sigma = n \left[\frac{u(\mu_2 - \mu_1)}{k} + g(\rho_2 - \rho_1) \right] - Tn^3 \quad (6.14)$$

The maximum growth rate occurs when

$$n = \left[\frac{u(\mu_2 - \mu_1) + kg(\rho_2 - \rho_1)}{3kT} \right]^{1/2} \quad (6.15)$$

For a flow with speed $u = 10^{-4}$ m/s, viscosity contrast 10^{-3} Pa s, and Hele–Shaw permeability 10^{-7} m², and with surface tension $T = 70$ mN/m², we find that the wavelength of the instability has length of order 0.15 m. The expression (6.14) also illustrates that the system is unstable for small values of n , but that above a critical value, all wavenumbers are stable, as expected (see Figure 6.5).

In a porous rock, the effects of surface tension strictly only apply on the scale of the grains, across the pores; however, we will see in the next chapter that owing to the possible flooding of the pore space with both fluids, there is an effective capillary pressure in the pore space which depends on the saturation of each phase within the pore space. There is also typically a capillary entry pressure for the non-wetting phase if a non-wetting fluid migrates into a porous layer.

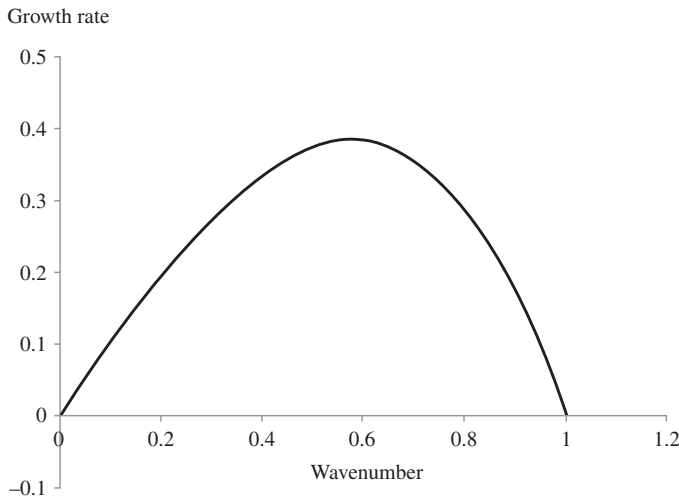


Figure 6.5 Calculation of the dimensionless growth rate of the viscous fingering instability (Saffman–Taylor) as a function of the wavelength, for the case of an immiscible front in which surface tension can stabilise the front.

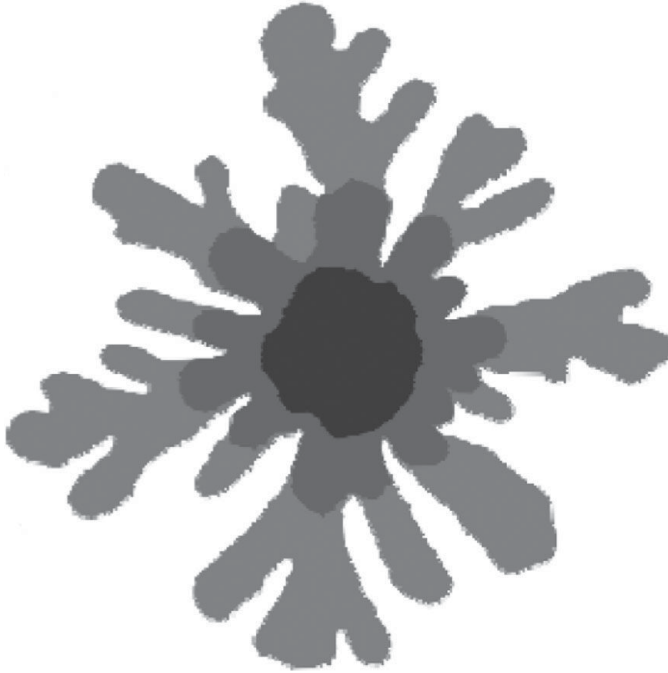


Figure 6.6 Evolution of a viscous fingering instability in a circular Hele–Shaw cell. Three images, in different shades of blue, are superposed to illustrate the evolution with time of the fingers. A black and white version of this figure will appear in some formats. For the colour version, please refer to the plate section.

6.3 Axisymmetric flow

With a radially spreading flow issuing from a point source, the linear instability evolves in time since the radius of the interface increases with time, and this leads to a transition in the most unstable modes. For example, Figure 6.6 shows the instability which develops when air is injected into a Hele–Shaw cell filled with glycerol at three successive times, shown by the different shades. Initially the interface is approximately circular, but then breaks up into a series of fingers which then bifurcate into more fingers as they develop non-linearly. To explore this process, we consider a radially spreading flow, with a constant injection rate and consider perturbations to the interface in the form of azimuthal waves of the form $A_n(t) \exp(in\theta)$ where we denote position as (r, θ) in polar coordinates. We then develop the linearised equation for the evolution of each $A_n(t)$ by perturbing the pressure upstream and downstream of the interface, and matching the jump in pressure with the surface tension.

To solve for the pressure field, p , we note that the pressure on each side of the interface is now given by Laplace’s equation in a radial geometry, leading to

$$p_{rr} + \frac{1}{r}p_r + \frac{1}{r^2}p_{\theta\theta} = 0 \quad (6.16)$$

The base state is given by

$$p_j^o = -\frac{\mu Q}{2\pi k} \ln r + c_j \quad \text{for } j=1,2 \quad (6.17)$$

and the first-order perturbations, driven by the interface, are given by the azimuthal modes, $n \geq 1$

$$p_j^1 = (-1)^j \beta \left(\frac{r^n}{R^n} \right)^{(-1)^{j-1}} \exp(in\theta) \quad (6.18)$$

for the inner, $j=1$ and outer $j=2$ regions of the fluid, such that the perturbations decay from the interface. We match the perturbation to the fluid speed at the interface with the speed of the perturbation of the interface, which is located at $r = R(t) + A_n(t)\exp(in\theta)$, where $R(t) = (Qt/\pi)^{1/2}$. Also, we match the change in dynamic pressure across the perturbed interface with the change in surface tension associated with the perturbation to the position of the interface. After some algebra we obtain the expression for the growth rate of mode n , with amplitude $A_n(t)$

$$\frac{1}{A_n} \frac{dA_n}{dt} = \frac{Q_n}{2\pi R^2} \frac{\mu_2 - \mu_1}{\mu_1 + \mu_2} - \frac{Q}{2\pi R^2} - \frac{n(n^2 - 1)Tk}{R^3(\mu_1 + \mu_2)} \quad (6.19)$$

where subscript 2 denotes the outer fluid and R is the radius of the interface. Since the base state is evolving with time, as manifest by the gradual increase of R with time, the growth of the modes is not exponential as for the planar case, and indeed the growth rate for each mode varies non-monotonically with R .

In Figure 6.7 we plot the right-hand side of the above equation to determine the growth rate of the instability as a function of radius for illustrative parameter values. Each mode becomes unstable at a given radius, with the surface tension stabilising that mode for smaller radii. Also, each mode reaches a maximum growth rate as the radius reaches a specific point; the growth rate of that mode subsequently wanes as the radius continues to grow. As a result, if a perturbation is initially composed of all wavelengths, then as the radius grows, the amplitude of progressively larger wavenumbers become the largest, until the perturbation becomes non-linear. The gradual evolution of the amplitude of the modes is shown in Figure 6.8 and this identifies how the mode with the largest amplitude gradually becomes of higher wavenumber with time.

6.4 Fluid annuli and droplet formation

The viscous instability has substantial implications for the recovery of oil through the injection of water. If the water is more mobile it will tend to finger through the oil

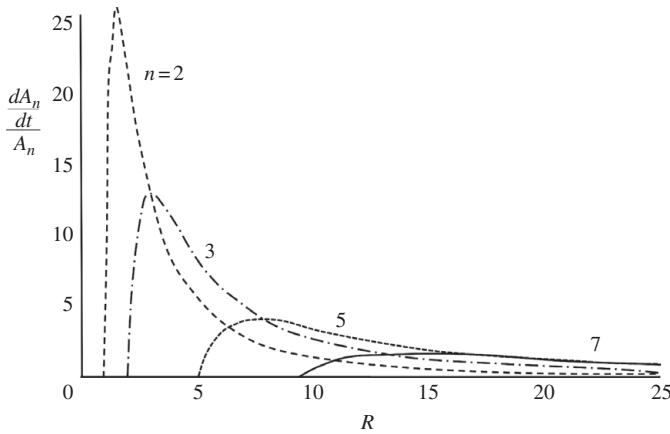


Figure 6.7 Illustration of the variation of growth rate of the different azimuthal modes, as indicated by the numbers on the curves, for injection of fluid from a central well, into a porous layer, with two-dimensional axisymmetric flow. The horizontal axis corresponds to the radius of the flow front. After Cardoso and Woods (1993).

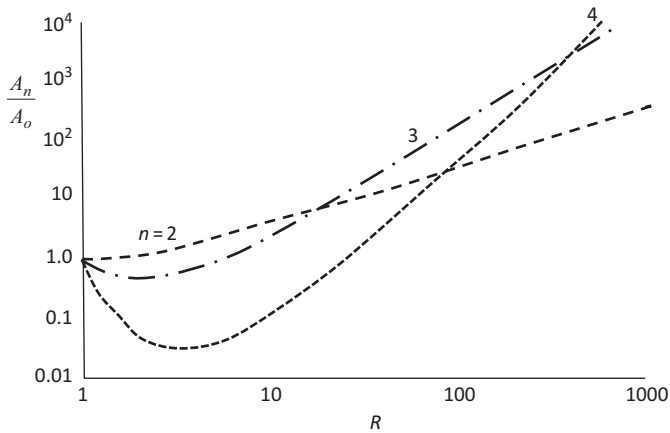


Figure 6.8 Amplitude of each mode as a function of the radius of the interface, relative to the initial amplitude of the disturbance of that mode. Curves are shown for azimuthal modes 2, 3 and 4. As the radius increases the most unstable mode coincides with a greater wavenumber; this leads to a cascade of the most unstable mode with radius. After Cardoso and Woods (1993).

towards the producing well, thereby leaving considerable amounts of oil in the formation. In order to suppress or limit the development of the instability, a number of polymer systems have been developed to viscosify the injected water in an attempt to stabilise the front. However, in many cases, the chemical solutions are expensive and cannot be supplied with all the injected water. Instead, a finite slug of chemical which acts to viscosify the water may be injected with the water, and this is then followed by a water flood. The presence of a viscous fluid ahead of the injected water leads to

the development of two interfaces. In some situations, the leading interface involves a viscous fluid displacing the oil (or a previously water-flooded region) and this interface will typically be stable to viscous instability. The trailing front involves the relatively mobile injection water displacing the viscosified fluid, and so is unstable. The stability of the overall system depends on the viscosity ratio of the two outer fluids, but the presence of the intermediate layer may affect the growth rate and morphology of the instability; indeed, since one of the interfaces of the intermediate layer may be unstable, it may break up into droplets. The benefit of the viscosifier may then lie in delaying, rather than preventing, the onset of instability. Cardoso and Woods (1993) analysed this instability in detail, by using a perturbation expansion for each of the two interfaces, in a fashion analogous to the single front described above. From this they showed that, even in the case that the overall interface of the two outer fluids is stable, one of the interior interfaces may be unstable and that this can lead to break up of the annulus into droplets (cf. Figure 6.9). This effect is important in that it identifies how the addition of a third fluid may lead to delay in the growth of the interfacial instabilities but also that the intermediate layer may be breached by the fingering process,

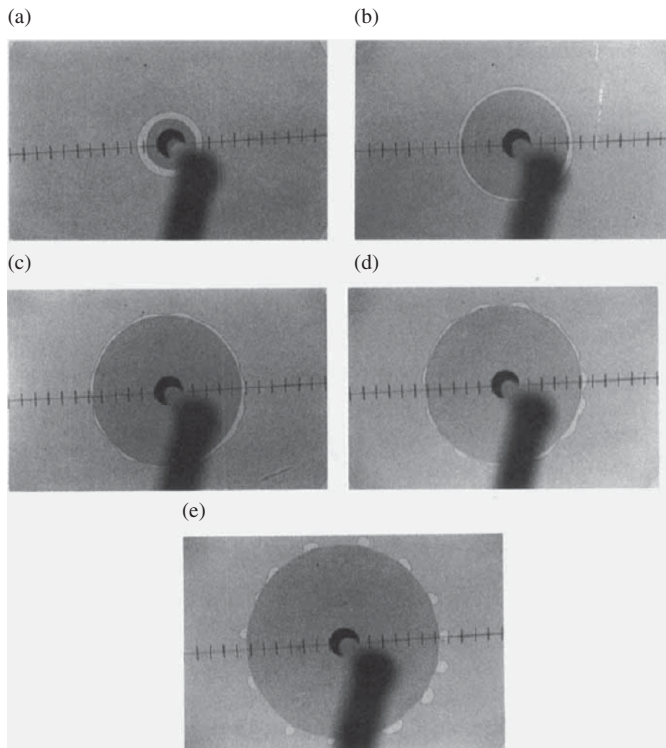


Figure 6.9 Illustration of the formation of a series of droplets on the boundary of the fluid–fluid interface as the annulus breaks up through viscous instability. After Cardoso and Woods (1993).

reducing its effectiveness. We return to the effect of polymer floods on the pattern of flow in a reservoir in Chapter 8.

In many porous rocks, the heterogeneity of the formation can lead to irregularities in the shape of the flow front and these in turn can control the wavelength of the viscous instability, but may also dominate the spreading of the interface by viscous instability as fluid migrates along the higher permeability pathways. As a result, although viscous instability is pervasive in leading to the dispersal of interfaces, it occurs in tandem with the process of dispersion, as described in the previous chapter, and, for immiscible displacements in a porous layer, it is also influenced by the effects of two-phase flow, which we describe in the next chapter. However, at the end of this chapter, we discuss viscous fingering in a Hele–Shaw cell of variable aperture.

6.5 Instability of reaction fronts

The instability mechanism identified for the Saffman–Taylor instability can be seen in many other processes in porous media in which there is an increasing pressure gradient across a front. For example, with a dissolution front, the region of rock upstream of the front, where the dissolution has already occurred, will have an elevated permeability, while downstream the rock is unreacted and still has the original permeability. As a result, the reaction front will become unstable and develop dissolution channels. One important process where such an instability is critical is in the acidising process (cf. Hinch and Bhatt, 1990). In a number of oil-production systems in which there is water injection, the formation water containing barium in solution may reach the production well at one height in the producing zone, while the injected water containing sulfate may reach the production well at a different height, if it follows a different more permeable layer through the formation. When these solutions mix, barium sulfate may be precipitated, leading to scale formation and a loss of permeability of the production well. In order to mitigate this phenomenon, acid is injected into the well with the objective of dissolving the scale and restoring the permeability of the formation. Although there may be some kinetics controlling the dissolution rate, and we explore this in more detail in Chapter 8, a simple model to demonstrate the process arises if we assume that there is a sharp reaction front across which the permeability changes from k_1 to k_2 . Typically, such a reaction front advances at a fraction λ of the interstitial speed, i.e. with speed $\frac{\lambda u}{\phi}$, dependent on the stoichiometry of the reaction (Chapter 8). If we follow the stability approach used to study the viscous instability, given in Section 6.1, but now applied at the reacting interface, we find that across this interface, which has speed $\lambda u/\phi$, the perturbation to the speed of the front requires that (cf. Eq. 6.7)

$$\sigma\eta = -\frac{\lambda k_1 n p_1}{\phi \mu_1} = \frac{\lambda k_2 n p_2}{\phi \mu_2} \quad (6.20)$$

since the interface migrates at a fraction λ of the interstitial speed, while the pressure continuity condition (cf. Eq. 6.8) is of the form

$$p_1 - \frac{\mu_1 u \eta}{k_1} = p_2 - \frac{\mu_2 u \eta}{k_2} \quad (6.21)$$

where the perturbation pressures upstream and downstream have magnitude p_1 and p_2 respectively (cf. ϵa_i , Eq. 6.5). Combining these relations, following the same approach as in Section 6.1, we find the growth rate of perturbations

$$\sigma = \frac{\lambda u n}{\phi} \left(\frac{\frac{\mu_2}{k_2} - \frac{\mu_1}{k_1}}{\frac{\mu_2}{k_2} + \frac{\mu_1}{k_1}} \right) \quad (6.22)$$

where subscripts 1 and 2 denote the properties upstream and downstream of the front. Here, the rock upstream has reacted already while the fluid downstream carries off the dissolved material and hence may suffer a change in viscosity, and density, the latter of which we neglect herein. If the permeability of the unreacted rock, k_2 , is smaller than that of the reacted rock, k_1 , corresponding to a dissolution reaction, then the system will tend to be unstable, and the dissolution front will break up into small channels, provided the effect of any change in viscosity of the fluid following the dissolution is smaller than the effect of the change in permeability. It is also seen that a precipitation reaction tends to be stable, since the permeability will decrease from upstream to downstream as the pore spaces become filled with precipitate, $k_2 > k_1$.

Such instabilities are influenced by molecular diffusion, which can diffuse the reactants and lead to cut-off of the smallest wavelengths, but also by the kinetics of the reaction which typically leads to formation of a reaction zone across which the fluid properties change, as described in Chapter 8. Other fronts involving phase change and reaction also exhibit instability in some situations. For example, the migration of a boiling front can become unstable, as described in Chapter 11 in relation to geothermal systems. Some recent analysis and experiments on the stability of reacting fronts have been reported by Riolfo *et al.* (2012).

6.6 Instabilities in unconsolidated porous media

In young sedimentary rock, the grains may not be fully cemented and so even though buried below other sediment, the permeable layer is unconsolidated. In permeable rocks, the load of the overlying rock is supported by a combination of the pore pressure in the formation and the stress associated with the grain–grain contacts in the permeable rock. With a sufficient load supported by the grain–grain contacts, the medium may behave as a solid framework through which the fluid can migrate. However, if the pore pressure increases and supports more of the load, then the effective stress of the medium decreases, for constant load, and the frictional forces between particles

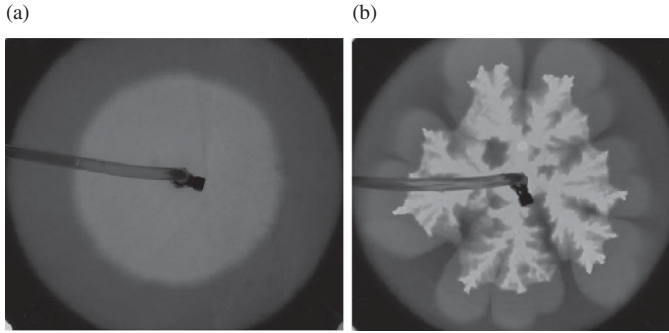


Figure 6.10 Instability of flow in an unconsolidated porous layer. At low flow rates (a) the fluid migrates as a Darcy flow, whereas at higher flow rates, the grains are mobilised and channels develop as the grains are displaced to the side of the flow (b). Photograph courtesy of G. Del Ioio. A black and white version of this figure will appear in some formats. For the colour version, please refer to the plate section.

are reduced so that grain–grain motion becomes possible provided there is space. Indeed, as the pore pressure increases, the stress on the surrounding layers eventually increases, leading to deformation and creation of this space. The grains may then become mobile. Since the grain–fluid mixture has a very high resistance to flow, for near close packed grains, any fluid displacing the grains will tend to develop channels through the medium rather than displacing the granular mixture in the direction of flow, in a fashion akin to the Saffman–Taylor instability.

In a series of experiments using a Hele–Shaw cell packed with sand, this process has been demonstrated by injecting fluid from a central source (Del Ioio and Woods, 2014). With a low injection pressure, the fluid pressure within the cell remains small, and the system remains stable, with the flow migrating as a Darcy flow (Figure 6.10a). However, as the injection pressure increases, in these experiments, the cell begins to deform, and as the load taken by the grains falls, grain–grain motion ensues, leading to formation of pure fluid channels as the granular suspension is displaced sideways (Figure 6.10b). This is an important process, since it effectively increases the permeability of the sand pack in the near injection region where otherwise the pressure gradients for Darcy flow are greatest. As a result, the overall flow rate for a given applied pressure becomes substantially larger. Indeed, the resistance to flow in the channels is very small compared to the porous layer.

As a simple demonstration of the impact of the channels on the flow, consider the far-field pressure, at radius R to be constant, as in the laboratory, then the flow is given from Darcy’s law by the approximate relationship

$$Q = \frac{k\Delta p}{\mu} \frac{1}{\ln\left(\frac{R}{r_i}\right)} \quad (6.23)$$

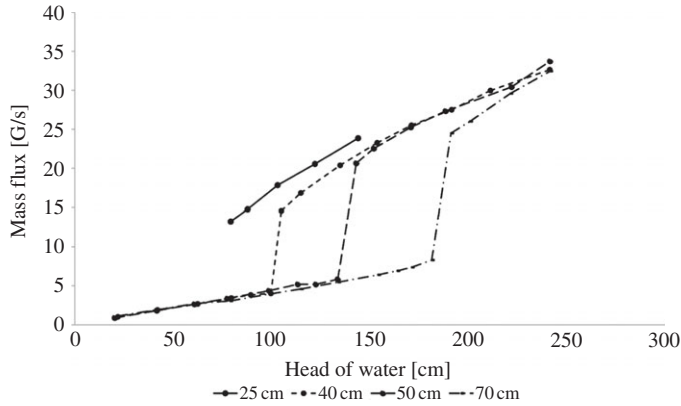


Figure 6.11 Variation of the flow rate with source pressure for conditions before instability, for which the flow rate is low, and after instability at higher pressure, for which there is a significant jump to larger values of the flow rate. Curves are given for four values of the overpressure of the confining vessel. Figure courtesy of G. Del Ioio.

where r_i is the inner radius of the porous layer, outside of which the sand pack is unchannelised. As r_i increases with channelisation, the flow rate also increases. If the well radius r_w is very small, then the change in flow rate as r_i grows to values of order 10 times the well radius may be very substantial. This effect may be seen in data from the laboratory experiments in which the flow rate increases rapidly once the system reaches a critical pressure such that the cell is sufficiently deformed to allow particle motion, and formation of fluid channels. Subsequently, the flow rate has much larger values for a given injection pressure owing to the presence of the channels (Figure 6.11).

6.7 Fingering in fractures of variable width

In many fractures which transmit fluid from the well to the permeable formation, the fracture width may be non-uniform. In this case, the flow speed may vary with position in the fracture, leading to a preferred mode of instability and non-linear finger development. Such control from the geometry of the fracture is important since any naturally occurring fractures will be of variable aperture thickness.

As a simple model of the phenomenon, we can consider a long fracture, $0 < x < L$ of thickness $b(y) = b_o(1 - |y|/W)$, where y is the cross-fracture position, $-W < y < W$ and $L \gg W$. If we model the flow along the fracture, in the x direction as driven by an applied pressure gradient along the fracture, then the flow speed along the cell of fluid i

$$u = - \frac{b^2}{12\mu_i} \frac{\partial p}{\partial x} \quad (6.24)$$

where we assume the pressure is independent of the cross-fracture position, and that the flow is directed along the fracture. If fluid 1 displaces fluid 0, and $V = \mu_1/\mu_o$, then the pressure gradient is related to the total flux along the cell Q according to the relation

$$-2 \frac{\partial p}{\partial x} \left[\int_0^w \frac{b^3}{12\mu_1} dy + \int_w^W \frac{b^3}{12\mu_o} dy \right] = Q \tag{6.25}$$

where the injected fluid is assumed to lie in the region $-w(x, t) < y < w(x, t)$.

The conservation of injected fluid, at position x along the cell, is given by

$$\frac{\partial}{\partial t} \int_0^{w(x,t)} b dy = - \frac{\partial Q_1(w(x, t))}{\partial x} \tag{6.26}$$

where the flux of fluid 1 at position x along the fracture is given by

$$Q_1(w(x, t)) = \int_0^{w(x,t)} b u dy \tag{6.27}$$

Combining (6.24)–(6.27) leads to the relation for the evolution of $s = w(x, t)/W$ along the fracture

$$\frac{\partial s}{\partial t} + \frac{4VQ}{Wb_o} \left(\frac{(1-s)^2}{[1+(V-1)(1-s)^4]^2} \right) \frac{\partial s}{\partial x} = 0 \tag{6.28}$$

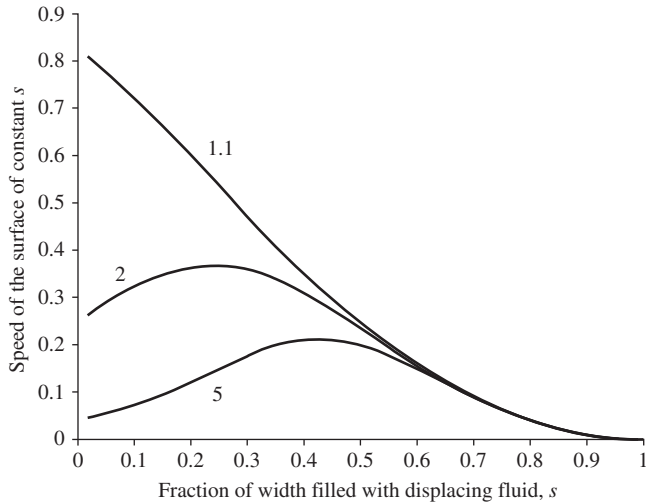


Figure 6.12 Illustration of the speed of surfaces of the displacing fluid, of a given width s , as they advance along the Hele–Shaw cell of non-uniform cross-sectional area, as given by Eq. (6.29). Curves are given for $V = 1.1, 2$ and 5 .

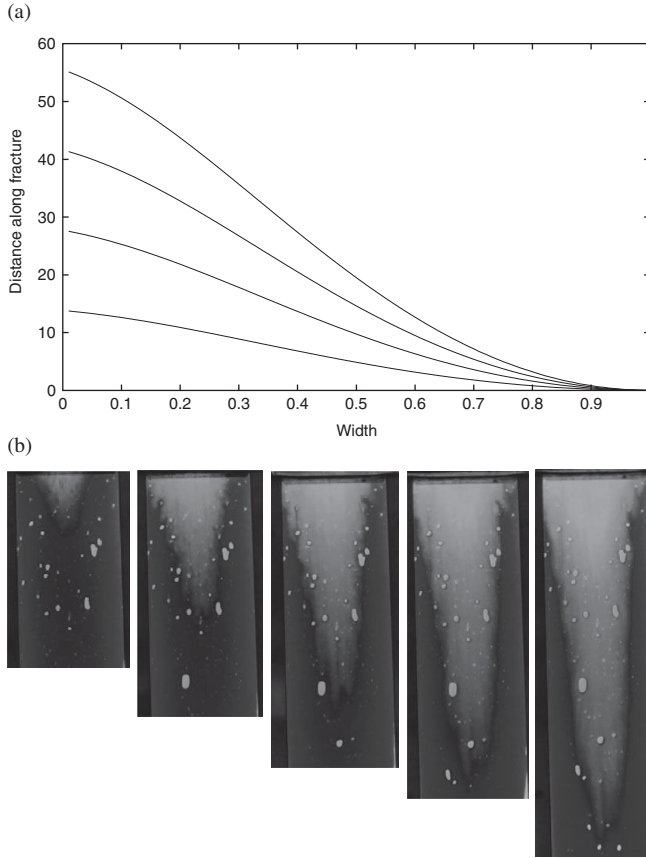


Figure 6.13 (a) Variation of $x(s, t)$ as a function of s for 4 times following the injection of fluid into the cell. (b) Series of photographs of the time evolution of a laboratory experiment, illustrating the displacement of blue glycerol with green corn syrup in a Hele–Shaw cell in which the gap varies from 1 mm at the edge of the cell to 2 mm at the centre of the cell. A black and white version of this figure will appear in some formats. For the colour version, please refer to the plate section.

This is a non-linear wave equation which illustrates how the position of surfaces with a given value of s , $x(s, t)$ say, varies according to

$$\frac{dx(s, t)}{dt} = \frac{4QV}{Wb_o} \frac{(1-s)^2}{[1+(V-1)(1-s)^4]^2} \quad (6.29)$$

For $V < 4/3$, this speed decreases monotonically with s (Figure 6.12) and so the displacing fluid becomes progressively stretched out along the centre of the cell. The above solution then represents a non-linear solution for a viscous finger in a cell of slowly varying aperture. Figure 6.13 illustrates the growth of the finger with time as it advances along the fracture, and compares this with a laboratory experiment illustrating the growth of such a non-linear finger. In the case $V > 4/3$, there is a maximum value

of $dx(s, t)/dt$ at a particular value of s , $0 < s < 1$ (Figure 6.12). This implies that a shock forms at the nose of the flow, across which the flux is conserved. The shock forms since s cannot be multi-valued at a given position x . The injection of a more viscous fluid thus leads to a partial stabilisation of the fingering associated with the variable width of the cell. More details of such shocks are given in Chapter 7.

6.8 Exercises

1. Develop a model for the stability of the interface between a layer of fluid which fills the space between two planes connected by a hinge at $x=0$ initially separated by angle θ in the case that the hinge is opened with angular velocity ω . Assume that initially the fluid fills the gap to a distance L from the hinge at $t=0$, and that there is air beyond this point. In developing a model of the flow, you may assume that the flow advances with the cross-plane averaged uniform speed, and that the resistance of the planes to the flow dominates the friction, producing an effective permeability $d^2/12$ where the gap spacing is d .
2. Calculate the stability of a circular ring of fluid which is extracted from a point sink in a Hele–Shaw cell, in the case that the external boundary of the fluid is bound by air. Describe how the most unstable mode evolves in time if the extraction rate is constant.

7 Two-phase flow

When modelling oil–water flows or CO₂–water flows in porous media, one of the key challenges lies in the description of the effects of the immiscibility between the two phases and its impact on the flow. Within each pore space, a fraction of the volume will be occupied by each phase, known as the saturation of that phase. The interaction with the pore walls also depends on which phase is preferentially in contact with the solid, which depends on the wetting characteristics of the two fluids. A very significant body of work has been carried out in developing methods to measure and characterise these properties in porous rocks in which the complexity of the pore structure and the diversity of the minerals within the porous structure can lead to non-unique and spatially variable properties. The books by Bear (1972), Dullien (1991) and Lake (1991) provide more details of some of the multi-phase flows which may arise in porous rocks. The objective of this chapter is to introduce some of the fundamental ideas concerning two-phase flow in a porous layer, and to explore the consequences of these ideas in terms of the evolution of saturation fronts as one fluid displaces another.

7.1 Wetting

In order to determine the relative wetting properties of two fluids in a porous layer, we turn to Young's law, which relates the interfacial tension between each fluid phase and the solid surface σ_{as} and σ_{bs} with the interfacial tension between the two fluid phases, σ_{ab} , according to the relation (see Figure 7.1)

$$\sigma_{ab} \cos \theta = \sigma_{as} - \sigma_{bs} \quad (7.1)$$

where θ is the contact angle of the fluid–fluid interface with the solid surface. In the case that

$$\frac{\sigma_{as} - \sigma_{bs}}{\sigma_{ab}} > 1 \quad (7.2)$$

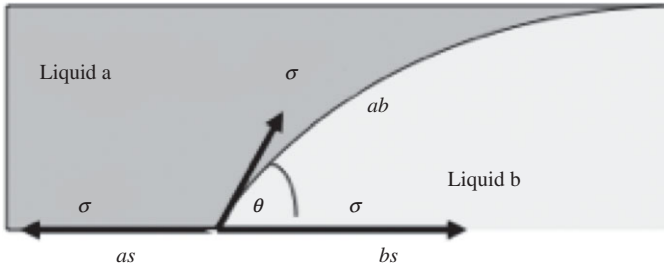


Figure 7.1 Illustration of the relation between the interfacial tension and the contact angle, for two fluids in contact with a solid surface. In this figure, fluid *b* is the wetting phase.

then there is no solution to (7.1) for the contact angle θ and so one fluid phase, the wetting fluid, will be in contact with the surface at all points. This is known as total wetting, whereas if $0 < \theta < \pi/2$ then the fluid *b* is known as the wetting fluid, but for $\pi/2 < \theta < \pi$, then fluid *a* is the wetting phase. There is a fundamental difference between the flow of the wetting and non-wetting phases, since the non-wetting phase tends to migrate through the centre of the pore spaces, and is lubricated by the wetting phase, whereas the wetting phase is in contact with the solid surfaces and therefore follows a no-slip condition. This leads to an increase in resistance to flow.

The motion of a wetting phase migrating into a porous layer and displacing the non-wetting phase is known as an imbibition flow, since the wetting phase is drawn into the porous layer along the surfaces of the porous matrix. In contrast, when a non-wetting phase displaces the wetting phase in a porous matrix, the flow is called a drainage flow, and the advancing fluid tends to migrate through the centre of the pores.

During an imbibition flow, as the wetting phase increases its volume fraction in each pore space, droplets of the non-wetting fluid may become stranded in the centre of the pores, leaving a residual saturation of the non-wetting phase. This phase may be unconnected through space. The critical size for such droplets depends on the interfacial tension between the two fluids which tends to suppress the deformation of the interface as the viscous stress drives the fluid forward through the pore throats (Figure 7.2a)

In a drainage process, the wetting phase is displaced and this leads to some residual trapping of the wetting phase in the corners of the pores, on thin films around the grains, and in pendular rings of fluid between touching grains. The residual saturation of the wetting fluid in such a flood typically has value of about 0.1–0.2 of the pore space, although again it depends on the detailed structure of the material (Figure 7.2b). Depending on the geometry, there may be islands of the porous matrix which are isolated by the films of wetting fluid, and through which the non-wetting fluid may not enter, if the pore openings are too small to distort the interface through the opening.

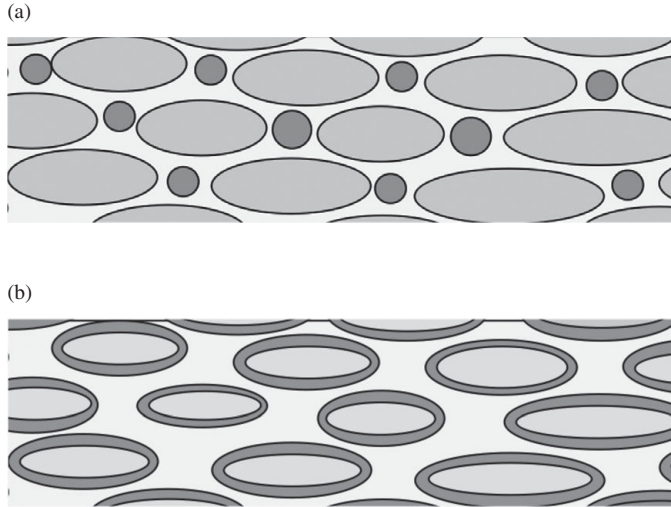


Figure 7.2 (a) Schematic of the topology of a wetting and non-wetting fluid in the limit of small saturation of the non-wetting fluid, illustrating the droplets of non-wetting fluid trapped within the pore spaces between grains. (b) Schematic of the topology of a wetting and non-wetting fluid in the limit of large saturation of the non-wetting fluid, illustrating the connected non-wetting fluid, while the wetting fluid manifests itself as films around the grains, some of which may be unconnected.

7.2 Capillary entry pressure

The result of the interfacial tension σ_{12} , is to create a pressure difference between the two fluids, 1 and 2. In a simple capillary the magnitude of this pressure jump, the capillary pressure, has value of order

$$p_c = \sigma_{12} \left(\frac{1}{r_1} + \frac{1}{r_2} \right) = \frac{2\sigma_{12}}{r^*} \quad (7.3)$$

where r_i are the principal radii of curvature of the interface and r^* is defined by Eq. (7.3). However, in a porous rock, the capillary pressure varies over space, and depends on the local geometry of the pore space. It has a complex spatial dependence but is often modelled in terms of a continuous function of the saturation of each phase in the porous matrix. One important detail relates to the hysteresis between capillary pressure during the imbibition process and the drainage process: with imbibition, the wetting phase enters the pore spaces, and so there is no threshold capillary entry pressure for the advancing fluid to enter the pore spaces. In contrast, during a drainage flow in which the formation is initially flooded with the wetting phase, there is a threshold capillary entry pressure for the non-wetting phase to pass through the pore throats and displace the wetting fluid (Figure 7.3). As the wetting phase saturation decreases

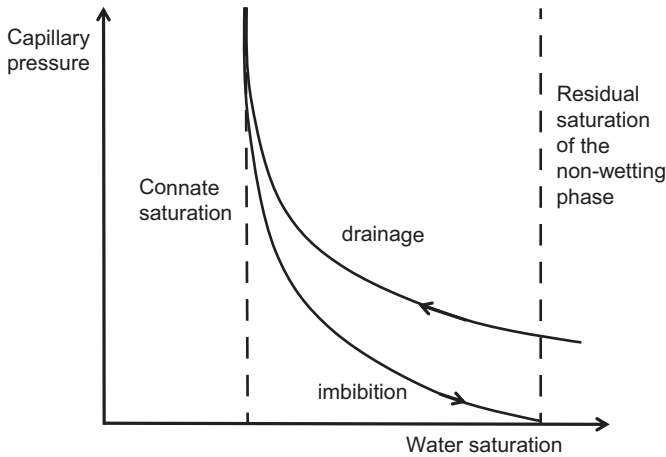


Figure 7.3 Illustration of the difference in the capillary pressure associated with imbibition- and drainage-type flows. There is a capillary entry pressure for a drainage flow as the non-wetting phase requires a minimum pressure to pass through pore throats when at very low saturation. The residual saturation of the non-wetting phase may correspond, for example, to droplets of the non-wetting phase trapped in the centre of the pores (Figure 7.2a). The connate saturation of the wetting phase corresponds to the saturation of the irreducible water which remains when the non-wetting phase has displaced the wetting phase from the pores (Figure 7.2b). This may correspond to a water film over the grains, or to water trapped in the very small openings and gaps between grains, places into which the non-wetting fluid cannot enter owing to the interfacial tension.

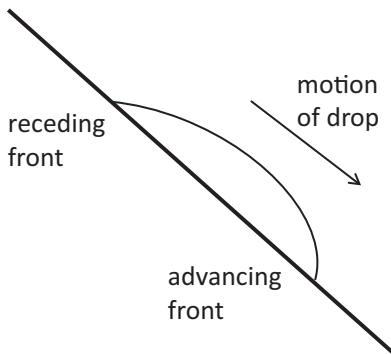


Figure 7.4 Hysteresis in the contact angle on the upstream and downstream side of a moving drop.

to small values, the capillary pressure increases since it becomes increasingly difficult to displace the remaining wetting phase because the interface between the fluids requires distortion to progressively smaller radius of curvature. One common observation of hysteresis of a draining and imbibition flow is that the contact angle of a drop of water moving on a pane of glass is different on the advancing and the receding front (Figure 7.4).

Various models have been developed to quantify the capillary pressure, based on the dimensional scaling that capillary pressure varies as

$$p_c = \sigma \left(\frac{\phi}{k} \right)^{1/2} J(s_w) \quad (7.4)$$

This essentially relates the surface tension, σ , and the lengthscale associated with the permeability $(k/\phi)^{1/2}$, with the capillary pressure, modified by a function J of the saturation, s_w , which represents the volume fraction of the pore space occupied by the wetting fluid. J may have a different functional form for imbibition and drainage in order to capture the above hysteresis.

The other property which arises in the above discussion is the residual saturation (minimum) of the non-wetting phase and connate saturation (minimum) of the wetting phase. These determine the limiting values for the recovery of each phase when it is displaced by the other. There are numerous models and experiments in which the displacement process on the pore scale has been studied in detail. Typically it is found that the residual saturation depends on the capillary number of the flow, which is the ratio of the viscous stress to the capillary stress

$$Ca = \frac{\mu u}{k\sigma} \quad (7.5)$$

with the residual saturation typically varying from 0.1–0.2 as the capillary number Ca falls below values typically of order 0.01–0.001.

7.3 Gas cap size and transition zones

The capillary pressure has an important control on the static properties of fluids, and especially the interface between immiscible fluids, in porous layers. First, the depth of a layer of buoyant, non-wetting fluid which can accumulate below a seal rock, with a capillary entry pressure p_e is given by

$$h = \frac{p_e}{g(\rho_w - \rho_o)} \quad (7.6)$$

where $(\rho_w - \rho_o)$ is the density difference between the wetting, w , and non-wetting, o , phase.

This simple result illustrates how the capillary entry pressure determines the efficacy of a particular seal rock to suppress the upward motion of a non-wetting fluid phase, and the possible volume of that fluid which may be trapped below the seal. Such effects play a key role in the formation of oil and gas reservoirs, as well as in influencing the distribution of CO_2 following injection into a reservoir for geosequestration. As hydrocarbons migrate upwards through the geological strata, they accumulate in anticlines

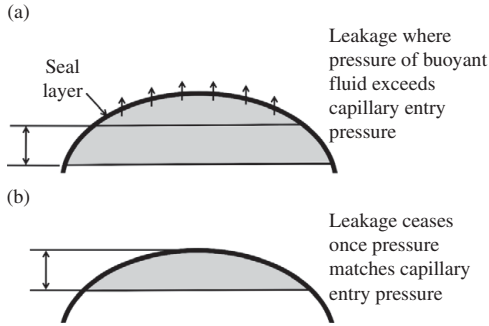


Figure 7.5 Illustration of (a) the leakage of a buoyant non-wetting fluid through a seal layer while the depth of the buoyant fluid is sufficient for the overpressure to exceed the capillary entry pressure into the seal and (b) an equilibrium pool of liquid which is just trapped below a capillary seal.

and other structural traps. If they deepen beyond the depth given by Eq. (7.6) then the overpressure can drive the hydrocarbon upwards through the seal into the overlying geological strata. However, assuming that the seal rock remains water wet, once the depth of the hydrocarbon layer below the seal falls to the depth given by (7.6), the remaining hydrocarbon is trapped.

For example, with an oil–water surface tension of about 70 mN/m^2 and a permeability of 10^{-14} m^2 , the capillary entry pressure may be of order $70\,000 \text{ Pa}$. With a density contrast of 200 kg/m^3 between the oil and water, we may expect an oil layer of depth of about 35 m below a seal layer. If the oil is denser, the depth of the seal would be greater, while a gas layer, of much lower density may only have a trapped gas cap of order $15\text{--}20 \text{ m}$, depending on the depth of the reservoir. Such trapping may also be key in the migration of CO_2 and DNAPL plumes through layered rock. The capillary entry pressure restriction may lead to trapped pockets of CO_2 forming wherever the heterogeneities within the geological strata form structural traps and for which there is an effective capillary entry pressure (see Chapter 10; Farcas and Woods, 2009). Note that with a gas cap, if there is a background hydrological flow, there will be a pressure gradient along the cap, in the along-flow direction of order $\mu u/k$, and this will tilt the lower interface of the gas cap to an angle θ to the horizontal so that the buoyancy pressure gradient in the cap, $\Delta\rho g \sin\theta$ matches the along-cap pressure gradient associated with the flow, $\mu u/k$.

In many systems in which there is a buoyant phase overlying an immiscible relatively dense phase, the capillary pressure and preferential wetting of one phase leads to a region in which the fluids intermingle in the sense that the saturation continuously varies across the interface between the two fluids. This process arises as the wetting fluid is drawn into the non-wetting fluid region along the grain boundaries. The depth of the transition zone, and the variation of saturation within this transition zone, $s(h)$, is then controlled by a balance between the capillary pressure driving the intermingling and the buoyancy force which stabilises the region (Figure 7.6)

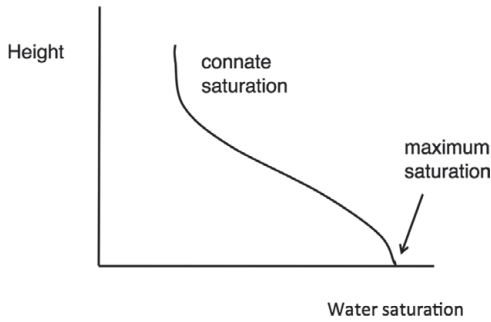


Figure 7.6 Variation of the saturation across a capillary transition zone as the saturation of the wetting phase varies from the connate saturation, which is the minimum irreducible saturation and the maximum saturation when the non-wetting fluid is displaced from the medium.

$$p_c(s(h)) = (\rho_w - \rho_o)gh \quad (7.7)$$

Brooks and Corey (1959) carried out experiments to measure the capillary transition zone in a series of rock types, and found that in many natural samples, the transition zone, across which the capillary pressure varies, extends a distance of order 10–100 cm, although in some systems, with small grain sizes, the transition zone could be much larger. The capillary transition zone represents a static balance, but in order to establish the zone from an initially planar interface between the two phases a transient exchange flow will develop, and we consider this later in the chapter.

7.4 Two-phase flow

The above static problems illustrate the impact of the capillary pressure on the distribution of the fluid within a porous layer. If the fluid is also migrating through the matrix, then the effects of wetting and the capillary pressure can have a profound impact on the flow. If a pressure gradient is applied across a porous medium saturated with two immiscible fluids, then the pressure gradient will act on each phase, driving a flow, but each of the phases will respond differently, since the non-wetting phase is lubricated by the wetting phase, and the wetting phase has a no-slip condition with the walls of the matrix. Also the pressure within the non-wetting phase will equal that in the wetting phase plus the capillary pressure. These two effects can lead to substantial differences between the flow of each phase. There are many works on this general topic, owing to its importance for oil recovery and other two-phase-flow problems in porous media (e.g. Bear, 1972; Lake, 1989); here we present a simplified model to illustrate some of the key physics.

It is useful to start by writing the effective Darcy law for each phase. For simplicity, we adopt a one-dimensional analysis, although the system may be readily generalised to three dimensions. In the wetting phase w , we can write

$$u_w = -\frac{k_w k}{\mu_w} \frac{\partial p_w}{\partial x} \quad (7.8a)$$

where k_w , known as the relative permeability, $0 < k_w < 1$, denotes the reduction in the effective permeability seen by phase w when it only occupies a fraction of the pore space. It is assumed to be a function of the saturation, s_w ; in principle it also depends on the viscosity contrast between the fluids, and the structure of the porous matrix but we will proceed with a simplified picture in which the main dependence is on the saturation. This model also assumes a unique dependence of the relative permeability on the saturation which may not always be borne out in a real porous rock, especially owing to local fluctuations in pore structure, shape and grain size, and also since the two-phase flow within a three-dimensional pore space does not need to be unique. However, the parameterisation $k_w(s_w)$ represents an averaged phenomenological description of the process, and our purpose is to explore the implications of this model in terms of the macroscopic dynamics, especially since these implications may be quite profound. Later in the chapter, we also present a detailed calculation for flow in a tube or two-dimensional slot, which is a well-defined and precise flow problem, and which exhibits some similar phenomena predicted by this model of relative permeability. In the non-wetting phase we have, in a similar way,

$$u_{nw} = -\frac{k_{nw} k}{\mu_{nw}} \frac{\partial p_{nw}}{\partial x} \quad (7.8b)$$

where subscript nw denotes a property of the non-wetting phase. The conservation of mass of the phase w is expressed in terms of the evolution of the saturation of phase w , with saturation s_w , according to the form

$$\phi \frac{\partial s_w}{\partial t} = -\frac{\partial u_w}{\partial x} \quad (7.9)$$

The equation for the conservation of the total flux of fluid, per unit area, has the form

$$Q = u_w + u_{nw} \quad (7.10)$$

Equations (7.8a) and (7.9) lead to the local evolution of saturation

$$\phi \frac{\partial s_w}{\partial t} = \frac{\partial}{\partial x} \left(\frac{k_w k}{\mu_w} \frac{\partial p_w}{\partial x} \right) \quad (7.11)$$

while the total flux follows the relation

$$Q = -\left(\frac{k_w k}{\mu_w} \frac{\partial p_w}{\partial x} + \frac{k_{nw} k}{\mu_{nw}} \frac{\partial p_{nw}}{\partial x} \right) \quad (7.12)$$

The capillary pressure relates the pressure in the non-wetting phase to that in the wetting phase

$$p_{nw}(s_w) = p_w(s_w) + p_c(s_w) \quad (7.13)$$

Combining Equations (7.11)–(7.13), we can substitute for $\frac{\partial p_w}{\partial x}$ to find the governing equation for the saturation

$$\phi \frac{\partial s_w}{\partial t} + Q \frac{dF}{ds_w} \frac{\partial s_w}{\partial x} = - \frac{\partial}{\partial x} \left(\left(\frac{k_{nw} k F}{\mu_{nw}} \frac{dp_c}{ds_w} \right) \frac{\partial s_w}{\partial x} \right) \quad (7.14)$$

where the function F is the ratio of the flux of the wetting phase to the total flux, sometimes called the fractional flow, and this has value

$$F = \left(1 + \frac{k_{nw} \mu_w}{k_w \mu_{nw}} \right)^{-1} \quad (7.15)$$

From a physical perspective, the flux of the wetting phase varies from (i) the case where it has value zero, when the saturation equals the residual saturation and all the flow is of the non-wetting fluid, to (ii) the case when it represents all the flow, Q , once the saturation of the wetting phase has increased until there is just the residual saturation of the non-wetting phase left in the formation. Assuming the flux increases and decreases smoothly, this leads to a curve of the form shown in Figure 7.7.

The above Eq. (7.14) for the evolution of the saturation is an advection diffusion equation in which one may envisage the speed of the saturation surfaces is $\frac{Q}{\phi} \frac{dF}{ds}$. Given the shape of F shown in Figure 7.7, this suggests that, in general, the fronts of constant small and large values of saturation migrate more slowly than those with intermediate values, and as a result, there will tend to be steepening of the saturation gradient until a shock develops, connecting a region of intermediate saturation to one of low saturation, as depicted in Figure 7.8b. Neglecting effects of capillarity, the shock solution is known as the Buckley–Leverett solution (e.g. Bear, 1972; Lake, 1991).

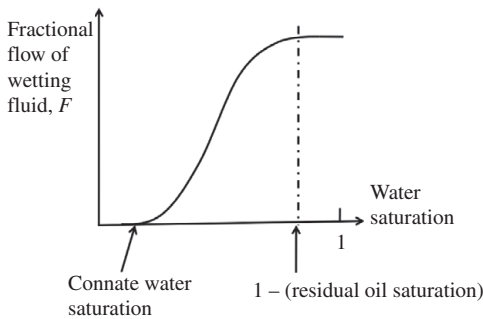


Figure 7.7 Illustration of the fractional flow of the wetting phase as a function of the saturation of the wetting phase.

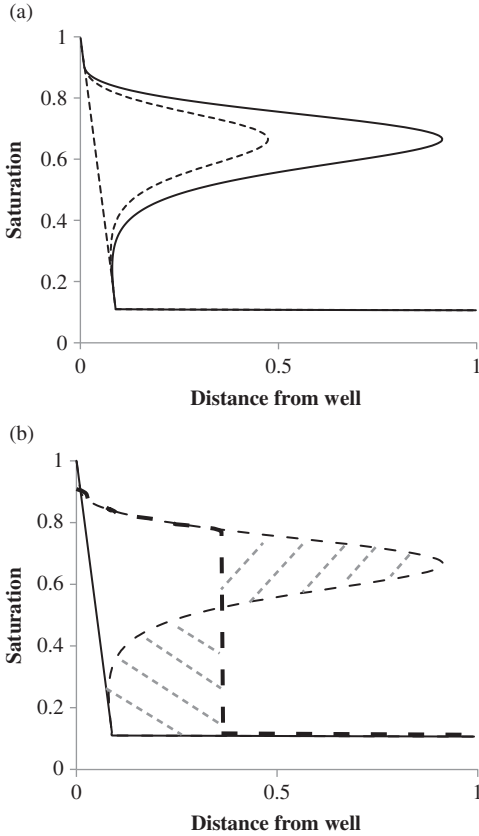


Figure 7.8 (a) Time development of a non-monotonic saturation profile as a function of the position downstream as a result of the non-monotonic speeds of different saturation surfaces, and the associated advection of the saturation surfaces by the flow as predicted by Eq. (7.14). (b) Formation of a shock to allow for a unique value of saturation at each point in the invading wetting fluid. Shaded zones have equal area.

We can predict the location and propagation speed of the steady shock which develops by using a mass balance approach in which the flux supplied to the shock as it advances with a speed $\frac{dL(s_s)}{dt}$ matches the change in the advective flux of the wetting phase upstream and downstream of the shock

$$\phi(s_s - s_o) \frac{dL(s_s)}{dt} = Q[F(s_s) - F(s_o)] \tag{7.16}$$

where subscript s here denotes the value upstream of the shock and o the value downstream, in the region in which the saturation has the far-field value. We can also observe that the speed of the shock matches the speed of the saturation surface just upstream of the shock so as to produce a steady-state shock

$$\frac{dL(s_s)}{dt} = \frac{Q}{\phi} \frac{dF(s_w)}{ds_w} \Big|_{s_w=s_s} \tag{7.17}$$

Combining these two equations leads to the result that at the shock the saturation satisfies the relation

$$\frac{dF(s_w)}{ds_w} \Big|_{s_w=s_s} = \frac{F(s_s) - F(s_o)}{s_s - s_o} \tag{7.18}$$

as shown by the graphical construction in Figure 7.9.

Behind the shock, the saturation surfaces move at progressively slower speeds, and so a rarefaction or dispersive wave develops, with the saturation surfaces becoming progressively more spread out in space until eventually the saturation reaches the residual value (Figure 7.10).

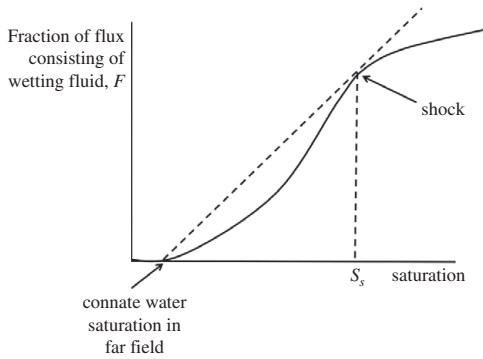


Figure 7.9 Illustration of the variation of the flux of the wetting phase, here taken as water, as a function of the saturation of the pore space to this wetting phase. Also shown is the dashed line connecting the saturation of the upstream shock, with the saturation of the formation upstream, so that the steady shock conserves mass.

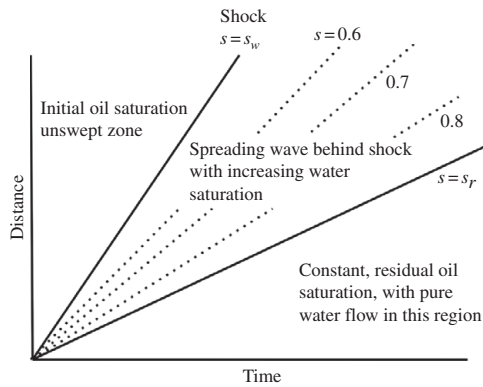


Figure 7.10 Illustration of the migration of saturation surfaces in space and time upstream of the shock front.

The speed of each of the saturation surfaces, s , is given by the value $\frac{Q}{\phi} \frac{df}{ds}$, so that the time required for that saturation surface to reach a particular location L say is given by the relation

$$t(s) = \frac{L\phi}{Q} \left(\frac{\partial F(s)}{\partial s} \right)^{-1} \quad (7.19)$$

Near the shock the saturation gradients are much larger than in the dispersive rarefaction wave near the source. In this region of larger gradient, the effects of capillarity may be important in determining the gradient of saturation across the shock. Indeed, the saturation Eq. (7.14) shows that the effect of the capillarity is to smooth out variations in the saturation in a diffusive fashion and that the lengthscale over which such fluctuations are smoothed and hence the thickness of the shock is given by

$$L_c = \frac{1}{Q} \left(\frac{k_{nw} k}{\mu_{nw}} \frac{dp_c}{ds_w} \right) F \frac{ds_w}{dF} \text{ with } s_w = s_s \quad (7.20)$$

The detailed structure of the adjustment zone around the shock front depends on the functional form for the capillary pressure and the relative permeabilities. These properties are empirical relations, but there are some reference values for these properties which provide useful parameterisations. First, van Genuchten has proposed that the capillary pressure is given by an expression of the form

$$p_c(\hat{s}) = \sigma \left(\frac{\phi}{k} \right)^{1/2} \left[\hat{s}^{-1/m} - 1 \right]^{1/n} \quad (7.21)$$

in terms of the dimensionless wetting phase saturation

$$\hat{s} = \frac{s - s_r}{s_m - s_r} \quad (7.22)$$

This leads to a capillary pressure curve of the form shown in Figure 7.11, where m and n are parameters of the model and s_r denotes the minimum saturation of the wetting phase while s_m denotes the maximum saturation.

Meanwhile, the relative permeabilities have been parameterised as functions of the saturation in a number of models; one model which has had widespread application was presented by Corey (1954) and Brooks and Corey (1959) and has the form

$$k_{nw}(s) = (1 - s^2)(1 - s)^2 \text{ and } k_w(s) = s^4 \quad (7.23a,b)$$

leading to curves of the form shown in Figure 7.12. The asymmetry in the curves is associated with the difference between the wetting and the non-wetting phases. These models have been compared with small-scale core experiments in which oil–water mixtures flow through a rock sample and there is a vast literature on the subject, in which rocks from different geological formations have been sampled and tested. Our

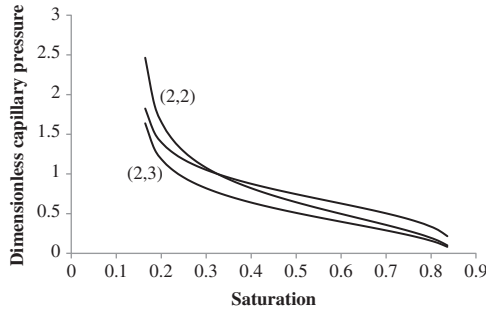


Figure 7.11 Typical capillary pressure curve as predicted by the van Genuchten law for (m, n) pairs given by $(2, 2)$, $(3, 2)$ and $(2, 3)$, with the $(2, 2)$ and $(2, 3)$ curves being labelled. The x -axis is the normalised saturation \hat{s} , Eq. (7.22).

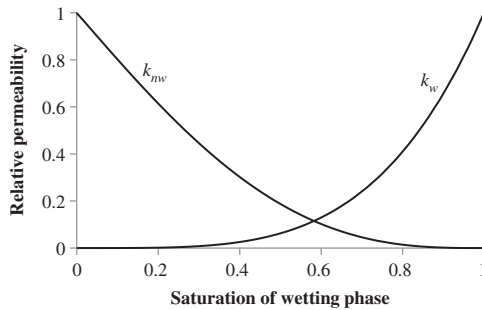


Figure 7.12 Asymmetry in the relative permeability for oil and for water owing to the fact that one phase wets the solid, as parameterised by the Corey and Brooks model.

purpose here is to present the principal results about the Buckley–Leverett shock formation and the dispersive spreading of the saturation surfaces following this shock, rather than become immersed in a review of the many data and models, but there are many fascinating texts on the subject (e.g. Dullien, 1991).

One observation is that in a real oil-producing system, for example, the oil–water production curve data evolve from oil flow to mixed flow with progressively more water. As well as the effects of fractional flow in a single homogeneous layer, as discussed in this chapter, the effect of low or high permeability lenses of rock, and an overall layered rock structure, will lead to an effective intermingling of the injected water with the oil within the formation, so that the oil travel time along different flow paths is very different. As a result, there will be a gradual increase in the water fraction of the produced fluid as a function of time. In developing strategies for the continued production of oil from reservoir, the challenge is often to distinguish how the oil–water production history is influenced by the effect of fractional flow in one layer, the pattern of sweep in each layer and the dispersion effects associated with the macroscopic structure of the formation (Chapters 3–5).

7.5 The thin gap analogue

Many calculations have been carried out to test the predictions of the above model, with the details varying for different rock types. However, the phenomena we have predicted should also arise if one fluid displaces a second immiscible fluid within a narrow gap or capillary tube. We now show that in this situation, the flow also leads to prediction of a shock front and ensuing dispersive tail. In fact, we can demonstrate an analogous process for miscible flow provided the timescale is shorter so that mixing between the fluids will be small and the interface may be regarded as being localised in terms of there being a sharp transition from one fluid to the other, although the interface can become dispersed along the cell. For convenience we consider the migration of a front between fluids within a two-dimensional narrow gap and neglect any effects of interfacial tension (Figure 7.13).

If we assume that there is no slip on the walls of the gap, and that the position of the interface relative to the walls changes slowly along the gap, so that the along-gap pressure gradient, $\frac{\partial p}{\partial x}$, is approximately uniform in the cross-gap direction then we find that for each of the two fluids $i = 1, 2$, the along-gap flow is given by

$$\mu_i \frac{\partial^2 u_i}{\partial y^2} = \frac{\partial p}{\partial x} \tag{7.24}$$

Assuming the velocity and shear stress are continuous across the interface, the equation for the fractional flow of fluid 1 is

$$F(\beta) = \frac{Q_1}{Q_1 + Q_2} \tag{7.25}$$

where

$$Q_1(\beta) = -\frac{H^3}{3\mu_1} \frac{\partial p}{\partial x} (\beta^3 - 3\beta^2) \tag{7.26}$$

and

$$Q_2(\beta) = -\frac{H^3}{3\mu_1} \frac{\partial p}{\partial x} (3\beta(1 - \beta)(\beta - 2) - 2V(1 - \beta)^3) \tag{7.27}$$

Here V is the viscosity ratio $V = \mu_1/\mu_2$ and fluid 1 is located in the regions $(1 - \beta)H < y < H$, $-(1 - \beta)H > y > -H$, with fluid 2 in the region $-(1 - \beta)H < y <$

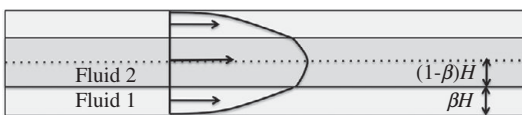


Figure 7.13 Illustration of the problem of displacing fluid 1 with fluid 2 in a capillary tube.

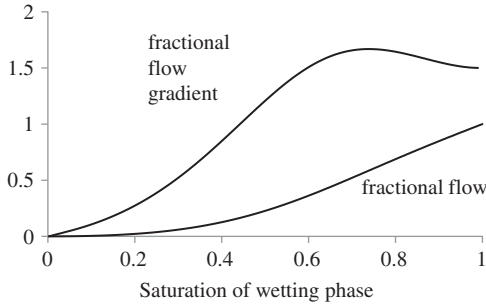


Figure 7.14 Fractional flow curve and gradient of fractional flow curve, as a function of the saturation of the wetting phase, β , in a two-dimensional gap, with a wetting fluid displacing a non-wetting phase when the viscosity of the wetting phase is four times that of the non-wetting phase.

$(1 - \beta)H$. In Figure 7.14, we plot the fractional flow, and the gradient of the fractional flow as a function of β , the fraction of the gap which is filled with fluid 1, the fluid in contact with the wall. We assume the fluid is symmetrically distributed within the gap. It is seen in the figure, with $V = 4$, that the speed of the surfaces of constant saturation, β , which is proportional to $dF/d\beta$, varies non-monotonically with β , so that we expect a shock to develop at the leading edge of the flow front (cf. Figure 7.8), followed by a dispersive tail as for the Buckley–Leverett type solution. As the viscosity ratio changes, the shape of $F(\beta)$ changes and so the detailed structure of the interface changes. In this simplified model, we have not included the effects of interfacial tension or buoyancy forces, but these can be included (see Lajeunesse *et al.*, 1999). Although this is a two-dimensional analysis, if the viscosity of fluid 2 is larger than fluid 1, we may expect fingering to develop in the direction normal to the page (Chapter 6).

7.6 Capillary imbibition

The above analysis of the displacement of one phase by a second has identified the classic Buckley–Leverett shock solution owing to the non-monotonic dependence of the speed of surfaces of constant saturation with increasing saturation. This flow leads to the shock front, across which the saturation of the displacing phase changes from that in the far-field of the reservoir (here we have assumed that this has the residual saturation), to a larger value; behind this shock there is then a spreading dispersive wave as the saturation of the displacing phase increases to the fully saturated value, leaving behind only the residual saturation of the displaced fluid phase in the reservoir. This flow is driven by the applied pressure at the source, displacing the fluid already in place.

A second, different flow regime can develop as a result of the capillary forces, for example, if one region of the reservoir has a different saturation from another part

of the reservoir. If there is no net flow through the reservoir, then the flow involves an exchange of the two fluids, so as to produce a region of intermediate saturation, providing there is no capillary entry pressure threshold which prevents the non-wetting phase migrating through the reservoir; this should be satisfied in the regions of the formation in which both of the fluid phases are continuous in space or alternatively, in a water-wet fractured rock, water may be injected into the fractures, and then a capillary-driven exchange flow may draw water into the matrix and drive oil back into the fracture. The relaxation of the system to an equilibrium is then governed by the equation for two-phase flow derived earlier, but with no net flow. This leads to the one-dimensional equation (Eq. 7.14)

$$\phi \frac{\partial s_w}{\partial t} = - \frac{\partial}{\partial x} \left(\frac{k_{nw} k F}{\mu_{nw}} \frac{dp_c}{ds_w} \frac{\partial s_w}{\partial x} \right) \quad (7.28)$$

We now solve this subject to the initial conditions that at $t = 0$, $s_w = s_1$ for $x > 0$ and $s_w = s_2$ for $x < 0$. This is a non-linear diffusion equation, with the scaling for the diffusivity depending in part on whether the mobility of the wetting phase, $k_w k / \mu_w$ is larger or smaller than the mobility of the non-wetting phase $k_{nw} k / \mu_{nw}$, as expressed by the term $k_{nw} F / \mu_{nw}$. In general, this value may change across the transition region. If the capillary pressure gradient with saturation is fairly uniform across the transition zone, then the region where $k_{nw} F / \mu_{nw}$ is smallest may dominate the flux, since the saturation gradient will tend to concentrate at that point. In the case that $k_{nw} / \mu_{nw} \gg k_w / \mu_w$ for example, then the diffusivity may be approximated as

$$D_{eff} = - \frac{k k_w}{\phi \mu_w} \frac{dp_c}{ds_w} \quad (7.29)$$

and the imbibition process satisfies the approximate relation

$$\frac{\partial s_w}{\partial t} = D_{eff} \frac{\partial^2 s_w}{\partial x^2} \quad (7.30)$$

with solution

$$s_w(x, t) = s_2 + \frac{1}{2} (s_1 - s_2) \left(1 + \operatorname{erf} \left(\frac{x}{2(D_{eff} t)^{1/2}} \right) \right) \quad (7.31)$$

In a typical example (Behbahani *et al.*, 2006), consider the case in which there is a capillary adjustment zone across which the saturation changes from $s_2 = 0.4$ to $s_1 = 0.6$ with $dp_c/ds_w \approx 30$ kPa over this range. If $\mu_{nw} = 0.001$ Pa s and $k_{nw} \approx 0.3$ in a rock of permeability $k = 0.1 D$, we find $D_{eff} = 10^{-5}$ m²/s. This shows that the imbibition-driven exchange flow, which has a width of order $(2D_{eff} t)^{1/2}$ has thickness of about 1 m after 1 day, and 10 m after about 1 year, as the process slows. This represents a significant rearrangement of fluid within the system by the counterflow. It is possible to solve the problem numerically, in the more usual case that D_{eff} varies in space across the imbibition region, to find the shape of variation of the saturation across the self-similar

transition zone, rather than using the simplified problem illustrated herein. However, the lengthscale of the adjustment zone will depend on similar scaling laws to that in the error function, with the additional possible complication that as the saturation changes, the non-linear variation in the diffusivity changes the timescale of the process, essentially because the relative permeabilities of the two phases change with saturation.

As mentioned above, a complementary problem arises if a preferentially wetting fluid is injected into a fractured reservoir. The fractures may fill with the injected fluid, leading to a diffusive front of the wetting fluid migrating from the fractures and into the matrix blocks beside the fractures. Provided the two fluid phases remain continuous and no capillary pressure thresholds prevent an exchange flow developing between the fractures and the matrix, one then expects a capillarity-driven exchange flow to develop between the matrix and the fractures. The non-wetting phase, e.g. oil, will flow into the fractures and will be swept off along the fractures with the injected water.

In such a situation, the flow into the fractures is again self-similar but now localised in the half-space $x > 0$, with solution given in terms of the saturation of the wetting phase s_w ,

$$s_w(x, t) = s_2 + (s_1 - s_2) \operatorname{erf} \left(\frac{x}{2(D_{eff}t)^{1/2}} \right) \quad (7.32)$$

in the idealised case of a constant diffusivity in this transition zone. In this case, s_2 , the saturation adjacent to the fracture will have the value given in terms of the residual saturation of the oil, s_{ro} , as $s_w = 1 - s_{ro}$. If there is a boundary to the reservoir beyond which there is no flow, at $x = L$ say, then once the diffusive saturation wave spreads to this boundary, a second regime of capillary imbibition will develop, in which the saturation in the region $0 < x < L$ gradually builds to value $1 - s_{ro}$, with zero gradient of saturation at $x = L$, leading to the solution of Eq. (7.28) of the form

$$s_w(x, t) = s_2 + (s_1 - s_2) \sin \left(\frac{\pi x}{L} \right) \exp \left(-\frac{\pi^2 D_{eff} t}{L^2} \right) \quad (7.33)$$

This illustrates the long-term exponential decay of the flux driven by the capillary imbibition in a finite domain, subject to the simplifying approximations of this model.

Using the parameters as above, it is seen that the early time flux is given by $\phi \left(\frac{D_{eff}}{2t} \right)^{1/2}$ per unit area of matrix adjacent to the fracture and this has value of order 10^{-5} – 10^{-6} m/s over times from 1 day to 1 year, using the simple case above. If a well accesses a series of fractures, with overall area 10^3 – 10^4 m², then this can contribute a significant amount of production. However, at later times the flow wanes exponentially, according to this model, with flux into the fracture, per unit area, of magnitude

$$\phi D_{eff} (s_1 - s_2) \frac{\pi}{L} \exp \left(-\frac{\pi^2 D_{eff} t}{L^2} \right) \quad (7.34)$$

This form of evolution of the flux is similar to experimental data from numerous tests showing an initial phase of decay of the production rate prior to the saturation front reaching the far boundary of the domain followed by a long-time exponential decay as suggested by separable solution (7.33); indeed exponential decay was proposed by Ma *et al.* (1997) through an empirical fit to experimental data on imbibition.

In less permeable formations, or with more viscous oil, the capillary imbibition will be much slower: indeed at early times, the flow decreases as the square root of the permeability and the inverse of the square root of the viscosity, if the mobility of the oil falls below that of the supply liquid. Capillary imbibition is used in many water-wet systems, for example fractured chalk or other carbonate fields where this capillary-driven exchange can provide significant additional resource.

If the matrix is oil wet, however, then the capillary entry pressure may inhibit the invasion of the injected water into the oil-filled matrix; such reservoirs are hard to produce. Various chemical approaches have therefore been developed to change the viscosity/interfacial tension of the injected liquid in an attempt to change the wetting characteristics or to change the capillary entry pressure (see Lake, 1991).

7.7 Exercises

1. A buoyant oil of density $\rho - \Delta\rho$ ponds at the top of a two-dimensional wavy aquifer structure of thickness d and with upper surface which has position $h(x)$ below the surface of the Earth. There is a background hydrological flow with total flux q of fluid of density ρ . Find an equation for the shape of the oil–water interface given that the oil is static. If $h(x) = H_0 + a \sin(2\pi x)$: where $a \ll d$ and $L \gg d$, find the maximum volume of oil which can be trapped between successive low points of the top surface of the aquifer. You may assume the aquifer has permeability k and the water has viscosity μ . If the upper boundary of the aquifer has a seal rock with capillary entry pressure ρgb , where $b < a$ find the volume of oil which may be trapped in the aquifer between two successive low points of the upper surface of the aquifer (cf. Woods and Espie, 2012).
2. A pipe connects the centre of a horizontal Hele–Shaw cell to a reservoir of water of viscosity μ_w with fixed head Δp relative to the air initially filling the cell. If the cell is initially filled with air, and the plates of the Hele–Shaw cell are water wet, with a capillary pressure p_c at the water–air interface, explore how the radially spreading imbibition front of water advances in the Hele–Shaw cell, assuming that $p_c + \Delta p > 0$.
3. Repeat the calculation of Exercise 2 in the case that the cell is initially filled with oil, of viscosity μ_o , such that the oil is able to flow freely out of the outer radius of the cell, $r = R$. Calculate the rate of advance of the water front, assuming it is the wetting phase, and that there is a capillary pressure p_{co} at the interface. Comment on the stability of this front to the Saffman–Taylor instability.

8 Fluid–rock interactions

We now explore a number of important processes related to the interaction of fluid injected into a porous layer and the porous layer itself. The main focus in the present work relates to the heat transfer in porous layers, reactions of the injected fluid with the rock, and the migration and gelling of polymers injected into the porous layer. These processes are of critical importance for the geothermal industry, but also for modelling water injection in oil fields.

We first describe how thermal fronts propagate through a porous rock, and can lead to instability owing to thermal fracturing of the rock or changes in fluid viscosity across the thermal front. We then explore reactions which arise if the injected fluid is undersaturated or supersaturated with respect to a mineral in the formation, or if the injected fluid contains acid designed to dissolve some of the matrix. Acid injection treatment is very common in some reservoirs in which insoluble salts precipitate through mixing of formation and injected water, of different chemistry; the precipitate can reduce the flow significantly in or near the wells. One important scale which forms is barium sulfate: this forms when sulfate-bearing injected water mixes with barium-laden formation water. Often this occurs near the production well as water from different zones of the reservoir intermingle. In some wells, acid treatment is needed very frequently to dissolve such scale.

The problems of heat flow and reaction are then combined, to explore dissolution or precipitation reactions associated with the injection of cold and initially saturated solution which heats up in moving through a hot rock, becomes undersaturated and dissolves some of the mineral in the formation. We show that these thermally driven reactions can either partially or fully dissolve the mineral in the formation, and lead to a reduction in the permeability which may lead to channeling. We note that a very illuminating account of reactions in porous rocks has been presented by Phillips (1991); the account we present is complementary to that presentation in that we focus on acidising and thermally controlled reactions.

Continuing the theme of reacting flows, we explore the impact of the gelling of polymers, which may be carried with the injected liquid. Such polymers may lead to a change in the effective rheology of the migrating fluid or in some cases they may gel and become arrested in the formation, leading to a change in the permeability in

the regions where they gel within the reservoir. There is an extensive literature on polymer rheology and gelling, and their effects in reservoir flow processes (e.g. Sorbie, 1991; Lake, 1991). Gelling may be desirable in a porous rock in order to block up a part of the formation. We explore the effect of polymers in which there may be controlled triggering of the gelling process, through encapsulation in, for example, a soluble or thermally sensitive shell. We describe the use of such polymers to help manage the problems of water breakthrough at a producing well which may occur following a programme of water injection into a reservoir (cf. Chapter 2), as water tends to migrate along the high permeability pathways in the reservoir. The gel is used to block these pathways in the reservoir so that subsequently, water injected into the system will migrate through other zones of the reservoir. The analysis we present is aimed at introducing some of the concepts of gelling, especially in terms of the spatial distribution within the formation. We note that there are additional problems relating to the viscosification of the injected liquid and development of non-Newtonian rheology, but the focus in this chapter is on permeability modification through gel formation.

In all models presented in this chapter, we assume that within the pore spaces, the fluid is uniformly mixed in concentration, so that the diffusion within a pore space is not rate limiting for the reactions. With molecular diffusivity of 10^{-9} m²/s and a flow speed of order 10^{-5} m/s, this requires pore spaces to be smaller than about 0.1 mm. With larger pores or faster flow, some concentration gradients may develop in the fluid within a pore. This can lead to a delay in the reaction, with the diffusion-controlled transport of material within pores introducing an effective reaction time which scales as δ^2/D . In addition, the reaction rate may depend on the activity of the reactants and their active surface area per unit volume, as well as the temperature. Owing to the complex and variable morphology of the pore spaces and throats, and possible dispersive mixing, in the following models, we allow for a first-order rate of reaction, where we envisage that this rate of reaction combines these different controls (cf. Phillips, 1991).

8.1 Thermal energy conservation

In contrast to an inert phase, such as a passive tracer, which migrates with the flow, the thermal energy, or strictly enthalpy, has a different advection speed from the fluid owing to the heat exchange between the fluid and the rock. This is because as the fluid migrates past the rock grains, then if there is a temperature contrast there will be some heat transfer (Figure 8.1). The typical time for a fluid parcel to migrate past a grain, δ/u , can be compared with the time for thermal diffusion across a grain, δ^2/κ . In the limit of rapid diffusion, the fluid and grains are in good thermal contact, and locally the system is isothermal. Given the thermal diffusivity has value of about 10^{-6} – 10^{-7} m²/s, and typical flow speeds are 10^{-5} – 10^{-8} m/s, the condition for thermal equilibrium requires grains smaller than about 0.1–0.01 m. We infer that most sediment deposits are in very good local thermal equilibrium with the fluid.

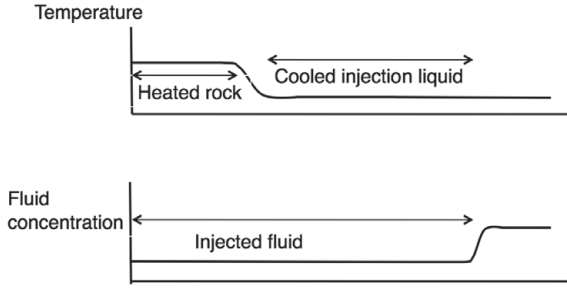


Figure 8.1 Illustration of the difference in position of the fluid and thermal fronts as hot fluid migrates into a porous layer, owing to the thermal inertia as heat exchange between the fluid and grains leads to a region near the source of fluid with the temperature of the source, while the leading edge of the invading fluid adjusts to the original temperature of the formation.

In developing the equation for the conservation of thermal energy, we include the thermal energy of both the matrix and the fluid, while the advection only occurs in the fluid. Similarly, thermal diffusion acts through both the liquid (subscript l) and solid matrix (subscript m), and as an approximation we use the space-averaged value to approximate the thermal diffusivity, so that property f has average value

$$\bar{f} = (1 - \phi)f_m + \phi f_l \quad (8.1)$$

The conservation law therefore takes the form

$$\overline{\rho C_p} \frac{\partial T}{\partial t} + \rho C_{pl} \mathbf{u} \nabla T = \bar{K} \nabla^2 T \quad (8.2)$$

where T is the temperature, ρ is the density and C_p , is the specific heat. The equation denotes the volume average of the solid and liquid, based on the porosity ϕ . The equation identifies that the advection speed of temperature surfaces is given by

$$\Gamma u = \left[\frac{\rho C_{pl}}{\overline{\rho C_p}} \right] u \quad (8.3)$$

This speed has a value in the range $1.1-1.2u$, where u is the Darcy speed, since the pre-multiplier, Γ , a dimensionless constant has value $1.1-1.2$ depending on the porosity and the specific fluids. Since the fluid migrates with the interstitial speed u/ϕ , it follows that with $\phi \approx 0.2$ the thermal signal travels at a speed of about $0.2-0.3$ of the fluid and hence lags far behind the fluid front. Physically, we can understand this process since the porous matrix undergoes a change in thermal energy as it is flooded with the injected fluid. This thermal energy is transferred to the leading part of the injected fluid, which now lies ahead of the thermal front, and has the temperature of the formation (Figure 8.1).

For example, in Figure 8.2, we include three photographs showing fluid of one initial temperature, 35°C and which is dyed red migrating into a porous bead pack

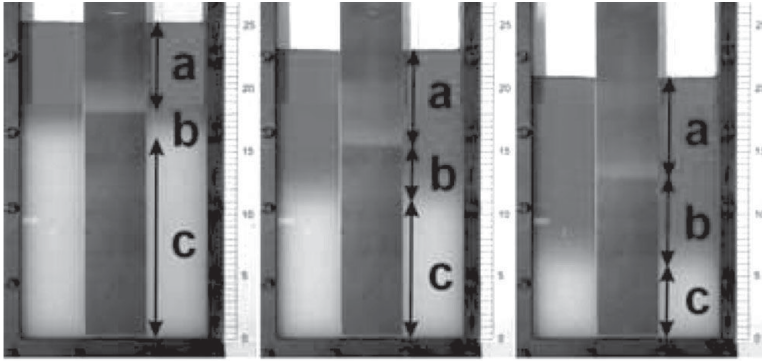


Figure 8.2 Illustration of the migration of a thermal front within a porous layer. Hot red fluid is injected at the top of the bead pack and the fluid migrates down through the pack with the red front illustrating the advance of the fluid. The advancing temperature front is recorded by the change in colour of a liquid-crystal strip in contact with the bead pack; the region in which the liquid-crystal strip has a change in colour migrates down through the bead pack, but at a slower speed than the red dye owing to the thermal inertia. After Menand *et al.* (2003). A black and white version of this figure will appear in some formats. For the colour version, please refer to the plate section.

initially maintained at a second temperature, 17°C and containing clear fluid. The tank has a black liquid-crystal strip in the direction of the flow, and this changes colour at about 26°C , which is intermediate between the injected and original temperatures. The travelling thermal front migrates with speed similar to the Darcy speed (Eq. 8.3) while the red dye in the fluid injected into the formation advances with the advection speed, which is about 2.5 times as large as the thermal front speed in this experiment, with $\phi = 0.4$.

As we have seen, mechanical dispersion operates over a range of scales associated with the presence of heterogeneities in the porous formation; the reason that the mechanical dispersion is so significant for tracer transport results from the very small value of the molecular diffusivity. However, the thermal diffusivity in porous rocks has a value of order $\kappa \sim 10^{-7} - 10^{-6} \text{ m}^2/\text{s}$ and so for scales of order 0.1–1.0 m, corresponding to localised regions of different permeability, and flow speeds of order $10^{-5} - 10^{-6} \text{ m}^2/\text{s}$, the thermal Peclet number, ud/κ is of order unity, so that the effects of dispersion of the flow are comparable to the thermal diffusion. Only with larger scales or faster flows is the thermal dispersion likely to dominate the thermal diffusivity. In a layered system, for example with a lens, $i=1$, of high or low permeability, of thickness H_1 , embedded in a formation, $i=2$, of thickness H_2 , then if the travel time along the formation L/u_i is larger than the thermal diffusion time across the layers, H_i^2/κ , then the lens will tend to thermally equilibrate, and the effective advection speed of the thermal front across both layers, will then scale as the average

$$\Gamma u = \frac{\Gamma_1 u_1 H_1 + \Gamma_2 u_2 H_2}{H_1 + H_2} \quad (8.4)$$

where u_i are the speeds in the two layers, $i = 1, 2$. This thermal equilibration can lead to enhanced dispersion of the thermal front, and a similar effect arises through the loss of heat from the boundaries of the permeable flow domain. The analysis of thermal fronts described in the present chapter primarily relates to relatively thick layers or short injection times in which we may consider the cross-flow heat loss to be small; the modelling is developed to account for heat loss in Chapter 11 in considering geothermal heat flow problems.

Owing to the spatial separation of the thermal front and fluid front, the injected fluid changes temperature, producing a region filled with fluid of different density and viscosity, and perhaps solubility, relative to the minerals in the matrix. The effects of this thermal inertia can be key in considering reactions between the injected fluid and minerals. We will return to these effects later in this chapter in considering reactions between the injected fluid and minerals in the rock, as well as in exploring how thermally sensitive polymers evolve as they flow into a formation. Thermal effects can also influence the migration of plumes of CO_2 or aqueous solutions of different temperature and salinity. As the injected fluid migrates into the formation, it adjusts in temperature and this can change the viscosity and magnitude or sign of the buoyancy of the flow (Chapter 11). In Chapter 11, we also revisit the effects of thermal inertia in our discussion of geothermal power generation, focusing on the problem of the injection of cold water which then boils as it moves through the formation.

8.2 Instability of a thermal front

One interesting feature of a thermal front is that the change in fluid properties across the front have the potential for instability. Typically, injection of water into the sub-surface leads to a decrease in the viscosity of the fluid as it warms up, and this will keep the interface stable. In parallel with this, there may also be changes in the density of the fluid, as the temperature changes, and we consider this in more detail in Chapter 11.

In the case of the injection of cold fluid into a reservoir, as the formation near the well-bore cools, it may begin to contract somewhat owing to the change in temperature. This can lead to the generation of stress within the formation and ultimately the formation of cracks. The cracks will typically be aligned in the direction of maximum principal stress, since they are opening up the rock in the direction of the minimum principal stress. The fractures lead to an increase in the effective permeability of the formation, and the continuing injection fluid may then advance along the fractures. With a planar front advancing into the permeable rock, the effect of this increase in permeability has some analogies with the stability of a dissolution front (cf. Chapter 6). If the advancing thermal front develops a sinusoidal perturbation, then the cooling front will become localised about these perturbations. As the perturbations develop, the

lengthscale κ/u provides a limit to the minimum scale for the perturbations, since on shorter scales, thermal diffusion will smooth the cross-flow perturbations. With a flow speed of 10^{-6} m/s, this leads to a scale of order 1 m, although we note that the solid mechanics of fracturing may impose additional scales on the problem, as the fractures may advance ahead of the cooled zone.

In the case of injection of hot water into a formation, perhaps as part of an aquifer thermal energy storage system (Chapter 11), the reduced viscosity of the injected liquid may lead to an instability across the thermal front, as the fluid cools and becomes more viscous, in a fashion analogous to the Saffman–Taylor instability, although with a mass flux across the thermal front. Again, there will be a small wavelength cut-off owing to thermal diffusion.

8.3 Compositional reactions

We now consider a reaction between the matrix and the fluid in which the reaction rate depends on the presence of reactant in the fluid and in the formation. Such reactions occur for example when a fluid which is unsaturated with respect to a mineral in the rock, migrates through the rock and dissolves the mineral. Indeed, if a porous layer is made by filling a tank with glass beads and a small mass of salt powder, uniformly mixed through the beads, and the pack is then immersed in saturated salt solution, the system will react if the salt solution is displaced downwards by a solution of fresh water. With a uniform flow through the pack, the system sets up a simple travelling wave structure across the reaction front, as found in a laboratory experiment in which the salinity of the water was measured across the reaction front (Figure 8.3).

In this experiment, 10 wt% of the solid matrix was composed of sodium chloride powder and the remainder was glass ballotini, of radius 0.5 mm. As the reaction front migrated through the cell, the salinity of the water passing through the front increased from being fresh to taking a value 23 wt%, comparable to the saturation value. The interface is stable in this experiment since the saturated aqueous solution has a density of about 1.2 times that of the fresh water, and the flow is sufficiently slow that this buoyancy stabilisation prevents the interface becoming unstable owing to the potential dissolution instability.

Before developing a model for the structure of the reaction front, we can use a simple mass balance to describe the speed of the front, in terms of the mass of salt required per unit volume of fluid in order that the fluid becomes saturated in salt. Near the source, the bead pack becomes depleted in salt, while at the leading part of the input fluid, the injected fluid is saturated in salt (Figure 8.4).

In order to calculate the speed of the reaction front, we can use the mass balance of salt, in that if the region of salt depleted rock has extent λut while the extent of the liquid zone is ut/ϕ , then the conservation of salt requires

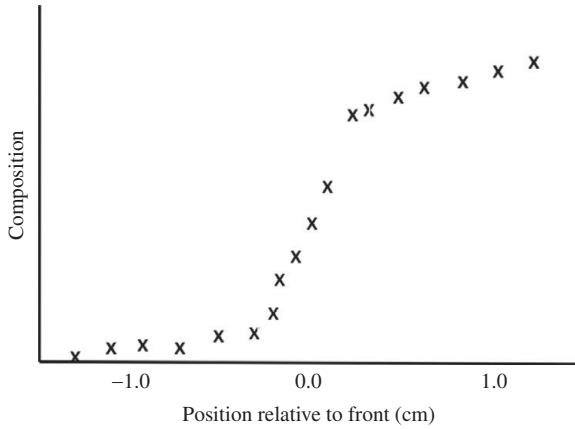


Figure 8.3 Illustration of an experimental measurement of the concentration gradient across a reaction front, in a bead pack, to demonstrate the localised nature of the front. The reaction zone extends about 1 cm from the near uniform concentration upstream to the near uniform concentration downstream, suggesting a very short reaction time compared to the flow rate. In this experiment, the porous layer consisted of 90% glass beads of radius 0.5 mm, and 10% NaCl powder. The undersaturated fresh water migrated through the pack at a speed 0.1 mm/s, and dissolved the salt in the matrix. Measurements of the salinity were taken from an array of sampling ports at different heights on the pack. A key observation from this experiment is the localised nature of the reaction front, suggesting that in this case, the advection associated with the flow controls the reaction, rather than the reaction kinetics. Note, in this experiment, the interface is stabilised by gravity in that the aqueous solution is denser than the fresh water, and with the low flow rates this tends to suppress the dissolution instability which might arise (cf. Chapter 6).

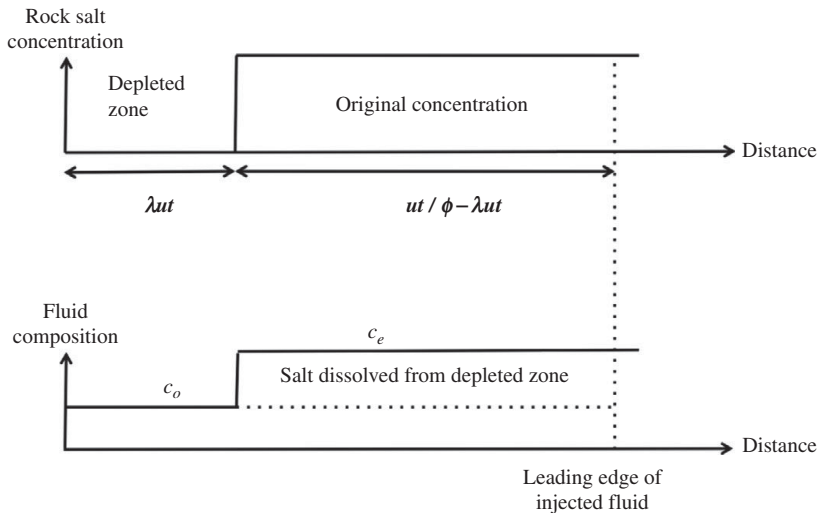


Figure 8.4 Structure of the reaction front relative to the speed of the front, illustrating the depletion of the reacting species in the fluid downstream and the solid matrix upstream.

$$\lambda u s_o (1 - \phi) = (u t / \phi - \lambda u t) (c_e - c_o) \phi \quad (8.5)$$

where s_o is the fraction of the matrix which consists of salt and c_o and c_e are the initial and saturated concentrations of salt in the liquid (Figure 8.4) giving the value for the dimensionless position of the reaction front

$$\lambda = \frac{c_e - c_o}{\phi (c_e - c_o) + s_o (1 - \phi)} \quad (8.6)$$

In practice the reaction will not be a sharp front, but will be an extended region around this centre of mass position, as seen in the experimental data above. There are two processes which can lead to the dispersal of the front as explained by Phillips (1991). First, salt in solution may diffuse upstream through the liquid; as a result, even with equilibrium dissolution of the salt powder, a gradient of salt develops in the fluid upstream. Second, there may be some kinetic control on the dissolution process such that there is a reaction rate which depends on the concentration of solid and is also proportional to the degree of undersaturation of the solution. A simple model for this is a first-order reaction model in which the rate of reaction is assumed to be proportional to the mass of salt, and the degree of undersaturation of the liquid, with the constant of proportionality γ which depends on the activity, the surface area per unit mass, and the temperature. This gives rise to the governing relations for the salt concentration in the fluid c , and the salt mass fraction in the solid, s ,

$$\phi \frac{\partial c}{\partial t} + u \frac{\partial c}{\partial x} = \gamma (c_e - c) s + \phi D \frac{\partial^2 c}{\partial x^2} \quad (8.7a)$$

$$(1 - \phi) \frac{\partial s}{\partial t} = -\gamma (c_e - c) s \quad (8.7b)$$

Here β is a stoichiometry constant which relates the mass of solid salt required per unit mass dissolved in the solution. In the limit of small diffusivity, these coupled equations admit a travelling wave-type solution in the case that $c = c_o$ and $s = 0$ far upstream and $c = c_e$ and $s = s_o$ far downstream, given by

$$c(x - \lambda u t) = c_e + (c_o - c_e) f \quad ; \quad s(x - \lambda u t) = s_o g \quad (8.8)$$

where integration of the equations from far upstream to far downstream requires that

$$\lambda = \frac{c_e - c_o}{(c_e - c_o) \phi + s_o (1 - \phi)} \quad (8.9)$$

which is equivalent to the mass balance relation (8.6) and which implies that $f = 1 - g$ with $f(\eta)$ satisfying the equation

$$\frac{df}{d\eta} = -\Gamma f(1 - f) \quad \text{with} \quad \Gamma = \frac{\gamma s_o}{u(1 - \phi \lambda)} \quad (8.10)$$

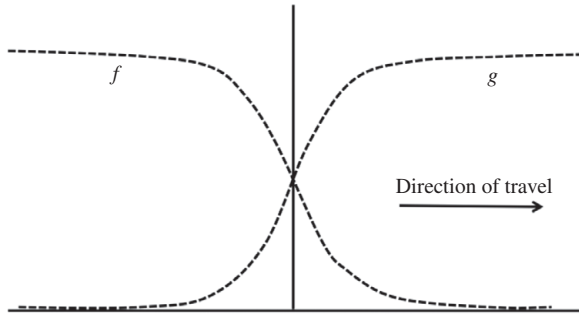


Figure 8.5 Illustration of the mass balance for a travelling wave solution for a reaction front. f is the degree of undersaturation of the reacting species in the fluid and g is the mass of material which can react with this species in the fluid. Upstream there is no material remaining in the solid matrix, while downstream the fluid is saturated in the reacting species.

This has an exact travelling wave solution, with speed λu , given by

$$f = \frac{1}{1 + \exp(\Gamma(x - \lambda ut))} \quad (8.11)$$

as shown in Figure 8.5.

In principle, we might be interested in the adjustment to this travelling wave solution from an initial injection of unsaturated fluid into the reactive permeable matrix. Initially the reaction front will develop at the leading edge of the fluid, but it will rapidly migrate backwards to the equilibrium travelling wave solution, as the rock near the source becomes depleted in salt, and both the upstream and downstream branches of the travelling wave solution can develop. This transient adjustment can be calculated numerically in the half-space $x > 0$, by imposing the flux of fresh fluid at $x = 0$ for $t > 0$. A typical calculation is shown in Figure 8.6, in which the x -axis has been scaled with respect to the position of the reaction front at each time. It is seen that as time evolves, the structure of the reaction zone adjusts to a solution of the form shown in Figure 8.5.

8.4 Thermally controlled reactions

In modelling reactions in permeable rock, it may be key to account for the effects of temperature on the reactions. We have seen that porous media have thermal inertia as heat is exchanged between the solid matrix and the fluid, and that this leads to an internal thermal boundary layer in the fluid. As a result, if a fluid is injected into a porous rock at a temperature different to the formation, then even if the fluid is in equilibrium with the minerals at the injection temperature, as it heats up or cools on migrating through the porous layer, it will evolve out of equilibrium and this may lead to either

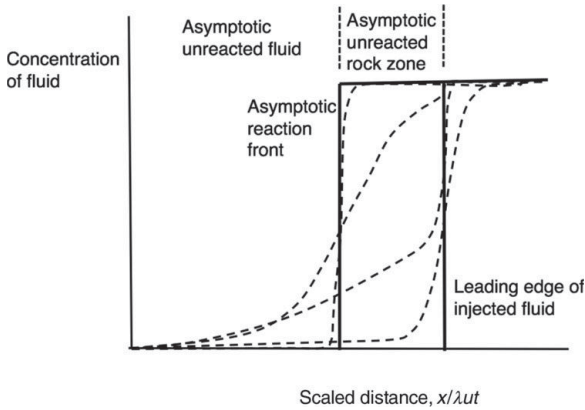


Figure 8.6 Transient adjustment of the reaction front from the leading edge of the fluid to the travelling wave solution which travels at a fraction of the speed of the leading edge of the fluid.

dissolution or precipitation. In the case in which the fluid becomes undersaturated, two situations may then arise, and we consider each in turn.

In modelling such systems, we require a phase diagram which indicates how the equilibrium composition of the liquid varies relative to the temperature: for the example herein, this is shown by the liquidus curve in Figure 8.7. In this figure the liquidus curve denotes the temperature at which the dissolved salt composition in the liquid is just at equilibrium. If the temperature decreases, then salt will precipitate from solution, decreasing the composition as the temperature falls. Conversely if the fluid remains in contact with the solid salt phase, then as the temperature rises, some of this salt will dissolve to increase the salt composition of the liquid as the temperature rises. Eventually, all the solid salt phase is dissolved and then the temperature can rise with no change in composition, and the solution becomes superheated. The amount of solid salt in the formation therefore has an important effect on the dissolution reaction which occurs with a moving thermal front across which the temperature increases.

8.5 The partial dissolution reaction

First, in the case in which the mass of salt in the matrix upstream of the thermal front is more than sufficient to return the injected fluid downstream of the thermal front to equilibrium, then the reaction front remains slaved to the thermal front, and only a fraction of the salt dissolves. In such a situation, we can calculate the fraction of the salt which dissolves to return the formation to equilibrium by a mass balance as shown in Figure 8.8, assuming the thermal front is localised in space.

The equilibrium fluid concentration increases across the thermal front as the cold injected fluid heats up (line AC, Figure 8.7). As a result of this, at the thermal front,

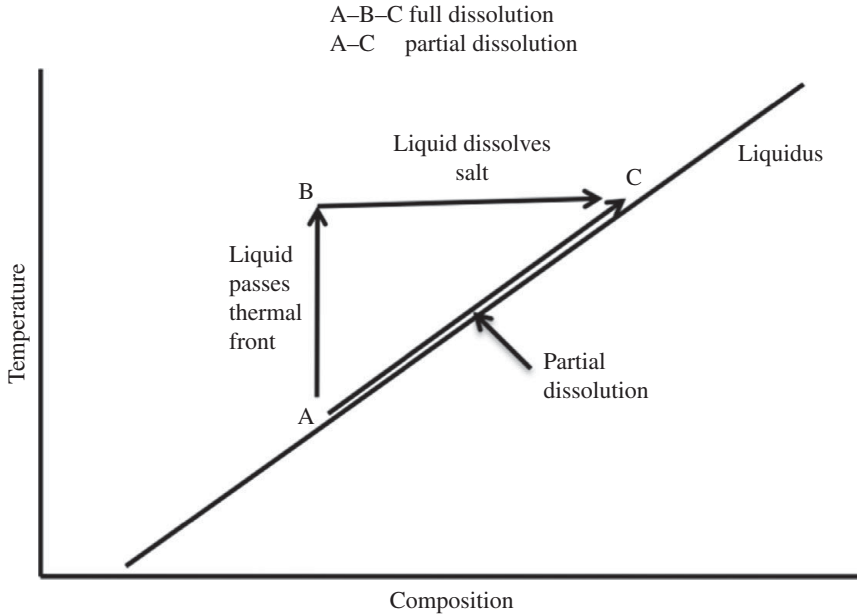


Figure 8.7 Illustration of the variation of the liquidus curve with temperature. For a given liquid concentration, once the temperature falls to the liquidus temperature, solid precipitate may develop, and remain in equilibrium with the liquid. Above this temperature, all the material is liquid. The path AC along the liquidus corresponds to a partial dissolution reaction in which a fluid heats up as it migrates into a porous medium, and in the process it partially dissolves some of the salt phase (Figure 8.8). The path ABC corresponds to a full dissolution reaction, in which the salt which lies between the source and the thermal front is insufficient to maintain the fluid in compositional equilibrium, and so some of the salt ahead of the thermal front also dissolves, leading to a separation in space of the thermal and dissolution fronts (see Figure 8.10).

the salt in the rock is dissolved to provide the additional salt in solution in the liquid passing through the thermal front. As a consequence there is a decrease in the salt content of the rock at the thermal front, with the salt which was originally upstream of the thermal front (Figure 8.8) now being in solution in the liquid downstream of the thermal front.

In this case, the problem is to calculate the decrease in the salt concentration in the rock upstream of the thermal front. If the mass of salt in solution increases from concentration c_o to value c_e then the mass of mineral dissolved in the injected fluid, now downstream of the thermal front, is

$$(ut/\phi - \Gamma ut)(c_e - c_o)\phi \quad (8.12)$$

while the mass of salt upstream of the reaction front decreases from s_e to value s_D where by mass balance

$$s_D = s_e - (1/\phi - \Gamma)(c_e - c_o)\phi / [(1 - \phi)\Gamma] \quad (8.13)$$

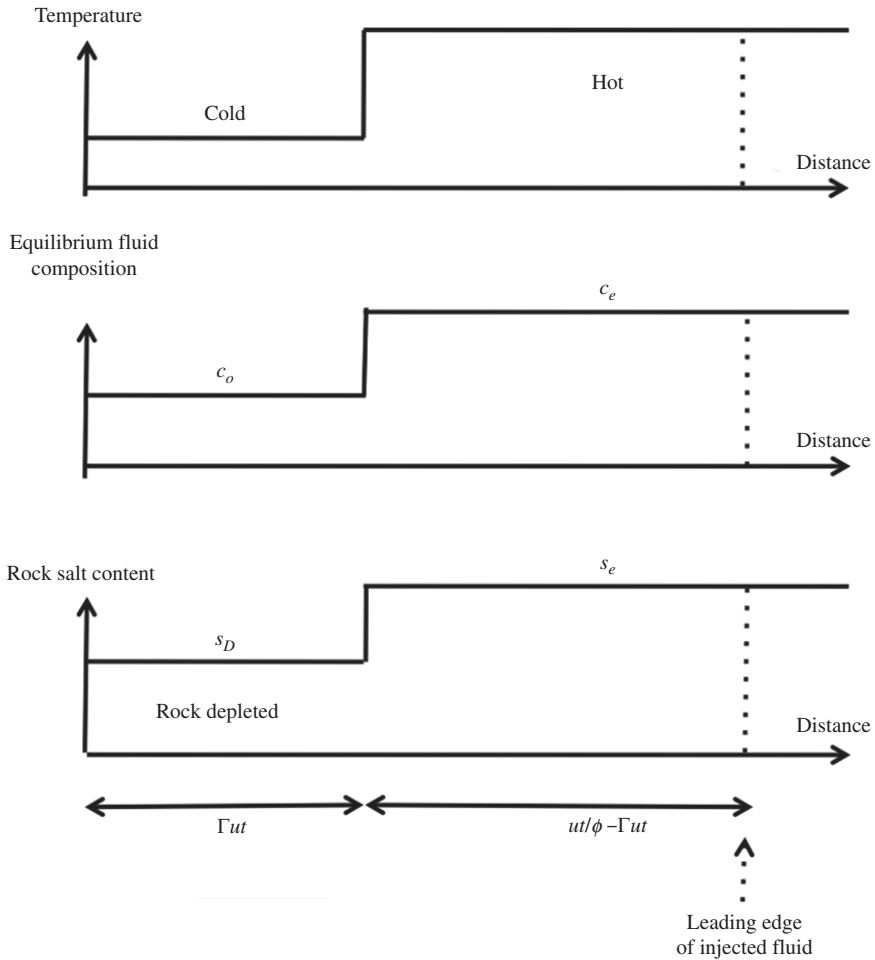


Figure 8.8 Illustration of the thermal and solutal changes across a thermal front in the case of a partial dissolution front. The reaction front is slaved to the thermal front.

In order that this solution can develop, we require that $s_D \geq 0$, so that there is some solid salt remaining upstream of the reaction front.

We can calculate the evolution of the reaction front to this localised travelling front solution, by solving for the thermal field, and then the compositional field in the liquid, assuming it adjusts towards equilibrium through dissolution everywhere in space. We assume the dissolution has a rate constant which we parameterise as γ as in the simple reaction model above, Eq. (8.7). Neglecting latent heat associated with the dissolution, the thermal front is then given by the solution of the thermal advection–diffusion equation and has the form

$$T = \frac{(T_o + T_1)}{2} + \frac{(T_1 - T_o)}{2} \operatorname{erf} \left(\frac{x - \Gamma ut}{2(\kappa t)^{1/2}} \right) \tag{8.14}$$

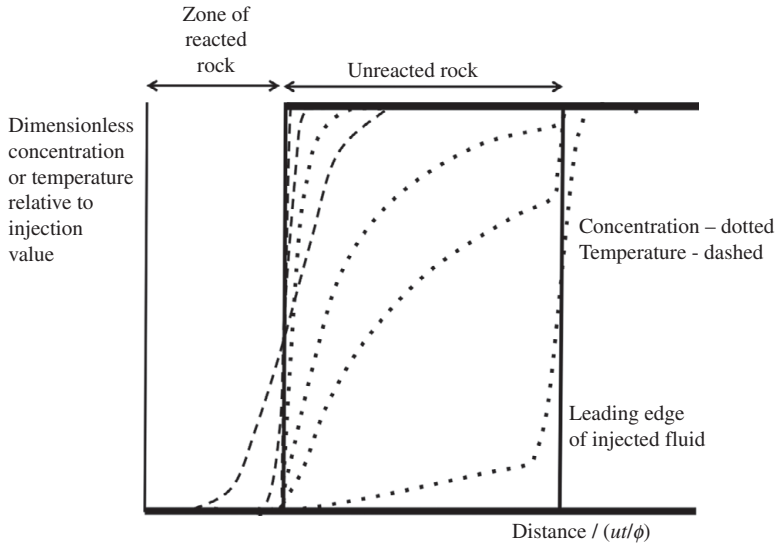


Figure 8.9 Illustration of the transient evolution of the temperature and composition in which the partial dissolution reaction develops. The compositional front (dotted line) becomes driven by the thermal front (dashed line) after an initial transient, as indicated by the sequence of compositional profiles with time. The long-time asymptotic zone of reacted and unreacted rock are also shown.

where T_o is the upstream temperature and T_1 is the downstream temperature. The equation for the composition is then given by the relation

$$\phi \frac{\partial c}{\partial t} + u \frac{\partial c}{\partial x} = \gamma(c_e(T) - c)s \quad (8.15)$$

Figure 8.9 presents a solution of the evolving temperature (dashed line), and also composition (dotted line), with time, as a front advances into a porous layer and dissolves some of the salt in the matrix. The figure shows distance normalised with respect to the position of the injected fluid front. The temperature asymptotes to the solution (8.13) and the compositional front is initially located at the fluid front, but as the reaction takes place, the compositional field also rapidly adjusts towards the thermal front with the reaction rate imposing a lengthscale u/γ for the reaction, which becomes small compared to the location of the advancing thermal front.

8.6 The full dissolution reaction

If the injected liquid is sufficiently undersaturated on being heated to the reservoir temperature, then the partial dissolution model leads to the prediction that $s_D < 0$ (Eq. (8.13)). The reason for this unphysical prediction is that there is insufficient salt upstream of the thermal front to keep the solution in equilibrium. Instead, the dissolution front now extends well beyond the thermal front, since there is insufficient

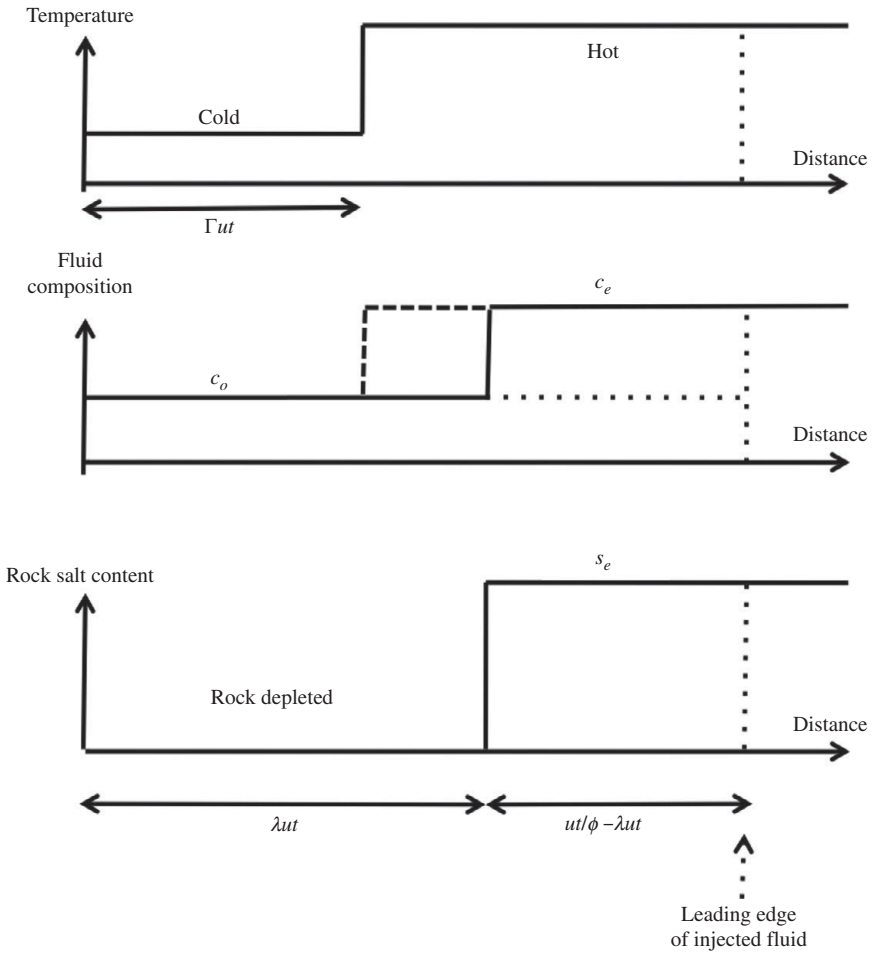


Figure 8.10 Structure of a reaction front produced through the heating of the injected fluid, in the case that the rock becomes depleted of salt upstream of the thermal front, so that the reaction front advances more rapidly than the thermal front. Dashed lines denote the equilibrium saturation profile.

salt upstream of the thermal front to return the fluid to compositional equilibrium (see Figure 8.10). The problem now becomes one of defining the location of the reaction front downstream of the thermal front.

In this case, Figure 8.10 illustrates that the mass of newly dissolved salt in the injected fluid downstream of the reaction front, M_d , is given by

$$M_d = (ut/\phi - \lambda ut)(c_e - c_o)\phi \tag{8.16}$$

while the mass of salt dissolved from the rock, M_s , which supplies this additional salt in the fluid downstream of the dissolution front, is given by

$$M_s = \lambda uts_e(1 - \phi) \tag{8.17}$$

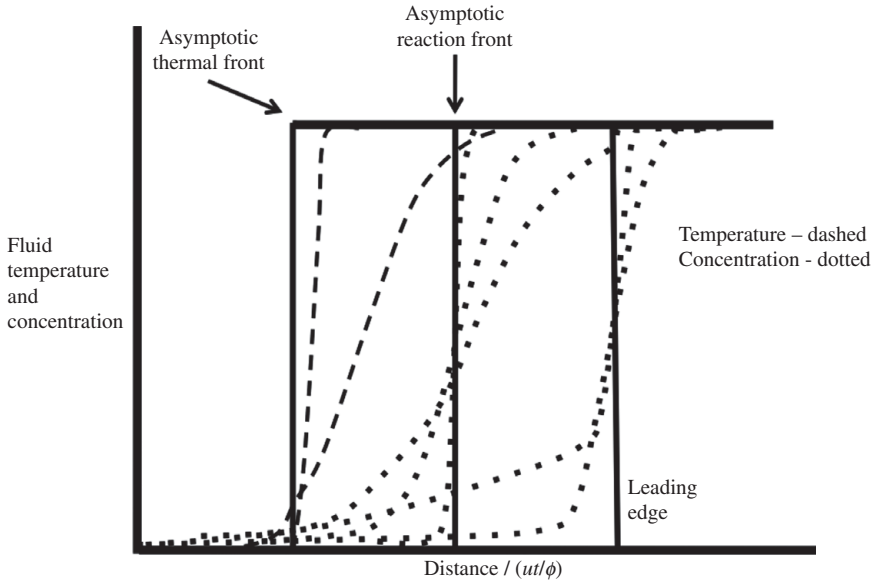


Figure 8.11 Evolution in time of the thermal field (dashed) which converges to the asymptotic thermal front, and the liquid concentration (dotted) which converges to the asymptotic reaction front, as a function of time, showing the convergence to the frontal solution. The horizontal axis has been scaled so that the position of the leading edge of the injected fluid is always unity to help interpret the convergence to the travelling wave solutions.

Matching these expressions leads to the prediction that the location of the dissolution front, now downstream of the thermal front, is given by

$$\lambda = \frac{(c_e - c_o)}{(c_e - c_o)\phi + s_e(1 - \phi)} \quad (8.18)$$

This reaction front speed is directly analogous to the compositional reaction speed described in Section 8.3 above in which an unsaturated fluid enters a porous matrix and dissolves the salt in the matrix (Eq. (8.16)), although here the reacting fluid only becomes superheated (i.e. undersaturated) after passing through the thermal front.

We can again solve the initial value problem for the evolution of the salt content (Eq. (8.7b)) of the porous layer as a function of time, and for the evolution of the temperature and composition of the fluid with time, which again follow the relations (8.14) and (8.15). The transient solutions for the fluid temperature (dashed) and composition (dotted) shown in Figure 8.11 lead to the prediction that the solution converges towards the travelling front solution illustrated in Figure 8.10.

It is possible to envisage more complex reaction fronts in which the original injected fluid has multiple components, and is super- or undersaturated with respect to the salt in the formation at the formation temperature, but also that the temperature of the injected

fluid is different from that in the porous layer. However, the solutions above provide the building blocks to develop these more complex solutions. In Chapter 11 we describe an experimental technique to model reaction fronts in porous layers using solutions of sugar and salt in the presence of salt crystals. These experiments however also lead to density changes across the reaction fronts and we explore how this can control the dynamics of the reaction.

8.7 Polymer floods

As mentioned in the introduction to the chapter, it is possible to add polymers to the fluid injected into oil fields with the purpose of gelling the polymer at some location within the reservoir, thereby reducing the flow through that part of the reservoir (Figure 8.12). In general, it is not desirable to add the active polymer directly into the field since it may gel up near the injection point and this may have a very substantial impact on the flow rate since the flow typically spreads radially in this region, with the largest pressure decrease near the source (cf. Eq. (6.23); Figure 6.11); formation of a polymer skin near the well can lead to a very large pressure drop and hence reduction in flow rate. Ideally, the polymer would be injected into the field prior to being activated, with a trigger causing the polymer to activate within the field away from the injection well. There are various types of trigger possible, including the use of an encapsulant to contain the unactivated polymer until some point in the field where the encapsulant releases the polymer (e.g. van Triet *et al.*, 2014); a kinetic delay in the activation of the polymer may also be possible, essentially limiting the reaction of the polymer with the formation fluid. For the purposes of modelling the formation of a polymer gel within a field, we explore two simplified models. First a model in which we envisage the polymer is released from an encapsulant at a time τ following injection, and in the second model we envisage the polymer is injected with cold water and only becomes active once it reaches a region of the reservoir which is sufficiently hot. In both cases, we assume the gelling process is an order-one reaction dependent on the mass of unreacted polymer which is present.

8.8 Polymer released from a dissolving encapsulant

The polymer may be injected within an encapsulant which shields the polymer from the formation water, for example, but which gradually dissolves within the permeable rock, eventually allowing the polymer to contact the formation fluid and gel. The dispersal of

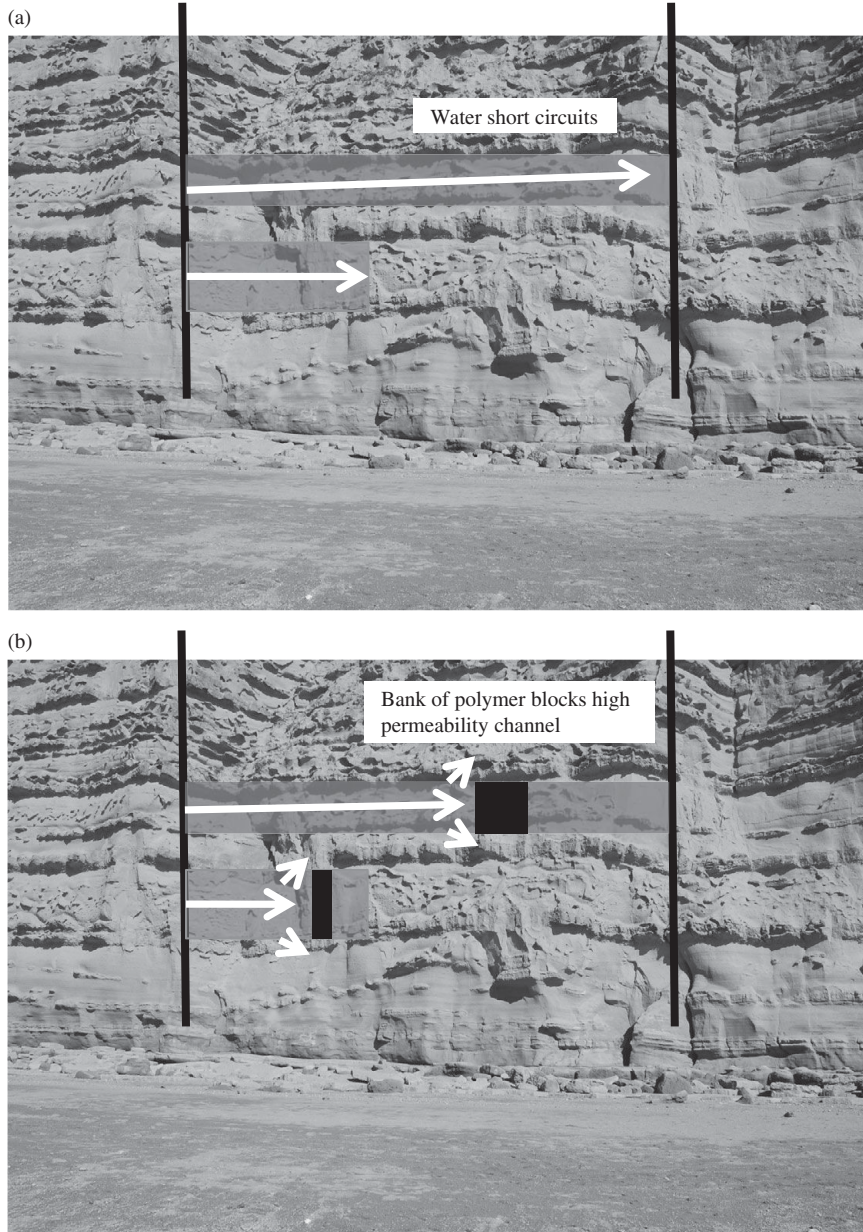


Figure 8.12 Schematic of the injection of polymer to plug or reduce the permeability of a highly permeable layer, following recovery of oil from this layer. A black and white version of this figure will appear in some formats. For the colour version, please refer to the plate section.

the injected liquid and any effects of two-phase flow may then lead to a diffuse region in which the polymer gels. We now develop a simplified one-dimensional model for the gel formation in a one-dimensional flow to provide insight into some of the controls on the polymer distribution in space and time.

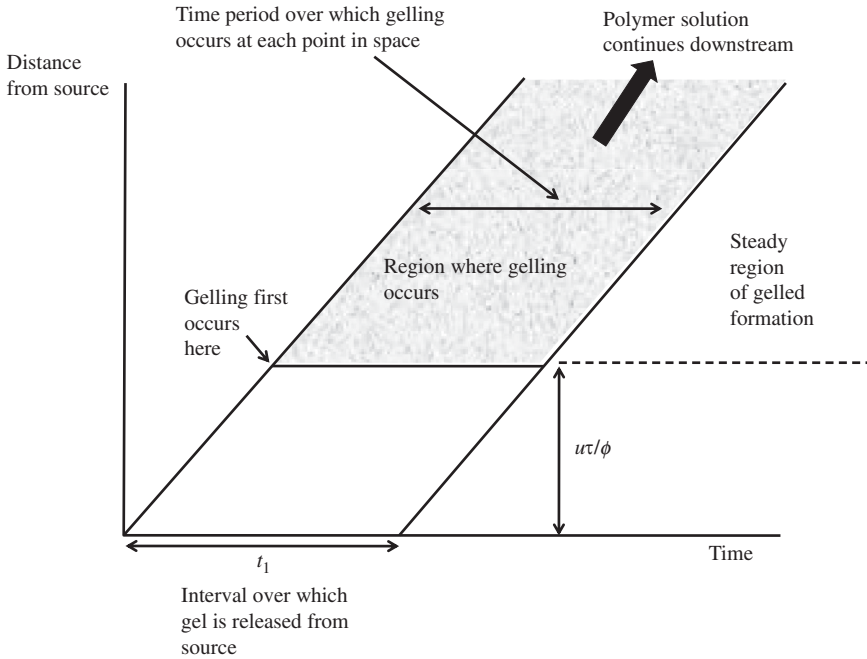


Figure 8.13 Characteristic diagram illustrating the region in space and time where the polymer gelling occurs as the polymer solution passes through the porous layer.

To model the flow, we envisage that the encapsulant dissolves after a time τ in the rock (Figure 8.13) and then the polymer gels with a rate constant λ . As the ungelled polymer migrates through the formation, it may disperse with a longitudinal dispersivity D (Chapter 5). We also assume that the gel is trapped in the pore space, reducing the permeability and hence increasing the pressure gradient. One of the uncertainties in such a model is that successive parcels of ungelled polymer laden fluid migrate through the same pore space, and in principle lead to further gel formation. In the simplified model presented below, we assume that this ungelled polymer is able to migrate through any pre-existing gel, although that may not always be the case if the length-scale for the flow through the gel becomes smaller than the size of the ungelled polymer; this potential filtration process merits further investigation. The associated change in permeability is likely to be non-linear, as the flow path becomes progressively more blocked and successive polymer molecules are added to those already deposited at that point in space. In the following model we assume a constant flow rate, and so implicitly the pressure associated with the flow increases. With experimental modelling, one could develop a model for the change in permeability in terms of the mass of polymer which gels at each point, and then explore the flow in the case of a constant pressure boundary condition, although this is beyond the scope of the present discussion.

We can write down a family of conservation equations for the formation of the gel, by introducing a concentration of ungelled polymer c and gelled polymer G . We assume the gel formation commences after it has been released from an encapsulating shell, at time τ after it has entered the porous rock and that the concentration of ungelled polymer then decays with a rate constant proportional to the concentration

$$\phi \frac{\partial c}{\partial t} + u \frac{\partial c}{\partial x} = -\lambda \phi H(t - \tau) c + \phi D \frac{\partial^2 c}{\partial x^2} \quad (8.19)$$

where $H(t - \tau)$ is the step function defined as $H(x) = 1$ if $x > 0$ and $H(x) = 0$ if $x \leq 0$, and this is the parameterisation of the time delay of the onset of gelling. The mass of gelled polymer then evolves in time according to

$$\phi \frac{\partial G}{\partial t} = \lambda \phi H(t - \tau) c \quad (8.20)$$

We could also assume the permeability varies with G according to a non-linear dimensionless function $F(G)$,

$$k(G) = k_o F(G) \quad (8.21)$$

so that the speed satisfies

$$u = -\frac{k(G)}{\mu} \frac{\partial p}{\partial x} \quad (8.22)$$

although in the present analysis, we assume a constant flow rate; with a model for $F(G)$ a more general class of problems can however be explored.

In the case in which there is relatively little dispersion of the concentration, $D \sim 0$, the above equations can be solved using the method of characteristics by following parcels of fluid once they have been injected into the formation (Figure 8.13). If the polymer gel is supplied over a time interval $0 < t < t_1$ from an injection well $x = 0$, then the concentration of ungelled polymer in a parcel of fluid once it has passed the point $x_g = u\tau/\phi$ where gelling commences, is given by

$$c = c_o \exp\left(-\frac{\lambda \phi}{u} \left[x - \frac{u\tau}{\phi}\right]\right) \quad \text{for } x > x_g \quad (8.23)$$

As the polymer cloud passes through the matrix, gel continues to form in the matrix, according to the gel formation relation (8.20) and (8.23) so that at the point $x(> x_g)$, the amount of polymer will increase from the time of first arrival of the polymer cloud to a maximum at the time at which the whole cloud has passed, and this final value is given by combining (8.20) and (8.23),

$$G(x, t) = t_1 \lambda c_o \exp\left(-\frac{\lambda \phi}{u} \left[x - \frac{u\tau}{\phi}\right]\right) \quad \text{provided } t > t_1 + \frac{x\phi}{u} \quad (8.24)$$

The above solution for the concentration of the gel illustrates that the concentration of gel decays exponentially in space beyond the region where the gel is initially

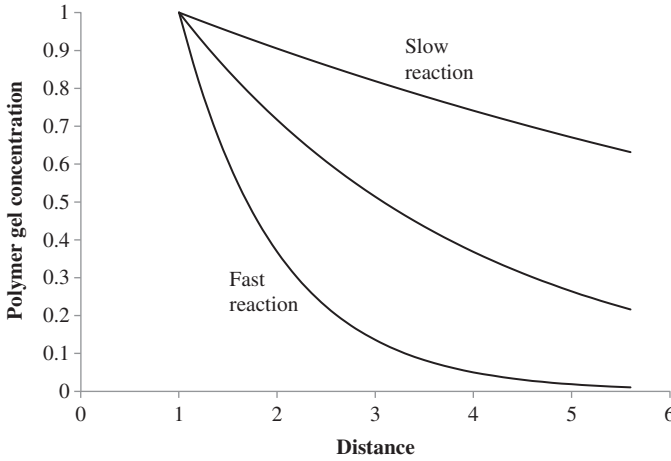


Figure 8.14 Illustration of the variation of the polymer concentration with distance into the rock; each curve is scaled relative to the maximum concentration on that curve, which coincides with the point at which the polymer first begins to react, $x = u\tau/\phi$. The distances are scaled relative to the distance at which the polymer is first released from the encapsulant, $u\tau/\phi$, and the three curves correspond to the polymer reaction distance $u/\lambda\phi$ having value 1 (fast reaction), 3 and 10 (slow reaction) times the initial release distance $u\tau/\phi$.

released from the soluble encapsulant, as shown in Figure 8.14. The maximum concentration and the rate of decay depend on the reaction constant λ . In turn this will have an impact on the change in permeability of the formation since the relationship between the gel concentration and the permeability is typically non-linear; in any event, the change in permeability of the formation is likely to differ substantially for a given mass of polymer as the spatial distribution of the gelled zone changes (Section 8.10). Combining the model for the spatial distribution of the gel with a model of the variation of permeability with gel concentration would enable optimisation of the impact of a finite mass of gel.

8.9 Polymer activated by a thermal trigger

In some cases, polymer may be released from an encapsulant and become activated through a thermal trigger. For example, the polymer PNIPAM may be thermally triggered, so that above 32°C , a suspension of the polymer in water forms a gel and the liquid becomes much more viscous. If this is placed in a porous layer, the gel tends to become trapped in the pore space once the gelled polymer particles grow to a size in excess of the pore throats. This can lead to a substantial reduction in the permeability of the matrix. In contrast, for lower temperatures, $< 32^\circ\text{C}$, the polymer remains as individual molecules, which are not cross-linked, and so does not have a substantial impact

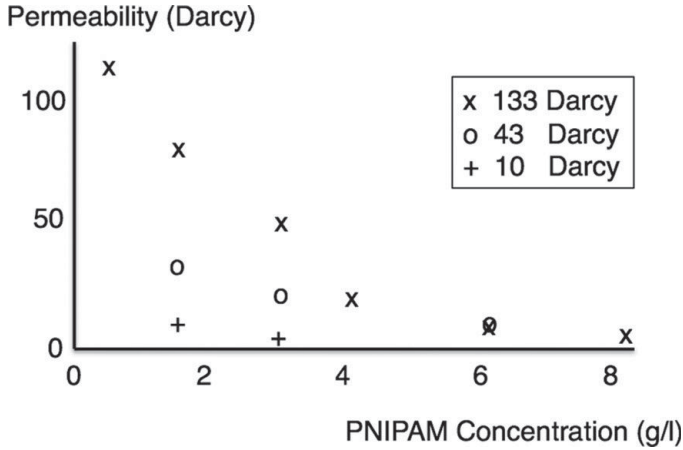


Figure 8.15 Change in the permeability of a bead pack following the heating of the bead pack to 45°C and the formation of a PNIPAM gel. Data show the permeability as a function of the concentration of the PNIPAM and symbols correspond to different initial values of the permeability prior to formation of the gel. These correspond to initial bead sizes. After van Triet *et al.* (2014).

on the viscosity of a water solution. Experiments carried out by van Triet *et al.* (2014) show the reduction in the permeability of a bead pack which arises when a solution containing cold polymer is heated above 32°C (Figure 8.15).

To model the gelling of such a polymer, one may envisage that if the cold polymer is injected in a finite slug, then as the fluid invades the hot porous layer, the successive parcels of polymer-laden fluid will reach the thermal front and gel (Figure 8.16). If the gelling process has some kinetic delay, so that once the polymer is sufficiently warm the rate of polymer gelling depends on the concentration of the ungelled polymer then we can write an analogous model to Eqs. (8.19–8.20) for the time-delay release of polymer but now accounting for the critical temperature T_c at which gelling commences. In this case we also assume that the polymer gel concentration increases in time at each point as progressively more polymer arrives at that point.

$$\phi \frac{\partial c}{\partial t} + u \frac{\partial c}{\partial x} = -\lambda \phi c H(T - T_c) + \phi D \frac{\partial^2 c}{\partial x^2} \quad (8.25)$$

$$\frac{\partial T}{\partial t} + \Gamma u \frac{\partial T}{\partial x} = \kappa \frac{\partial^2 T}{\partial x^2} \quad (8.26)$$

$$\phi \frac{\partial G}{\partial t} = \lambda \phi c H(T - T_e) \quad (8.27)$$

Suppose the polymer slug is released between the times $t=0$ and $t=t_1$ as shown on the characteristic diagram Figure 8.16. The polymer slug speed, u/ϕ , is greater than the thermal front speed, Γu , and hence the first polymer will begin to gel on entering the formation. However, the latter part of the polymer slug, released at times $t > 0$, will need to travel through the porous medium some distance to reach the thermal front

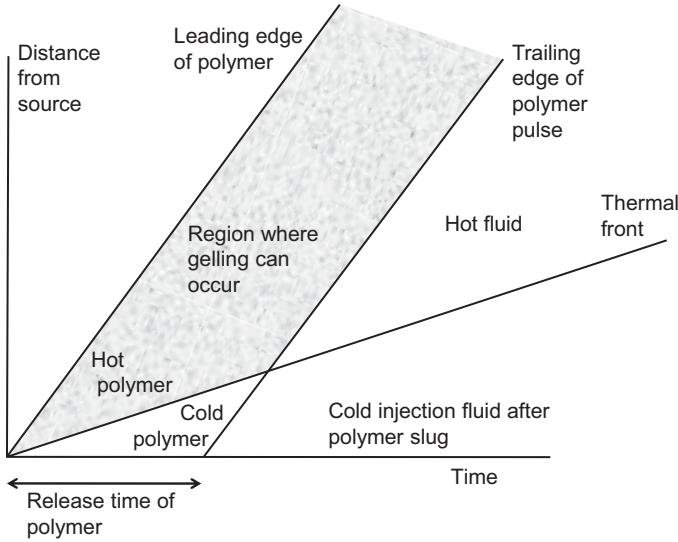


Figure 8.16 Characteristic diagram of a polymer which gels as a result of passing through a thermal front. Note that once gelled, we assume the polymer is immobile and that the gelling reaction is irreversible so the polymer remains in place.

prior to commencing gel formation (Figure 8.16). We assume in this model that the polymer can migrate through the gelled zone, and that the reaction is not reversible on the timescale of the flow. For example, polymer released at time t_o , where $0 < t_o < t_1$, will migrate through the porous rock with interstitial speed u/ϕ catching the thermal front, of speed Γu , at time $t_T(t_o)$ and position $x_T(t_o)$ say, where

$$x_T(t_o) = \Gamma u t_T(t_o) = u(t_T(t_o) - t_o)/\phi \tag{8.28}$$

At this point the polymer is heated up and the gelling process then commences. As this parcel of fluid migrates forward through the formation ahead of this point, it remains hot and the concentration of ungelled polymer, c , will wane as it continues gelling with the rate constant λ . At the time $t_T(t_o)$, the initial fraction of the polymer slug, released in the time interval $0 < t < t_o$ will have travelled ahead of the thermal front, and so this polymer will be undergoing the gelling process. The polymer released after time, t_o , does not catch up with the thermal front until it has travelled to points further from the source, $x > x_T(t_o)$ (Figure 8.16). The trailing edge of the polymer slug reaches the thermal front at the point $x_T(t_1)$ and for points further downstream from the source than this, the gel which forms in the matrix will have contributions from all the polymer initially released (Figure 8.16).

In the limit of small dispersion and small thermal diffusivity, the solutions for the concentration of the polymer in the liquid, and for the concentration of gel which forms from the solution, beyond the thermal front, are found by the method of characteristics,

following each parcel of polymer as it travels beyond the thermal front. At time t , the concentration of ungelled polymer carried by the liquid, at the position $x > x_T(t_o)$ where

$$x_T(t_o) = \frac{\Gamma u t_o}{(1 - \phi \Gamma)} \quad (8.29)$$

downstream from the source varies with the time of release $t_o = t - \phi x/u$ according to

$$c(x, t) = c_o \exp \left[-\frac{\lambda \phi}{u} \left(x - \frac{\Gamma u t_o}{(1 - \phi \Gamma)} \right) \right] \quad (8.30)$$

where $t_o = t - \phi x/u$, $0 < t_o < t_1$

If $t > \phi x/u + t_1$ or $t < \phi x/u$ there is no polymer at position x (see Figure 8.16).

The final concentration of gelled polymer in the matrix a distance x from the source is found by integrating Eq. (8.27) in time at this value of x using the solution (8.30) for the concentration. For $x < x_T(t_1)$ we integrate over the interval $\phi x/u < t < t_T(t^*)$ where t^* is the time of release of that polymer which meets the thermal front at x , $x = x_T(t^*)$. For $x > x_T(t_1)$ we integrate over the interval $\phi x/u < t < t_T(t_1)$. This leads to the result

$$G(x) = c_o \frac{[1 - \phi \Gamma]}{\phi \Gamma} \left[1 - \exp \left(-\frac{\lambda \phi x}{u} \right) \right] \quad \text{if } x < \frac{u \Gamma t_1}{1 - \Gamma \phi} = d \quad (8.31)$$

$$G(x) = c_o \frac{[1 - \phi \Gamma]}{\phi \Gamma} \left[\exp \left(-\frac{\lambda \Delta T \phi x}{u} \right) \right] \left(\exp \left(\frac{\lambda \Delta T \phi d}{u} \right) - 1 \right) \quad \text{if } x > d \quad (8.32)$$

In the region $0 < x < x(t_1)$, the amount of gel progressively increases with distance, as more of the slug of polymer gels at that point, but beyond this the amount of gel then decreases, since the gel becomes progressively more depleted since it has already gelled at points closer to the source. This is shown in Figure 8.17.

The above picture of the migration and gelling of a polymer has neglected the effects of thermal diffusion and dispersion. These act to spread the active polymer zone, but if the polymer slug is of sufficient extent, $u t_1 / \phi$ compared to the dispersion and thermal diffusion scales, κ / u , D / u then the diffusion will only act to spread the boundary region of the polymer, rather than change the overall structure of the solution. Typically, κ / u is of order 0.1–1.0 m, and so with injection for longer than 1–2 hours, with $u \sim 10^{-5}$ m/s, dispersion will not dominate.

The solutions also assume that the polymer gel zone is stable to frontal instabilities, with the gelling reaction being irreversible. However, this may not always be the case, and if the gel can break down when the cold front migrates through the gel, that front may become unstable in a similar fashion to a dissolution front (Chapter 6), since the permeability is reduced by the advancing fluid. As a result, a series of channels may develop in which the water following the polymer slug can migrate through the polymer, reducing the potential effectiveness of the polymer treatment.



Figure 2.1 Photograph of the Kimmeridge source rock in the cliffs on the beach at Kimmeridge Bay, Dorset. The photograph also shows the active gathering station on top of the cliffs, at which oil from a deeper reservoir directly below is being produced at the surface. Photo courtesy of D. van Sommeren. A black and white version of this figure will appear in some formats.



Figure 2.4 Tullig Point, County Clare, Western Ireland. A distributary channel illustrating the highly layered nature of a deltaic environment. A black and white version of this figure will appear in some formats.

(a)



(b)



(c)



Figure 2.3 (a) Kilbaha Bay, County Clare, Western Ireland. A multilayered turbidite deposit illustrating how the sand layers are separated by smaller grain-size shale rock which acts as a seal between layers. (b) Cliffs on the coast near Kilbaha Bay, illustrating the laterally extensive stacked turbidite deposits, interspersed with thin layers of seal rock. (c) Loop Head Cliffs, County Clare, Western Ireland, showing a series of laterally extensive distal turbidite fan deposits. Note the fold in the layers at the right-hand side of the photograph.

(a)



(b)



(c)



Figure 2.5 Photograph of the Bridport Sandstone, Dorset, UK. (a) Panoramic view of the cliffs and (b) a close-up showing the complexity of the layering, with each layer being in the range of 2–5 m thick; (c) close-up of a single layer in the sequence bound above and below by cemented horizons. Photograph courtesy of D. van Sommeren. A black and white version of this figure will appear in some formats.

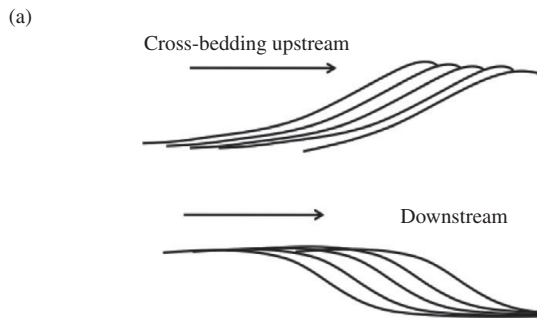


Figure 2.6 (a) Cartoon of cross-bed formation owing to deposition migrating upstream or downstream. Illustration of cross-bedding on walls of (b) Glen Canyon, USA, and (c) in the Tabernas Basin, Spain. The bedding has a very fine scale and variable direction relative to the strata leading to potentially complex flow trajectories through the formation. A black and white version of this figure will appear in some formats.

(a)



(b)



(c)



Figure 2.8 (a,b) Photographs of a fluvial deposit, Dingle Peninsula, Ireland, illustrating the intricate pattern of cross-bedding, and the local variability in grain sizes and layer permeability. The lower panel illustrates a fault running orthogonal to the bedding direction. (c) Photograph of very heterogeneous layering in a sedimentary deposit at Point Lobos, California, showing pebble laden deposits, of order centimeters in size, interleaved with fine sandy deposits. A black and white version of this figure will appear in some formats.

(a)



(b)



(c)



(d)

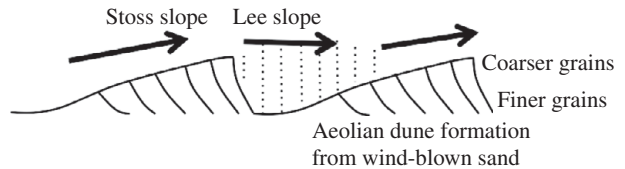


Figure 2.9 (a–c) Photograph of an aeolian deposit in the Dingle Peninsula, Western Ireland, illustrating (a) the lee side of the slope, with multiple parallel layers and (b,c) close-ups of the layering showing the highly stratified nature of the layering on both metre and centimetre scales. (d) Schematic to illustrate the formation process of aeolian dune formation, with successive layers forming as the dune migrates. A black and white version of this figure will appear in some formats.

(a)



(b)



(c)



Figure 2.10 Photograph of (a) a small sand-injection structure breaking through on overlying layer of sediment; (b) a side view of a small-scale deformation structure in the formation, with a vertical scale of about 50 cm and length 1 m; (c) an illustration of the folding of sediment layers following deposition in a turbidite deposit in Tabernas Basin, southern Spain. Here the scale is about 15–20 m. A black and white version of this figure will appear in some formats.

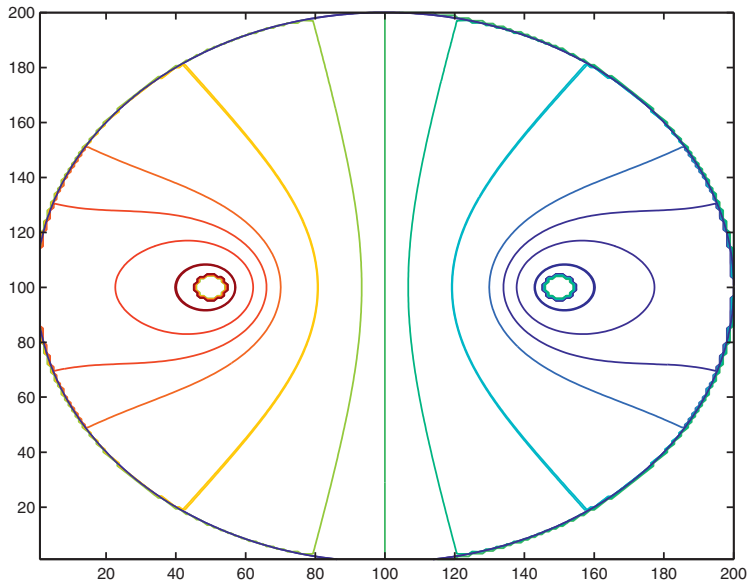


Figure 3.2 Potential field for a source–sink flow confined within a circular boundary. Source and sink are located along a common diameter, each midway between the centre and the circumference of the model reservoir. A black and white version of the figure will appear in some formats.

(a)



(b)

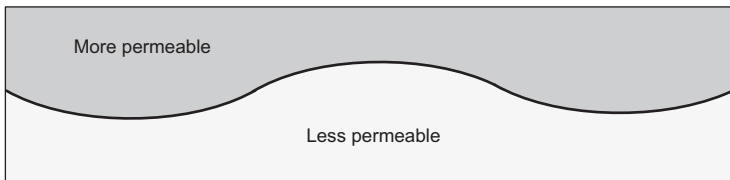


Figure 3.9 (a) Illustration of a wavy horizon in a shallow marine sediment in the Dingle Peninsula, South West Ireland; (b) cartoon of a sinuous interface used in the modelling of effective permeability. A black and white version of this figure will appear in some formats.

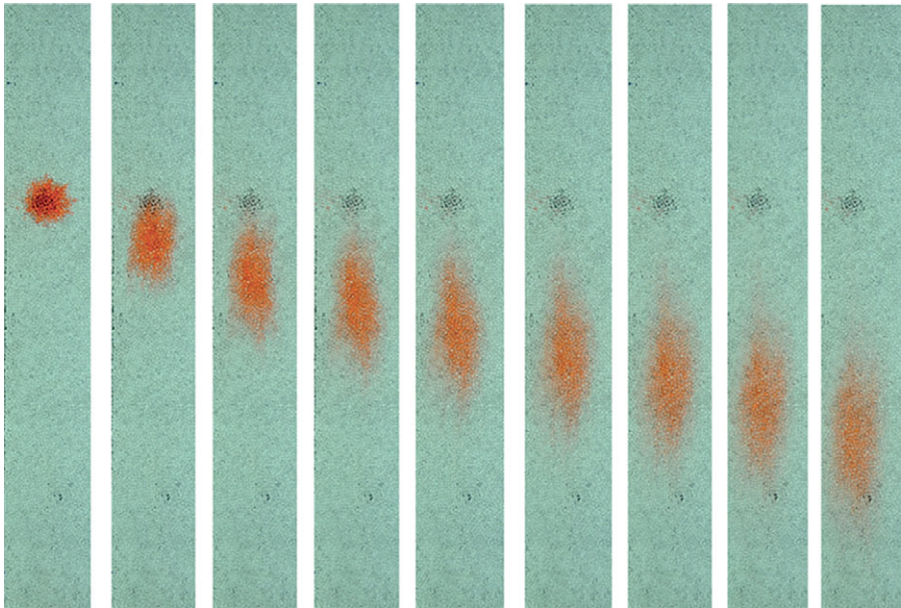


Figure 5.1 Illustration of the longitudinal and transverse dispersion of a parcel of dye as fluid migrates through a porous layer. The flow is from top to bottom, and the dye streak is seen to spread much more rapidly in the along-flow longitudinal direction than the cross-flow transverse direction. Photograph courtesy of C. Otto. A black and white version of this figure will appear in some formats.

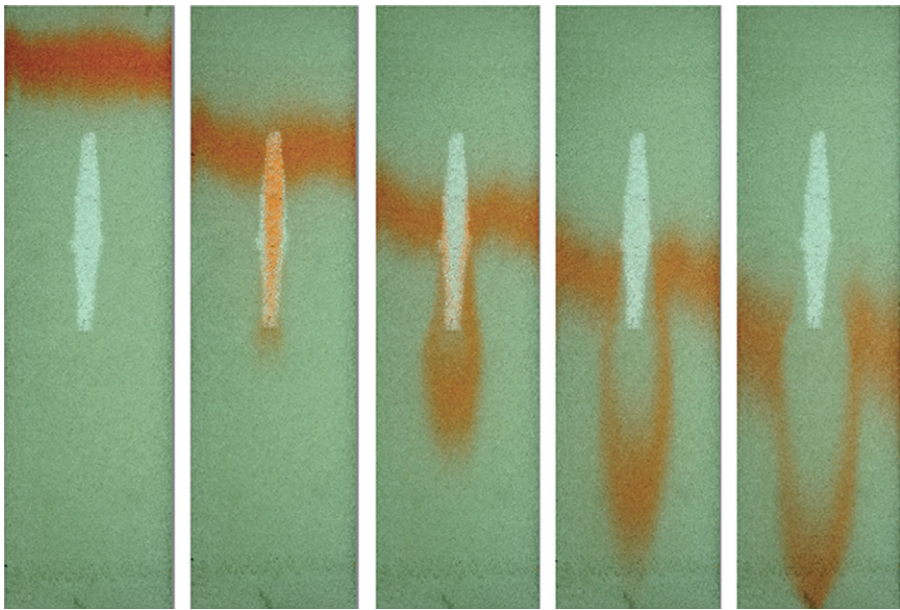


Figure 5.8 Experiment in which fluid is injected from the top and travels down through a thin bead pack which includes a high permeability lens. The lens may be identified as the bright elliptical region in the centre of the porous layer. The figure illustrates the migration and distortion of an initially horizontal line of red dye as it moves through the high permeability lens. The flow short-circuits into the lens, and then emerges downstream leading to considerable dispersion. Photographs courtesy of C. Otto. A black and white version of this figure will appear in some formats.

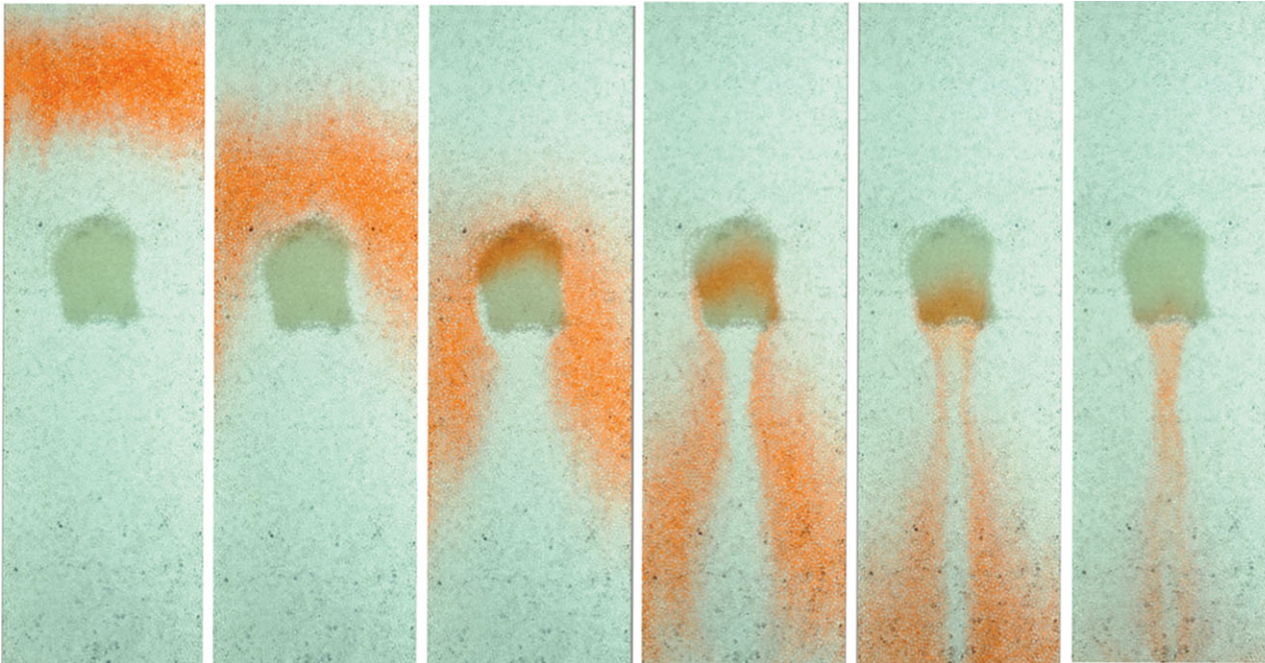


Figure 5.9 Experiment in which fluid is injected from the top and migrates down through a high permeability porous layer which includes a low permeability region, which may be identified as the darker zone in the centre of the cell. The figures show the migration and distortion of an initially horizontal line of red dye through the low permeability lens in a flow which is uniform far upstream and far downstream. The dye is retarded in the lens, and then emerges in a thin plume trailing behind the original red dye front. Photographs courtesy of C. Otto. A black and white version of this figure will appear in some formats.

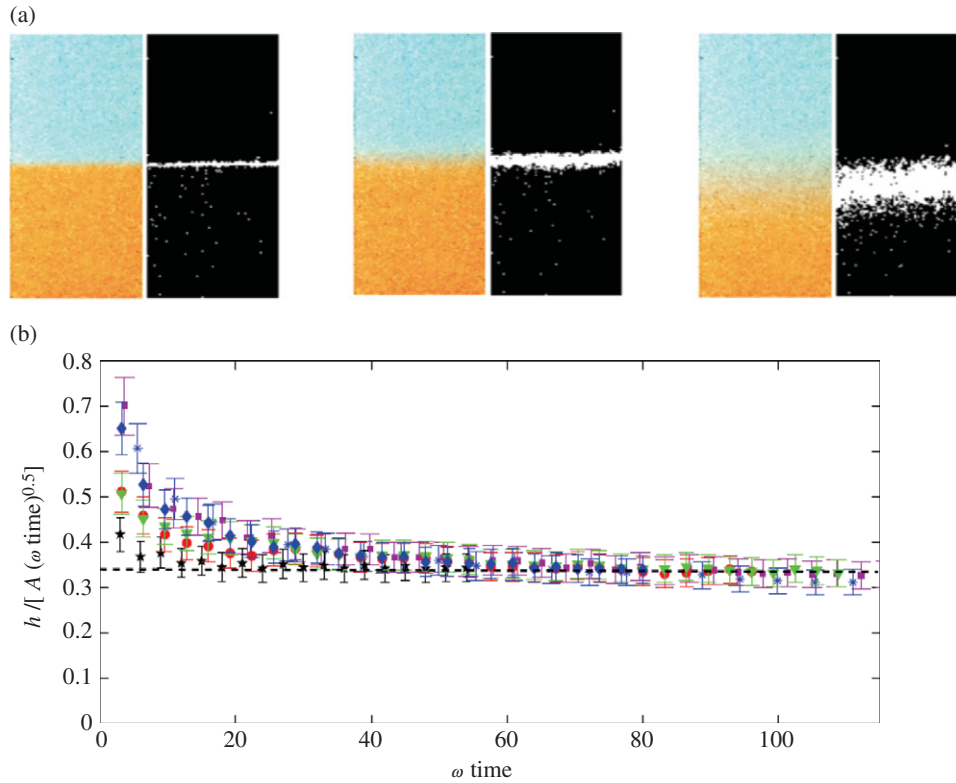


Figure 5.12 (a) Illustration of the mixing at an interface with an oscillatory flow, showing the broadening of the intermediate coloured zone between the lower and upper layer fluid, with successive oscillations, and a black–white image illustrating the growth of the region of intermediate concentration. (b) Estimate of the dispersion coefficient, as compared to laboratory data, by comparing the thickness of the mixed zone h with $a(\omega t)^{1/2}$. Figure courtesy of C. Otto. A black and white version of this figure will appear in some formats.

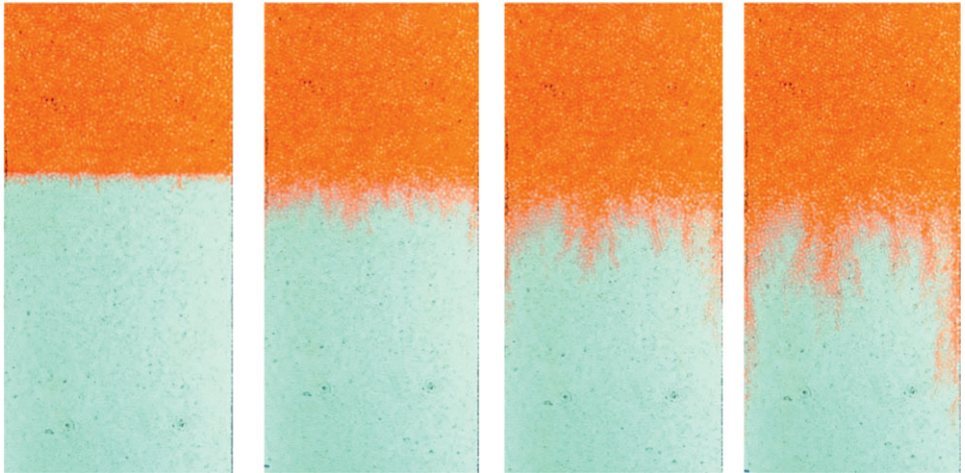


Figure 6.1 Development and evolution of miscible fingers in a porous bead pack as water displaces a more viscous sugar solution. The motion is in the downwards direction in the figure. Small fingers of the red water migrate through the sugar solution in an irregular pattern, developing a zone of intermingled fluid, which grows with time. There is little mixing of the phases during this experiment owing to the relatively long time for diffusion across the fingers compared to the time of the experiment. Figure courtesy of C. Otto. A black and white version of this figure will appear in some formats.

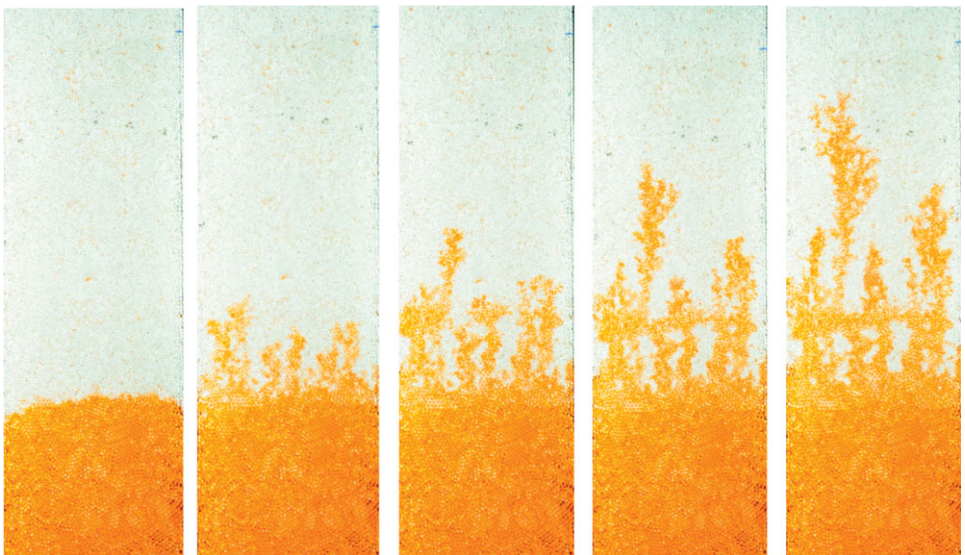


Figure 6.2 Viscous fingering produced as water (red) migrates upwards and displaces oil (clear) in a bead pack of width 10 cm. The intermingled zone grows with time. Figure courtesy of C. Otto. A black and white version of this figure will appear in some formats.

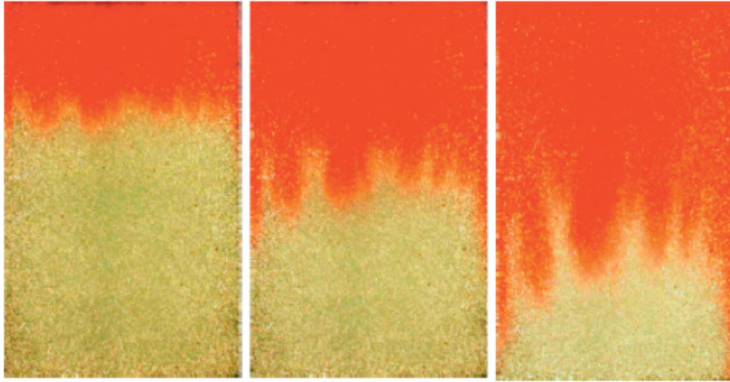


Figure 6.4 An example of gravitational instability as a layer of saline dense red liquid migrates downwards into a layer of less dense clear fresh water in a bead pack. A black and white version of this figure will appear in some formats.

(a)



(b)

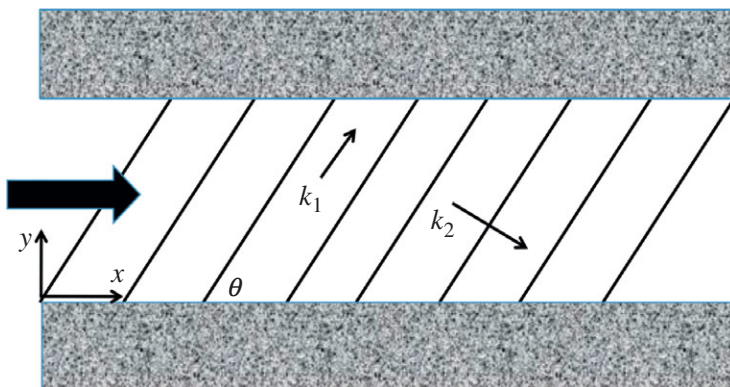


Figure 3.16 (a) Photograph of cross-bedding in Glen Canyon, USA. The horizontal scale of the figure is about 10 m and (b) schematic diagram of cross-bedded deposit, with angle θ between the orientation of the bedding and the impermeable bounding rock, as used in the model prediction of cross-flow. A black and white version of this figure will appear in some formats.

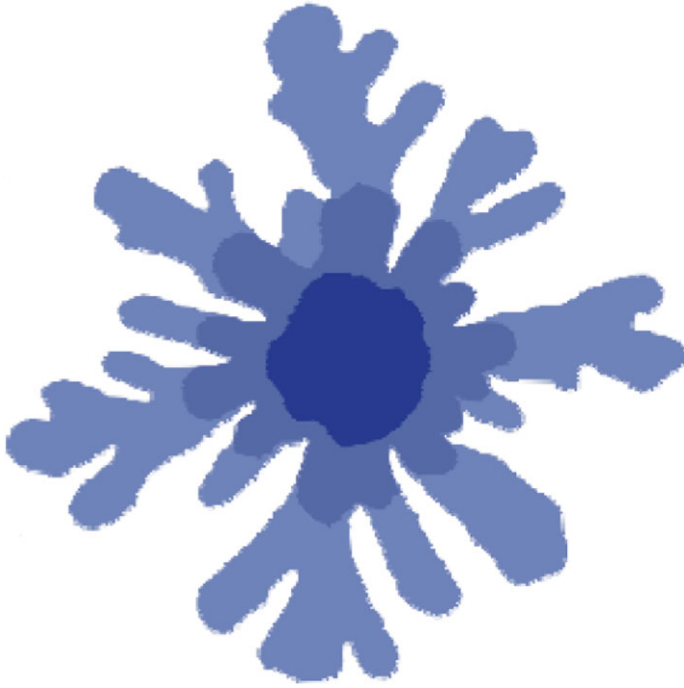


Figure 6.6 Evolution of a viscous fingering instability in a circular Hele–Shaw cell. Three images, in different shades of blue, are superposed to illustrate the evolution with time of the fingers. A black and white version of this figure will appear in some formats.

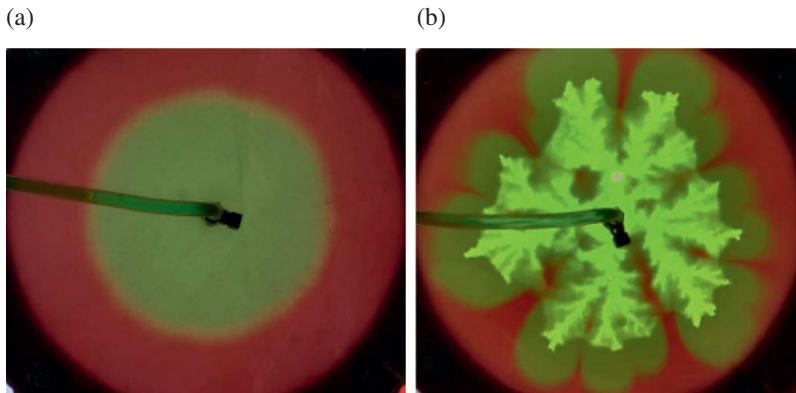


Figure 6.10 Instability of flow in an unconsolidated porous layer. At low flow rates (a) the fluid migrates as a Darcy flow, whereas at higher flow rates, the grains are mobilised and channels develop as the grains are displaced to the side of the flow (b). Photograph courtesy of G. Del Ioio. A black and white version of this figure will appear in some formats.

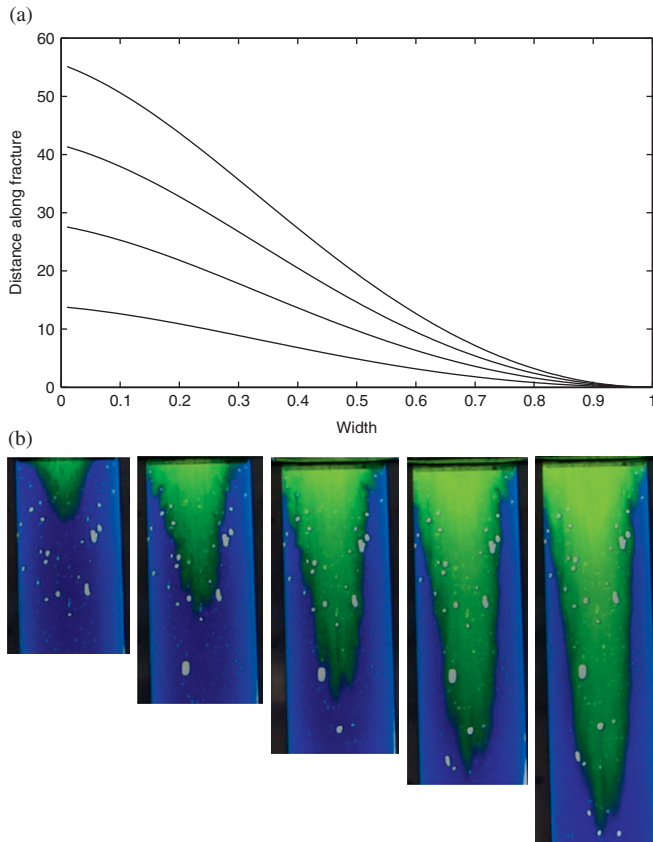


Figure 6.13 (a) Variation of $x(s, t)$ as a function of s for 4 times following the injection of fluid into the cell. (b) Series of photographs of the time evolution of a laboratory experiment, illustrating the displacement of blue glycerol with green corn syrup in a Hele–Shaw cell in which the gap varies from 1 mm at the edge of the cell to 2 mm at the centre of the cell. A black and white version of this figure will appear in some formats.

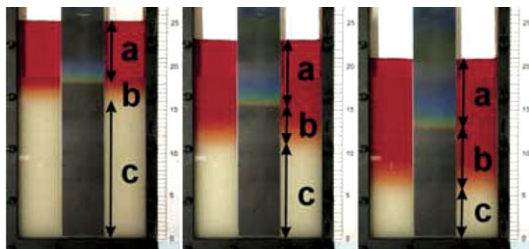


Figure 8.2 Illustration of the migration of a thermal front within a porous layer. Hot red fluid is injected at the top of the bead pack and the fluid migrates down through the pack with the red front illustrating the advance of the fluid. The advancing temperature front is recorded by the change in colour of a liquid-crystal strip in contact with the bead pack; the region in which the liquid-crystal strip has a change in colour migrates down through the bead pack, but at a slower speed than the red dye owing to the thermal inertia. After Menand *et al.* (2003). A black and white version of this figure will appear in some formats.

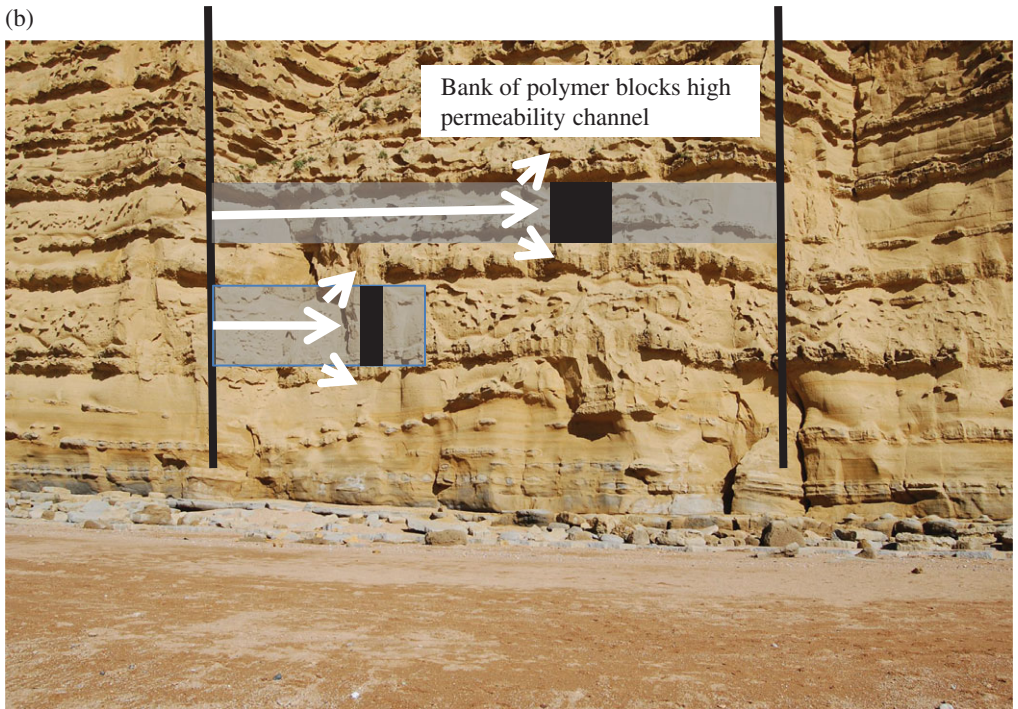
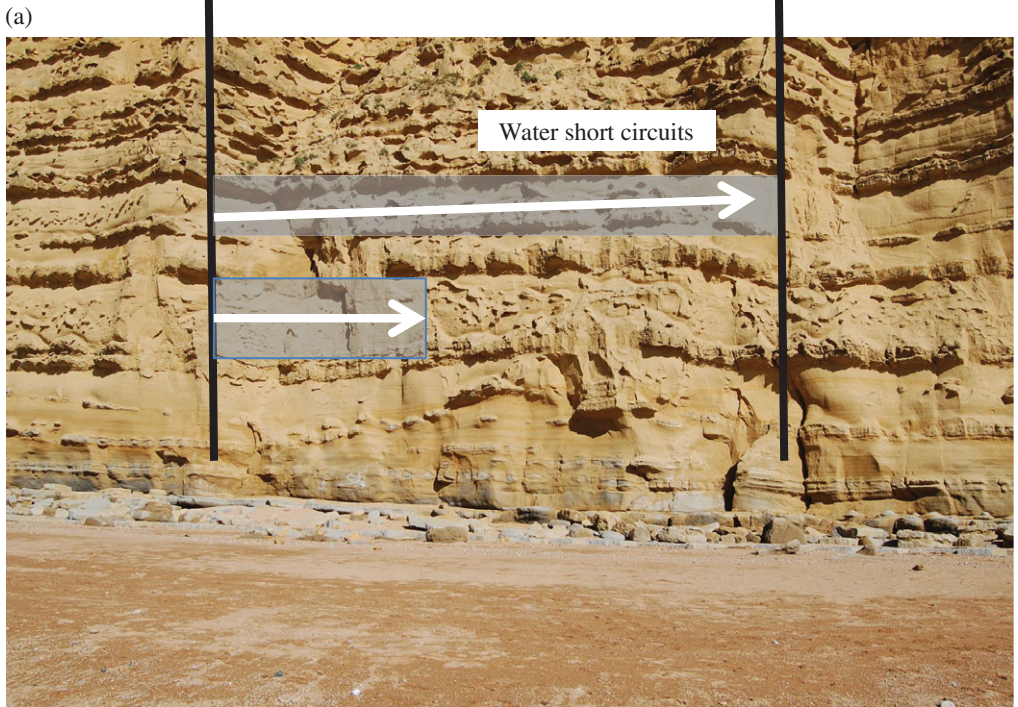


Figure 8.12 Schematic of the injection of polymer to plug or reduce the permeability of a highly permeable layer, following recovery of oil from this layer. A black and white version of this figure will appear in some formats.

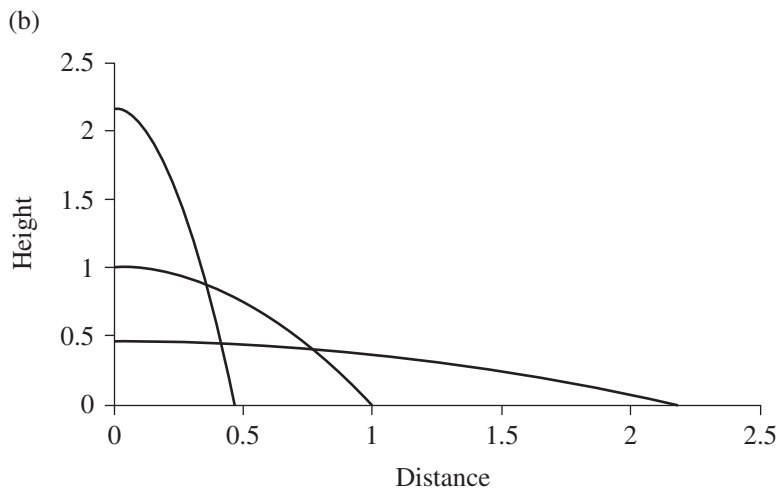
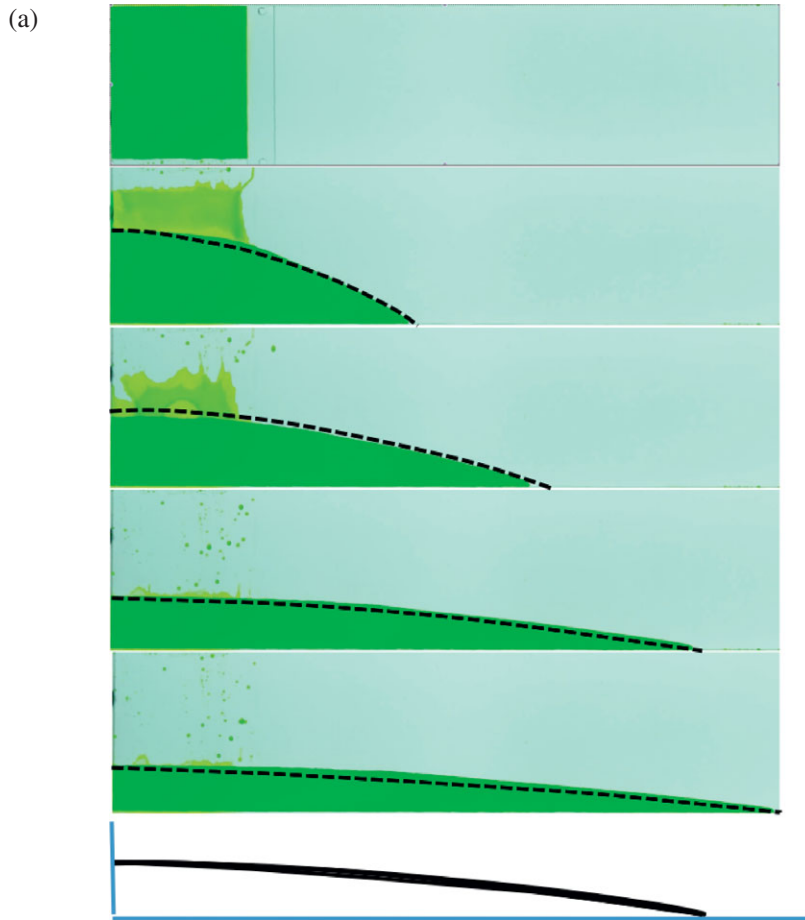


Figure 9.6 Shape of the evolving gravity-driven flow produced by the release of a finite volume of fluid in a two-dimensional Hele–Shaw cell. Note in the early images, there is a thin film left on the plates which gradually drains with time, although at long times, as the current speed decreases, this draining film becomes very small. Photo courtesy of Caren Otto. A black and white version of this figure will appear in some formats.

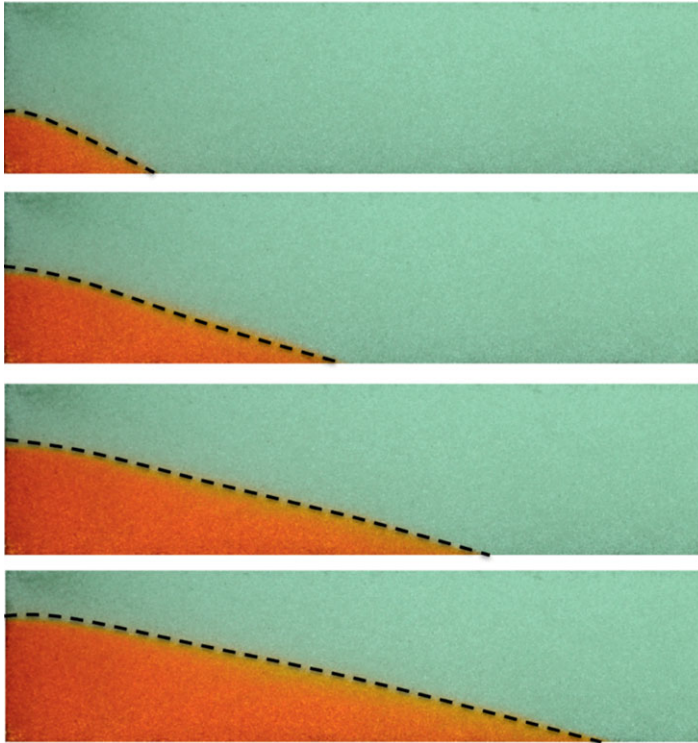


Figure 9.7 Shape of the evolving gravity-driven flow produced by a constant flux of fluid supplied to a two-dimensional bead pack. A black and white version of this figure will appear in some formats.

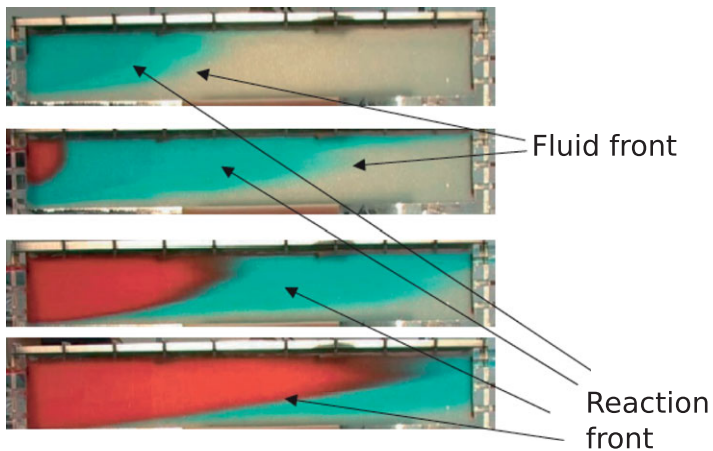
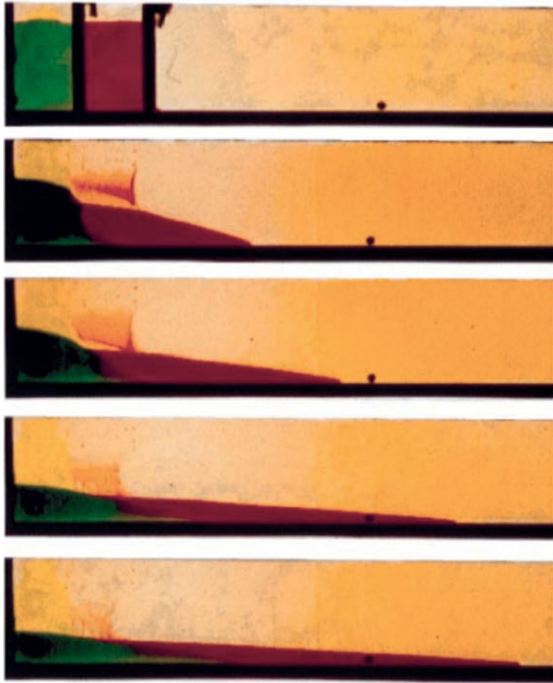


Figure 9.27 Illustration of a reaction front migrating through a confined porous layer. The reaction is driven by the injection of fresh water which reacts with salt powder in the porous layer. The original fluid in the formation is saturated salt solution in equilibrium with the salt powder, and on reaction the injected fluid density matches that of the original formation fluid. The colour of the injected fluid is changed from blue to red to help visualise the flow. After Verdon and Woods (2007). A black and white version of this figure will appear in some formats.

(a)



(b)

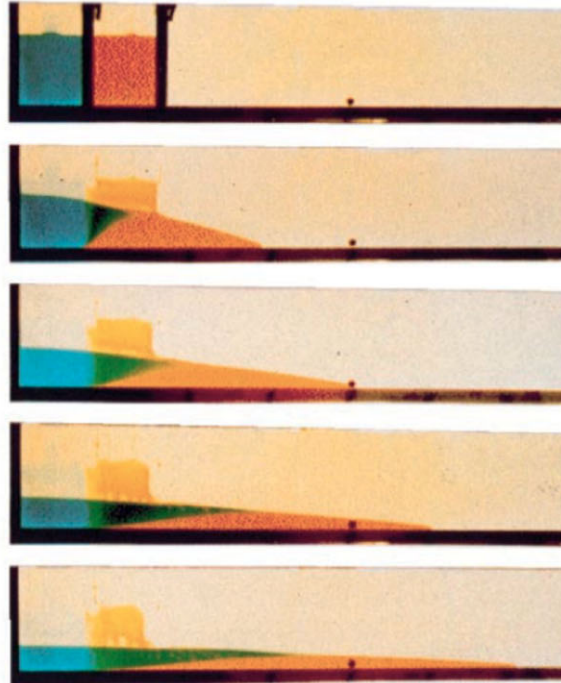


Figure 9.13 Illustration of the motion of a two fluid gravity current in a Hele–Shaw cell showing the cases in which the less dense fluid is also (a) less viscous and (b) more viscous (after Woods and Mason, 2000). A black and white version of this figure will appear in some formats.

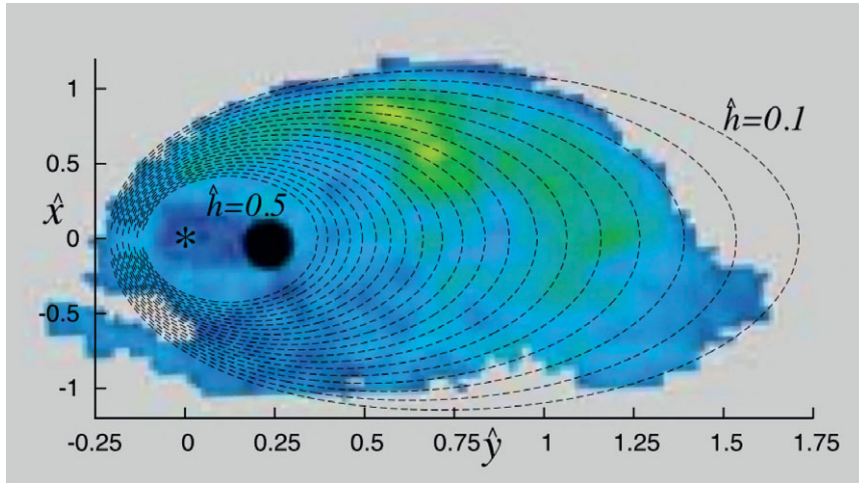


Figure 9.26 Comparison of the upslope draining plume model Eq. (9.99) with the shape of the plume in Horizon 1 observed from seismic data at the Sleipner field in the North Sea. After Farcas and Woods (2013). A black and white version of this figure will appear in some formats.

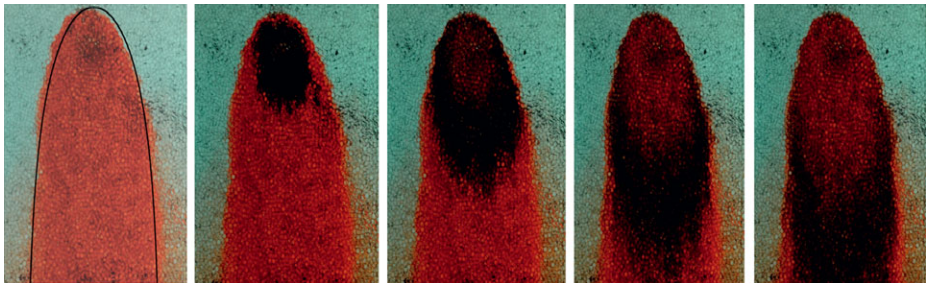


Figure 10.7 Experiment in a porous bead pack illustrating the steady plume structure near the injection point, when saline fluid is injected into a bead pack initially containing fresh water. In the first panel, a solid line, corresponding to the theoretical model of the outer boundary of the plume is compared with the experiment. In the following panels, a pulse of dark dye is added to the injected plume fluid and the evolution of the dye front may be seen as it flows from the source and adjusts to the flow far downstream.

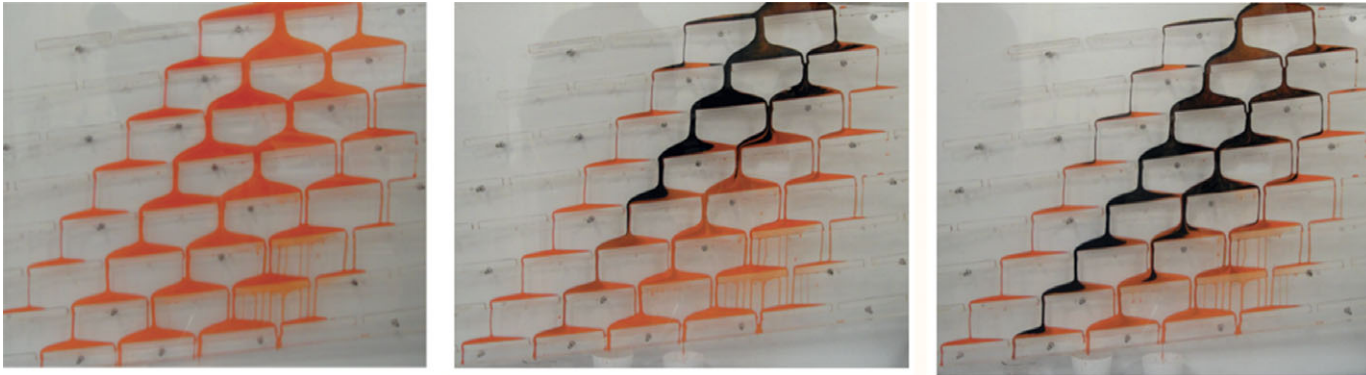


Figure 10.10 Flow of a plume around a series of inclined baffles as shown by a Hele–Shaw cell in which there is a series of inclined baffles, over which a cloud of dense red syrup flows. By changing the colour of the dye in the supply fluid from red to dark blue part way through the experiment, the dispersion and non-uniform speed of the flow may be observed. The darker dye migrates faster in the centre of the plume than at the edges. A black and white version of this figure will appear in some formats.

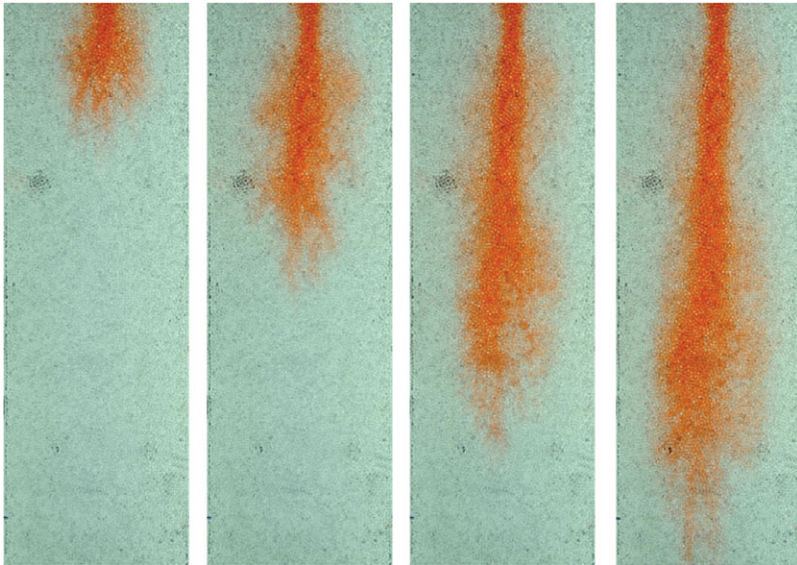


Figure 10.6 Time evolution of a plume of saline fluid, produced by a constant fluid injection rate, descending into a bead pack initially saturated with fresh water. A steady plume tail develops, feeding the dispersively mixing head. This head appears to leave a halo of intermediate density fluid around the continuing tail. Photograph by Caren Otto. A black and white version of this figure will appear in some formats.

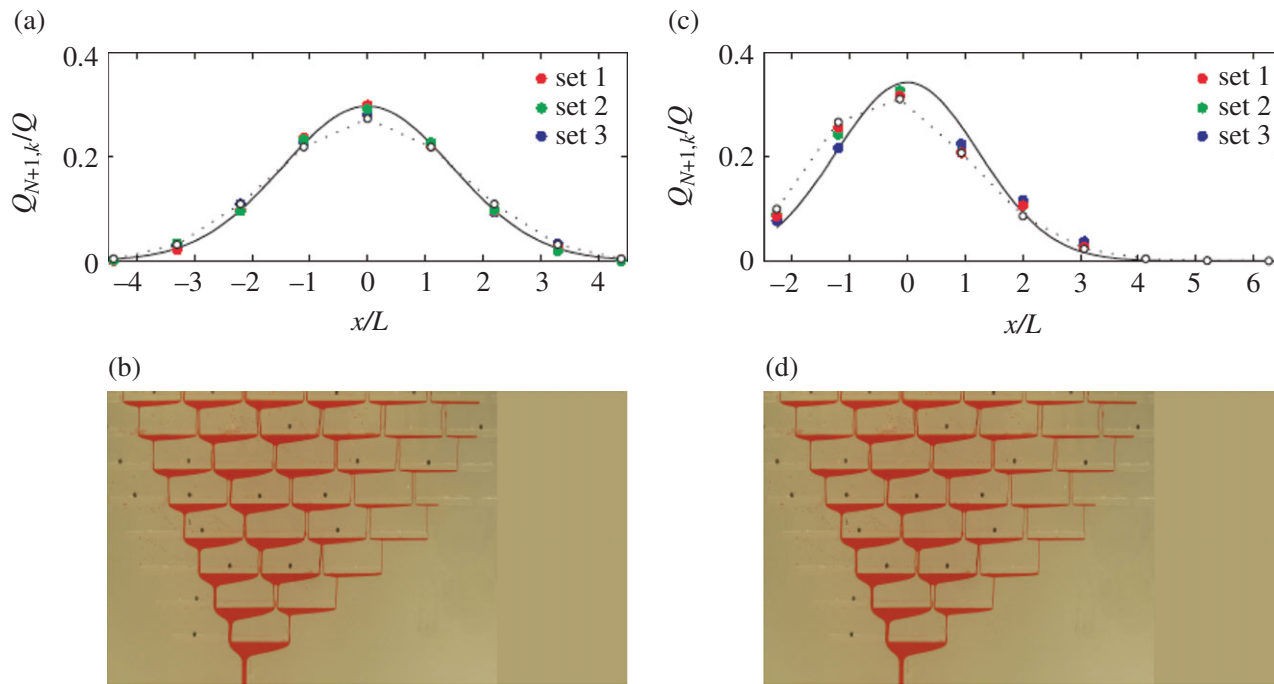


Figure 10.8 Dispersion of a vertical plume around a series of baffles. In this example, the system is shown upside-down, as for the dispersal of a CO_2 plume through a layered, fractured reservoir. Two experiments correspond to the release of fluid in a symmetric and an axisymmetric distribution of baffles showing the pattern of flow and the spatial distribution of the volume flux after passing through the baffles. After Hesse and Woods (2010). A black and white version of this figure will appear in some formats.

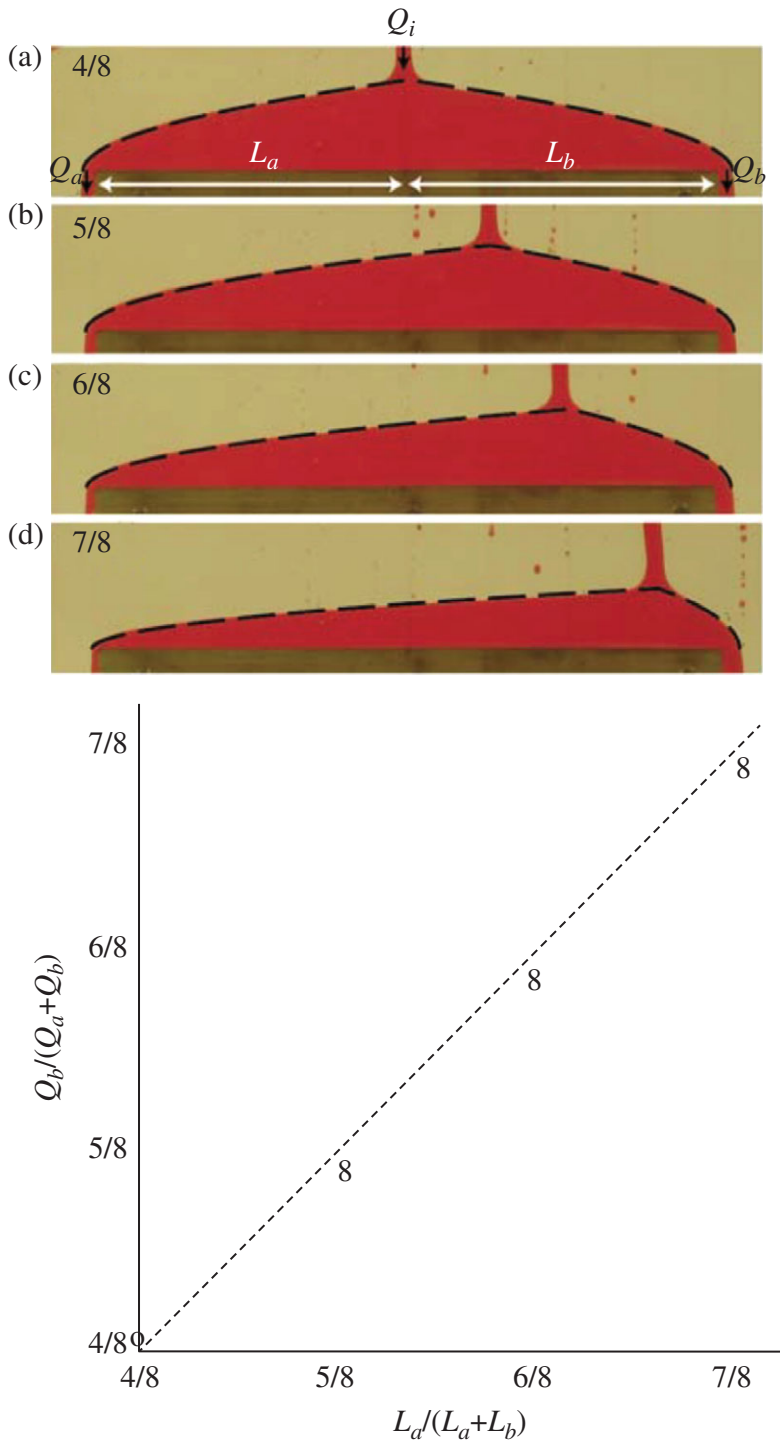


Figure 10.9 Flow past a baffle in a Hele–Shaw cell, with different locations of the impinging plume relative to the centre of the baffle. The figure shows the measured flux and the predicted flux on the longer side as a function of the position of the plume relative to the centre. A black and white version of this figure will appear in some formats.

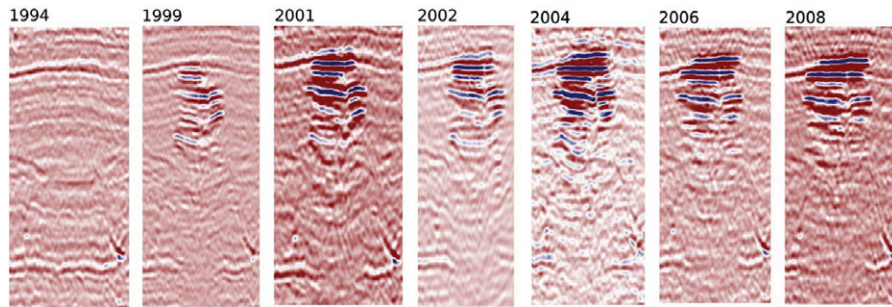


Figure 10.2 Illustration of the seismic reflection profile associated with the migrating cloud of CO₂ spreading in the Sleipnir field in the Norwegian North Sea. Seven images are shown at progressively later times following the start of the injection of CO₂, indicating the migration pattern of the CO₂. After Boait *et al.* (2012). A black and white version of this figure will appear in some formats.

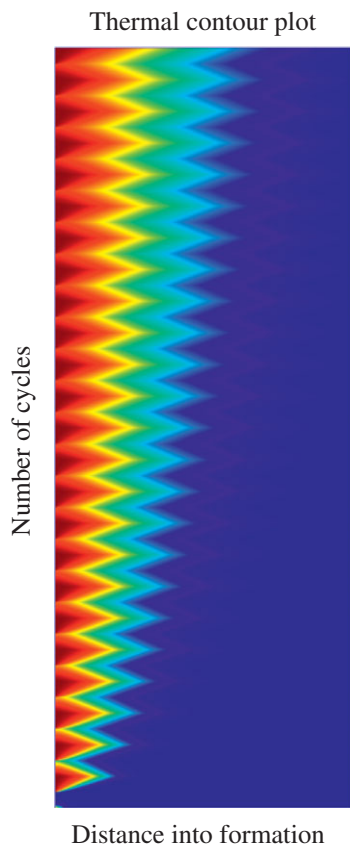


Figure 11.14 Gradual spreading of the injected thermal energy (horizontal axis) to form a region of hot rock over 23 cycles of injection and extraction, with time shown on the vertical axis. The thermal signal gradually diffuses into the far field, ahead of the maximum extent of the injection fluid.

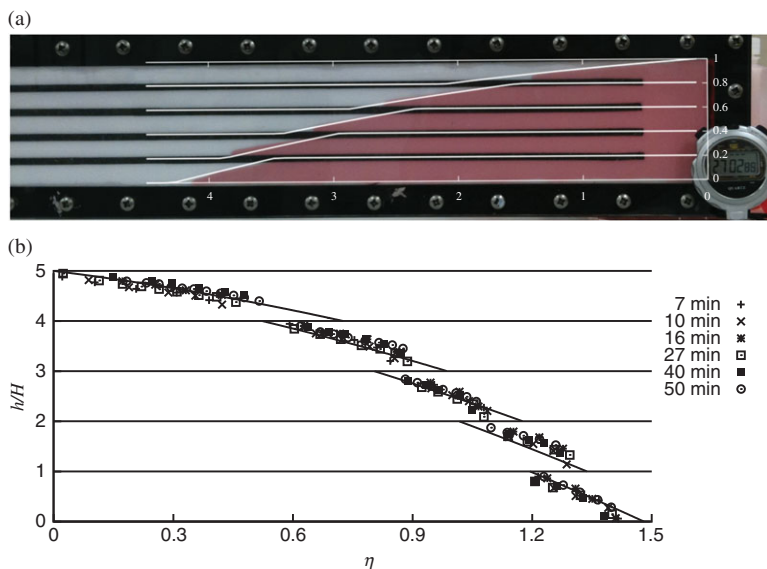


Figure 10.12 (a) Flow in a five-layer Hele–Shaw cell as a model of the dispersal of the flow in a multi-layered rock. The white line shows the prediction of the model for the dispersal in each of the layers. (b) Experimental measurements at a series of times scaled by the similarity coordinate, showing the collapse to the self-similar solution. (b) courtesy of A. Farcas. A black and white version of this figure will appear in some formats.

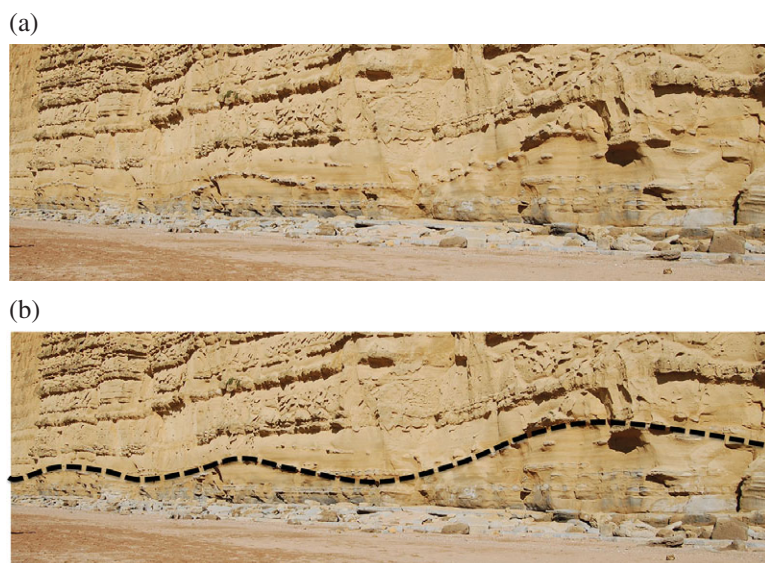


Figure 10.15 Illustration of a wavy irregular boundary between two layers of sediment, from West Bay, Bridport, Dorset; (b) illustrates the outline of the wavy layer. The crest-to-crest distance is about 10 m. A black and white version of this figure will appear in some formats.

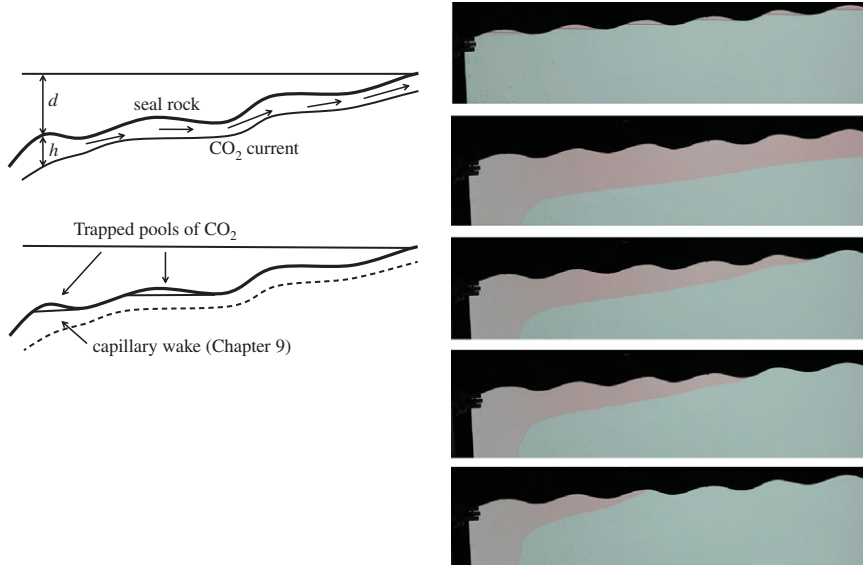


Figure 10.16 Time evolution of a current of red glycerol running downslope over the wavy bed, illustrating the thinning and thickening of the flow over the wavy topography, as the flow sets up a steady state (photographs are shown upside down). The region wetted by the fluid represents the region where there will be capillary trapping. In the last image, the source is removed and the current allowed to drain downslope. The regions behind each of the crests on the wavy boundary is shown by the dotted line in the bottom panel, illustrate the regions where there are trapped pools of fluid remaining after the source is removed. A black and white version of this figure will appear in some formats.

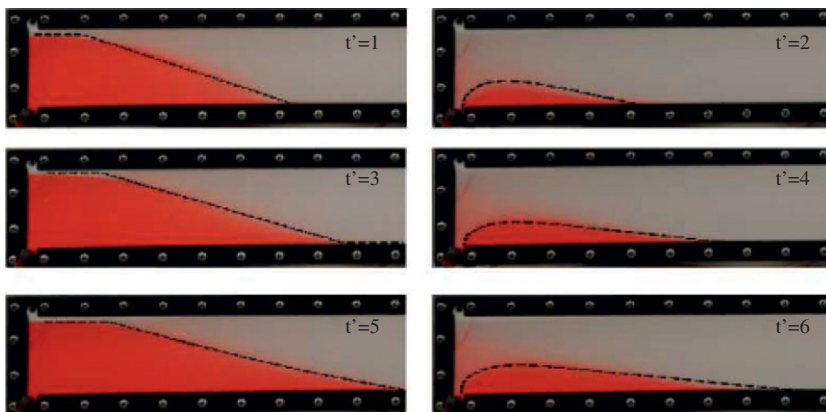


Figure 11.17 Experimental measurement of the current at the end of the injection and extraction phases of the first 3 cycles; the experiment was carried out using a Hele–Shaw cell with two layers of glycerol, the lower of which was more dense and dyed red. This lower fluid was periodically injected into the cell. After Dudfield and Woods (2014). A black and white version of this figure will appear in some formats.

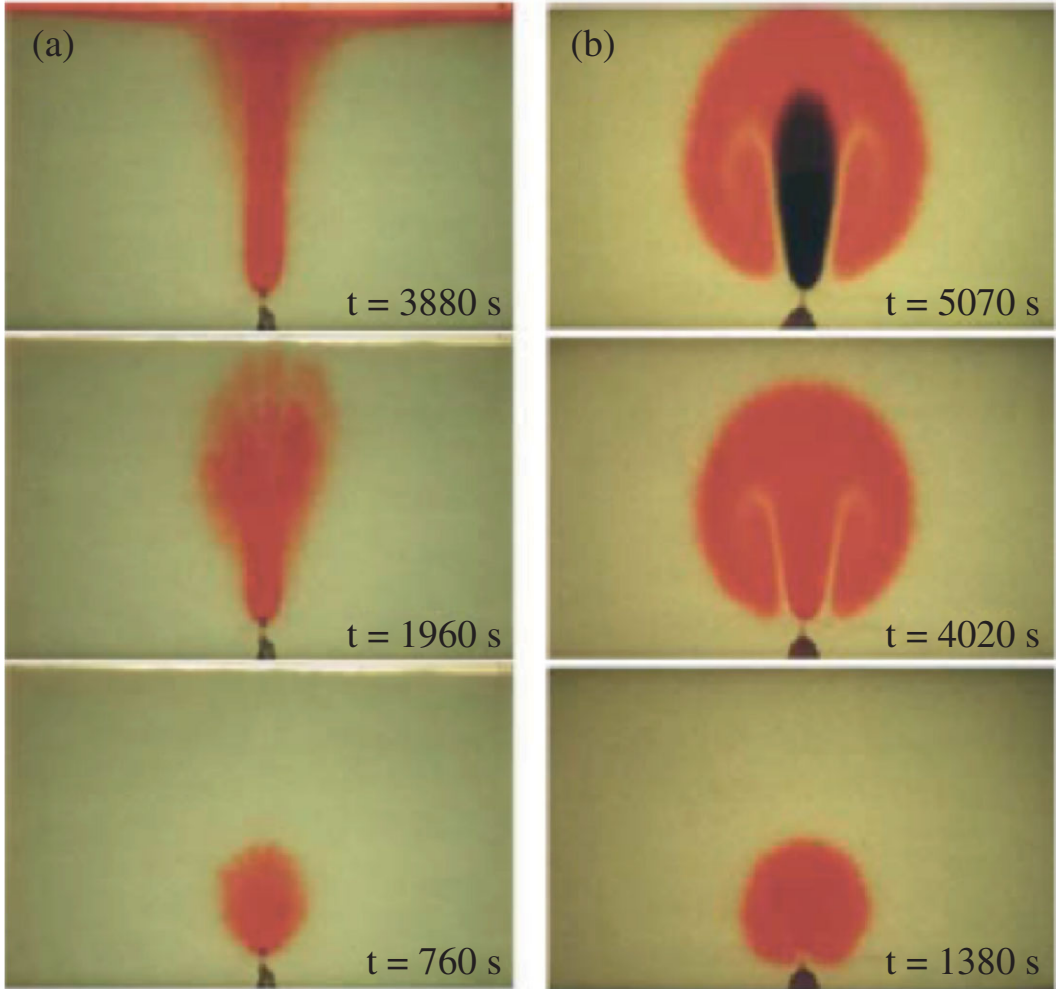


Figure 11.8 Three frames, at successive times illustrating the buoyancy-driven flow in a porous medium driven by (a) a fresh plume migrating through an initially saline solution of the same temperature, and (b) a hot plume migrating through an initially cold fluid of the same composition. During the experiment, the colour of the injected fluid is changed from red to blue to help visualise the flow pattern. After Menand *et al.* (2003). A black and white version of this figure will appear in some formats.

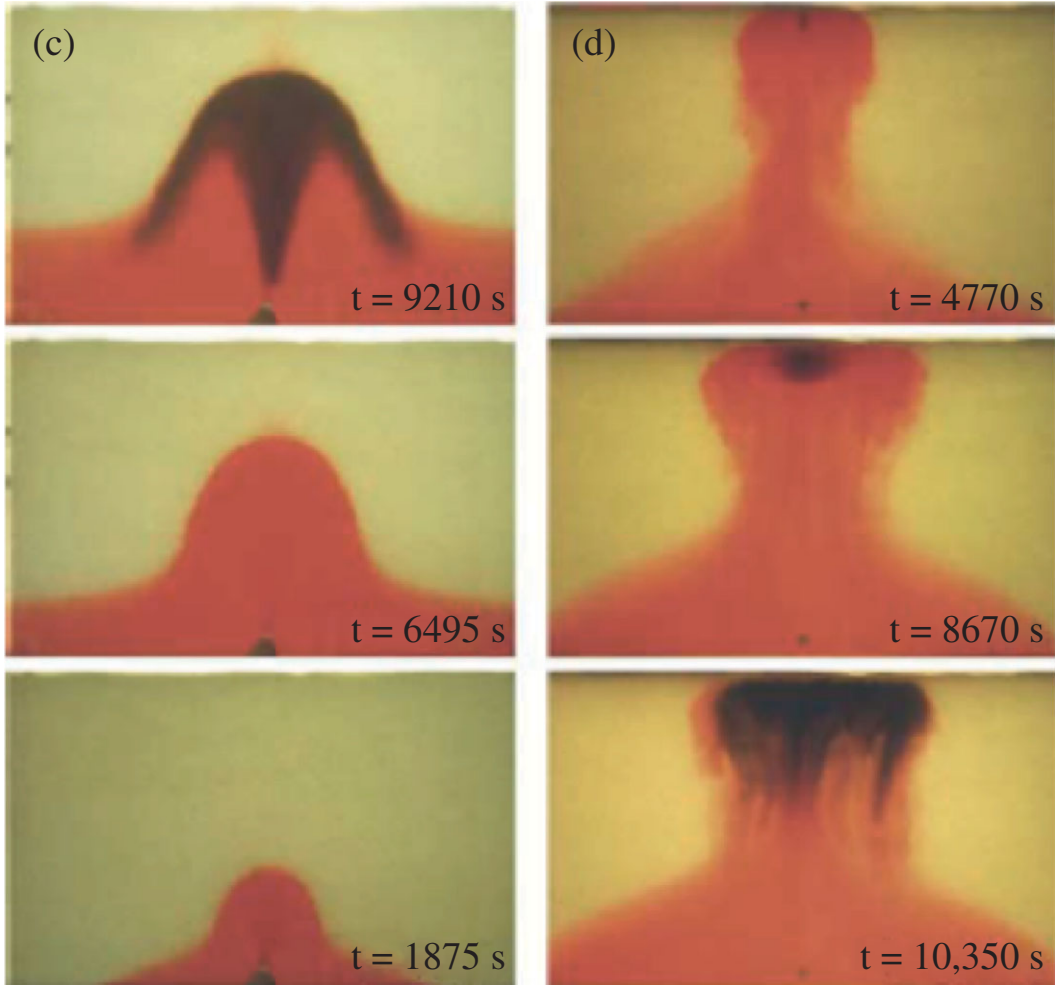


Figure 11.9 Three frames at successive times illustrating the buoyancy-driven flow of a hot, compositionally enriched injection fluid through a porous layer, in the case that the injection fluid is initially less dense than the original fluid in the porous layer. The fluid is injected from (c), the base (left-hand panels) and (d), the top of the layer (right-hand panels). During the experiment the colour of the dye in the injected fluid is changed from red to blue to help visualise the flow pattern. After Menand *et al.* (2003). A black and white version of this figure will appear in some formats.

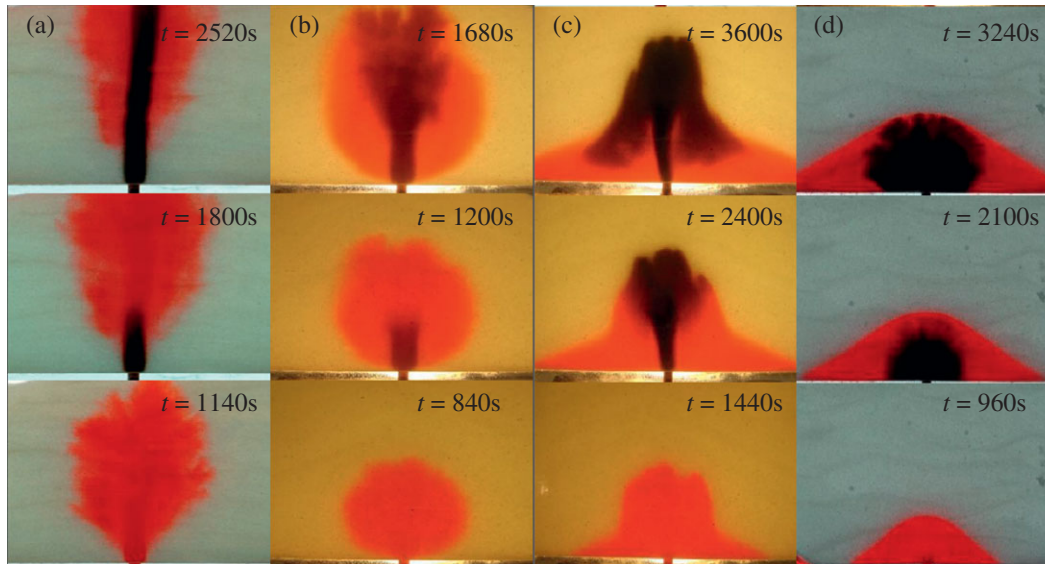


Figure 11.12 Figure illustrating the pattern of flow when a sugar–salt solution is injected into a bead pack saturated with a sugar–salt solution of different sugar content. The bead pack includes a small fraction of salt powder, and as the injected fluid enters the system it dissolves some of this salt, leading to a change in density. The different patterns of flow are illustrated by the sequence of three photographs in each of cases a–d. In a the injected fluid is less dense than the original solution in the bead pack both before and after dissolving the salt, and thereby forms a compositional plume; the halo around the centre of the plume denotes the earlier plume fluid once it has dissolved some of the salt and become of intermediate density between the formation fluid and the injected fluid. This rises more slowly than the more recent injection fluid which rises along the dissolution channel in the centre of the bead pack, until eventually reaching some salt higher in the bead pack. The flow pattern is visualised by changing the colour of the injected fluid from red to black during the experiment. In b the injected fluid is initially more buoyant but becomes neutral on reacting with the salt, and this is analogous to the thermal plume shown in Figure 11.8b. In case c, the injected fluid is initially buoyant but becomes dense on reacting with the salt powder, this leads to a dissolution channel which rises directly above the source, and then a collapsing fountain of dense fluid around the channel which feeds a laterally spreading gravity current on the base of the system. In d the injected fluid is initially dense, but becomes even more dense on reacting with the salt powder, therefore forming a dense laterally spreading gravity current. Photographs courtesy of Will Rayward-Smith. A black and white version of this figure will appear in some formats.

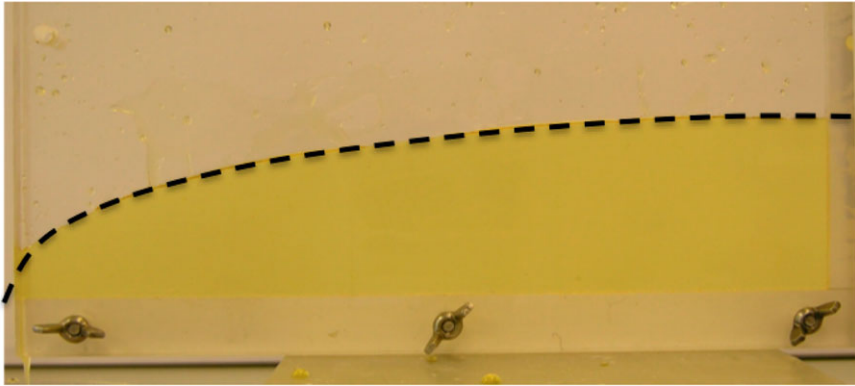


Figure 12.2 Analogue experiment of gas draining from a porous layer using syrup draining from a Hele–Shaw cell, with an initial constant depth in the cell. A black and white version of this figure will appear in some formats. After Farcas and Woods (2007).



Figure 12.12 Illustration of a shale sample showing the very layered, fine structure of the rock. A black and white version of this figure will appear in some formats.

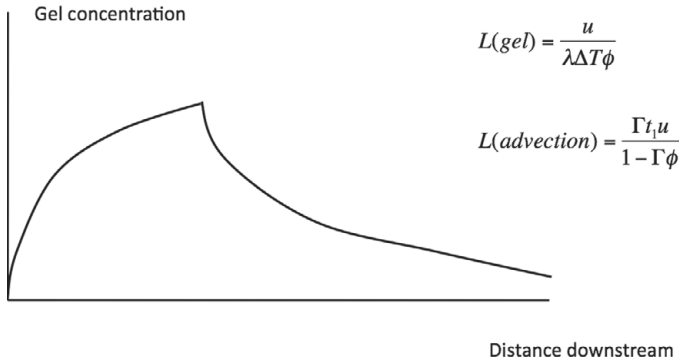


Figure 8.17 Illustration of the variation of the gel concentration with distance downstream from the source when a thermally sensitive polymer is released into the formation and begins to gel once it reaches a temperature threshold. The thermal front migrates at a constant fraction of the fluid speed. The mass of gel initially increases with distance, since near the source, only a fraction of the polymer gels, since the thermal front moves forward, while further from the source nearly all the polymer has passed the thermal front. In the far field, the gel concentration then begins to wane since the initial polymer pulse was finite.

8.10 Polymer injection into a multi-layer formation

At the outset to this chapter, we mentioned the role of polymers in diverting fluid within a reservoir so that the zones of high permeability from which water has been displaced can be blocked and subsequently the main flow arises through other layers. The effectiveness of such a strategy is dependent on whether the geological strata are connected or remain independent, and on the volume of the polymer slug injected into a system. In the previous models of polymer contained within an encapsulant, we assumed the encapsulant released the polymer after a time τ following injection, with the injection being a continuous process over time t_1 . The shape of the gel zone was then dependent on the kinetics of gelling, following the release of the polymer at the point $u\tau/\phi$ within the reservoir. However, one can also envisage a batch process, in which a volume of polymer is mixed with a volume of injection fluid prior to injection, and then pumped into the formation. In this case, if the encapsulant releases the polymer a time τ after being mixed with the injection fluid, then the polymer will spread out as a slug within the reservoir. The length of this slug d will be related to the injection volume, if for simplicity, we neglect effects of dispersion. The polymer will then become active at the same time. In the limit that the gelling, which occurs over a timescale $\tau_g = 1/\lambda$, is rapid compared to the time to travel a distance comparable to the length of the slug, $\tau_a = d\phi/u$, so $\lambda d\phi/u \gg 1$, then to leading order, the polymer gels on activation, producing a zone of length d of reduced permeability, k_G .

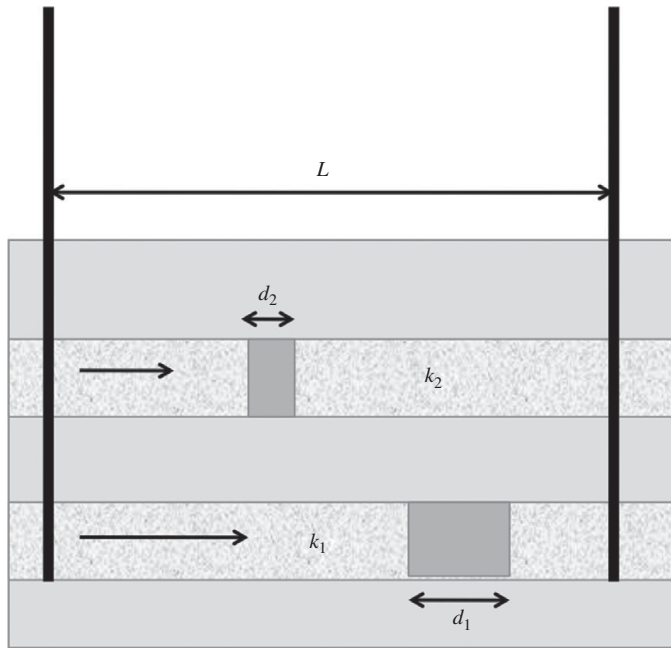


Figure 8.18 Schematic of the location of polymer gel in a two-layer system, in which one layer is of higher permeability and so takes up more of the polymer pulse. Figure 8.19 illustrates the resulting change in the permeability ratio of the two layers, following the placement of the polymer slug.

In this limit, we can compare the impact of the polymer treatment in two layers of different permeability (Figure 8.18). If the two layers independently connect an injection and production well, and have permeability k_1 and k_2 , then the ratio of the flow in each layer, per unit depth of that layer, equals the ratio of the permeabilities. If the gelling occurs after the polymer has been injected, then the ratio of the volume of polymer which is injected into each of the layers, per unit depth of that layer, also equals the permeability ratio. Hence the layer with larger permeability receives more polymer and thereby will suffer a larger reduction in permeability. For a simplified case of a channelised deposit, or with a linear injection and production well, in which the injector and producer are a distance L apart, and in which the flow is primarily one dimensional, the effective permeability of each layer, i , after formation of the gelled zone, is given by

$$\bar{k}_i = \frac{k_i k_{gi} L}{k_i d_i + k_{gi} (L - d_i)} \quad (8.33)$$

where d_i is the extent of the polymer in layer i , $d_i = dk_i / (k_1 + k_2)$, with d the total length of polymer slug, and k_{gi} is the permeability of the region of layer i in which the polymer has gelled.

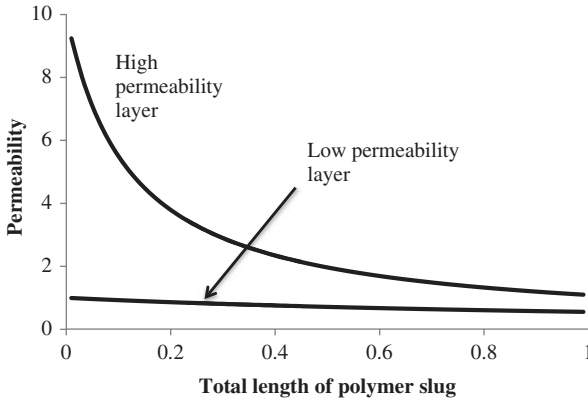


Figure 8.19 Variation of the permeability of the high and low permeability layers following injection of a polymer slug (Eq. (8.33)). The polymer slug gels and is assumed to reduce the permeability by a factor of 10 ($k_{gi} = 0.1k_i$). It is seen that the permeability of the original low permeability layer decreases much more slowly as the length of the polymer slug increases, since this layer receives less of the polymer, in proportion to the initial permeability ratio. As a result, the total flow decreases primarily through the suppression of the flow in the high permeability layer. This reduces the high flow rates of water until more of the oil has been swept, although the overall flow rate decreases.

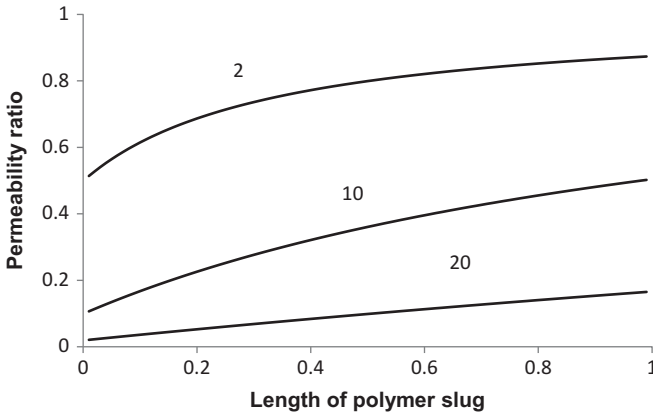


Figure 8.20 Ratio of the permeability of the low permeability layer to the high permeability layer as a function of the length of the slug of polymer injected into the reservoir. Curves correspond to different initial values of permeability ratio (2, 10 and 20). As more polymer is added and then gels, the difference in the permeability of the two layers decreases.

In Figure 8.19 we show the variation of the permeability of each layer as a function of the length of the polymer slug d for the case in which the initial permeabilities of the two layers are 1 and 10, in arbitrary units (Eq. (8.33)). The permeability of the layer with the higher initial value of permeability decreases more rapidly as polymer is added since it receives more of the polymer. Indeed, in Figure 8.20 we show how the permeability ratio decreases as the amount of polymer added to the system is increased.

This result illustrates how in the continuing flow, the polymer leads to diversion of a larger fraction of the injected fluid through the lower permeability zone, and so although the permeability of both layers decrease, thereby decreasing the flow rate for a given pressure forcing, more of the continuing flow migrates through the less well swept regions. This may be relevant in oil production systems, since it provides a strategy to reduce the flow in the layers through which water has already reached the production well. As a result the fraction of water in the produced fluids will decrease. In later field life, this can be a dominant factor in extending the life of the wells, owing to the cost of treating the produced water compared to the value of the hydrocarbons produced. There are many possible extensions to the modelling presented herein, including the effects of hydraulic connections between the layers, dispersion and instability of the polymer fronts; the analysis presents a picture of some of the controls on siting polymer gels within a reservoir, and their impact on the production.

8.11 Exercises

1. A reservoir consists of two permeable layers of permeability k_1 and k_2 directly in contact. A polymer slug of extent d is injected into the formation from a long line well, leading to a one-dimensional flow in each layer normal to the well. There is a time delay τ before it gels, where τ is longer than the time to inject the gel into the reservoir. The gel is virtually impermeable. Describe the location of the slug of polymer in each of the layers at the time they gel, assuming a total flow rate Q per unit length along the well. Also, describe the flow path of liquid injected into the system following the gelling of the polymer, assuming that the slugs of polymer in each of the layers do not overlap.
2. A reservoir consists of a laterally extensive layer of permeability k and thickness H inclined at angle θ to the horizontal. Fresh water is injected from a line well along a horizontal line $y=0$ and extracted from a second horizontal well at $y=L$. The geothermal temperature is $T_G(y) = T_o - Gy^\circ\text{C}$ ($G > 0$). Calculate how the temperature in the field evolves with time if fluid of temperature T_1 is injected into the injection well. If the formation fluid is in equilibrium with the minerals in the rock, and the solubility of mineral a varies with temperature as $c = c_a + \alpha(T - T_o)$ calculate the pattern of precipitation of mineral associated with the migration of the formation water, and the following front of injected water, assuming that the injection well is deeper than the production well. You may assume that there is negligible heat loss to the surrounding rock.
3. If the gelled polymer reduces the permeability of the formation from value k to value $k \exp(-G)$ where G is the mass of polymer gelled at that point in the formation, calculate the effective permeability of a permeable rock between a source $x=0$

and sink at $x=L$ if polymer is released from a dissolving encapsulant, according to Eqs. (8.19–8.24). Explore how the permeability changes as c_o and t_1 are changed such that $c_o t_1$ is a constant corresponding to the injection of a constant mass of polymer. You may assume the injection rate u , the gelling delay time τ and kinetic constant λ are fixed.

4. (Numerical exercise) Develop a model for the effect of a polymer gelling in a porous medium in a discrete way using a pore-network model in which there is a regular grid of pathways from node to node. Flow is modelled by assuming each node has a pressure, and the flow between neighbouring nodes is proportional to the pressure difference. By imposing a pressure on an upstream and downstream boundary, the flux through the system can then be calculated. For example, in two dimensions, a square grid can be used for the network. If a polymer floods the pore network and is assumed to produce gel flocs in a fraction f of the pathways, the macroscopic permeability will decrease. Gelled flocs of the polymer may be assumed to accumulate in particular pathways of the network between adjacent nodes with probability f , making the pathway of lower permeability. If a large number of realisations for the distribution of the flocs is taken, and for each distribution the effective permeability is measured, one can determine the range of permeabilities of the gelled system. For a critical range of values of f , there will be two types of distributions of flocs in space: ones for which there is no path remaining which does not pass through a node–node pathway which hosts a polymer floc, and ones for which there remains a polymer-free path from the injection to the extraction point somewhere in the network. By numerical calculation find how the ratio of the number of each of these path types depends on f . (See van Triet *et al.*, 2014, for more details of these types of calculations: note the continuum modelling in this chapter has assumed that the system is sufficiently large that well defined mean properties may be used in modelling the gelling process.)

9 Gravity-driven flow in porous media

In the analysis we have considered to this point, we have largely focused on pressure-driven flows, and the impact of heterogeneous pore structure, immiscibility and viscosity contrasts in driving the flow and reactions. However, in a number of situations in porous media, the flow is controlled or influenced by buoyancy forces, and this leads to different patterns of flow. We have touched on the role of density differences in driving instability of a moving front in our discussion of the Saffman–Taylor type instability (Chapter 6), and in the discussion of the migration of gas and oil through capillary-pressure-limited seal layers above anticline-type traps (Chapter 7). In this chapter we consider the dynamics of buoyancy-driven flows, largely associated with the injection of fluid of one density into a porous layer saturated with a fluid of a second density.

The role of the buoyancy forces on the flow depends on the geometry of the flow, and can lead to a range of different phenomena. We can envisage two end members for gravity-driven flows, namely vertical plumes in which the flow is parallel to the gravitational acceleration and horizontal flows, in which fluid of one density migrates along a boundary, displacing a second fluid of different density. In this chapter, we focus on the case of gravity-driven flows along horizontal or sloping boundaries, while in Chapter 10 we consider vertical flows, including the dynamics of both plumes, but also vertical exchange flows. We also consider how buoyancy affects the dispersion associated with such flows as they migrate through porous layers, exploring both the pore-scale dispersion, and the combination of buoyancy forces with heterogeneity of the rock structure in causing dispersion and mixing. The simplified models we present illustrate some important differences with the dispersion associated with pressure-driven flows described in Chapter 5. Finally, in Chapter 11, we explore some of the flows which result from the combination of density differences produced by temperature and compositional contrasts between the injected and formation fluid: owing to the thermal inertia, this leads to flows in which the buoyancy evolves within the flow, including the possibility of reversing buoyancy.

The effect of buoyancy on flow in porous media is important in a number of engineering applications in which fluid is injected into the formation to displace a second fluid including the recovery of oil and gas, sequestration of CO_2 , and the recovery of thermal energy from geothermal systems.

Buoyancy forces associated with the difference in density between the oil and water can have an important impact in understanding the pattern of water flooding especially in more permeable reservoirs and far from injection wells, as the flow spreads and the pressure gradients decrease. If we consider injection of a volume flux Q from a point source, into an aquifer with a vertical extent H , which extends a large distance laterally from the well, $L \gg H$, with angle of inclination θ to the horizontal, then if we assume that the flow spreads axisymmetrically from the well, and for the moment neglect gravity so that the flow floods the whole depth of the layer, the speed at radius r from the well will have value

$$u = \frac{Q}{2\pi Hr} \quad (9.1)$$

The cross-layer buoyancy-driven speed, u_b , owing to the density difference $\Delta\rho$ between the injected and formation fluid, is given by

$$u_b = \frac{k\Delta\rho g \cos\theta}{\mu} \quad (9.2)$$

where k is the permeability of the formation. This becomes comparable to the radial flow speed when the flow front has reached a radius

$$r = \frac{Q\mu}{2\pi Hk\Delta\rho g \cos\theta} \quad (9.3)$$

At this point, we expect the slumping of the flow front under gravity to become significant. In a typical case that $Q \sim 0.01 \text{ m}^3/\text{s}$, $\Delta\rho = 10\text{--}100 \text{ kg/m}^3$, $\mu = 0.001 \text{ Pa/s}$, and $k = 0.1$ Darcy, with $\theta < 10^\circ$, the radius (9.3) is related to the depth of the layer according to $r \sim 10^4/H$ and so with a thin permeable layer, of order 10 m thick, the buoyancy-driven flow will only produce a significant gravity slump after a distance of order 10^3 m, and within this radius, the flow is essentially pressure-driven. In contrast, with a layer 50–100 m deep, the buoyancy-driven slumping flow will be significant when the flow has spread of order 10^2 m from the source, and buoyancy effects then become important in the flow (Figure 9.1).

In a more steeply dipping reservoir, the along slope component of gravity may be very important. If the layer is relatively thin, $H \leq 10$ m, then the flow may flood the whole depth of the layer, but the downslope buoyancy forces may impact the shape of the flood front between the injected and original fluid (Figure 9.2); alternatively a three-dimensional plume may rise from a point source of buoyant fluid. In Chapter 10 we explore these flows in more detail, developing a model for the shape of a steady buoyant plume in the absence of mixing (cf. Figure 9.2), and also exploring the dispersion of a buoyant plume as it rises and spreads out through a layered permeable rock.

Buoyancy-driven flows also arise with miscible gas injection in reservoirs, for example with CO_2 injection for enhanced oil recovery. Following an initial water flood in

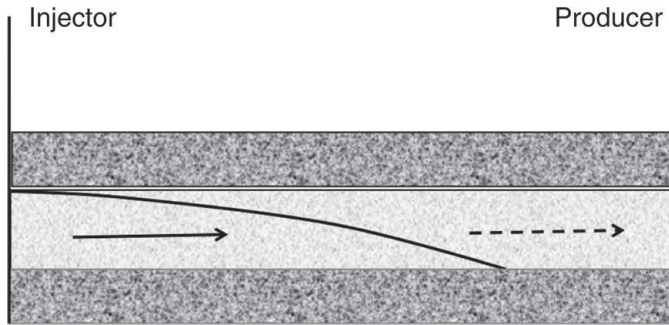


Figure 9.1 Illustration of the gravity-driven tonguing of a water flood as it displaces relatively dense oil within the formation.

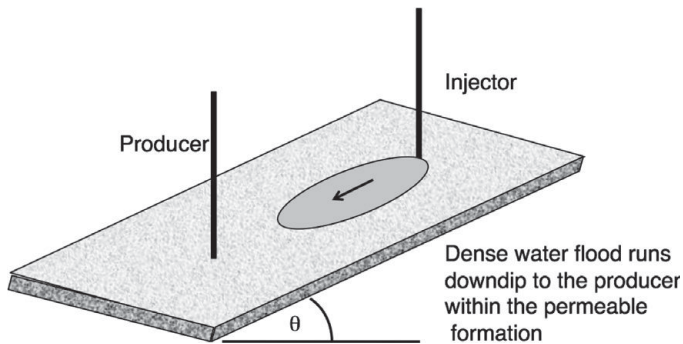


Figure 9.2 Water injection into an inclined reservoir in which the buoyancy force impacts the shape of the plume and hence the sweep efficiency as the water passes from the injector to the producer well.

a reservoir, the residual oil trapped in the pore spaces which have been swept by the initial water flood may have a relatively low saturation. As the gas advances through these pore spaces, it will dissolve into the remaining oil phase increasing the saturation of the oil–CO₂ mixture. This may enable a secondary displacement of the oil–CO₂ mixture by use of a second water flood, known as water-alternating-gas recovery. Although the subsequent recovery of hydrocarbons has a high CO₂ content, the gas does enable more of the oil to be mobilised. A key part of the flooding relates to the gravity override of the low viscosity gas phase which is influenced by the buoyancy. This motivates analysis of the role of buoyancy displacement flows within a porous layer of finite depth (cf. Figure 9.3).

With increasing concern about CO₂ emissions, there has also been interest in the dispersal of CO₂ injected into subsurface aquifers for CO₂ sequestration. Following the injection phase, the cloud of CO₂ injected into the subsurface will be controlled by buoyancy forces, and analysis of such flows provides estimates of the possible dispersal of the CO₂ in the subsurface. In this case, the migration of the CO₂ cloud is influenced

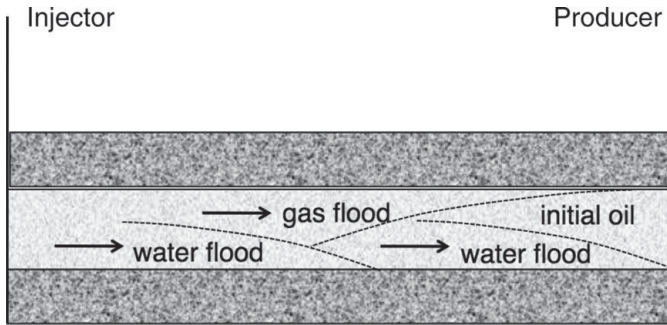


Figure 9.3 Illustration of the gravity-driven spreading of an alternating buoyant gas and dense water flood to displace oil within the formation.

by the capillary trapping of CO_2 at the rear of the flow, dissolution of the cloud into the underlying water and the effect of heterogeneities in the formation.

There are presently three large-scale CO_2 sequestration projects: the In Salah field in Algeria, the Sleipner field in the Norwegian North Sea and the Weyburn field in Canada. These fields span permeabilities from high values of about 10^{-12} – 10^{-13} m^2 at Sleipner to smaller values of 10^{-14} – 10^{-15} m^2 at the In Salah field. Different monitoring systems have collected seismic data and other subsurface data which can be used to infer the location of the CO_2 in time as the plumes of CO_2 spread under buoyancy and pressure forces through the layered strata (Verdon *et al.*, 2013). There has been much research aimed at uncovering some of the controlling processes related to the migration of supercritical CO_2 in the subsurface given it is a relatively low density (400 – 700 kg/m^3) and low viscosity (0.0001 – 0.0003 Pa s) phase relative to water, which has density ~ 1000 kg/m^3 and viscosity 0.01 – 0.001 Pa s depending on pressure and temperature. (Note, supercritical fluids exist above the critical temperature and pressure under which conditions there is no distinction between the liquid and the gas phase.) For context, CO_2 injection rates of about one million metres cubed per year are envisaged for typical storage wells.

One concept for the sequestration of CO_2 emerging from these studies is to inject the CO_2 into anticlines, which are structural traps in subsurface aquifers (Figure 9.4). The process of migration into the trap and the subsequent dissolution of the CO_2 into the underlying groundwater from the trap have been explored in some detail (e.g. Hesse *et al.*, 2008; Woods and Espie, 2012; Szulczewski *et al.*, 2013). In migrating through an aquifer, the capillary trapping of the CO_2 phase in the wake of the plume of CO_2 can lead to a substantial fraction of the plume being trapped and becoming immobile prior to reaching the anticline (Figure 9.5), depending on the volume injected and the volume of pore space in the aquifer and we explore this below. In Chapter 10 we describe some of the controls on the long-term dissolution of the CO_2 ; these are primarily associated with the supply of unsaturated groundwater either from the host aquifer

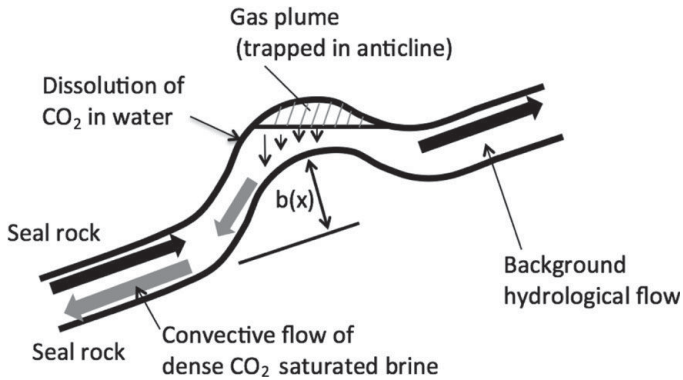


Figure 9.4 Illustration of a CO_2 plume trapped in an anticline, involving the dissolution into groundwater and subsequent convection as dense CO_2 -laden water exchanges with the less dense, unsaturated aquifer water.

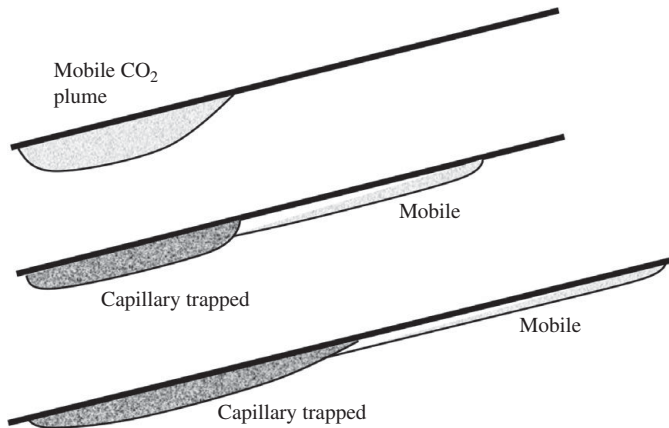


Figure 9.5 Illustration of the capillary trapping of the rear of a CO_2 plume as it runs along an impermeable boundary, with some dissolution of CO_2 into the formation water developing on the lower surface of the plume.

containing the CO_2 or through exchange flow with adjacent aquifers, connected to the original aquifer by a series of fractures through the impermeable geological strata.

There is a related class of problem associated with subsurface geological waste repositories for disposal of radioactive material; these repositories can become sources of hydrogen gas if organic material in the repository comes into contact with water. Although the volume of release of hydrogen is likely to be much smaller than in the case of CO_2 sequestration, with estimates suggesting volumes of order 1000 m^3 , if this gas breaches the repository boundary and enters fractured volcanic rock or layered sedimentary rock, the migration of the hydrogen, which can also transport radionuclides, may involve some analogous buoyancy-driven flow problems (Woods and Norris, 2010). It is worth noting, however, that many such repositories are being

designed to reside within very low permeability clay horizons in the subsurface and in that case the problems related to gas migration are very different owing to the very low permeability of the clay.

The migration and dispersal of LNAPL and DNAPL contaminants can also be influenced by buoyancy forces. LNAPL is typically associated with the spillage of oils into the subsurface. The oils are light and after descending through the vadose zone, i.e. the shallow water-unsaturated geological strata, they spread on the surface of the water table. DNAPLs, typically associated with chemical solvents and other industrial chlorinated petroleum products, are dense, and these migrate through the groundwater, forming a dispersed cloud of contaminant within the water table. Since they are weakly soluble in the water, as the background hydrological flow migrates past the contaminants, they can produce laterally extensive plumes of contaminated groundwater. Prediction of the spatial distribution of contaminated plumes of groundwater and strategies for their cleanup are critically dependent on knowledge of the original distribution of the LNAPL and DNAPLs within the geological strata. In turn, this depends on the balance of buoyancy and capillary effects controlling their flow from the surface source and through the geological strata. We consider some of the problems relating to the balance of buoyancy and capillary forces as flow migrates along low permeability layers later in this chapter.

The problems described above relate to buoyancy-driven flows in which the density difference is associated with the composition of the two fluids. There is, however, a different class of problem related to heat flow in the ground, in which density changes associated with temperature differences between different regions of an aquifer can be key. Such problems arise in geothermal reservoirs in which water is injected and extracted to mine the thermal energy stored in the permeable rock. Density changes of the water as it heats up can lead to an important control of buoyancy forces on the propagation pattern of the fluid, and we consider this in more detail in Chapter 11. Of particular importance are flows in which the composition and temperature of the injection water differ from that in the host rock. This can lead to some very curious flow patterns in which the buoyancy evolves with distance in the flow because the thermal and compositional fields migrate through the formation at different speeds. There is also an important class of problem involving the boiling of water injected into the formation, in which the density difference between the water and vapour can control the surface area and hence rate of vaporisation of the liquid. We also consider these effects in more detail in Chapter 11.

We commence with a discussion of two-dimensional flows, for example associated with injection from a line well, in which a buoyancy-driven flow leads to a horizontally spreading gravity current (Figures 9.1 and 9.6). We first consider the case of a very deep formation, in which the displacement flow of the original fluid in the formation is small compared to the injected fluid. We then develop this analysis to assess the flow which develops in a formation of finite vertical extent, in which case the motion

of both fluid phases is key and accounts for various effects which can modify the flow, including reactions, capillary trapping, dissolution and leakage into neighbouring geological layers (cf. Figures 9.2, 9.3). In Chapter 10, we build on this by assessing the dispersion of such flows in heterogeneous rocks.

9.1 Point release of buoyant fluid

A pedagogical problem to consider is the two-dimensional gravity-driven flow produced when fluid of density ρ_1 migrates along a horizontal boundary from a line source and the displacement of the original fluid in place, of density, $\rho_2 = \rho_1 - \Delta\rho$, does not impose a significant backpressure on the flow. This occurs, for example, in the vadose zone, when fluid is injected at a point and then spreads along an impermeable boundary (Figure 9.6).

Before constructing the exact solutions, it is helpful to infer the scalings for the current length $L(t)$ and depth $H(t)$ as functions of time using simple arguments. For example, for a finite release of fluid in two dimensions, with volume per unit length in the cross-flow direction, V_o , a current with length $L(t)$ and maximum depth $H(t)$ has nose speed

$$\frac{dL}{dt} \sim \frac{\Delta\rho g H}{\mu L} \quad (9.4)$$

Coupling this with the volume conservation, $\phi H L \sim V_o$ we expect that the length will scale with time as

$$L(t) \sim \left(\frac{\Delta\rho g V_o t}{\mu \phi} \right)^{1/3} \quad (9.5)$$

We now develop the governing equation for the flow and develop some exact solutions which confirm this physical scaling analysis. In a porous layer in which there is an impermeable horizontal boundary, $z = 0$, and along which dense fluid spreads under gravity, the flow becomes relatively long and thin, with lengthscale L and depth H , $\ll L$, so that the continuity equation leads to the balance (Figure 9.6)

$$\nabla \cdot u = 0 \rightarrow v = O\left(\frac{Hu}{L}\right) \ll u \quad (9.6)$$

and as a result, the vertical pressure gradient is approximately hydrostatic, so that

$$p(x, z, t) = p_H + \int_z^H \rho g dz = p_H + \int_z^h \rho_1 g dz + \int_h^H \rho_2 g dz \quad (9.7)$$

where $h(x, t)$ is the local depth of the flow, as a function of the horizontal position x and time t and p_H is a reference pressure at height H above the boundary. Here we have assumed that there is no mixing between the injected and reservoir fluid. The

horizontal component of Darcy's law then takes the simplified form

$$u = -\frac{k}{\mu}(\rho_1 - \rho_2)g \frac{\partial h}{\partial x} \quad \text{for } 0 < z < h \quad (9.8)$$

at each height in the current.

The local equation for the conservation of mass takes the form

$$\phi(h) \frac{\partial h}{\partial t} = -\frac{\partial}{\partial x} \left(\int_0^h u(x, z, t) dz \right) \quad (9.9)$$

In the case that the permeability is uniform in the layer, this leads to the non-linear diffusion-type equation which governs the evolution of the depth of the flow

$$\frac{\partial h}{\partial t} = \left(\frac{k\Delta\rho g}{\mu\phi} \right) \frac{\partial}{\partial x} \left[h \frac{\partial h}{\partial x} \right] \quad (9.10)$$

while the conservation of mass in the formation is given by the balance between the volume of the current and the mass injected

$$V(t) = \int_0^{L(t)} dx \int_0^{h(x,t)} \phi(z) dz \quad (9.11)$$

In the case in which a finite volume of fluid is released, or with a flux of fluid at $x = 0$ which varies as a power of time so that the volume of fluid in the current is given by

$$V(t) = Qt^\gamma \quad (9.12)$$

these equations admit self-similar solutions, which represent the natural solutions of the differential equation, in the absence of any external lengthscale. To find the solutions from the differential equation, we try an ansatz of the form

$$h(x, t) = D \left(\frac{t}{\tau} \right)^\alpha f \left(\frac{x}{\left(\frac{t}{\tau} \right)^\beta D} \right) \quad (9.13)$$

where the timescale and lengthscale, τ and D are given in terms of the natural buoyancy speed

$$S = \frac{kg\Delta\rho}{\mu\phi} \quad (9.14)$$

and the quantity Q (Eq. (9.12)) by using dimensional analysis leading to the relations

$$\tau = \left(\frac{S^2}{Q} \right)^{\frac{1}{\gamma-2}} \quad \text{and} \quad D = \left(\frac{Q}{S^\gamma} \right)^{\frac{1}{2-\gamma}} \quad (9.15)$$

On substitution of this ansatz into the governing equation, we seek values for the exponents α and β such that the governing equation is purely a function of the similarity variable

$$\eta = \frac{x}{\left(\frac{t}{\tau}\right)^\beta D} \quad (9.16)$$

This leads to the relations

$$\alpha = \frac{2\gamma - 1}{3} \quad ; \quad \beta = \frac{\Gamma + 1}{3} \quad (9.17)$$

and the ordinary differential equation for the shape of the current,

$$3 \frac{d}{d\eta} \left(f \frac{df}{d\eta} \right) = (2\gamma - 1)f - (\gamma + 1)\eta \frac{df}{d\eta} \quad (9.18)$$

Finally the boundary conditions relating to the conservation of mass require that at the end of the current, where $\eta = \eta_o$,

$$f(\eta_o) = 0 \quad ; \quad \int_0^{\eta_o} f(\eta) d\eta = \left(\frac{t}{\phi} \right) \quad (9.19)$$

In general, this non-linear differential equation for f requires numerical solution. However, in the special case of a finite volume release of fluid, the differential equation can be integrated exactly since $\gamma = 0$ and the shape equation becomes

$$3 \frac{d}{d\eta} \left[f \frac{df}{d\eta} \right] = -f - \eta \frac{df}{d\eta} \quad (9.20)$$

with exact solution

$$f(\eta) = \frac{1}{6} \left(\eta_o^2 - \eta^2 \right) \quad \text{where} \quad \eta_o = \left(\frac{9}{\phi} \right)^{\frac{1}{3}} \quad (9.21)$$

This solution is shown in Figure 9.6 at a series of times, together with the result of a laboratory experiment in which a finite volume of fluid was released at the end of a Hele–Shaw cell. The shape of the top surface is shown on each of the images, taken at four different times after release of the lock gate; these have been rescaled and superposed in the lowest image on the figure. The differences in these profiles are smaller than the line thickness in the plot and coincide with the parabolic solutions (9.21).

The self-similar slumping allows the current to become thinner and more laterally extensive in time, while maintaining the same shape. As anticipated by the scalings (9.4) and (9.5), the current length $L(t)$ and depth at the origin, $h(0, t)$ evolve according to the relations

$$L(t) = \eta_o D \left(\frac{t}{\tau} \right)^{1/3} \quad (9.22a)$$

$$h(0, t) = \frac{\eta_o^2 D}{6} \left(\frac{\tau}{t} \right)^{1/3} \quad (9.22b)$$

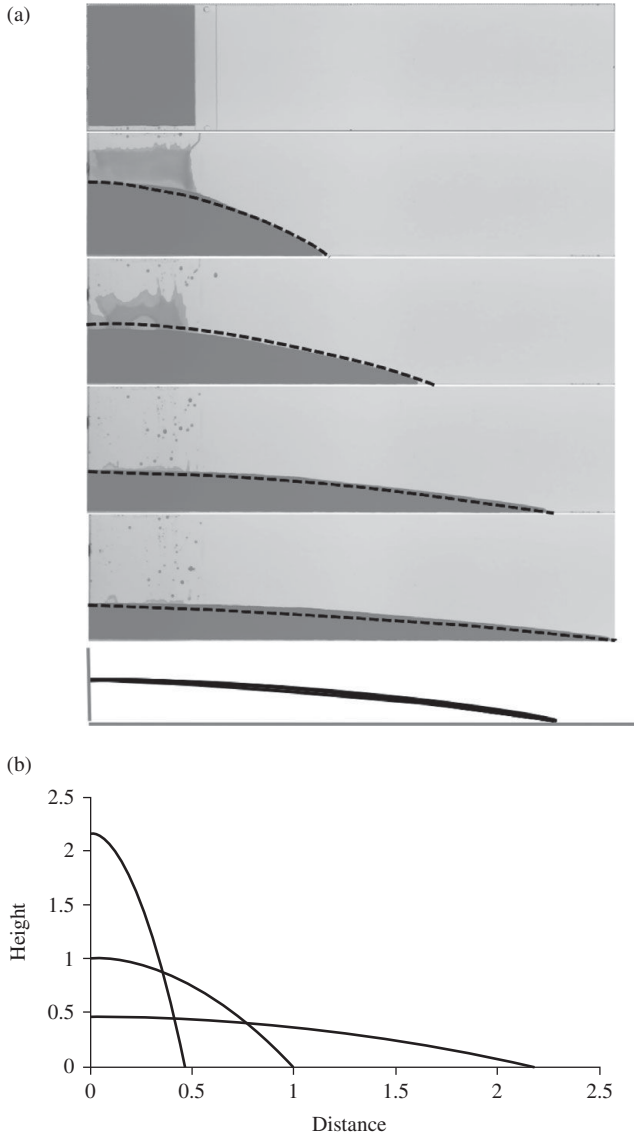


Figure 9.6 Shape of the evolving gravity-driven flow produced by the release of a finite volume of fluid in a two-dimensional Hele–Shaw cell. Note in the early images, there is a thin film left on the plates which gradually drains with time, although at long times, as the current speed decreases, this draining film becomes very small. Photo courtesy of Caren Otto. A black and white version of this figure will appear in some formats. For the colour version, please refer to the plate section.

This fundamental solution provides key insight into the dynamics of a buoyancy-driven flow, where the horizontal pressure gradient is produced by the variation of the depth of the flow as a function of position along the boundary. In Figure 9.7, we present a series of images of a gravity current produced by a constant flux of saline solution,

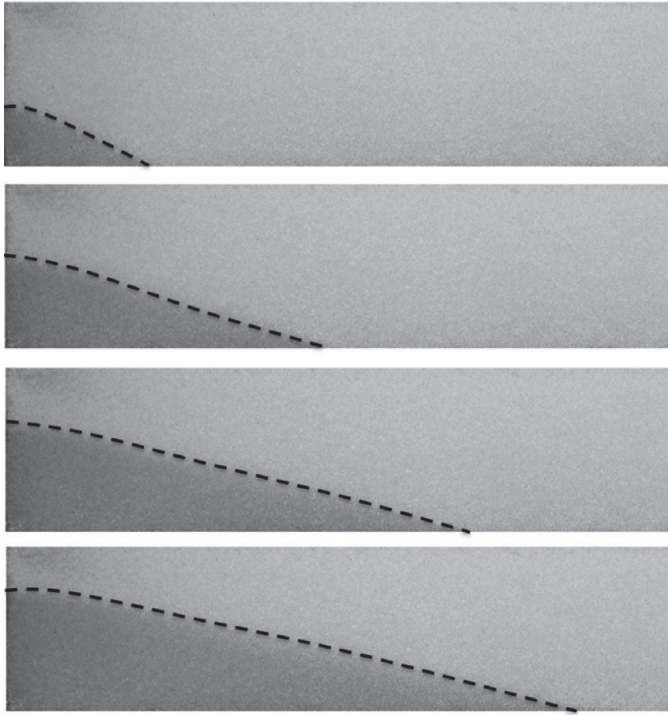


Figure 9.7 Shape of the evolving gravity-driven flow produced by a constant flux of fluid supplied to a two-dimensional bead pack. A black and white version of this figure will appear in some formats. For the colour version, please refer to the plate section.

Q per unit length, in a two-dimensional porous bead pack originally filled with fresh water. In this case, the length increases as

$$L \sim \left(k \frac{\Delta \rho g Q t^2}{\mu \phi} \right)^{1/3} \quad (9.23)$$

and the theoretical solution for the flow, based on Eq. (9.18), with $\gamma = 1$ has been superposed on each image.

There are many extensions to this model which enable more realistic or complex rock morphologies to be studied.

9.2 The leaky boundary

If the boundary of the porous layer includes a thin seal layer of thickness b and of much lower permeability, k_b , than the main flowing layer, k , so that $k_b/b \gg k/h$, where h is current depth, then, as the flow migrates along the boundary, a small fraction of the

flow may drain through the boundary, this may be modelled by a sink or loss term in the equation for the conservation of mass. If the drainage is controlled by the local head of the dense fluid in the current, this drainage will be proportional to the depth of the flow, and the permeability of the low permeability ‘seal’ layer. Assuming that the low permeability layer is underlain by a more permeable layer, the rate of drainage of fluid per unit length will then be given by the depth of the flow

$$loss = \frac{k_b \Delta \rho g h}{\mu b} \quad (9.24a)$$

and the governing equation for the two-dimensional current depth becomes

$$\frac{\partial h}{\partial t} = S \frac{\partial}{\partial x} \left(h \frac{\partial h}{\partial x} \right) - \lambda h \quad (9.24b)$$

where $\lambda = \frac{k_b S}{kb}$. The draining of the flow leads to loss of fluid from the current, and this may be found by integrating Eq. (9.24b) along the length of the flow, leading to the expression for the evolution of the volume of fluid per unit length in the cross-flow direction

$$V = \phi \int_0^{L(t)} h(x, t) dx \quad (9.25)$$

given in terms of the source flow Q by

$$\frac{dV}{dt} = Q(t) - \lambda V \quad (9.26)$$

with solution

$$V(t) = \exp(-\lambda t) \left[V(0) + \int_0^t Q(t') \exp(\lambda t') dt' \right] \quad (9.27)$$

By transforming time,

$$\tau = \frac{(1 - \exp(-\lambda t))}{\lambda} \quad (9.28)$$

we can find the exact solution for the depth of the current in the case of a finite release (Figure 9.8)

$$h(x, t) = \frac{V(0)^{2/3}}{6S^{1/3}\tau^{1/3}} \exp(-\lambda t) \left(9^{2/3} - \frac{x^2}{V(0)^{2/3}S^{2/3}\tau^{2/3}} \right) \quad (9.29)$$

where the maximum run out distance varies with time according to the relation

$$x_m = \left[\frac{9V(0)kb}{\phi k_b} (1 - \exp(-\lambda t)) \right]^{1/3} \quad (9.30)$$

as the current drains into the underlying strata. This model has been tested with experiments in a Hele–Shaw cell in which syrup spreads between two parallel vertical planes, with a narrow gap at the base of the cell representing the low permeability seal layer.

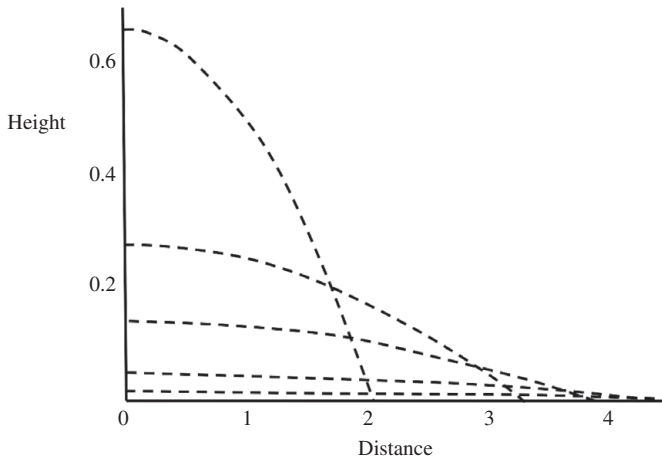


Figure 9.8 Shape of the evolving gravity-driven flow produced by a finite volume of fluid released into a Hele-Shaw cell with a leaky base. Profiles are shown at a series of dimensionless times $\tau = 1, 5, 10, 20$ and 30 .

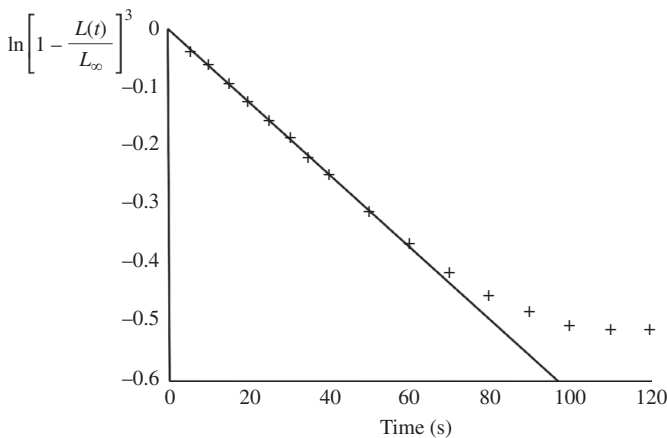


Figure 9.9 Comparison of the length of a draining gravity current as a function of time, following the release of a fixed volume of fluid, with the model prediction (9.30). After Pritchard *et al.* (2001).

As the current drains through the base it spreads laterally, eventually runs out of fluid (Figure 9.9).

On the field scale, the maximum run out distance for a two-dimensional current, which is given by (9.30) for large time, can be found for typical parameters. For example, with an initial volume 100 m^2 per unit length normal to the flow, with a seal rock of thickness 0.1 m and permeability 10^{-4} times that of the main formation, then the run out length is approximately 100 m . The timescale to reach this distance in a layer with permeability 1 Darcy , and with fluid of density difference 100 kg/m^3 is a few years. This is consistent with the buoyancy-driven flow being of speed $S \sim 10^{-5} \text{ m/s}$.

This provides a source term for the flow in the neighbouring permeable layer, and illustrates how a buoyancy-driven flow may gradually leak through a low permeability boundary of a porous layer, even with a large permeability contrast. In building a model of the flow in a layered medium, this calculation introduces important constraints on how the different layers should be characterised, and in particular, on what constitutes seal rock. Woods and Farcas (2009) extended this model to account for a finite capillary entry pressure which can suppress the leakage of the fluid through the low permeability boundary once the current becomes too thin.

9.3 Rapid injection and drain back: the dipole

An interesting exact solution to the non-linear diffusion equation relates to the so-called dipole or drainback solution, in which a volume of fluid rapidly invades a porous layer, for example, through a fracture or an injection well, and then, subsequently, the fluid drains out of the layer and back into the fracture. As the draining occurs, the remainder of the fluid is able to spread into the formation under gravity thereby contacting a fraction of the porous layer with the injected fluid, until it has all drained back into the fracture. This flow, in which the depth of the current is zero both at the origin, $h(0) = 0$, beside the fracture, and in the far field, as the current spreads outwards, has the curious property that the dipole moment D is conserved (Barenblatt, 1996), where

$$D = \int_0^{L(t)} xh(x, t) dx \quad (9.31)$$

By seeking a similarity solution and constraining the exponents in time such that the dipole moment is conserved and that the boundary conditions at $x = 0$ and in the far field are satisfied, we find that the solution to the non-linear differential equation (9.10) has the form (Barenblatt, 1996)

$$h(x, t) = \frac{1}{6} \left(\frac{D}{St} \right)^{1/2} \left(40^{3/8} \eta^{1/2} - \eta^2 \right) \quad \text{where} \quad \eta = \frac{x}{(DSt)^{1/4}} \quad (9.32)$$

The structure of this flow solution is shown in Figure 9.10. From the solution, we see that the current only occupies the finite region of the porous layer, given in similarity space as

$$0 < \eta < \eta_e = 40^{1/4} \quad (9.33)$$

where the depth of the flow at the nose of the current, $h(\eta_e) = 0$.

In practice, a flow entering the reservoir will take some time to adjust to this solution, but as the solution shows, the flow then drains away with the volume per unit length decreasing as the inverse one quarter root of time, while the nose of the current continues to advance into the formation. In the case of a layer which has depth

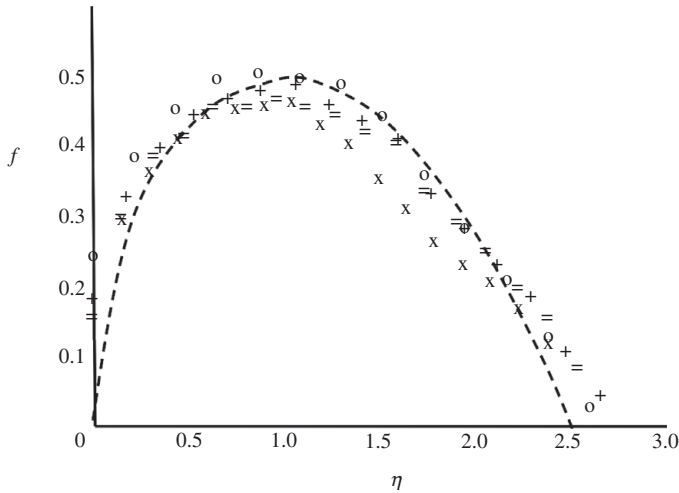


Figure 9.10 Shape of the evolving gravity-driven flow produced by a finite release in a two-dimensional porous layer—, here a Hele–Shaw cell, in the case that the flow can drain back through an opening at the end of the cell $x = 0$. The figure compares the laboratory data of the shape of the current with the theoretical solution, for observations at a series of times. After King and Woods (2003).

of order 10 m and extends 10 m into the formation following injection over a period of months, for example corresponding to a wet winter in which there may be recharge of the permeable layer, the dipole moment has value of about 500 m^3 . Assuming the current adjusts to the dipole solution, then with a transport speed of $S \sim 10^{-5} \text{ m/s}$, the leading edge of the current will have travelled to a distance of about 20 m into the rock after 1 year while some of the flow drains into the fracture. If the flow persists, then after 10 (100) years, there will be a fraction of about 0.3 (0.1) of the fluid remaining, and the nose will have advanced to a distance of about 35 (60)m.

This solution may be extended to account for draining through the lower boundary of the formation by rescaling time as in Section 9.2; details are given by King and Woods (2003).

9.4 Multiple fluids and stratified currents

Although the similarity solutions we have described are special solutions, and only apply for specific boundary conditions, they do provide useful insight into the motion of two-fluid currents in a porous layer. The similarity solutions for a single discrete release may be extended to consider the motion of two discrete volumes of fluid of different density and viscosity spreading into a porous layer.

This type of flow may arise, in principle, if a fluid is injected into a porous rock in an attempt to contain a second, hazardous liquid which may have infiltrated the rock at an

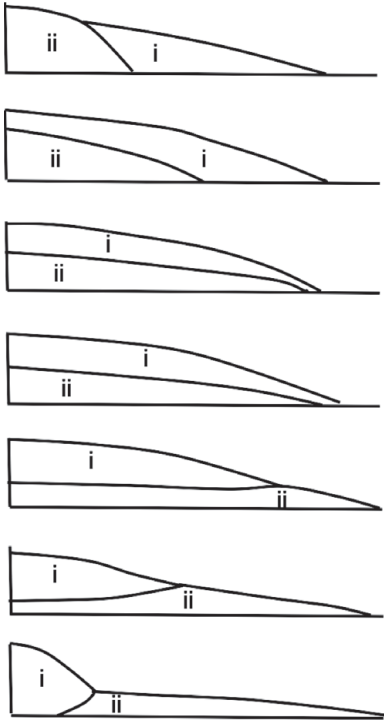


Figure 9.11 Illustration of the different modes in which a two-fluid gravity current spreads from a source as a function of the difference in viscosity of the two fluids. Fluid i becomes progressively more viscous in the successive panels. After Woods and Mason (2001).

earlier time. The second fluid may perhaps be seeded with a time-delay polymer with the objective that the gelling process is triggered after the liquid has spread through the rock for a particular time at which it can contain the spill. This two-fluid model also sets the scene for exploring the dynamics of reacting currents in which there is an internal interface across which the fluid properties change.

Physically the structure of two-fluid currents may be inferred by observing that the less dense fluid will overlie the denser fluid, and the less viscous fluid will tend to outrun the more viscous fluid. However, the detailed topology of the flow will depend on the volume ratio, the viscosity ratio and also buoyancy ratio of the two fluids. Given this physical picture, it follows that there are a series of different spreading patterns of two fluids, with the interface between the two fluids sloping forwards or backwards, as illustrated in Figure 9.11. In this figure, the fluid labelled i is less dense than the fluid labelled ii, but, as we move from the top panel to the bottom panel, the viscosity ratio varies from fluid i being much less viscous to fluid ii being much less viscous.

To model the motion of such a flow, and derive the profiles shown in Figure 9.11, we again assume the flow becomes long and thin, with the pressure being hydrostatic in the cross-flow direction. If we label the buoyancy of the less dense fluid as $\Delta\rho_u$ and

the buoyancy of the denser fluid as $\Delta\rho_l$, then the pressure in the upper fluid is

$$p_u(x, y) = p_o(y) + \Delta\rho_u g(h_u + h_l - y) \quad (9.34)$$

while that in the lower fluid is

$$p_l(x, y) = p_o(y) + \Delta\rho_l g(h_l - y) + \Delta\rho_u g h_u \quad (9.35)$$

with p_o the reference pressure in the background fluid. We then use conservation of fluid in each phase with Q_i the flux of fluid i ,

$$\phi \frac{\partial h_i}{\partial t} = -\frac{\partial Q_i}{\partial x} \quad (9.36)$$

coupled with Darcy flow, to develop an equation for the evolution of the depth of each layer of fluid as a function of the distance from the source. This leads to the governing equations

$$\frac{\partial h_u}{\partial t} = \left[\frac{k\Delta\rho_u g}{\phi\mu_u} \right] \frac{\partial}{\partial x} \left(h_u \left(\frac{\partial h_u}{\partial x} + \frac{\partial h_l}{\partial x} \right) \right) \quad (9.37a)$$

$$\frac{\partial h_l}{\partial t} = \left[\frac{k\Delta\rho_u g}{\phi\mu_l} \right] \frac{\partial}{\partial x} \left(h_l \left(\frac{\partial h_u}{\partial x} + \frac{\Delta\rho_l}{\Delta\rho_u} \frac{\partial h_l}{\partial x} \right) \right) \quad (9.37b)$$

As may be seen in the equations, the key parameters are the viscosity ratio, $V = \mu_u/\mu_l$, the buoyancy ratio, $R = \Delta\rho_l/\Delta\rho_u$, and the volume ratio $F = V_u/V_l$. By direct analogy with the original problem of the finite release of one fluid (Section 9.1), these equations admit self-similar solutions of the form

$$h_u = V_u^{1/2} \tau^{-1/3} f_u(\eta) \quad \text{and} \quad h_l = V_u^{1/2} \tau^{-1/3} f_l(\eta) \quad \text{where} \quad \eta = \frac{x}{V_u^{1/2} \tau^{1/3}} \quad (9.38)$$

with $\tau = tS_u/V_u^{1/2}$ $S_u = \frac{k\Delta\rho_u g}{\phi\mu_u}$ and

$$-\frac{d}{d\eta}(\eta f_u) = 3 \frac{d}{d\eta} \left(f_u \left(\frac{df_u}{d\eta} + \frac{df_l}{d\eta} \right) \right) \quad (9.39)$$

and

$$-\frac{d}{d\eta}(\eta f_l) = 3V \frac{d}{d\eta} \left(f_l \left(\frac{df_u}{d\eta} + R \frac{df_l}{d\eta} \right) \right) \quad (9.40)$$

The shape factors for the upper and lower layers of fluid, $f_u(\eta)$ and $f_l(\eta)$ can be described by piecewise continuous parabolae, as in the solution for the finite volume release of single fluid. However, in the present problem, the depth of one of the fluids typically falls to zero before the other (Figure 9.11) and so there is a change in the shape of the parabola describing the continuous fluid, such that the depth and flux of fluid are continuous across this transition. The different regimes of the flow, illustrated in Figure 9.11, can be mapped in terms of the volume ratio and viscosity ratio of the fluids, for a given buoyancy ratio, as shown in Figure 9.12. The changes in regime correspond

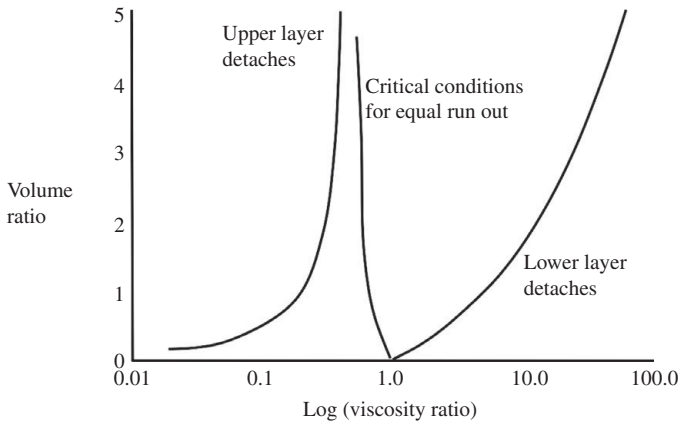


Figure 9.12 Regime diagram illustrating the different morphologies of a two-fluid gravity current in a porous layer as a function of the viscosity ratio and the volume ratio of the two volumes of fluid (Woods and Mason, 2001).

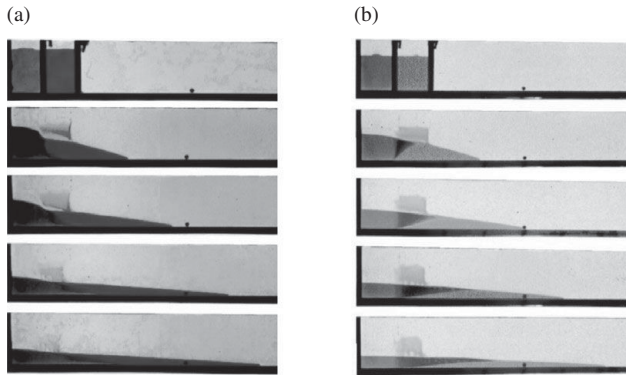


Figure 9.13 Illustration of the motion of a two fluid gravity current in a Hele–Shaw cell showing the cases in which the less dense fluid is also (a) less viscous and (b) more viscous (after Woods and Mason, 2001). A black and white version of this figure will appear in some formats. For the colour version, please refer to the plate section.

to the cases in which the upper and lower layer have the same run out distance as a function of time, and also the cases in which one of the fluids just remains in contact with the point $x = 0$. Illustrations of experimental models of two-fluid gravity currents are shown in Figure 9.13 for the case of (a) a less viscous and (b) a more viscous upper layer (further details of this analysis are given by Woods and Mason, 2001).

9.5 Reacting fronts

In Chapter 8 we explored the kinematics of pressure-driven reaction fronts, such as the acidising reaction or a thermally controlled reaction. Also, in Chapter 6, we noted that

if a reacting interface commences as a planar front, then by analogy with the Saffman–Taylor instability, a precipitation front remains stable, while a dissolution front tends to become unstable and develop dissolution channels. However, in many systems, the reacting injected fluid may be of different density from the original reservoir fluid, and as it spreads from the injection site, the buoyancy forces can dominate the flow. This leads to a reaction front whose morphology is controlled by the buoyancy forces. The lateral extent and spatial distribution of the reaction front then depends on whether the reaction is one of dissolution or precipitation. Although the pressure-driven dissolution front is unstable to non-linear channel formation, we will see that with buoyancy-driven flow, a dominant buoyancy-driven channel develops.

The solutions for two-fluid gravity currents presented in the previous section provide insight into the migration of a gravity-driven reaction front. However, since reaction fronts migrate more slowly than the fluid, there is mass transfer across the reaction front. There will then be a fluid–fluid front ahead of the reaction front where the reacted, injection fluid meets the original formation fluid. For simplicity, in this analysis, we assume the change in density or viscosity of the reacting fluid as it passes through the reaction front is small relative to the impact of the change in permeability across the reaction front. This is likely to be the case in situations where reactions arise near the channel throats in the porous medium, since a small change in the throat diameter can lead to a large change in the resistance to flow and hence permeability.

As the flow evolves, and the reaction front becomes laterally extensive compared to the vertical extent of the reaction front, then the pressure will remain approximately hydrostatic, and the flux of fluid which migrates across the reaction front will lead to a two-zone gravity current, corresponding to the flow upstream and downstream of the reaction front, with different permeabilities. If the density difference between the reacting fluid and the original fluid is $\Delta\rho$, then the pressure is governed by the relation

$$p = p_o(y) + g\Delta\rho(h_l + h_u - y) \quad \text{for } 0 < y < h_l + h_u \quad (9.41)$$

where the reaction front is located at $y = h_l$ and the reacted fluid which has passed through the reaction front is located in the region $h_l < y < h_l + h_u$. If we denote the flux in the lower layer of unreacted fluid, which approaches the reaction front by Q_l , and the flux in the upper layer of reacted fluid, which advances ahead of the reaction front as Q_u , then it follows that

$$Q_l = -h_l \frac{k_l}{\mu} \frac{\partial p}{\partial x} \quad ; \quad Q_u = -h_u \frac{k_u}{\mu} \frac{\partial p}{\partial x} \quad (9.42)$$

where k_l is the permeability of the reacted rock, which lies between the source and the reaction front at $h = h_l$, and k_u is the permeability of the unreacted rock. The model can be completed by noting that if the reaction front advances at a rate λu where λ depends on the stoichiometry of the reaction with the rock (Chapter 8), then the conservation of

mass in the region of unreacted fluid advancing towards the reaction front requires that

$$\phi \frac{\partial h_l}{\partial t} = -\lambda \frac{\partial Q_l}{\partial x} \quad (9.43)$$

and the overall conservation of mass then requires that

$$\phi \frac{\partial h_u}{\partial t} = -(1 - \lambda) \frac{\partial Q_l}{\partial x} - \frac{\partial Q_u}{\partial x} \quad (9.44)$$

Note that these equations apply to the region in which unreacted fluid migrates through the reaction front, so that $\frac{\partial h_l}{\partial t} > 0$. If there is any region of the flow in which the flow reverses at the reaction front, so that reacted fluid migrates across the front, then the reaction at this point will cease, and a region of reacted fluid will develop within the reacted rock – this is not described by these equations, although in principle this is a straightforward extension of the modelling in which account needs to be made of the location of the region of reacted fluid within the reacted rock. However, in the present discussion, we consider the case of a constant injection rate, in which a two-dimensional reaction front propagates forward everywhere and the above model admits self-similar solutions to describe the flow.

The solutions identify the important difference between the morphology of a dissolving and a precipitating flow. In the former case, the fluid dissolves a high permeability channel along the base of the permeable layer (for a relatively dense injected fluid compared to the original formation fluid). A region of unreacted rock above the dissolution channel then becomes invaded by the reacted injection fluid as it spreads from the dissolution channel as shown in Figure 9.14b. In the case of precipitation, the fluid generates a zone of low permeability near the well, and as the injection fluid advances across the reaction front it enters a region of higher permeability where it can spread forward ahead of the reaction front much faster, thereby forming a relatively thin gravity-driven current (Figure 9.14a).

The distance travelled by these gravity-driven reaction fronts depends on the volume of fluid required to react with unit volume of rock, as given by λ , and the permeability

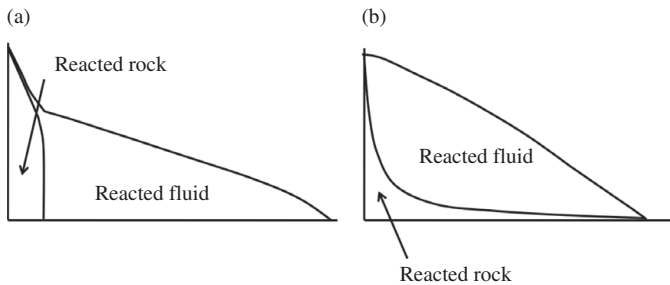


Figure 9.14 Illustration of the migration of (a) a precipitation front and (b) a dissolution front driven by gravity. More details of these solutions are given by Raw and Woods (2003).

ratio of the reacted and unreacted rock. In the case of an acidising reaction, in which the objective is to dissolve scale in the formation near the well. However if there is a large change in permeability and if the buoyancy forces are important in the flow, as would be the case with relatively slow injection, or a vertically extensive interval of rock, it may be that a relatively shallow and laterally extensive channel develops, rather than the acid dissolving all the scale near the well (Raw and Woods, 2003).

9.6 Capillary trapping

One fascinating problem related to the motion of gravity currents in porous media arises in problems where there is some mass loss from the current associated with motion of the fluid interface through the porous layer. For example, in the vadose zone, if a finite mound of liquid spreads along a horizontal boundary under gravity then in the descending region of the flow near the centre of the current, a fraction of the fluid is trapped by capillarity, and this leads to a gradual reduction in the overall mass of the flow, while in the ascending region far from the source the flow continues to migrate forwards. Since there is no independent lengthscale for this trapping which occurs on a pore scale, we expect the flow to be self-similar. However, the exponent governing the rate of loss of mass with time should be governed by the fraction of the flow which is capillary trapped. This problem has been described by Barenblatt (1996), and has relevance for the problems of boiling in geothermal reservoirs, in which, as a variant on the original problem, it is the leading part of the current across which there is loss of mass through boiling (see Chapter 11). A further problem for which this process arises are currents of CO_2 migrating through water-saturated aquifers, in which the CO_2 can become capillary trapped, in a fashion directly analogous to that in a mound of water. Here we focus on the case of an initial volume ϕV of fluid which spreads out along an impermeable horizontal plane.

If a fraction of the fluid s is capillary trapped as the flow evacuates the porous layer, then the governing equation for the flow, expressed in terms of the depth of the flow (for a long thin current), has the form

$$\frac{\partial h}{\partial t} = S \frac{\partial}{\partial x} \left[h \frac{\partial h}{\partial x} \right] \quad \text{if} \quad \frac{\partial h}{\partial t} > 0 \quad (9.45a)$$

for the advancing and invading region and

$$(1 - s) \frac{\partial h}{\partial t} = S \frac{\partial}{\partial x} \left[h \frac{\partial h}{\partial x} \right] \quad \text{if} \quad \frac{\partial h}{\partial t} < 0 \quad (9.45b)$$

for the trailing and descending region, where, as before, $S = \frac{k\Delta\rho g}{\mu\phi}$ is the buoyancy-driven interstitial flow speed. The boundary conditions for a finite release are that

$$\frac{\partial h}{\partial x} = 0 \quad \text{at } x = 0 \quad (9.46)$$

and the condition at the nose of the current, $x = x_N(t)$, that the depth of the current falls to zero, $h(x_N) = 0$. Somewhere within the current, there is a point, x^* say, at which the depth does not change in time, while ahead of this point the depth increases and behind this point the depth falls. At the point at which $\frac{\partial h}{\partial t} = 0$, the flux is continuous

$$\left[Sh \frac{\partial h}{\partial x} \right]_{x_-^*}^{x_+^*} = 0 \quad (9.47)$$

and the depth is also continuous

$$[h]_{x_-^*}^{x_+^*} = 0 \quad (9.48)$$

We now seek solutions for which the total volume of fluid decreases with time as

$$V(t) = V_o \left(\frac{t}{\tau} \right)^{-\gamma} \quad (9.49)$$

where τ is a timescale and V_o is a volumescale for the flow, per unit distance in the cross-flow direction for a two-dimensional flow.

The self-similar solutions have the form

$$h = V_o^{1/2} \left(\frac{t}{\tau} \right)^\alpha f \left(\frac{x}{V_o^{1/2} \left(\frac{t}{\tau} \right)^\beta} \right) \quad (9.50)$$

Equation (9.45) requires that $\alpha = 2\beta - 1$ while volume conservation (Eq. (9.49)) requires that $\alpha + \beta = -\gamma$, and also that

$$\int_0^\lambda f(\eta) d\eta = \frac{1}{\phi} \quad (9.51)$$

where the leading edge of the flow, $\eta = \lambda$ satisfies $f(\lambda) = 0$. The problem is completed by noting that the rate of change of the mass of the current, associated with the capillary trapping, can be found from the governing equations

$$\frac{d}{dt} \int_0^{\lambda(t/\tau)^\beta} h(x, t) dx = Sh \frac{\partial h}{\partial x} \Big|_{x_+^*} - \frac{S}{1-s} h \frac{\partial h}{\partial x} \Big|_{x_-^*} \quad (9.52)$$

We can solve this problem numerically using a shooting technique: we choose a value of γ and solve Eqs. (9.46–9.51) to find the solution for f . We then test whether the condition (9.52) is satisfied, and iterate until it is satisfied, at which point we have the value γ for that value of s . The relation between γ and s is shown in Figure 9.15; we present the analogous problem of boiling in Chapter 11.

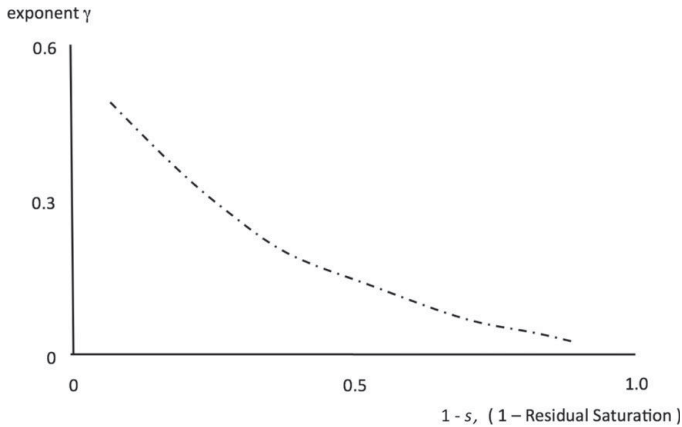


Figure 9.15 Variation of the exponent in the power law decay, $V = V_o(t/\tau)^{-\gamma}$ as a function of the fraction of the fluid which is not trapped by capillarity at the rear of the current, $1 - s$, for the gravity-driven slumping of a current in which a fraction s of the pore space retains fluid as the current evacuates those pores.

9.7 Flow on a slope

In the case that a buoyancy-driven flow migrates through an inclined porous layer with impermeable boundaries there is a component of gravitational acceleration along the slope as well as across the slope. This fundamentally changes the controls on the propagation of the flow, since the alongslope component of gravity exerts a constant buoyancy force which leads to a steady advection along the slope. In contrast, the problems we have considered so far have related to spreading on a horizontal surface for which the flow is controlled by non-linear diffusion-type spreading associated with the cross-flow component of gravity.

We first consider the motion of a buoyant fluid within a deep aquifer for which the fluid will run upwards under the upper sealed boundary and we assume the motion of the fluid in the ambient has only a small influence on the buoyant injected fluid, although we return to this issue later in the chapter. In this case, the injected fluid spreads upslope as a thin current, and the pressure in the cross-slope direction is hydrostatic, leading to the governing equation

$$\frac{\partial h}{\partial t} + S \sin \theta \frac{\partial h}{\partial x} = S \cos \theta \frac{\partial}{\partial x} \left[h \frac{\partial h}{\partial x} \right] \quad (9.53)$$

where the slope has angle θ , to the horizontal, x is the distance upslope and as before

$$S = \frac{k \Delta \rho g}{\mu \phi} \quad (9.54)$$

For a constant flux, Q , per unit width, the flow migrates upslope with depth

$$h = \frac{Q\mu}{k\Delta\rho g \sin\theta} \quad (9.55)$$

while at the nose of the current there is an adjustment zone controlled by the cross-slope component of gravity as given by the expression on the right-hand side of Eq. (9.53). Details of this adjustment are presented by Rayward-Smith and Woods (2011). With a finite release of fluid, the flow migrates upslope and gradually slumps in the cross-slope direction, as governed by the solution for a spreading finite release on a horizontal plane, but now the centre of mass of the fluid migrates upslope with the constant speed (Huppert and Woods, 1995)

$$u = \frac{k\Delta\rho g \sin\theta}{\phi\mu} \quad (9.56)$$

9.8 Capillary trapping in a plume running upslope

In the case of a current running upslope, if there is any capillary trapping of the flow, then the trapping now occurs at the trailing edge of the flow, behind the point of maximum height. This trailing surface migrates more rapidly than the leading surface of the flow by conservation of mass in the current. For a two-dimensional flow the equation for the evolution of the trailing edge of the current, where x is the distance upslope, is

$$(1 - s) \frac{\partial h}{\partial t} + S \sin\theta \frac{\partial h}{\partial x} = S \cos\theta \frac{\partial}{\partial x} \left[\frac{\partial h}{\partial x} \right] \quad (9.57a)$$

where, as in Section 9.6, we denote the residual saturation of the fluid in the pore space, as left by the current, by the variable s , and S is given by Eq. (9.54). In contrast, the leading edge follows the law

$$\frac{\partial h}{\partial t} + S \sin\theta \frac{\partial h}{\partial x} = S \cos\theta \frac{\partial}{\partial x} \left[\frac{\partial h}{\partial x} \right] \quad (9.57b)$$

In the case of a finite release, such that the flow driven by the cross-slope slumping, as given by the right-hand side of (9.57), is slow compared to the advection associated with the along slope component of gravity as given by the second terms on the left-hand side of (9.57), then the flow structure may be calculated by tracking the location along the slope of the advancing and the receding surfaces of the current. Owing to the capillary trapping, the trailing edge of the current advances more rapidly, and so, in making this calculation, at each time, we track the depth at which the leading and trailing currents meet. At that time, this becomes the point of maximum depth in the flow, and only those parts of the current which were originally shallower than this remain mobile (see Figure 9.16). If initially the current location has leading edge given

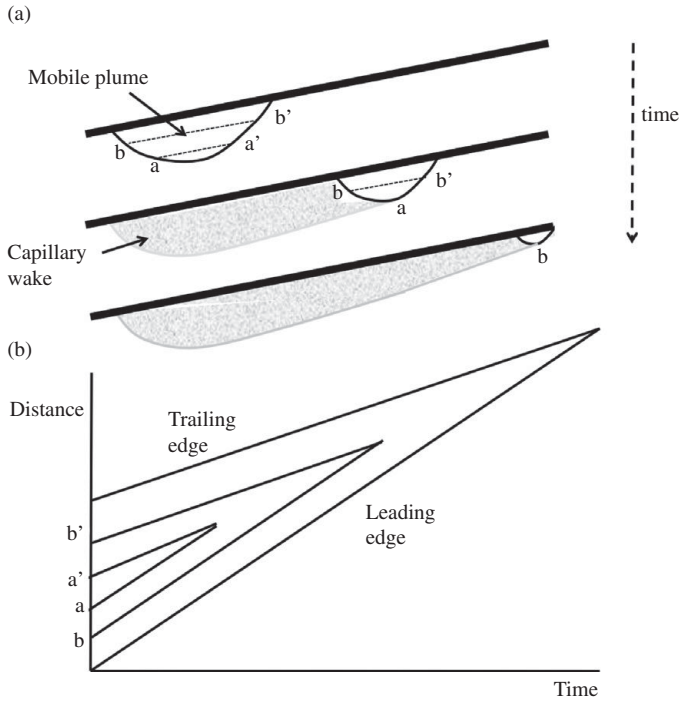


Figure 9.16 Characteristic diagram showing the trailing edge catching up with the leading edge through capillary trapping, leading to waning of the current. Eventually there is no mobile fluid remaining. The points a – a' and b – b' denote points with the same depth on the upstream and downstream face of the plume of mobile CO_2 and the characteristic diagram illustrates how they meet once this depth coincides with the maximum depth of the current.

by $x_+(h)$ and trailing edge given by $x_-(h)$, as a function of the depth, then after time t , those parts of the current on the leading edge, on which the interface ascends, have position

$$x(h, t; x_+) = x_+ + S \sin \theta t \tag{9.58}$$

while those parts of the current on the trailing edge, on which the interface descends and hence results in capillary retention of some of the fluid, have position

$$x(h, t; x_-) = x_- + \frac{S \sin \theta}{(1 - s)} t \tag{9.59}$$

as a function of the depth h . As described above, the depth for which these two positions, one on the ascending and one on the descending current, coincide at each time t corresponds to the maximum depth of the current at that time.

$$x_+ = x_- + S \sin \theta \left[\frac{1}{1 - s} - 1 \right] t \tag{9.60}$$

This solution is illustrated on the characteristic diagram (9.16), also showing the wake of capillary trapped fluid.

This calculation is of relevance for the potential sequestration of CO₂ in which a plume of CO₂ spreads upslope in an aquifer and leaves a capillary trapped wake in its trail. The model provides an estimate for the distance at which a plume ceases to be mobile, by calculating when the rear of the original trailing edge and front of the original leading edge of the flow meet. If the original plume has length L , the time T at which it ceases to be mobile is given by

$$T = \frac{L(1-s)}{S \sin \theta s} \quad (9.61)$$

while the distance travelled and hence lateral extent of the capillary wake, X , from the rear of the original current is

$$X = \frac{L}{s} \quad (9.62)$$

Given that $s \approx 0.1-0.2$, we infer that capillary trapping is a very powerful effect in limiting the lateral distance travelled by a CO₂ plume.

The model also provides an estimate for the shape of the trapped capillary wake of the flow, by tracking the shape of the surface $h(x(t))$ at which the points initially located at $x_+(h, t = 0)$ and $x_-(h, t = 0)$ meet. Although the model neglects the effects of the non-linear diffusive spreading, it provides a good leading-order approximation for an initially long and thin plume, as may be determined by full numerical solution of Eqs. (9.57a,b).

9.9 Confined gravity-driven flows

The above analyses of buoyancy-driven flows are simplified in that we have neglected the flow of the original reservoir fluid, assuming the permeable layer is deep. However, in many cases, geological strata involve many layers of finite depth (Chapter 2), and so the injection of fluid can generate a comparable flow of the original formation fluid ahead of the invading front. When there is a significant density contrast between the fluids, the buoyancy force will cause the flow front to spread out and so the motion of the invading fluid can still be described in terms of the depth of the interface, but we now need to account for both fluids. There are a series of flow geometries and processes which may be examined, building from the unconfined problems described above. We include two important examples, the confined radially spreading current, and the confined two-dimensional flow up a sloping layer. We then turn to a more general problem of a three-dimensional gravity-driven flow along a sloping layer, in which there is motion both downslope and across-slope.

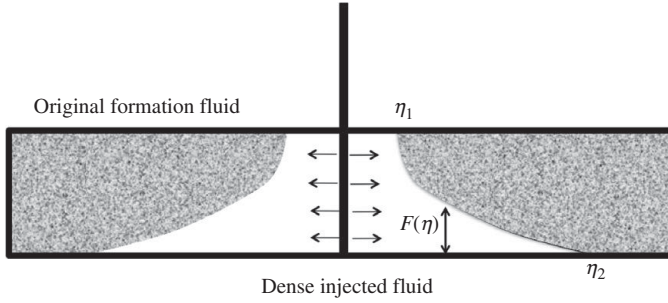


Figure 9.17 Schematic of a dense current flowing radially into a porous layer from a central, maintained source.

In the case of injection of a fluid of density ρ from a central well with a volume flow rate $Q(t)$ into an aquifer of depth H containing fluid of density $\rho - \Delta\rho$, we expect the flow to spread out along the lower boundary and become long and thin (Figure 9.17) and, to leading order, the vertical pressure gradient will be hydrostatic. However, there is now a net radial pressure gradient associated with the overall flow, $p_o(r, t)$, which we take to apply on the lower boundary of the domain, $z = 0$. Assuming the vertical pressure is hydrostatic, as occurs with a long thin flow, we find the general expression for the pressure

$$p(r, z, t) = p_o(r, t) + g\rho z \quad \text{if } 0 < z < h \tag{9.63}$$

$$p = p_o + \rho gh + (\rho - \Delta\rho)g(z - h) \quad \text{if } h < z < H \tag{9.64}$$

The local conservation of mass in the lower layer has the form

$$\phi r \frac{\partial h}{\partial t} = \frac{\partial}{\partial r} (ru_l h) \tag{9.65}$$

while in the limit of incompressibility, the flux of fluid, $Q(t)$, is constant at each radius, which requires that

$$Q = -\frac{2\pi rk}{\mu} \left[H \frac{\partial p_o}{\partial r} + \Delta\rho g(H - h) \frac{\partial h}{\partial r} \right] \tag{9.66}$$

Darcy’s law describes the horizontal flow in each layer,

$$u_l = -\frac{k}{\mu} \frac{\partial p}{\partial r} \quad \text{if } 0 < z < h \tag{9.67}$$

$$u_u = -\frac{k}{\mu} \frac{\partial p}{\partial r} \quad \text{if } h < z < H \tag{9.68}$$

Here, we have taken the viscosity in each layer to be the same, but this assumption may be relaxed, as described by, for example, Dudfield and Woods (2013). Combining

these equations leads to the relation for the depth of the invading fluid as a function of the radius,

$$r \frac{\partial h}{\partial t} + \frac{Q}{2\pi\phi H} \frac{\partial h}{\partial r} = \frac{k\Delta\rho g}{\phi\mu H} \frac{\partial}{\partial r} \left(rh(H-h) \frac{\partial h}{\partial r} \right) \quad (9.69)$$

In practice, to solve this equation, one imposes a far-field boundary at some finite distance R , but while the interface, $h(r, t)$, is located within this radius, the flow passing R is a uniform pressure-driven flow of the original formation fluid. It is worth noting that in reality, the effects of compressibility, in both the rock and the fluid, become important on very long scales, typically beyond the scale of the gravitational intrusion. They act to dissipate this pressure, as we describe in Chapter 12 in our discussion of compressible flow; as a result, near the source, the effectively incompressible gravity current dynamics we present herein applies.

Our interest lies in the shape and rate of propagation of the interface, $h(r, t)$, between the injected and original fluid, and this is given by a similarity solution of the form

$$h = HF(\eta) \quad \text{where} \quad \eta = r \left(\frac{2\pi\phi H}{Qt} \right)^{\frac{1}{2}} \quad (9.70)$$

and $F(\eta)$ satisfies

$$\left(1 - \frac{\eta^2}{2} \right) \frac{dF}{d\eta} = \Gamma \frac{d}{d\eta} \left[\eta F(1-F) \frac{dF}{d\eta} \right] \quad (9.71)$$

with the parameter

$$\Gamma = \frac{2\pi k\Delta\rho g H^2}{\mu Q} \quad (9.72)$$

Γ represents the balance between the flow rate associated with buoyancy-driven flow, compared to the flow rates associated with the injection, and so as Γ increases we expect more gravitational slumping.

In solving Eq. (9.71) we require boundary conditions, and in this context we note that at the origin, there is no flux of the original formation fluid, so that we require $F = 1$ at $\eta = 0$. We therefore seek solutions of the form

$$\begin{aligned} F &= 1 \quad \text{for} \quad 0 < \eta < \eta_1, \\ 0 < F < 1 &\quad \text{for} \quad \eta_1 < \eta < \eta_2 \quad \text{and} \\ F &= 0 \quad \text{for} \quad \eta > \eta_2 \end{aligned} \quad (9.73)$$

Equation (9.71) requires that

$$\frac{dF}{d\eta} = \frac{\eta_1^2 - 2}{2\Gamma\eta_1} \quad \text{at} \quad \eta = \eta_1 \quad (9.74)$$

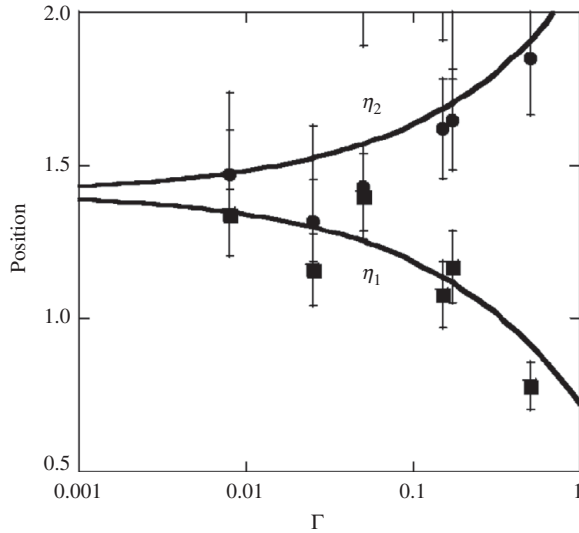


Figure 9.18 Variation of the inner and outer radius of the radially spreading, confined gravity current, η_1 and η_2 as a function of the gravitational parameter Γ . Data are from experiments of Mitchell and Woods (2006).

while

$$\frac{dF}{d\eta} = \frac{2 - \eta_2^2}{2\Gamma\eta_2} \quad \text{at } \eta = \eta_2 \quad (9.75)$$

Numerical calculations have determined the values of η_1 and η_2 as a function of Γ and these are shown in Figure 9.18 along with a series of experimental data points, reported by Mitchell and Woods (2006), with which the model was compared. In these experiments, dense saline solution was injected into a water-saturated bead pack, measuring 1 m by 1 m in horizontal dimension and 10 cm deep. The motion of the fluid was recorded through the side walls and base of the tank, to measure the values η_1 and η_2 , for a range of injection rates and density differences. Although there is scatter in the experimental data, the results do concur with the model.

9.10 Confined buoyancy-driven flow on a slope

Buoyancy-driven flow in a confined aquifer on a slope leads to an alongslope and cross-slope component of gravity as well as the alongslope pressure gradient; the problem is of interest as it leads to an advection–diffusion equation, in which the advection term has a coefficient which varies with the depth of the fluid. As a result, the flow may be solved using the method of characteristics, in an analogous fashion to the

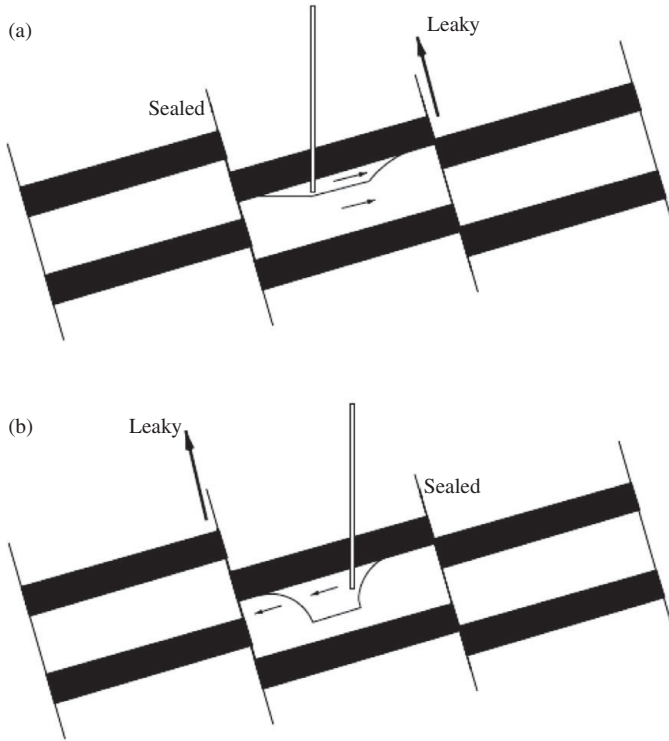


Figure 9.19 Illustration of a confined gravity-driven flow on a slope produced by injection into faulted geological strata; (a) corresponds to the case with an upslope leaking fault and (b) to the case with a downslope leaking fault. After Gunn and Woods (2011).

dynamics of the capillary trapped CO_2 plume running upslope, which we considered earlier. However, the wave speeds are now non-linear, and in some cases, the non-linear model leads to the prediction of wave steepening and hence localised jumps in depth of the fluid, while in other cases, it leads to the prediction of dispersion and spreading out of gradients in the depth of the current. Although the algebra is somewhat involved, we develop the non-linear advection–diffusion equation to enable illustration of some of these effects. MacMinn and Juanes (2010, 2011) and Gunn and Woods (2011) have considered the motion of a plume of buoyant fluid migrating up a sloping aquifer allowing for a source and a sink, which may be upslope or downslope, depending on the structure of the geological strata (Figure 9.19) and we draw from their analyses. This problem brings in more of the complexity of a real flow system, in that now we have a viscosity contrast, a density contrast and an applied flow (Figure 9.20). However, in this section our analysis remains two dimensional, as appropriate for a current supplied from a line source which is directed across-slope.

With a long thin aquifer, we anticipate again that the flow will become parallel to the boundary of the system, the x -axis and the cross-layer pressure gradient, in the

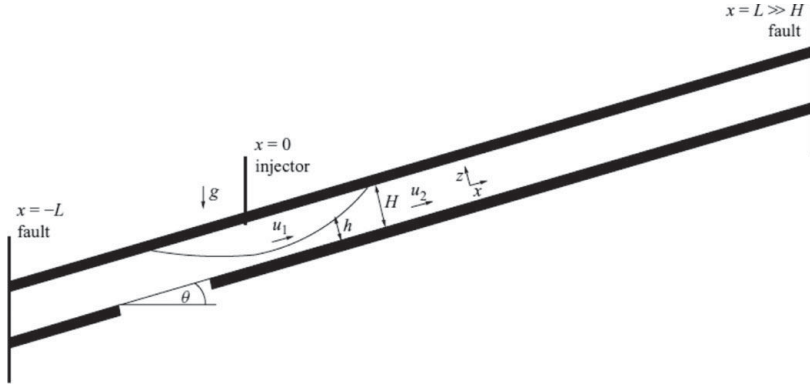


Figure 9.20 Schematic of a confined gravity-driven flow running upslope.

z direction will then be dominated by the hydrostatic pressure

$$p(x, z, t) = p_o(x, t) - \rho g z \cos \theta \quad \text{for } z < h \quad (9.76)$$

$$p(x, z, t) = p_o(x, t) - \Delta \rho g (z - h) \cos \theta - \rho g z \cos \theta \quad \text{for } z > h \quad (9.77)$$

If we apply Darcy's law to each layer, it takes the form

$$u_1 = -\frac{k}{\mu_1} \left(\frac{\partial p_o}{\partial x} - \Delta \rho g \cos \theta \frac{\partial h}{\partial x} + (\rho - \Delta \rho) g \sin \theta \right) \quad (9.78)$$

$$u_2 = -\frac{k}{\mu_2} \left(\frac{\partial p_o}{\partial x} + \rho g \sin \theta \right) \quad (9.79)$$

and the conservation of mass may be written in terms of the total flux at each point in the aquifer, with value Q between the source, at $x = 0$, and sink, at $x = L$, and zero elsewhere

$$Q_1 = (H - h)u_1 + hu_2 \quad \text{for } 0 < x < L \quad (9.80)$$

and

$$(H - h)u_1 + hu_2 = 0 \quad \text{for } x > L \quad \text{or } x < 0 \quad (9.81)$$

Combining these relations with the local conservation of mass for each layer, and introducing the dimensionless variables

$$\tau = t/t_s = \frac{\Delta \rho g k \sin \theta}{\mu_1 \phi H} t, \quad \zeta = \frac{x}{H}, \quad \hat{h} = \frac{h}{H} \quad (9.82)$$

the system reduces to the form (cf. Gunn and Woods, 2011)

$$\frac{\partial \hat{h}}{\partial \tau} = V \frac{\partial}{\partial \zeta} \left(\frac{\hat{h}(1 - \hat{h}) \left(1 + \cot \theta \frac{\partial \hat{h}}{\partial \zeta} \right) - \Gamma \hat{h}}{1 - \hat{h}(1 - V)} \right) \quad \text{for } 0 < \zeta < 1 \quad (9.83)$$

between the source and sink, and

$$\frac{\partial \hat{h}}{\partial \tau} = V \frac{\partial}{\partial \zeta} \left(\frac{\hat{h}(1 - \hat{h}) \left(1 + \cot \theta \frac{\partial \hat{h}}{\partial \zeta} \right)}{1 - \hat{h}(1 - V)} \right) \quad \text{for } \zeta > L \quad \text{and} \quad \zeta < 0 \quad (9.84)$$

elsewhere in the aquifer. In these expressions, the dimensionless controlling parameters are the viscosity ratio V and the ratio of the buoyancy flow to the forced flow, Λ defined as

$$V = \frac{\mu_1}{\mu_2}, \quad \Lambda = \frac{Q_1 \mu_1}{\Delta \rho g k H \sin \theta} \quad (9.85)$$

Equation (9.83) and (9.84) can be re-cast as advection–diffusion equations. As the current spreads out along the layer, the advective component dominates the flow, as described by the non-linear wave equation

$$\frac{\partial \hat{h}}{\partial \tau} + f_{\pm}(\hat{h}) \frac{\partial \hat{h}}{\partial \zeta} = 0 \quad (9.86)$$

where the speed of surfaces of constant \hat{h} vary non-linearly with \hat{h} according to the relations

$$f_{-}(\hat{h}) = -V \left(\frac{(1 - V)\hat{h}^2 - 2\hat{h} + 1}{(1 - \hat{h}(1 - V))^2} \right) \quad (9.87)$$

and

$$f_{+}(\hat{h}) = -V \left(\frac{(1 - V)\hat{h}^2 - 2\hat{h} + 1 - \Lambda}{(1 - \hat{h}(1 - V))^2} \right) \quad (9.88)$$

Here the + and – correspond to points up- and downslope of the source, with the sink located upstream of the source in this case. We can understand the evolution of the flow by considering how the speed of characteristics f_{\pm} vary with height of the interface above the base of the aquifer, \hat{h} . Some typical examples of the variation of f_{+} as a function of h are shown in Figure 9.21. Here it is seen that in the upper part of the aquifer, f_{+} is positive, whereas near the base of the aquifer f_{+} is negative. The change in the shape of the curve arises as the viscosity ratio and flux parameter change. With a smaller viscosity of the buoyant fluid, the region in which f_{+} is positive is smaller while with a larger flux, the minimum value of \hat{h} at which $f_{+} > 0$ is smaller. If f_{+} is positive then the characteristics, and hence current of that depth tend to advance upslope (Figure 9.21). In contrast, if for some values of \hat{h} , f_{+} is negative, then the current does not propagate upslope in this part of the aquifer, as shown on the regime diagram (Figures 9.22, 9.23). Also, in the case that the value of f_{+} increases with \hat{h} ,

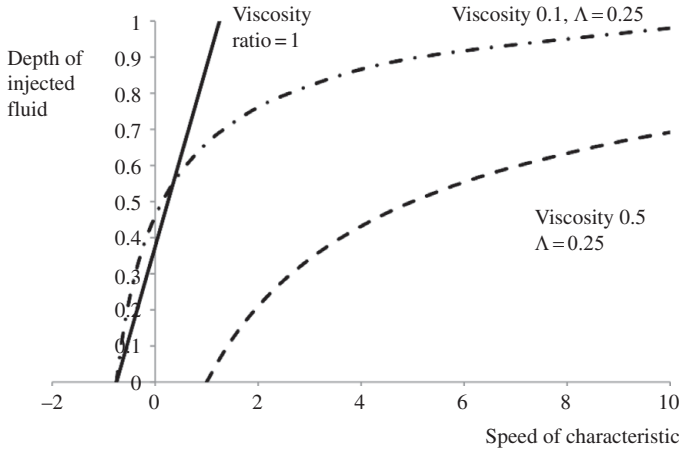


Figure 9.21 Speed of characteristics in the upslope direction, f_+ ; for the flow located between the source and sink shown as a function of the height of the interface above the base of the aquifer.

the characteristics near the upper boundary travel more quickly, and so the current disperses along the top boundary, essentially as a gravity tongue. Indeed this has an analytical solution given by

$$\hat{h} = \frac{1}{1 - V} \left(1 - \left(1 - \frac{\eta - V(\Lambda - 1)}{\eta + \frac{V}{1-V}} \right)^{1/2} \right) \tag{9.89}$$

provided $\hat{h} > 0$. The region in which the gravity tongue develops below the top boundary depends on the flux in this layer. If the current has a large flux, the flow fills the whole depth of the aquifer, but for smaller fluxes, the flow only migrates through the upper part of the aquifer. Using the functional form for f_+ we find this reduces to the requirement that

$$\Lambda > 1 \tag{9.90}$$

This suggests that if the input is not sufficiently fast, and the injected fluid is of sufficiently low viscosity, it will bypass much of the fluid in the formation, forming a gravity tongue.

The input fluid downslope of the injector becomes stationary in equilibrium, and so, in this case, the input fluid adjusts to having a horizontal boundary with the original fluid, as seen in Figure 9.22. In the case that the characteristics travel most rapidly at $h = 0$, corresponding to the base of the layer, then the input fluid advances up the slope with a near planar front. Given the expression for f_+ it can be shown that this occurs in the case that

$$V > 1 \text{ and } \Lambda > \frac{V}{V - 1} \tag{9.91}$$

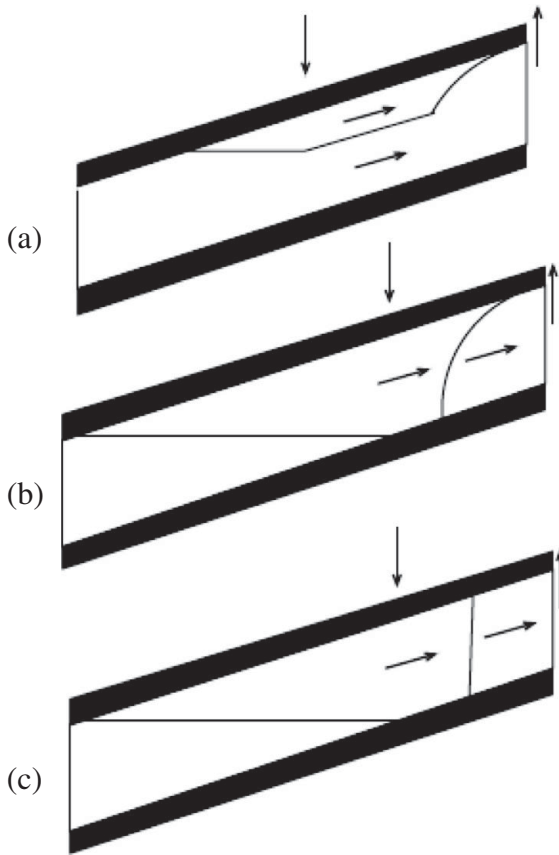


Figure 9.22 Three types of flow pattern as a function of the viscosity ratio and flow rate. (a) with a small flux the current does not flood the depth of the aquifer; (b) with a larger flux the current floods the whole depth of the aquifer; (c) if Eq. (9.91) is satisfied a shock forms which leads to a planar front travelling upslope. After Gunn and Woods (2011).

In Figure 9.23 we summarise this brief discussion of the different topology of the current in terms of the values of Λ and V , the two control parameters. Curves have been included which delineate the different types of behaviour of the flow (Figure 9.23) (cf. Gunn and Woods, 2011).

If there is a background flow in the aquifer this will modify these flows, and can lead to a wider variety of flow regimes. Also, if the producer well is located downdip of the injector, then in some cases a fraction of the buoyant injected fluid continues updip, leading to a greater flow of the original formation fluid downdip. This effect can be key for enhancing recovery of the formation fluid, rather than the short-circuiting of the injection fluid which arises in the case that the producer well is updip. Further details of the different flow morphology for a constant injection rate are given by Gunn and Woods (2012). The complementary problem of the motion of a volume of buoyant fluid, including capillary trapping, is given by McKibben and Juanes (2011).

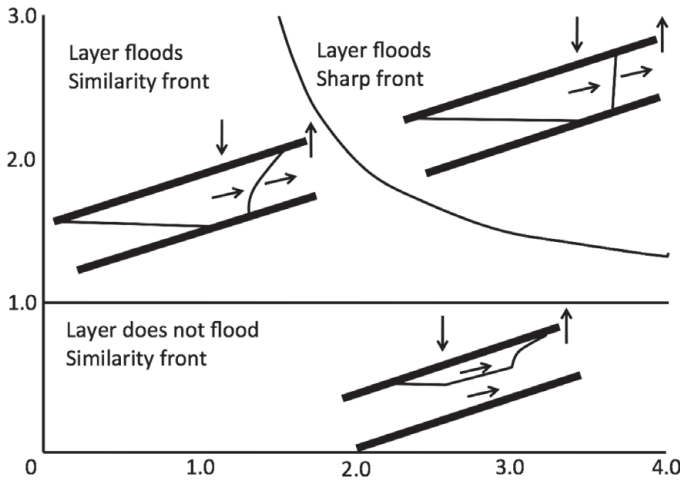


Figure 9.23 Regime diagram illustrating the three different flow patterns as a function of the viscosity ratio (vertical axis) and flow rate (horizontal axis) for a current running upslope in a confined aquifer. After Gunn and Woods (2011).

9.11 Three-dimensional gravity currents

The analysis presented in this chapter has primarily focused on two-dimensional flows, which are idealisations, but which may correspond in practice to the flows which develop from horizontal line wells either (a) within a compartmentalised or channelised system, in which there are lateral boundaries to the flow preventing the spreading of the flow in the along-well direction beyond the extent of the well, or (b) for that part of a flow in which the length of the well exceeds the lengthscale of any along-well slumping of the current. However, with a point source of buoyant fluid, or a relatively short line source in an inclined system, the flow will tend to run upslope, being confined by the upper boundary of the aquifer, but it will also tend to spread in the cross-slope direction, thereby forming a three-dimensional plume (Figure 9.24).

With a steady source volume flux, as the plume spreads upslope, it will become progressively thinner as it spreads in the cross-slope direction, and will eventually develop a steady-state shape. The upslope component of gravity leads to a constant speed in the upslope direction, and so this acts as a time-like coordinate, while the motion in the cross-slope direction arises from the gradient of the height interacting with the component of gravity in the cross-slope direction, leading to cross-slope spreading of the flow analogously to Section 9.1. In order to describe this flow, we consider a three-dimensional coordinate system, in which x denotes the cross-slope direction, y the upslope direction and z is normal to the slope. If the slope makes an angle θ to the horizontal, then the pressure within the spreading plume of buoyant fluid, at a point (x, y, z) relative to the

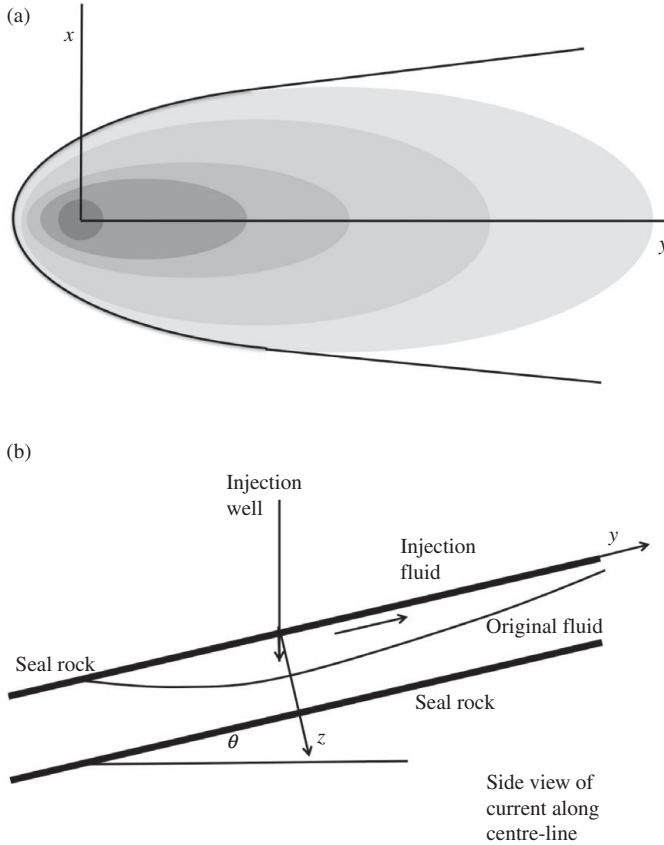


Figure 9.24 Schematic of a three-dimensional gravity current spreading upslope and cross-slope under gravity from a constant source. The top panel illustrates the variation of the depth of the current with distance from the source. The lower panel illustrates the variation of the depth along a line within the current, running in the upslope direction, parallel to the y -axis, as shown in panel a.

source, which we assume is located on the upper boundary of the aquifer, will be

$$P(x, y, z) = P_o + (\rho_w - \rho_g)gh \cos \theta + \rho_ggz \cos \theta - \rho_wgy \sin \theta \tag{9.92}$$

where ρ_w and ρ_g are the densities of the original and injected fluid and Darcy’s law for the motion of the injected fluid takes the form

$$\mathbf{u} = -\frac{k}{\mu} [\nabla P - \rho_g \mathbf{g}(0, -\sin \theta, \cos \theta)] \tag{9.93}$$

We now consider the case of a constant volume flux of fluid, Q , issuing from a source. The in-plane, depth averaged flux of source fluid, at each point, is then given by $\mathbf{F} = \mathbf{u}h$ and by conservation of mass, in steady state, this requires

$$\nabla \cdot \mathbf{F} = \frac{k\Delta\rho g}{\mu} \left[\cos \theta \nabla(h\nabla h) - \sin \theta \frac{\partial h}{\partial y} \right] = 0 \tag{9.94}$$

Once the flow has ascended the slope a sufficient distance that it is much thinner than the depth of the permeable layer, $h \ll H$, then we expect the flow to have a relatively small gradient in the upslope direction y , so the flux conservation relation reduces to the form

$$\cos \theta \frac{\partial^2 h^2}{\partial x^2} = 2 \sin \theta \frac{\partial h}{\partial y} \quad (9.95)$$

This is directly analogous to the equation governing the one-dimensional gravity-driven slumping of a current on a flat surface (Section 9.1, Eq. (9.10)), and so we infer that the solution for the height of the current has the form

$$h = \frac{H^{4/3} \tan \theta}{6y^{1/3}} \left(\eta_o^2 - \frac{x^2}{H^{4/3} y^{2/3}} \right) \quad (9.96)$$

where for convenience we have scaled the depth of the flow, h , so that

$$H = \left(\frac{Q}{u \sin \theta \tan \theta} \right)^{1/2} \quad (9.97)$$

and the lengths, x and y so that

$$\eta_o = \left(\frac{9}{2} \right)^{1/3} \quad (9.98)$$

This approximate solution is compared with a full numerical solution of Eq. (9.94) in Figure 9.25, illustrating the close correspondence of the asymptotic solution with the full numerical solution as the flow migrates upslope from the source. We note that there is a non-trivial region of adjustment from the source to this asymptotic far-field solution, since near the source, the flow may fill the whole depth of the aquifer (details of this transition are explained by Farcas and Woods, 2013); we also note that in these steady solutions there is no motion of the original reservoir fluid. This transient problem for a confined system has been discussed by DeLoubens and Ramakrishnan (2011).

It is possible to model the leakage of the current through the upper boundary, as would arise in the case of a network of fractures in the overlying seal rock (cf. Section 9.2). In that case, the flux conservation law becomes

$$\sin \theta \frac{\partial h}{\partial y} = \cos \theta \left(h \frac{\partial h}{\partial x} \right) - \frac{k_b h}{kb} \quad (9.99)$$

The solution for the steady draining through a uniform permeability boundary, developed in Section 9.2, can also be applied to this problem to describe the maximum distance upslope that the plume reaches before it has all drained through the boundary. By comparison with further full numerical solutions of the governing equation, Farcas and Woods (2013) have shown that these approximate solutions provide a good

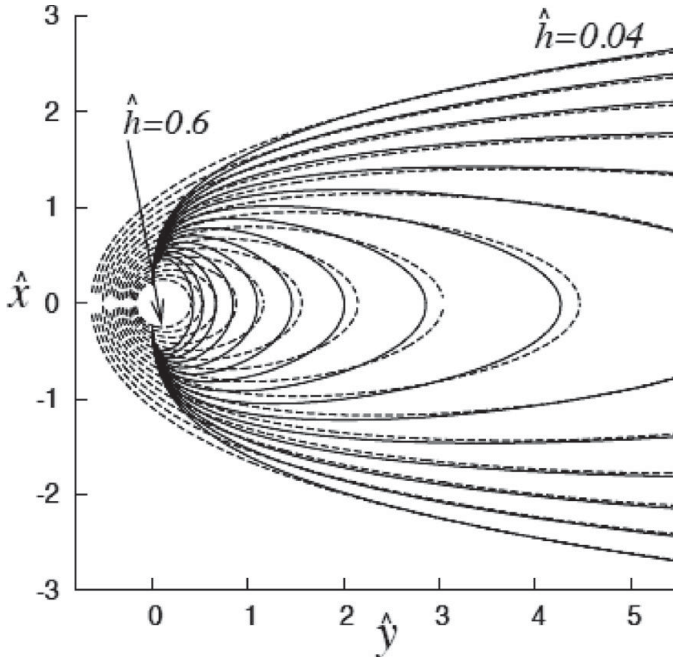


Figure 9.25 Comparison of the full numerical solution for the shape of a plume running updip from a source with the asymptotic solution for the flow in the far field Eq. (9.96). After Farcas and Woods (2013).

description of the draining flow, in the case that the draining is slow compared to the scale of adjustment to this solution from the near-source flow.

Such draining flows might provide insight into the shape of the plumes of CO_2 which may spread out on the upper low permeability boundary of a confined aquifer. For example, there are seismic observations of a plume spreading over the lowest low permeability horizon above the CO_2 injection well at the Sleipner field in the North Sea (Figure 9.26). The figure can be interpreted as showing the variation of the depth of the CO_2 plume spreading along the boundary of the permeable layer. The finite extent of the plume suggests that it may be draining upwards through the geological strata, so the low permeability rock may only provide a partial barrier to upward flow. The depth contours associated with a very simplified model of a buoyant plume running updip, and leaking through a permeable boundary, as governed by Eq. (9.99), and using parameters comparable to our understanding of the Sleipner field are shown by dotted lines in Figure 9.26. Although not identical to the Sleipner plume, it may be that this model captures some of the dynamics controlling such flows; we do note with caution that other processes such as dissolution can also impact the dispersion of such CO_2 plumes and hence interpretation of the data.

The models presented in this chapter provide a simplified picture of some complex buoyancy-driven flow problems, which enable assessment of the effect of different

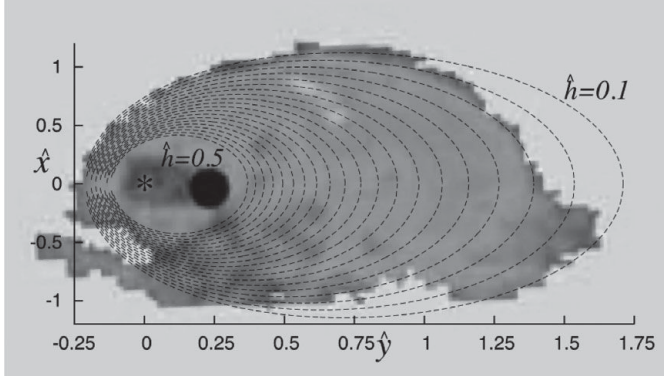


Figure 9.26 Comparison of the upslope draining plume model Eq. (9.99) with the shape of the plume in Horizon 1 observed from seismic data at the Sleipner field in the North Sea. After Farcas and Woods (2013). A black and white version of this figure will appear in some formats. For the colour version, please refer to the plate section.

processes on the dynamics. There are numerous other phenomena associated with buoyancy-driven flows in porous media and in the next chapter we explore the motion of vertical plumes, and some of the dispersion effects which can arise, especially when the flows interact with the geological structure of the reservoir.

9.12 Exercises

1. Fluid is injected into a horizontal reactive porous rock of depth H with a constant volume flux Q per unit length of a long horizontal injection well. The fluid reacts with the rock, and its density changes from the injection density $\rho - \Delta\rho$ to the density of the original fluid in the formation, ρ , which is in equilibrium with the reactive porous matrix. The reaction front is located in the region $h(x, t) < y < H$, and the speed of the reaction front is given by λu where u is the Darcy speed of the fluid at the interface. If the permeability of the matrix changes from k_l to k_u as a result of the reaction of the injected fluid with the matrix, show that the position of the reaction front (see Figure 9.27) is given by the equation

$$\frac{\partial F}{\partial t} + \frac{\partial}{\partial \zeta} \left[\frac{F}{1 + (\beta - 1)F} \right] = B \frac{\partial}{\partial \zeta} \left[\frac{F(1 - F)}{1 + (\beta - 1)F} \frac{\partial F}{\partial \zeta} \right] \quad (9.100)$$

where $\beta = k_u/k_l$ and the depth of the reacted zone is $F = 1 - h/H$. You may assume $B = \Delta\rho g H k_l / \mu Q$ where μ is the fluid viscosity, and Q is the constant injection rate per unit length of the injection well, and $\tau = t Q \lambda \beta / H^2$ where the dimensionless position ζ is given by $\zeta = x/H$.

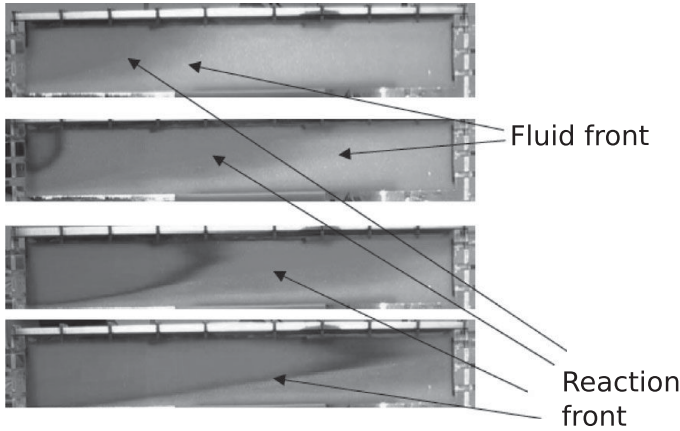


Figure 9.27 Illustration of a reaction front migrating through a confined porous layer. The reaction is driven by the injection of fresh water which reacts with salt powder in the porous layer. The original fluid in the formation is saturated salt solution in equilibrium with the salt powder, and on reaction the injected fluid density matches that of the original formation fluid. The colour of the injected fluid is changed from blue to red to help visualise the flow. After Verdon and Woods (2007). A black and white version of this figure will appear in some formats. For the colour version, please refer to the plate section.

Show that in the limit of small B this equation has solution

$$F = \frac{1}{\beta - 1} \left[\left(\frac{\tau - \tau_o}{\zeta - \zeta_o} \right)^{1/2} - 1 \right] \text{ for } \frac{\tau - \tau_o}{\beta^2} < \zeta - \zeta_o < \tau - \tau_o \quad (9.101)$$

while $F = 1$ for $\zeta < \zeta_o + (\tau - \tau_o)/\beta^2$ and $F = 0$ for $\zeta > (\tau - \tau_o) + \zeta_o$. Note Eq. (9.101) is analogous to the equation governing the average concentration of a fluid mixture when one fluid displaces a second miscible fluid of smaller mobility in a confined aquifer (Bear, 1972; Yortsos and Salin, 2006; Verdon and Woods, 2007).

2. Develop the equation for the motion of a gravity current in a porous layer in which the permeability increases with height from the base of the layer as $k(y) = k_o y$. Develop solutions for the rate of advance of the flow and the shape of the flow produced by a finite release of fluid. This problem represents an idealisation of the flow through a turbidite layer in which there is a vertical grading of the grain size.
3. CO_2 is injected from a long horizontal well into an aeolian reservoir, consisting of a laterally extensive inclined layer of rock, with angle θ to the horizontal, and of cross-layer thickness H , with $0 < y < H$. The permeability increases along the layer according to the relation $k(x) = k_o + k_1 x$. A discrete cloud of CO_2 is injected into the formation of volume V per unit length of the injection well, located at $x = 0$. Assuming the flow spreads upslope, and that a fraction f is capillary trapped from the wake of the flow, calculate the shape of the region of capillary trapped CO_2 produced at the wake of the flow, and the total distance travelled by the mobile cloud.

10 Buoyancy effects on dispersion

In Chapter 5, we discussed some of the mechanisms which can lead to the intermingling and mixing of fluids across interfaces as a result of both pore-scale dispersion, which appears to be dominated by mechanical mixing at high Peclet number, and macroscopic dispersion which is governed by the heterogeneity of the formation on larger scales, associated with lenses or layers of different permeability embedded in the medium. In Chapter 6, we briefly mentioned the role of buoyancy in promoting or suppressing the stability of a fluid interface and, in particular, showed that when a dense fluid overlies a less dense fluid, the interface may become unstable and develop fingers. With miscible displacements, these fingers can lead to intermingling and some mixing of the fluids, relative to the advance of a planar front. In the previous chapter, we explored some of the macroscopic flow patterns which may develop as a result of the buoyancy forces for flows in horizontal or inclined permeable strata. In particular we identified how the density interface between fluids tends to spread out along the boundaries of the flow domain, for example as a result of the formation of gravity currents. These flows may be regarded as leading to macroscopic mixing of the fluid through the combination of the buoyancy force and the structure of the porous formation. In this chapter we draw together some of these ideas to explore the controls on the intermingling and mixing of fluids for which there is a buoyancy contrast. Understanding this mixing can be critical in a number of situations. For example, with enhanced oil recovery, the density of the injected water may be changed with time as the composition of the water is changed; for example, a number of operators change the salinity of the injected water as this has been shown to have an impact on the residual saturation of oil. In an environmental context, the mixing of fresh and saline water in near coastal aquifers, or produced by intermittent, interseasonal rainfall, can again lead to mixing of different water masses.

In many geological systems, the rock strata are layered, and low permeability barriers between the more permeable layers may provide seal or partial seal for the flow. Furthermore, within individual layers, especially in fluvial type systems, there may be local lenses of shale, or deposits of higher permeability rock, as discussed in Chapters 2 and 5. With a buoyant fluid migrating through such a rock, the structure of the flow may be controlled by the geometry of the relatively impermeable layers

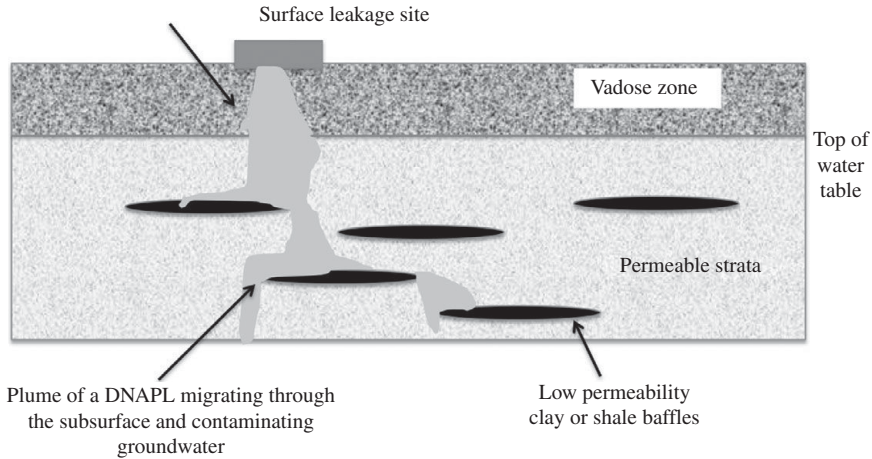


Figure 10.1 Illustration of the dispersal of a plume of a dense pollutant, perhaps such as DNAPL following leakage from a surface source, as it migrates through the subsurface, passing over impermeable baffles.

between the main layers of permeable rock. This may lead to dispersion and spreading of the buoyant fluid as it migrates through the formation. As well as the challenge for water flooding of reservoirs and mixing of fresh and saline water, such buoyancy-driven dispersion of a flow front can be key for the prediction of the path followed by LNAPL and DNAPL contaminants spreading through the subsurface, since the distribution of these liquids in the porous layer controls the source conditions for the subsequent dissolution as the background hydrological flow advances through the formation (Figure 10.1; Bear and Cheng, 2010). An analogous problem concerns the prediction of the path followed by hydrogen gas in the event that it escapes from a geological waste repository and migrates through the geological strata. Again, the dispersion of the gas and its distribution in structural traps within the formation can control the rate and pattern of dissolution of the gas in the background hydrological flow.

Another important example relates to the migration of very large volume plumes of CO_2 injected into subsurface aquifers for geological sequestration. Figure 10.2 illustrates the pattern of CO_2 spreading through the Sleipnir field in the Norwegian North Sea; the aquifer consists of nine main layers of permeable sediment, separated by low permeability shale layers which have some connectivity either through fractures or owing to the piecewise continuous nature of the lenses of low permeability material between the permeable strata (cf. Figure 9.26). Figure 10.2 shows the seismic reflection amplitudes of a series of horizons within a cross-section of the strata, taken at seven different times. The difference between the surveys and the initial survey is indicated by the brightening of the reflection intensity at certain horizons and this has been interpreted to indicate the presence of the CO_2 plume (Boait *et al.*, 2012), although precise determination of the plume location is challenging owing to the influence of

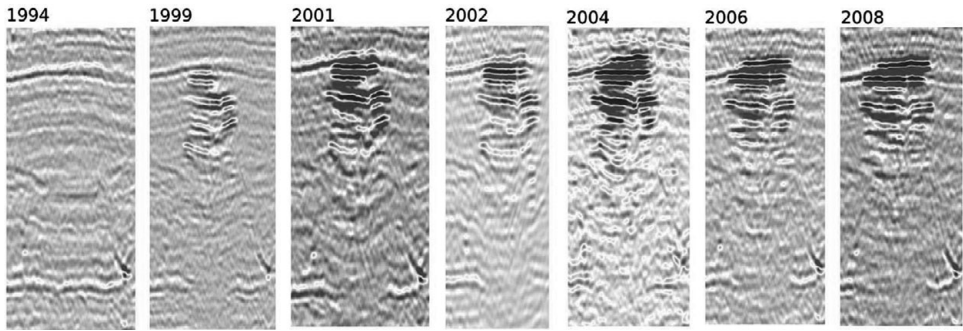


Figure 10.2 Illustration of the seismic reflection profile associated with the migrating cloud of CO₂ spreading in the Sleipnir field in the Norwegian North Sea. Seven images are shown at progressively later times following the start of the injection of CO₂, indicating the migration pattern of the CO₂. After Boait *et al.* (2012). A black and white version of this figure will appear in some formats. For the colour version, please refer to the plate section.

both fluid pressure changes and changes in the fluid saturation (water and CO₂) in the pore space on the reflection amplitude (Bickle *et al.*, 2007; Dudfield and Woods, 2013). It is seen that the CO₂ plume has ascended into all the nine layers, covering a vertical distance of order 200 m while it has spread laterally over distances of order 2–3 km, in each of the layers. This pattern of CO₂ dispersal produced during the injection phase is important since it then controls the distribution of the CO₂ which may be structurally trapped, or capillary trapped, and which will dissolve into the aquifer water over a longer time-scale as the aquifer water migrates through the formation.

An important process during CO₂ geo-sequestration concerns the dissolution of CO₂ into the formation water, which leads to the generation of CO₂ saturated water. This transition represents an important step in the risk management of the CO₂, since the dissolution into water is thought to substantially reduce the likelihood that the CO₂ can then migrate back to the Earth's surface. This is because CO₂ saturated water is typically denser than the original formation water. In modelling the dissolution process, the key issue concerns the rate at which unsaturated formation water can come into contact with the CO₂, since CO₂ is only weakly soluble in the formation water; typically a volume of water of order 100 times that of the CO₂ is required to dissolve the CO₂. Since the CO₂ saturated water is miscible with the unsaturated water, understanding the controls on the rate of mixing and intermingling of the saturated water with the original formation water is therefore key in determining the controls on the ongoing dissolution of the CO₂ (Szulczewski *et al.*, 2014).

We first review some of the effects of buoyancy contrasts on the dispersion and mixing across an advancing fluid interface. We then explore some models of buoyancy-driven flows in idealised geometries to provide insight into the key role that buoyancy can have on mixing. This includes exploring the structure of vertical buoyancy-driven plumes and buoyancy-driven exchange flows within heterogeneous rock, and the role

of layering in dispersing buoyancy-driven flows. Finally we turn to the long-term dispersive mixing of two miscible fluids of different density, in which the cross-flow diffusion balances the along-flow shear produced by the buoyancy. We note that there are still many more processes to explore on this subject.

10.1 Buoyancy effects on pore-scale mechanical dispersion

In a number of situations, a gravitationally unstable front may advance through a porous layer, for example as a result of the injection of water of density different from that in the formation. Although in some cases, this may be unstable to fingering, in other cases the buoyancy contrast may enhance the dispersive mechanical mixing across the interface. Conversely, with a stable density gradient one might imagine that the buoyancy forces suppress the pore-scale mechanical mixing. In Chapter 5, we explored how, for a passive tracer, pore-scale mixing was controlled by the local Peclet number of the flow, $Pe = ud/D$ where u is the pore-scale speed and d the pore size, while D is the molecular diffusivity. When there is a density contrast across a fluid–fluid front, we can introduce the ratio of the local buoyancy-driven flow speed $U = \frac{k\Delta\rho g}{\mu}$, which is a vertical flow, and the background vertical flow speed u to form a buoyancy parameter

$$\Gamma = \frac{k\Delta\rho g}{\mu u} = \frac{U}{u} \quad (10.1)$$

Following the work of Pfannuch (1963), Fried and Combarous (1971) and Bear (1972), there have been several studies to explore the mixing and dispersion across density interfaces. Here we report on a study by Menand and Woods (2005) who carried out a series of detailed experiments in a porous bead pack to explore the mixing across a moving vertical interface in the case that there is a density difference between the two fluids (Figure 10.4). They explored the role of both stable and unstable density jumps. Figure 10.3a illustrates the range of buoyancy parameter values, Γ , and Peclet numbers, Pe , explored in that study, and Figure 10.3b illustrates the effective dispersive mixing across the interface measured in the experiments with a stable density gradient, compared to the classical results for the case of dispersion of a passive tracer (cf. Chapter 5). It is seen that the effect of the stabilising buoyancy gradient is to suppress the mixing, although for large Pe , ($Pe > 500$) the dispersion coefficient seems to converge, albeit to a smaller value than for the tracer mixing case. This value appears nearly independent of the buoyancy parameter over a range of 100 in the value of Γ but we note that experiments have not been conducted at higher values of Γ and it may be possible that the dispersion is then further suppressed.

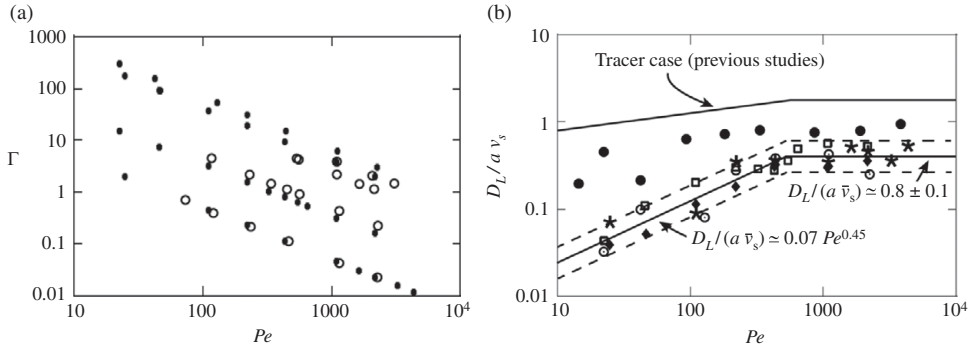


Figure 10.3 (a) Illustration of the range of values of Γ and Pe used in the experiments to explore dispersive mixing in a porous layer with a stable (solid symbols) and unstable (hollow symbols) density interface. (b) Experimental measurement of the longitudinal dispersion in the case of an advancing planar flow with a stable density interface. After Menand and Woods (2005).

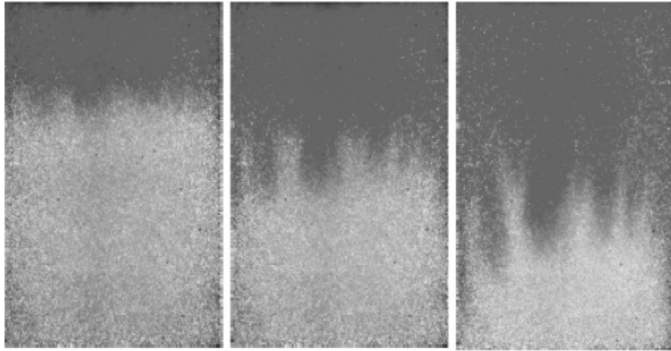


Figure 10.4 An example of gravitational instability as a layer of saline dense red liquid migrates downwards into a layer of less dense clear fresh water in a bead pack. A black and white version of this figure will appear in some formats.

In the case that the density interface is destabilising, as shown in the experiment in Figure 10.4, with sufficiently small flow, i.e. large Γ , we expect fingers to develop and run ahead of the interface. However, with small Γ , dispersive mixing may be enhanced relative to that of a passive tracer, and this may then delay or suppress the onset of convective mixing. Menand and Woods found that with $\Gamma < 0.1$, the dispersion always dominated the fingering instability, and although gravitationally unstable, the interface remains planar, but broadens through dispersive mixing. With larger values of Γ , the interface did eventually develop fingers, and there was a transition from a diffusive broadening of the interface, with a length which scales as $(D_L t)^{1/2}$, to a linearly growing interface zone, associated with the convective mixing driven by fingers (see Figure 10.4).

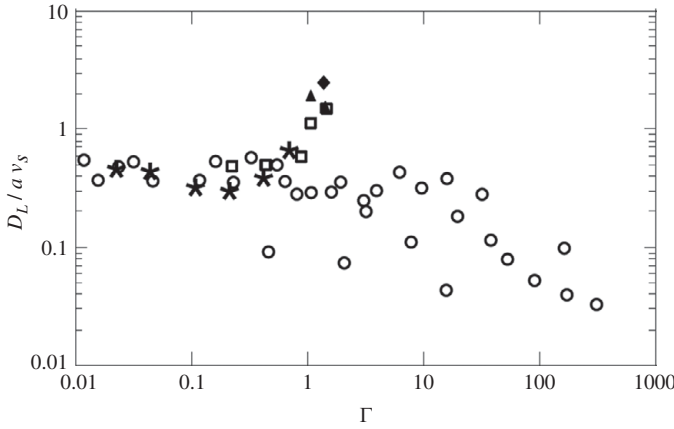


Figure 10.5 Variation of the dispersion coefficient as a function of the buoyancy parameter Γ (horizontal axis) for an unstable interface. Data may be approximated by the empirical laws (10.2) and (10.3). After Menand and Woods (2005).

Prior to the convective instability developing, the longitudinal mixing coefficient scales as

$$D_L \sim (0.4 \pm 0.1)av_s \quad \text{for } \Gamma < 0.2 \tag{10.2}$$

and

$$D_L \sim (1.2 \pm 0.2)\Gamma^{1.2}av_s \quad \text{for } \Gamma > 0.2 \tag{10.3}$$

as seen in Figure 10.5. Once the fingering zone developed, it was observed to grow at a rate $0.25Ut$, relative to the forced flow, which has interstitial speed $v_s = u/\phi$. However, the effect of dispersion delays the onset of the fingering regime since at early times the dispersion produces a zone of intermediate density which initially grows more rapidly than the fingering regime. The transition is observed to occur once the speed of the fingers exceeds the rate of deepening of the dispersively mixed zone

$$0.25U \geq \frac{1}{2} \left[\frac{D_L}{t} \right]^{1/2} \tag{10.4}$$

where the relations for D_L are given by (10.2, 10.3).

These results suggest that the dispersive mixing of an unstable density interface produced by flow normal to the interface can suppress or delay the convective mixing across the interface. For example, with a porous layer of permeability 10^{-13} , a grain size of 1 mm, and a density contrast of 10 kg/m^3 , in which there is a mean flow 10^{-6} m/s , the buoyancy parameter $\Gamma \sim 0.1\text{--}0.01$ and we expect the interface to remain stable to convective instability. With a smaller flow rate, convective instability can set in, and the interface zone with then deepen at a rate $0.25U$.

10.2 Convective plumes

When buoyant fluid is released from a point or line source rather than a planar source, as considered in the previous section, a localised plume develops. In a uniform porous medium, the leading front of the plume suffers a considerable amount of dispersive mixing. For example, in Figure 10.6, we see an experiment in which a two-dimensional plume of relatively dense saline fluid descends through a thin (in the direction of the page) permeable bead pack initially saturated with fresh water. The leading edge of the plume breaks up into a series of fingers of relatively dense fluid, which spread laterally as well as migrating downwards, thereby engulfing pockets of relatively fresh, light fluid, and leading to formation of a region of intermediate density between that of the plume and the ambient. This mixing seems to arise in part owing to the flow of the ambient fluid displaced around the advancing head of saline solution, as seen in Figure 10.6. If there is a steady source of fluid, then as the plume continues downwards, a more localised tail develops, and on the short scale of the laboratory experiment, for which transverse diffusion is small, this tail of the flow has a near vertical boundary between the plume fluid and the ambient. We do note, however, that there is a small annular halo of intermediate density fluid which remains from the earlier passage of the plume head, and this can be seen for some time behind the head. Meanwhile, the

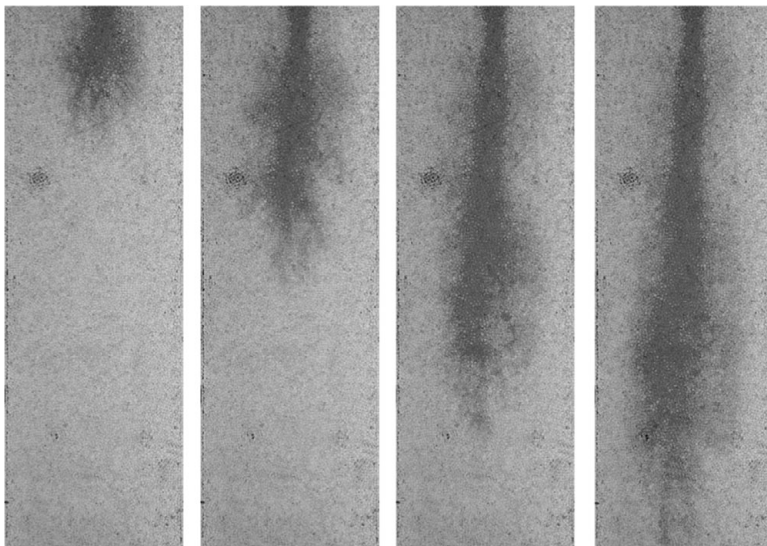


Figure 10.6 Time evolution of a plume of saline fluid, produced by a constant fluid injection rate, descending into a bead pack initially saturated with fresh water. A steady plume tail develops, feeding the dispersively mixing head. This head appears to leave a halo of intermediate density fluid around the continuing tail. Photograph by Caren Otto. A black and white version of this figure will appear in some formats. For the colour version, please refer to the plate section.

head region continues to grow and disperse, leading to a large region in which there is intermediate density fluid at the front of the plume (Figure 10.6).

At sufficiently long times, and sufficiently far downstream to avoid the influence of the finite source, transverse diffusion is likely to become important and we expect that in principle the flow would adjust to the classical solution for a spreading plume in which the buoyant convection matches the cross-flow diffusion, as given by Wooding (1963). Indeed, in Chapter 11 we explore this in the case of a thermal plume, for which the molecular diffusivity is much larger and hence the adjustment to equilibrium is faster. However, with a finite mass flux in which the buoyancy is produced by compositional differences in the fluids, this flow takes some time to establish. For a two-dimensional plume, we can estimate this by noting that in the absence of diffusion, the steady plume which develops behind the plume head has a steady width w which is given by the ratio of the volume flux, Q (per unit distance normal to the flow, i.e. into the page, Figure 10.6) and the uniform downward buoyancy-driven Darcy flow,

$$w = \frac{Q\mu}{k\Delta\rho g} \quad (10.5)$$

The time for transverse diffusion/dispersion (D_T) to penetrate a distance w is of order w^2/D_T . Thus the plume may advance a distance downstream of order

$$Z = \frac{Q^2\mu}{D_T k \Delta\rho g} = \frac{Q^s}{D_T U} \quad (10.6)$$

before transverse diffusion becomes dominant and the flow converges to the Wooding-type plume solution (Chapter 11). With a two-dimensional flux of $10^{-5} \text{ m}^2/\text{s}$, associated with a line release of fluid, and a permeability 0.1 Darcy, a saline plume may require of order 1000 years to adjust given $D_T \sim 10^{-10} \text{ m}^2/\text{s}$; in contrast a thermal plume, with $D \sim 10^{-6} \text{ m}^2/\text{s}$, may require only about 1 year. The interstitial speed of a buoyancy-driven aqueous plume in a formation with permeability 0.1 Darcy may be of order 10^{-6} – 10^{-7} m/s , and so it will traverse a layer of depth 10–100 m in a timescale of 3–300 years. Transverse diffusion in the tail of a compositionally driven buoyant plume is therefore not likely to dominate the flow during the process of injection in an industrial context. It may be that in smaller scale flows associated with geological processes, transverse diffusion does become more important, and this is discussed further in Chapter 11, especially in the context of thermal plumes.

Near the source, in a two-dimensional plume there is a region across which the flow adjusts from being a radially spreading two-dimensional flow to a downslope buoyant flow, of width as given by Eq. (10.5). This is shown in Figure 10.7 in which a plume was created in a vertical Hele–Shaw cell by injecting fluid from a point source and observing the transition from a radially spreading flow near the source, to a descending two-dimensional plume.

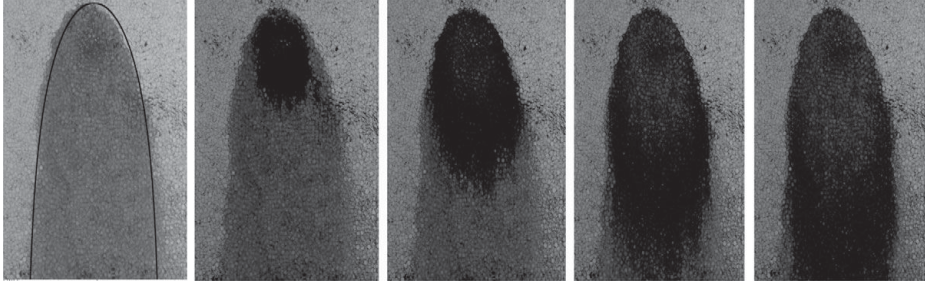


Figure 10.7 Experiment in a porous bead pack illustrating the steady plume structure near the injection point, when saline fluid is injected into a bead pack initially containing fresh water. In the first panel, a solid line, corresponding to the theoretical model of the outer boundary of the plume is compared with the experiment. In the following panels, a pulse of dark dye is added to the injected plume fluid and the evolution of the dye front may be seen as it flows from the source and adjusts to the flow far downstream.

The shape of the interface of such non-diffusing plumes, as they spread from the injection point and adjust to the steady downstream flow is also of interest (Figure 10.7). This shape may be determined by noting that the pressure along the interface is given by the hydrostatic pressure of the static reservoir fluid, $p_R = p_o + \rho gy$ where y is the distance downstream from the source, ρ is the density of the reservoir fluid, and p_o is the reservoir pressure at the level of the source. If the density of the injection fluid is $\rho + \Delta\rho$, then the pressure of the injection fluid at the interface, relative to the hydrostatic pressure of the injection fluid, $p_o + (\rho + \Delta\rho)gy$, is given by

$$p_I = -\Delta\rho gy \quad (10.7)$$

giving the Darcy speed of the plume far downstream as

$$U = k\Delta\rho g/\mu \quad (10.8)$$

so the viscous dissipation in the current exactly matches this buoyancy pressure gradient. However, to find the shape of the interface we need a second boundary condition and then need to solve a fully two-dimensional flow problem; this may be achieved by using complex potential theory, and in the next two pages we outline this method following the approach of Yih (1966). We first introduce the streamfunction, ψ , and velocity potential, ϕ_s for the flow

$$(u, v) = \left(\frac{\partial\phi_s}{\partial x}, \frac{\partial\phi_s}{\partial y} \right) = \left(\frac{\partial\psi}{\partial y}, -\frac{\partial\psi}{\partial x} \right) \quad (10.9)$$

It follows that $\phi_s = -Uy$ on the interface, and that ψ is constant on the interface. If we define the complex potential w as

$$w = \phi_s + i\psi \quad (10.10)$$

where $i = (-1)^{1/2}$ and define the transformed variables (ζ, η) according to

$$\xi = \zeta + i\eta = \frac{i}{u - iv} = \frac{i}{\frac{dw}{dz}} \quad (10.11)$$

with $z = x + iy$, then

$$\zeta = -\frac{v}{v^2 + u^2} \quad (10.12)$$

The right-hand side of expression (10.12) has value $1/U$ (Eq. (10.8)) on the interface, so that $\zeta = 1/U$ on the interface and so in (ζ, η) coordinates the interface is a line.

Finally, we can observe that on the interface $dw = d\phi_s = -Udy$, and so from the definition (10.11), we have that on the interface

$$\frac{i}{\xi} dz = dw = -Udy \quad (10.13)$$

Since ζ is constant on the interface, $d\xi = id\eta$ on the interface, and Eq. (10.13) leads to the result

$$\frac{1}{\xi} \frac{dz}{d\xi} = U \frac{dy}{d\eta} \quad (10.14)$$

Since the right-hand side of (10.14) is real, this requires that

$$\text{Im} \left(\frac{1}{\xi} \frac{dz}{d\xi} \right) = 0 \quad (10.15)$$

on the free surface. Yih notes that this is the second boundary condition required to determine the shape of the interface.

However, it still remains to find a solution which satisfies the boundary conditions. Fortunately, we know that for a two-dimensional point source of strength Q , $w = \frac{Q}{2\pi} \ln(z)$ and so from the definition of ξ (Eq. (10.11)), it follows that near the source, we can write

$$\frac{1}{\xi} \frac{dz}{d\xi} = \frac{iQ}{2\pi\xi} \quad (10.16)$$

In order to satisfy (10.15) on the interface, we then need to add some additional terms to the right-hand side of (10.16). First, we add a term $-iQU/2\pi(2 - U\xi)$, so that when $\xi = 1/U$, this balances the contribution from the source, and hence the solution satisfies (10.15). However, as shown by Yih, this leads to a radially diverging outflow, whereas we seek a descending dense plume. In order that the solution still satisfies (10.15) on the interface, we can add a sink-type term of the form

$$\text{Sink} = \frac{\alpha QUi}{2\pi(1 - U\xi)} \quad (10.17)$$

to the expression $\frac{1}{\xi} \frac{dz}{d\xi}$. We now seek the value for the strength of this sink, α , so that the interface asymptotes to a linearly descending downward plume $y \rightarrow -\infty$. If we integrate the relation

$$\frac{1}{\xi} \frac{dz}{d\xi} = \frac{Qi}{2\pi} \left(\frac{1}{\xi} - \frac{U}{2-U\xi} + \alpha \frac{U}{1-U\xi} \right) \quad (10.18)$$

we find the shape of the interface has the form

$$z = \frac{Q}{2\pi} i \left((2-\alpha)\xi + \frac{2}{U} [\ln(2-\xi U) - \ln(2)] - \frac{\alpha}{U} \ln(1-\xi U) \right) \quad (10.19)$$

where $\xi = \frac{1}{U} + i\eta$ on the boundary and $z = 0$ coincides with $\xi = 0$. By setting $\alpha = 2$ then

$$z = \frac{Qi}{\pi U} \left[\ln \left(1 - \frac{1}{i\eta U} \right) - \ln(2) \right] \quad (10.20)$$

This leads to the parametric relations for the boundary of the plume

$$x(\eta) = -\frac{Q}{\pi U} \tan^{-1} \left(\frac{1}{\eta U} \right) \quad \text{and} \quad y = -\frac{Q}{\pi U} \ln \left(\frac{(1 + \eta^2 U^2)^{1/2}}{2\eta U} \right) \quad (10.21)$$

This is compared with an experiment of a plume spreading through a bead pack, Figure 10.7. It follows that the height of the plume directly above the source where $\eta \rightarrow \infty$ is

$$h = \frac{Q \ln 2}{\pi U} \quad (10.22)$$

and as $\eta \rightarrow 0$, the plume width tends to Q/U and $y \rightarrow -\infty$. This steady plume shape provides an estimate of the area upslope of the source invaded by the plume. This may be useful for estimating zones of contamination and also for estimates of the residual trapping in this region once the supply terminates. For example, with a line well producing a flux $Q \sim 10^{-5} \text{ m}^2/\text{s}$ per unit length of the well, and a buoyancy speed 10^{-6} – 10^{-7} m/s , the plume may rise 5–50 m above the source.

We are unaware of a model which quantifies the controls on the mixing in the dispersing head of such a plume, and hence the halo of mixed fluid which forms around the plume. The mechanism of mixing appears to involve individual plumes of dense fluid, and so it may depend on the lengthscale of the plume, y , the width of the tail, w , and the speed of the plume which scales with U , implying a macroscopic dispersivity $D \sim Uwf(w/y)$, where f is function of the ratio of the width of the plume tail to lengthscale of the plume y . In some cases the dispersion may also depend on the pore-scale dispersivity. One of the challenges in applying such a model of the macroscopic mixing in a real system is that it is most likely to apply on long scales, for which the effects of the heterogeneity of the rock may also become important and we now explore these effects.

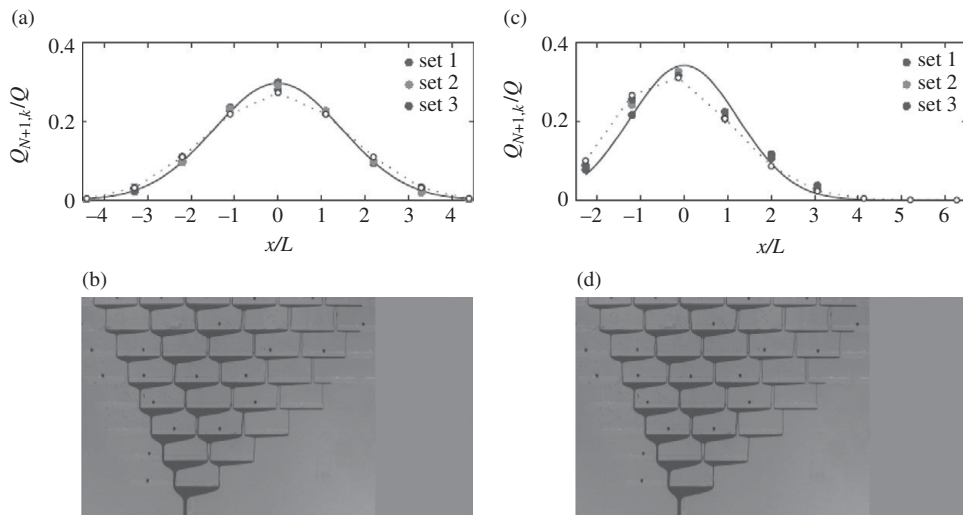


Figure 10.8 Dispersion of a vertical plume around a series of baffles. In this example, the system is shown upside-down, as for the dispersal of a CO_2 plume through a layered, fractured reservoir. Two experiments correspond to the release of fluid in a symmetric and an axisymmetric distribution of baffles showing the pattern of flow and the spatial distribution of the volume flux after passing through the baffles. After Hesse and Woods (2010). A black and white version of this figure will appear in some formats. For the colour version, please refer to the plate section.

10.3 Dispersal of a vertical plume by shale baffles

There are many types of heterogeneity in porous rocks, but one generic feature is the low permeability layers which form between successive layers of higher permeability coarser sediment, reflecting the intermittency over geological time of the process of formation of large sedimentary deposits. These low permeability layers may not always form spatially continuous barriers between successive layers, but may be localised, or may allow localised flow between successive layers of the permeable rock for example as a result of post-depositional compaction and fracturing. The impact of a series of such low permeability layers within an extensive vertical sedimentary porous formation is fundamental to the dispersal of a buoyant plume. The effect may be seen in a simple analogue model in which we show the dispersion of a plume of golden syrup, dyed red, as it migrates through a Hele–Shaw cell containing a series of horizontal baffles which obstruct the flow (Figure 10.8). When a fluid migrates around one baffle, there is a partitioning of the flow, so that a fraction migrates off each end of the baffle; as this process continues through many layers of baffles, the original localised plumes has become very dispersed.

The controls on the partitioning follow by considering the steady flux arriving at a point some distance along the baffle (Figure 10.9). The flux Q_a on side a of the baffle,

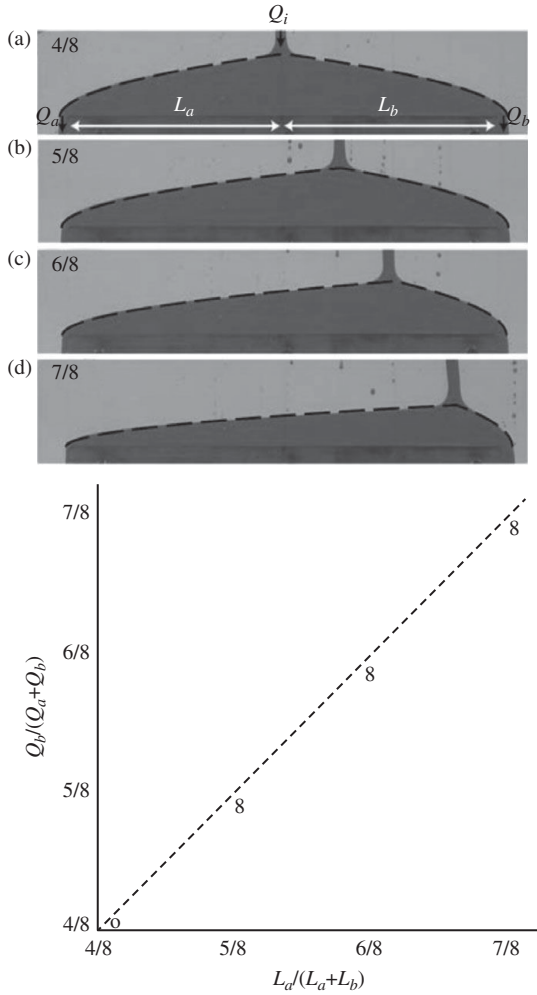


Figure 10.9 Flow past a baffle in a Hele–Shaw cell, with different locations of the impinging plume relative to the centre of the baffle. The figure shows the measured flux and the predicted flux on the longer side as a function of the position of the plume relative to the centre. A black and white version of this figure will appear in some formats. For the colour version, please refer to the plate section.

where L_a is the distance to the end of the baffle on side a , from the incoming plume, satisfies the equation

$$Q_a = -\frac{k\Delta\rho g}{\mu} h \frac{\partial h}{\partial x} \tag{10.23}$$

where

$$h(0) = h_o \text{ and } h(L_a) = 0 \tag{10.24}$$

showing that

$$Q_a L_a = \frac{k \Delta \rho g h_o^2}{2\mu} \quad (10.25)$$

For this two-dimensional analysis, it follows that the flux partitions between the two sides of the baffles, a and b , according to the inverse of the distance to that end of the baffle, L_a and L_b , so that

$$f_a = \frac{Q_a}{Q_a + Q_b} = \frac{L_b}{L_a + L_b} \quad (10.26)$$

as has been confirmed by experiment (Figure 10.9; Hesse and Woods, 2010).

If the flow passes over multiple baffles, then the flow will partition at each junction according to the above rule, and so in a regular series of layers of baffles, this leads to a continual horizontal spreading (Figure 10.8). The flux law (10.25) applied at each junction, leads to the prediction that the flow at each successive layer of baffles follows a binomial distribution, so that the flux passing the m th gap on the n th layers of baffles is

$$Q_{nm} = Q \left(\frac{(n-1)!}{m!(n-m-1)!} f^m (1-f)^{n-m-1} \right) \quad (10.27a)$$

where Q is the total flux, and f denotes the fraction passing to one of the sides of each of the baffles (Eq. (10.26)), and in the limit of a large number of layers of baffles, this becomes a Gaussian distribution for the flux per unit area as a function of the vertical, y , and horizontal, x , position, given by the relation

$$q(x, y) = \frac{QH^{1/2}}{L(2\pi y f(1-f))^{1/2}} \exp \left[-\frac{Hx^2}{2yL^2 f(1-f)} \right] \quad (10.27b)$$

where H is the vertical spacing between the successive layers of baffles. This expression shows that with many layers the plume disperses laterally according to the averaged relation

$$x = \left(\frac{2L^2 f(1-f)}{H} y \right)^{1/2} \quad (10.28)$$

Although this is an idealized problem, it identifies the challenge of describing flow through a complex geometrical structure within a layered porous medium. Any macroscopic description of the flow and dispersion should account for the horizontal buoyancy-driven flow produced by the baffles, even though the effective buoyancy force is vertical. For example, with baffles of horizontal length 10 m, and vertical spacing 3 m, then after rising a height of 100 m, the plume may be dispersed a horizontal distance 30–40 m depending on the distribution of intersection points of the plumes

on the baffles. If the flow was advancing and spreading according to an advection–dispersion equation of the form

$$U \frac{\partial c}{\partial y} = D \frac{\partial^2 c}{\partial x^2} \quad (10.29)$$

where $U = \frac{k\Delta\rho g}{\mu}$ (Eq. (10.8)) then the width of the plume would scale as $x \sim (2Dy/U)^{1/2}$. This suggests that the transverse dispersion produced by the baffles for this buoyancy-driven flow is given by

$$D_T \sim \frac{L^2 f(1-f)U}{H} \quad (10.30)$$

where U is the vertical buoyancy-driven flow speed. The effect described in this simplified system has been extended to a fully three-dimensional flow using numerical calculations, and analogous results have emerged (Green and Ennis-King, 2012).

10.4 Dispersion by inclined baffles

The problem of dispersion of a dense fluid through a series of layers of partially sealing rock becomes more involved if the baffles are inclined. Near the source, the flow may be sufficient to spread over both sides of the baffle and so the plume gradually disperses in the transverse direction. However, further from the source, when the dense downslope flow has dispersed sufficiently that the flow only runs off the downslope side of each baffle, then the transverse spreading of the plume ceases. Instead, a steady plume develops which propagates downwards but at an angle to the vertical. This angle is related to the geometry of the baffles (Figure 10.10).

We can extend the analysis to this more complex geometry, by calculating the flow over an impermeable inclined baffle. We solve the flow updip (+) and downdip (–) by adding in the component of gravity along the slope, and this leads to the relation for the up slope (+) and down slope (–) flow

$$Q_{\pm} = -\frac{k\Delta\rho g}{\mu} \left[h \frac{\partial h}{\partial x} \cos \theta \pm h \sin \theta \right] \quad (10.31)$$

We now seek the critical condition that all the flow just migrates downdip. In this case, the surface of the fluid upstream of the point of supply is horizontal. Therefore, if the point of supply is located a distance L_1 from the upstream end of the baffle, then, at the point at which the source fluid reaches the baffle, the depth of the current on the baffle will be $h_o = L_1 \tan \theta$ (Figure 10.11a). The critical flow Q_c such that all the flow just

passes over the downdip side of the baffle is therefore given by the implicit relation

$$\int_0^{h_0} \frac{h \cos \theta dh}{\left[\frac{\mu Q_c}{k \Delta \rho g} - h \sin \theta \right]} = L_2 \quad (10.32)$$

where L_2 is the distance of the point of arrival of the plume to the interface to the downdip end of the baffle (Figure 10.11a).

Relation (10.32) shows that the critical flux depends on the point along the impermeable layer at which the oncoming plume of buoyant fluid impinges the baffle, and the length of the baffle upstream and downstream of this point. The prediction of the partitioning of the flow between the upstream and downstream end of the baffle for $Q > Q_c$ is again in good agreement with experiments. This leads to a picture for the larger scale migration of a plume through a regular array of inclined baffles. Initially, the flow migrates over both sides of the baffles, continually dispersing the plume in the direction normal to the plane of the baffles. This process continues over successive layers of baffles until eventually the plume is sufficiently dispersed that the flow arriving on any baffle is smaller than the critical flux, Q_c , and the flow then only passes over the lower side of the baffles. The plume then spreads from row to row of the baffles, as a steady inclined plume, with angle of inclination ξ to the horizontal given by the geometry of the array of baffles

$$\tan(\xi) = \frac{L_2 \cos^2 \theta}{H + L_2 \sin \theta \cos \theta} \quad (10.33)$$

which is dependent on the inclination of the layers, θ , the distance from the point of arrival of the plume on the baffle and the downdip end of the baffle, L_2 , and the perpendicular distance between successive layers of baffles, H , as seen in the experimental model (Figure 10.10). Further details of the plume evolution are given by Rayward-Smith and Woods (2011).

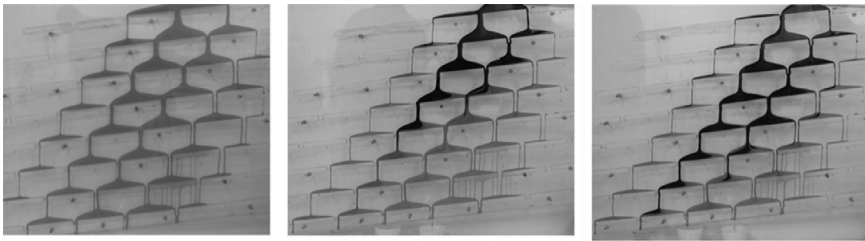


Figure 10.10 Flow of a plume around a series of inclined baffles as shown by a Hele–Shaw cell in which there is a series of inclined baffles, over which a cloud of dense red syrup flows. By changing the colour of the dye in the supply fluid from red to dark blue part way through the experiment, the dispersion and non-uniform speed of the flow may be observed. The darker dye migrates faster in the centre of the plume than at the edges. A black and white version of this figure will appear in some formats. For the colour version, please refer to the plate section.

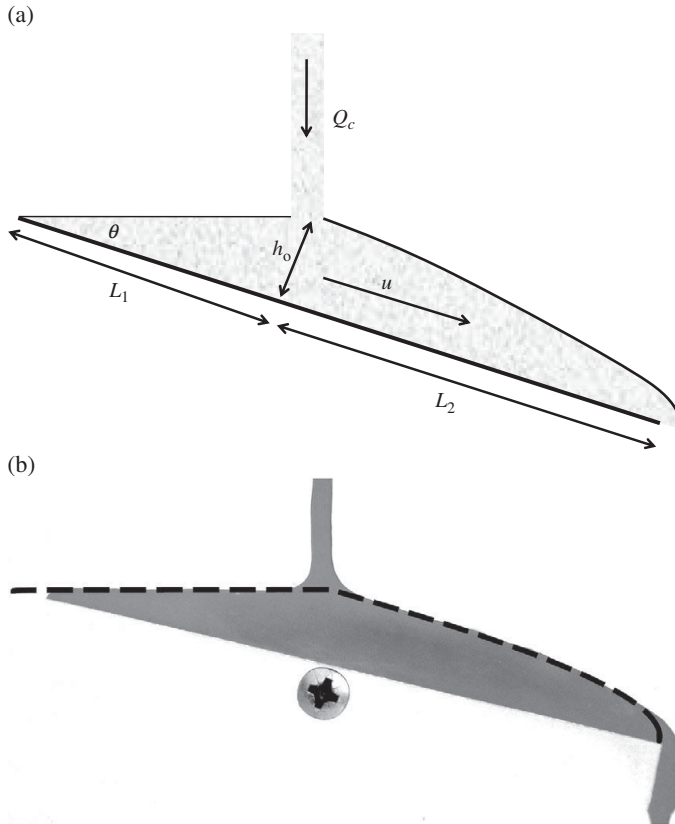


Figure 10.11 (a) Schematic of the plume running over an inclined baffle with the critical flux to drain downstream. (b) Experiment showing flow over a baffle with the critical flux. After Rayward-Smith and Woods (2011).

As mentioned above, it is interesting that with this buoyancy-driven flow, the spatially averaged motion of the plume over these series of baffles is not readily described by a macroscopic version of Darcy's law, with a mean vertical and horizontal permeability. This result is in contrast with the case of a pressure-driven uniform flow discussed in Chapter 3. One curious feature is that as the plume spreads out from the source prior to reaching the steady angled flow regime, the net vertical speed varies with position in the plume. This is because the vertical flow speed is controlled by the time for the spreading layer of CO_2 to migrate over each of the baffles. Near the source, the flow is deeper near the central baffles and so has a greater speed; but as the flow spreads, the current over each baffle becomes smaller and the speed decreases; indeed in Figure 10.10 we illustrate this effect by adding some blue dye to the established steady flow. It is seen that the blue fluid migrates in a very non-uniform fashion, in accord with the variation in the depths of the current over different baffles.

These plume structures are clearly idealised, but indicate the importance of the dispersal of fluid driven by buoyancy forces in a permeable rock consisting of a series of high permeability layers separated by impermeable baffles of finite lateral extent. It is curious to note that the effective transverse dispersion observed for a buoyancy-driven flow from a point source, and the subsequent inclination of the steady plume to the vertical when the baffles are inclined, is quite different from the plume which develops in a uniform porous layer shown in Section 10.2, for which the plume develops a near parallel-sided tail. If fluid is being injected into a porous layer for displacement or for sequestration, these differences in the possible flow pattern are likely to have a profound impact on the efficiency of the sweep pattern (for oil recovery) or the fraction of the formation into which the injected fluid may be sequestered (for CO₂ sequestration). Furthermore, if tracer tests are carried out to detect the flow pattern of the injected fluid, very different patterns may arise depending on such dispersal, and recognition of this is important for interpreting data sets which may often be relatively sparse in a spatial sense owing to the cost of drilling wells for monitoring.

10.5 Dispersion in a multi-layered horizontal system

As well as the transverse and longitudinal dispersion associated with a buoyancy-driven vertical plume in a layered, permeable rock with discrete baffles, buoyancy can have a significant impact on the effective longitudinal dispersion which arises when fluid is injected into a layered permeable rock, leading to the development of a series of parallel gravity-driven flows. For simplicity, we consider the case in which there are a series of layers each separated by a thin layer of low permeability seal rock. If the injection well has a constant source pressure, leading to an overpressure in the top-most layer of the formation, Δp say, then in the lower layers of the formation the flow will be driven by an additional buoyancy head which depends on the depth of that layer, h , below the top of the formation and so the driving pressure will be $\Delta p_n = \Delta p + \Delta \rho gh$.

If, for simplicity, the flow invades the vadose zone from a constant pressure reservoir, so that the permeable formation is initially unsaturated, the flow in each layer will consist of a region near the well in which the layer is fully flooded with the injected fluid, and a nose region in which the flow slumps to zero depth. For example, in the case of an increase in surface water, leading to a sustained period of drainage, water may be supplied through a fracture to each of the layers (Figure 10.12). In the n th layer, with overpressure Δp_n , the Darcy flow speed u_n in the fully saturated region, of length $L_n(t)$ is given by

$$u_n = \frac{k \Delta p_n}{\mu L_n} \quad (10.34)$$

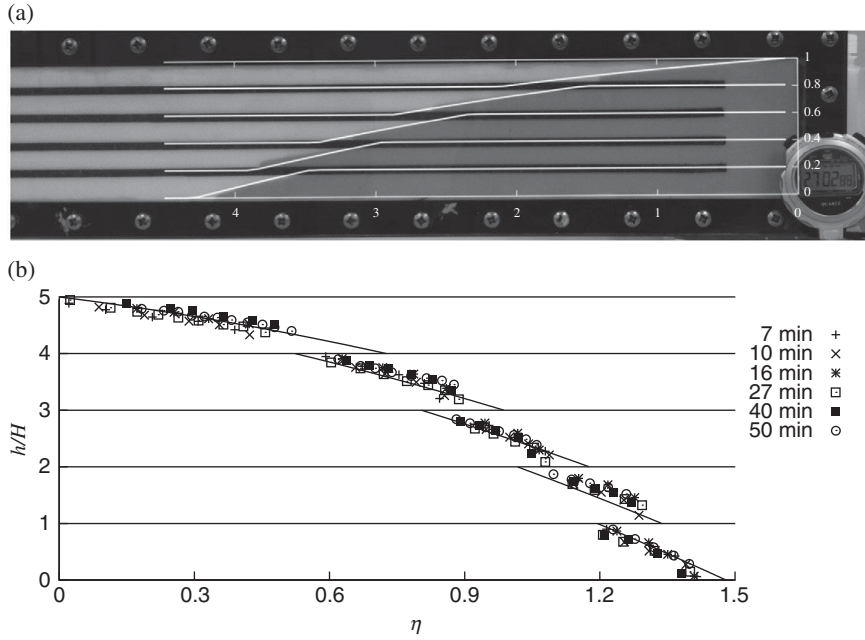


Figure 10.12 (a) Flow in a five-layer Hele–Shaw cell as a model of the dispersal of the flow in a multi-layered rock. The white line shows the prediction of the model for the dispersal in each of the layers. (b) Experimental measurements at a series of times scaled by the similarity coordinate, showing the collapse to the self-similar solution. (b) courtesy of A. Farcas. A black and white version of this figure will appear in some formats. For the colour version, please refer to the plate section.

The leading part of the flow, in which the flow only partially fills the layer, is governed by the gravity current equation (cf. Chapter 9, Eq. (9.10))

$$\phi \frac{\partial h_n}{\partial t} = \frac{k\Delta\rho g}{\mu} \frac{\partial}{\partial x} \left[h_n \frac{\partial h_n}{\partial x} \right] \tag{10.35}$$

At the edge of the fully saturated zone, the flow satisfies the boundary conditions

$$h_n = H \text{ and } -\frac{kh_n}{\mu} \frac{\partial h_n}{\partial x} = u_n H \text{ at } x = L_n(t) \tag{10.36}$$

while at the leading edge of the flow, $x = x_n(t)$, the depth $h = 0$. Mass conservation for the current in this layer leads to the relation

$$\phi \left[HL_n(t) + \int_{L_n(t)}^{x_n(t)} h_n dx \right] = \int_0^t Q_n(t) dt \tag{10.37}$$

where $Q_n(t)$ is the flux supplied to this layer at time t and is given by Eq. (10.34) $Q_n = u_n H$.

Solutions of this system of equations of the form $h_n = x/H(t/\tau)^{1/2}$ where $\tau = H^2/\mu/k\Delta p$ lead to the prediction of the flow rate in each layer of a multi-layered system, with the pressure in each layer as prescribed above. Comparison of the model predictions and an experiment in a Hele–Shaw cell illustrate the accuracy of the solution for the flow in a five-layer system (Figure 10.12).

In this multi-layered system, the flow speed u_n is different in each layer n of the geological strata, in accord with the different driving pressures. This is very different from the case of a single layer of permeable rock, of the same total depth as the sum of the layers, and with the same driving pressure. In that case, the buoyancy-driven horizontal flow speed would be vertically uniform, provided the formation is uniform, with a fully flooded region near the source, and a gravity-thinning nose to the flow, as shown in the solutions for gravity-driven flow in Chapter 9.

If a tracer was injected into the system after some time in an attempt to determine the travel time through the formation to an observation well, then this travel time would have different values in the different layers of the strata. In turn this would lead to an effective dispersion of the tracer as it migrates through the strata. As an example, we take the flow field given above for a ten-layer formation, and calculate the migration of a finite pulse of tracer which is injected at a specific time into the flow. The tracer, shown as the shaded area, follows a layer-dependent path as shown in the panels in Figure 10.13 which correspond to the location of the pulse of tracer at three times after it has been injected into the system. In the figures, the horizontal distance has been scaled with the total length of the flow; in the latter two panels the tracer appears closer to the nose of the flow because there is more fluid in the system.

If this tracer was measured at an observation well downstream, it would not arrive as a single pulse, but rather as a series of discrete pulses associated with the flow in each layer. If, in addition, we account for some longitudinal dispersion in each layer, then the observation well would detect a series of smoothed pulses of tracer, one from each

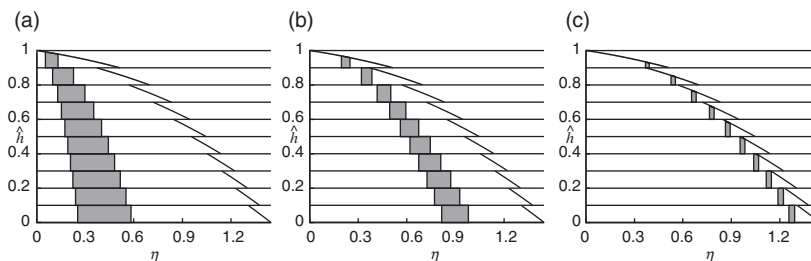


Figure 10.13 Dispersion of a pulse of tracer as it spreads under gravity through a series of ten layers in a permeable rock. The three panels illustrate the location of the tracer in each of the layers at three different times following injection of the dye into the spreading plume. The horizontal axis is scaled with the similarity variable so that the total volume of the current is in fact increasing between frames and so the volume of the dyed fluid represents a decreasing fraction of the whole current. Figure courtesy of A. Farcas.

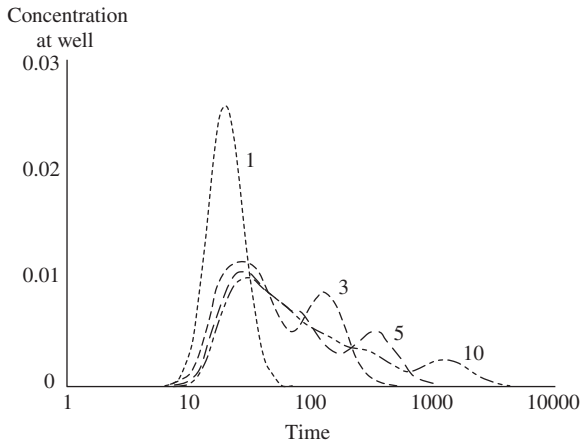


Figure 10.14 Illustration of the variation of the tracer concentration at an observation well as a gravity-driven flow migrates through a layered permeable rock. The different lines correspond to one-, three-, five- and ten-layer systems. The model includes a weak dispersion of the tracer within each layer, so that the profiles in the observation well are smooth, although they still detect the pulses from the tracer in the different layers arriving at the observation well. Figure courtesy of A. Farcas.

of the layers in the formation. In Figure 10.14, we illustrate a theoretical contaminant profile which would be collected at a given point in time, if a tracer becomes dispersed by the flow through a series of hydraulically separated layers. The curves correspond to the cases of one, three, five and ten layers. It is seen that there is a very substantial skewness in the distribution of the tracer with more layers, owing to the buoyancy effects. A further complication in the spreading pattern of the tracer arises once the tracer enters the nose of the current in which the depth $h_n < H$, since in this region the speed of the flow varies with position, leading to further dispersion.

As mentioned, insight about such buoyancy-driven dispersion is key for interpreting data from observation wells. For example, in CO₂ sequestration projects, it may be that tracer is added to the injected gas with a view to determining how this tracer subsequently spreads through space. Analogously, observation wells may be used to try to detect a plume of DNAPL spreading in the subsurface; again this may spread non-uniformly owing to such geometric controls on the flow. Distinguishing the different effects which can lead to such dispersion in buoyancy-driven flows, and the development of inverse models of the rock permeability structure from tracer data is an ongoing topic of research (Farcas and Woods, 2014).

10.6 Boundaries and buoyancy-driven dispersion through trapping

In many-layered porous rocks, the boundaries between layers become distorted over geological time through compaction and tectonic stresses, and this can lead to irregular



Figure 10.15 Illustration of a wavy irregular boundary between two layers of sediment, from West Bay, Bridport, Dorset; (b) illustrates the outline of the wavy layer. The crest-to-crest distance is about 10 m. A black and white version of this figure will appear in some formats. For the colour version, please refer to the plate section.

shaped and wavy boundaries. One fine example of such an irregular boundary between sedimentary layers can be seen at the Bridport sandstone in West Bay, Dorset, England (Figure 10.15).

If a buoyant-fluid phase migrates along such a boundary, for example as a plume of CO_2 advances through an inclined permeable formation, then a fraction of the flow can become trapped in the topographic highs. This will eventually lead to the flow being trapped as a dispersed phase along the boundary, from where it may then dissolve or perhaps leak through the low permeability seal layer. As an example, in Figure 10.16 we illustrate a photograph of a current of glycerol running along an inclined wavy boundary in a laboratory Hele–Shaw cell. The first few panels illustrate the transient development of the flow, and the last image shows the trapped pools of glycerol after the source has been removed. In the case of a CO_2 plume, there would likely be a capillary trapped zone throughout the region originally flooded with the CO_2 , as well as the pockets of trapped liquid, as indicated with the solid black line.

Analogous trapping can occur in oil reservoirs, such that following a water flood designed to sweep oil from the system, there may be dispersed pockets of water trapped by buoyancy at the lower boundary of the formation, in topographic pockets.

Geometric calculations of the volume of each of these topographic traps can be carried out, by observing that in equilibrium, the interface between the trapped injection fluid and the original formation fluid is horizontal. For CO_2 sequestration, this calculation can then be used to estimate the mass of fluid which may be structurally trapped compared to the mass of fluid which is trapped through capillary retention from the original steady plume. Although the volume of the formation in which there

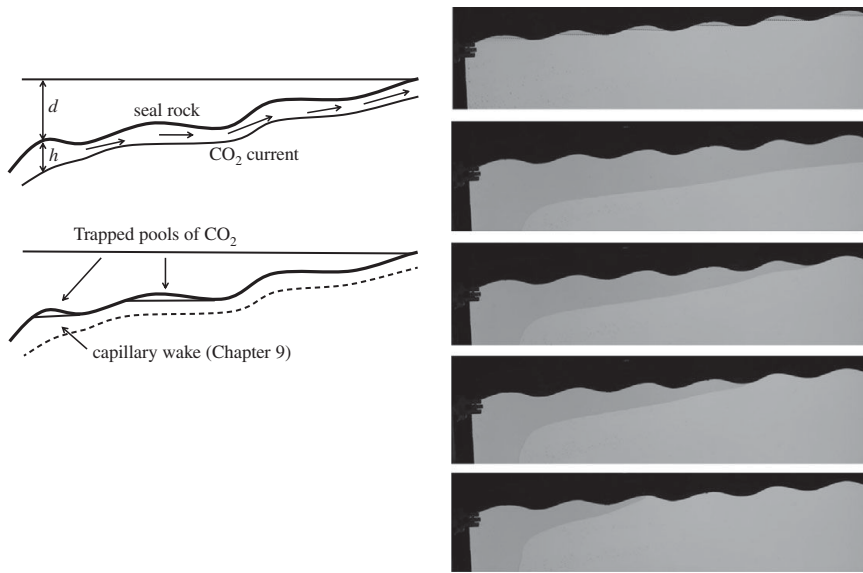


Figure 10.16 Time evolution of a current of red glycerol running downslope over the wavy bed, illustrating the thinning and thickening of the flow over the wavy topography, as the flow sets up a steady state (photographs are shown upside down). The region wetted by the fluid represents the region where there will be capillary trapping. In the last image, the source is removed and the current allowed to drain downslope. The regions behind each of the crests on the wavy boundary is shown by the dotted line in the bottom panel, illustrate the regions where there are trapped pools of fluid remaining after the source is removed. A black and white version of this figure will appear in some formats. For the colour version, please refer to the plate section.

is structurally trapped fluid may be smaller than the original depth of the gravity current of buoyant CO_2 , the structurally trapped fluid occupies a large fraction of the pore space, comparable to the maximum saturation of the non-wetting phase, while the capillary trapped fluid may only occupy a small fraction, comparable to the minimum saturation of the non-wetting phase (Chapter 7). As a result, the volume of fluid which is structurally trapped may be a significant fraction of the total trapped fluid. For example, in Figure 10.17, we illustrate a simple calculation of the total trapped mass per unit distance along an inclined permeable formation, averaged over one topographic trap, and compare the fraction of this which is structurally trapped to the fraction which is capillary trapped, in the case that the topography is composed of a series of sinusoidal perturbations from a flat inclined boundary. The horizontal axis illustrates how the fraction which is structurally trapped increases as the magnitude of the sinusoidal perturbation to the shape of the boundary increases, with the magnitude scaled relative to the thickness of the depth of the current with no boundary topography. As the amplitude increases, the current is required to deepen upslope of the lowest points on the boundary, and this leads to an increase in the ultimate capillary trapping and the topographic trapping.

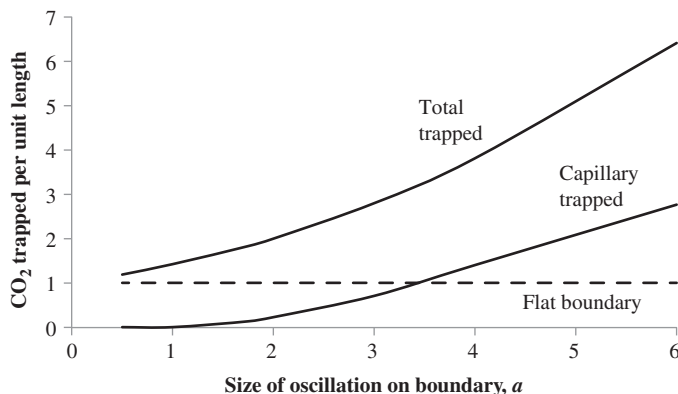


Figure 10.17 Comparison of the structurally trapped and capillary trapped fraction of fluid as a function of the magnitude of a wavy structure to the boundary of the flow domain (Figure 10.16).

Such trapping may lead to a substantial reduction in the total run out distance of a current, and a very different source topology for the subsequent dissolution of the fluid into the background hydrological flow. This may be relevant in the context of the cleanup of DNAPL spills as well as in predicting storage capacity in CO₂ storage reservoirs.

10.7 Exchange flows, mixing and controls on dissolution of CO₂

The previous section has highlighted how a buoyant fluid can become trapped in structural highs as it propagates along a boundary. This process is responsible for the formation of gas caps in oil reservoirs, or CO₂ pools during CO₂ sequestration. The seal rock may retain the buoyant phase by capillary trapping (Chapter 7, Section 7.3), or by having such low permeability that there is no significant flow through the seal. In the case of trapped CO₂, there may be some dissolution of the CO₂ into the underlying formation water, which can typically have a few wt% CO₂ in solution. If this occurs, the CO₂ saturated formation water becomes dense, and may mix downwards into the remaining formation water below. This leads to a continual resupply of unsaturated formation water to the interface, until all the formation water below the pocket of CO₂, within that permeable layer becomes saturated in CO₂. Following this phase of dissolution, any continuing dissolution will be driven naturally by a further supply of unsaturated water. This may be derived laterally from the far field of the aquifer as an exchange flow. Alternatively, there may be a convective exchange of CO₂ through a series of faults in a seal rock which connect the permeable layer which is host to the gas cap with a neighbouring permeable layer filled with unsaturated formation water of lower density (Figure 10.18).

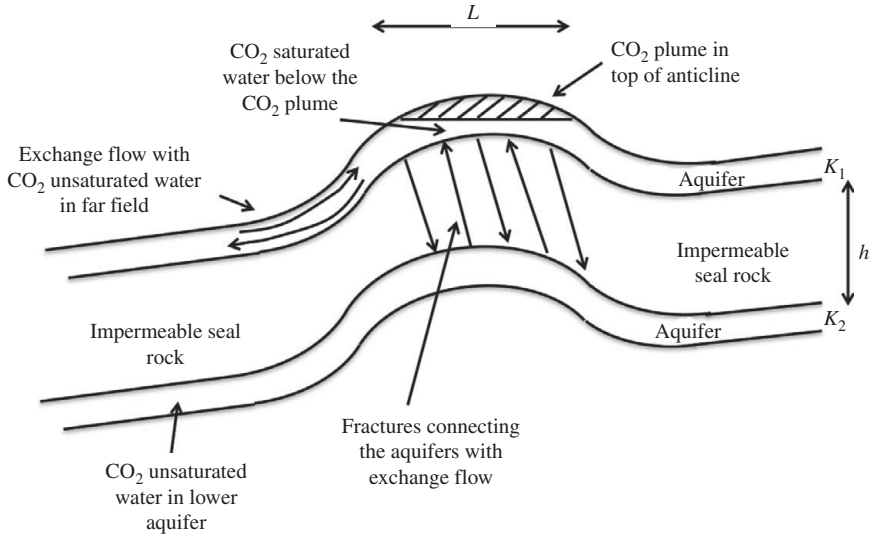


Figure 10.18 Illustration of the dissolution directly below a trapped pocket of CO_2 , the convective exchange in the aquifer and the exchange flow with the underlying aquifer.

The intermingling and mixing of the saturated and unsaturated formation fluid in each of these processes is key for determining the timescale for dissolution of a trapped pocket of CO_2 . The convective mixing process in a layer of depth H below a trapped pocket of CO_2 is driven by plumes of dense fluid separating from the boundary and mixing into the fluid below. Classical models of convection suggest that in the absence of background flows, then once the speed of plumes of CO_2 saturated and hence relatively dense fluid, $U = k\Delta\rho g/\phi\mu$ exceeds the rate of deepening of the boundary layer which is produced by molecular diffusion adjacent to the CO_2 , $u_D \sim (D/t)^{1/2}$, then convection will develop. In a finite layer of thickness H as u_D decreases to a value of order D/H , then the molecular diffusion will tend to homogenise the fluid, suppressing convection. Thus, in order that convection develops, we require $Ra = UH/D > O(1)$. This quantity is known as the porous Rayleigh number and is a measure of the intensity of any convective transport which may develop compared to molecular transport.

In a situation in which $Ra \gg 1$, unstable plumes are much smaller than the layer thickness, and convection will be vigorous. The flux of CO_2 is then expected to be independent of the depth of the layer, since the plumes are produced when a boundary layer of CO_2 saturated water adjacent to the dissolving pocket of CO_2 becomes unstable. This is a local process and in this case, the flux of CO_2 laden fluid per unit area scales as $U\Delta c$, where Δc is the difference in concentration of CO_2 in the descending plumes and the bulk of the fluid in the permeable layer immediately below the CO_2 pocket. As a result, in the absence of any lateral flows, the vertically averaged concentration of CO_2 dissolved in the underlying fluid will evolve according to a simple relation

$$H \frac{d\Delta c}{dt} = -\lambda U \Delta c \quad (10.38)$$

where λ is a constant. This simple physical picture, which follows from the original ideas of Howard (1964) for vigorous convection in a fluid has been compared with numerical calculations of convection and agrees well (Hewitt *et al.*, 2013). The key output of such a model is that the timescale for dissolution is $H/\lambda U$ and subsequently the aquifer fluid adjacent to the CO₂ pool becomes saturated in CO₂ provided there is sufficient CO₂ initially. With density differences of order 0.1–1.0 kg/m³, in a rock of 0.1 Darcy, this implies a timescale of order 30–300 years with $H \sim 10$ –100m. Since the water can only dissolve a few wt% of CO₂, this may only lead to dissolution of a depth of order 0.1–1.0 m of CO₂.

There may however be a series of deeper layers in the geological strata filled with unsaturated formation water, as may typically be the case in a layered deposit. If the seal rock separating the layers contains a series of fractures, then an exchange flow of unsaturated and CO₂ saturated water may develop between the different layers, leading to the continued supply of unsaturated water to the trapped CO₂ pocket and hence dissolution (Figure 10.18). The flux of unsaturated formation water and CO₂ saturated water across such a seal layer depends on the number of fractures and the direction of flow in each fracture, with multiple solutions being possible according to the number of upflow and downflow pathways which become established within the family of fractures. However, the typical flux of CO₂ associated with such an exchange flow is of order

$$F \sim nk_f d_f \frac{\Delta \rho g}{\mu} \Delta c \quad (10.39)$$

per unit length along the n fractures, where Δc is the difference in the mass fraction of CO₂ in the two layers above and below the seal rock, and k_f and d_f are the typical fracture permeability and width within the seal rock (Figure 10.18). The convective exchange between the two layers then controls the continuing dissolution, until the lower layer also becomes saturated. The timescale for the lower layer of depth H_l , to become saturated is now given from the evolution equation

$$\frac{d\Delta c}{dt} = \frac{nk_f d_f \Delta \rho (\Delta c) g}{\mu H_l} \Delta c \quad (10.40)$$

with timescale $\frac{H_l k}{nk_f d_f U}$ where n is the number of fractures per unit length. This leads to typical timescales of order 10³–10⁴ years, depending on the permeability of the fractures, which may be one or two orders of magnitude slower than the initial dissolution.

As well as vertical exchange flows, lateral exchange flows may develop with the unsaturated reservoir fluid further out in the original formation (Figure 10.18). These can lead to transport of unsaturated reservoir fluid to the CO₂ pocket and associated

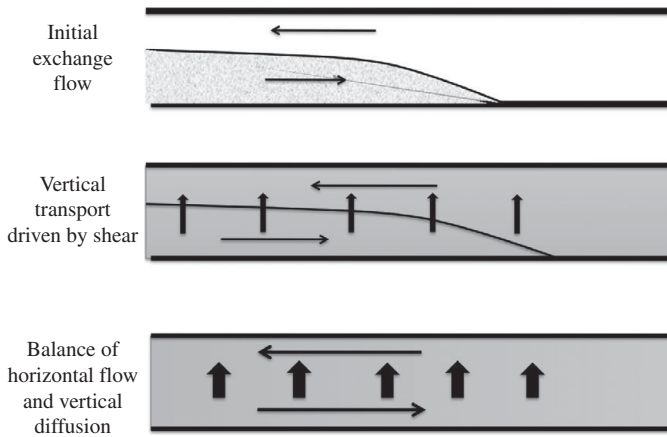


Figure 10.19 Transition from an exchange flow to a buoyancy driven dispersing flow in which the flow is sufficiently slow to allow vertical diffusion of concentration.

dissolution. There is a maximum transport rate associated with such flows, which limits the maximum dissolution rate. If a lateral exchange flow develops in the aquifer, then there will be an upper layer of aquifer water migrating in to the gas cap from the far field, with speed u_1 and depth h_1 , and an outflowing lower layer of CO_2 saturated fluid with speed u_2 and depth $H - h_1$. For an equilibrium exchange flow

$$u_1 h_1 = u_2 (H - h_1) \quad (10.41)$$

With a shallow inclination to the horizontal, of angle θ , the steady exchange flow in the upper and lower layers are given by

$$u_1 = \frac{k}{\mu} \left(\frac{dp}{dx} - \rho_u g \sin \theta \right) \quad \text{and} \quad u_2 = \frac{k}{\mu} \left(\rho_l g \sin \theta - \frac{dp}{dx} \right) \quad (10.42)$$

where x is the horizontal position from the gas cap. This leads to the prediction of a net flux of CO_2 from the saturated zone having value per unit length (cf. Woods and Espie, 2012)

$$F \leq \frac{k}{\mu} \frac{(\rho_l - \rho_u) g \sin \theta h (H - h)}{H} \Delta c \leq \frac{k}{4\mu} (\rho_l - \rho_u) g \sin \theta H \Delta c \quad (10.43)$$

For a shallow angle of inclination of order 1–5 degrees, this lateral exchange flow is of comparable magnitude to the vertical exchange flow (Eq. (10.40)) above. One can infer that the dissolution is a very long duration process which may require times in excess of 10^4 – 10^6 years depending on the volume of trapped CO_2 .

One complexity of these long-lived, slow exchange flows is the potential for cross-layer diffusion and homogenisation of the fluids. In a layer of thickness 1–10 m, the diffusion time will be between about 30–30 000 years assuming a molecular diffusivity of order 10^{-9} – 10^{-10} m^2/s . At the longer end of this spectrum, one might then expect the convective exchange flow to shut down, and we explore this in the next section.

10.8 Long-time buoyancy-driven dispersion

As well as the combination of heterogeneity and buoyancy in dispersing a flow, as illustrated above, we expect that at very long times, molecular diffusion or transverse dispersion across the flow will lead to redistribution of the buoyancy. As a result, the relatively sharp boundaries which we have assumed develop in buoyancy-driven flows, especially as they spread along horizontal or inclined boundaries, become smoothed. In this case, the flow may be described using the classical ideas of Taylor dispersion, as presented in Chapter 5. However, rather than the shear being imposed, the shear now naturally emerges as a consequence of the vertical redistribution of the buoyancy through molecular diffusion. We can explore this feedback by analysing the long-time behaviour of a buoyancy-driven flow in a long laterally extensive aquifer. For simplicity we consider a two-dimensional flow in the (x, y) plane produced for example by a line source of buoyancy directed normal to this plane. We assume there is a mean background flow Q per unit distance along the source in a layer of permeability k and thickness d ($0 < y < d$). In this calculation, we also assume that the line source of buoyancy at $x = 0$ leads to a constant value of the buoyancy at $x = 0$ relative to the far field, $|x| \rightarrow \infty$, corresponding to rapid local dissolution of a trapped plume of CO_2 (Section 10.7), although other boundary conditions could also be considered.

At long times, we expect the buoyancy field $b(x, y, t)$ to diffuse across the depth of the layer, d , where $b = g\Delta\rho/\rho_o$, with ρ_o a reference density, and $\Delta\rho = \rho - \rho_o$ and thus we can write b in the form

$$b(x, y, t) = \bar{b}(x, t) + \Delta b(x, y, t) \quad (10.44)$$

where the \bar{b} notation denotes a depth averaged quantity in the aquifer. As the flow evolves, we expect the fluctuations in the cross-layer direction to be relatively small, $\Delta b(x, y, t) \ll \bar{b}$, and this can be checked *a posteriori* from the solution. The pressure may then be written in terms of the pressure along the base of the layer, $p_o(x, t)$ at $y = 0$, together with the contribution from the buoyancy, assuming the flow is dominantly parallel to the boundary of the domain

$$p(x, y, t) = p_o(x, t) - \rho_o \bar{b}y - \rho_o gy \quad (10.45)$$

As in the analysis of Chapter 5, Section 5.6, the equation for the transport of the mean buoyancy in the x direction is given by

$$\phi \frac{\partial \bar{b}}{\partial t} + \bar{u} \frac{\partial \bar{b}}{\partial x} = \phi D_L \frac{\partial^2 \bar{b}}{\partial x^2} - \hat{u} \frac{\partial \hat{b}}{\partial x} \quad (10.46)$$

Since the flow along the aquifer is given by

$$u = -\frac{k}{\mu} \frac{\partial p}{\partial x} \quad (10.47)$$

we find that

$$\hat{u} = \frac{\rho_o dk}{2\mu} \frac{\partial \bar{b}}{\partial x} \left(\frac{2y}{d} - 1 \right) \quad (10.48)$$

The equation for the perturbations in the buoyancy field is given by the difference between the equation for the total buoyancy transport and that of the vertically averaged transport,

$$\phi \frac{\partial \hat{b}}{\partial t} + \hat{u} \frac{\partial \bar{b}}{\partial x} + \bar{u} \frac{\partial \hat{b}}{\partial x} + \hat{u} \frac{\partial \hat{b}}{\partial x} = \phi D_T \frac{\partial^2 \hat{b}}{\partial y^2} + \phi D_L \frac{\partial^2 \hat{b}}{\partial x^2} + \overline{\hat{u} \frac{\partial \hat{b}}{\partial x}} \quad (10.49)$$

As for Taylor dispersion in a forced flow, at long times, the dominant balance in Eq. (10.49) is between the distortion of the mean buoyancy field by the shear flow, (10.48), and the cross-layer diffusion/dispersion, once the front has propagated a distance which is large compared to the thickness so that the along-layer dispersion is small. This leads to the balance

$$\phi D_T \frac{\partial^2 \hat{b}}{\partial y^2} = \hat{u} \frac{\partial \bar{b}}{\partial x} \quad (10.50)$$

with solution

$$\hat{b}(x, y, t) = \frac{\rho_o dk}{\phi D_T \mu} \left(\frac{\partial \bar{b}}{\partial x} \right)^2 \left(\frac{y^3}{6} - \frac{dy^2}{4} + \frac{d^3}{24} \right) \quad (10.51)$$

to satisfy the zero flux boundary conditions on $y = 0$ and $y = d$ and the requirement that $\int_0^d \hat{b} dy = 0$. We can then calculate the dispersion term in the mean transport equation, $\overline{\hat{u} \frac{\partial \hat{b}}{\partial x}}$ and this leads to the mean transport equation for the buoyancy

$$\phi \frac{\partial \bar{b}}{\partial t} + \frac{Q}{d} \frac{\partial \bar{b}}{\partial x} = \phi D_L \frac{\partial^2 \bar{b}}{\partial x^2} + \frac{d^3}{120 D_T \phi} \left(\frac{k d \rho_o}{\mu} \right)^2 \frac{\partial}{\partial x} \left(\frac{\partial \bar{b}}{\partial x} \right)^3 \quad (10.52)$$

The first term on the right-hand side of the equation is the normal longitudinal dispersivity while the second term is the non-linear dispersion associated with the shear flow produced by the buoyancy and the ensuing cross-flow dispersion. An interesting solution to this problem arises in the case that the buoyancy is maintained at a constant value at the origin $x = 0$, with no background flow $Q = 0$, as in the exchange flow solutions described in the previous section. In this case, once the buoyancy has time to diffuse across the depth of the layer, the exchange flow evolves to the present buoyancy-driven dispersion described by Eq. (10.52) until at very long times, the longitudinal dispersion D_L dominates. In the early time of the mixing controlled by buoyancy-driven

dispersion, we match the first and last terms of Eq. (10.52) and in this case the buoyancy field is given by a similarity solution in which $\bar{b} = b_o$ at $x = 0$ and

$$\bar{b} = b_o F(\eta) \quad \text{where} \quad \eta = \left(\frac{30D_T \phi^2}{\eta^2 d^5 t} \right)^{1/4} x \quad (10.53)$$

and where $v = \frac{k\rho_o b_o}{\mu}$ is the characteristic buoyancy speed, with F satisfying the equation

$$-\eta \frac{dF}{d\eta} = \frac{d}{d\eta} \left[\frac{dF}{d\eta} \right]^3 \quad (10.54)$$

This has an exact analytic solution

$$F(\eta) = 1 - \frac{1}{(12)^{1/2}} \left[\eta(\eta_o^2 - \eta^2)^{1/2} + \eta_o^2 \sin^{-1}(\eta/\eta_o) \right] \quad (10.55)$$

with the condition $F(\eta_o) = 0$ requiring that $\eta_o = (192/\pi^2)^{1/4}$. This solution illustrates that the buoyancy-driven dispersion leads to a flux of buoyancy which decays at a rate proportional to

$$\frac{1}{4b_o^2} \left(\frac{d^3 v^2}{30D_T t^3} \right)^{1/4} \quad (10.56)$$

This flux of buoyancy regulates the flux of unsaturated fluid to the dissolution front, and hence determines the rate of dissolution. The buoyancy-induced dispersive flux decays much faster than that resulting from the longitudinal dispersion, D_L , and so eventually it is superceded by the transport associated with the longitudinal dispersion, D_L , which in the limit of slow flow is controlled by the molecular transport. Some numerical solutions illustrating this flow regime are given by Szulcwski *et al.* (2014).

In assessing the time at which the buoyancy-driven shear dispersion becomes important, we require that the diffusion cross-layer has become established, and this occurs after a time of order H^2/D . For typical systems in which $H \sim 10$ m and $D \sim 10^{-9}$ – 10^{-10} s, this may require 10^{11} – 10^{12} s corresponding to 10^4 – 10^5 years. The length of the mixed zone becomes comparable to the length of the diffusive mixed zone, $(Dt)^{1/2}$ after a time of order $t \sim \frac{H^4 v^2}{120D^3}$. In the case of a buoyancy-driven flow, the velocity may have value of order 10^{-7} m/s with $k = 10^{-12}$ m², $\Delta\rho = 10$ kg/m³ and $\mu = 0.001$ Pa s. In this case, the time at which diffusion becomes significant is of order 10^{15} s, corresponding to about 10^7 years. Such processes relate to the very long-term storage projects in the subsurface, or indeed to geological processes. However, it is important to recognise that on such long timescales, the assumption of a static reservoir may not be fully justified owing to other geological processes.

In assessing such models, it is relevant to observe that at a time of say 10^{12} s, the dispersed front is predicted to extend of order 10^3 – 10^4 m from the source. If there is a modest background hydrological flow, with speed of order 10^{-8} m/s, this will carry the dispersing zone downstream a distance of order 10^4 m, and so the dissolution

would then be controlled by the hydrological transport, and would not decay but would stabilise at a dissolution flux equal to the hydrological transport Q times the concentration difference between the CO_2 saturated and unsaturated water, with all the saturated water being carried downstream.

10.9 Exercises

1. If there is a pool of CO_2 near $x = 0$ which dissolves into the groundwater, show that in the case that there is a uniform hydrological flow Q along the aquifer directed from $x \gg 0$ to $x \ll 0$, then the effect of the production of dense fluid in the vicinity of the CO_2 trap will lead to a steady vertically averaged buoyancy distribution

$$b(x) = \left(b(0)^{2/3} - \frac{2}{3} \left(\frac{Q}{D} \right)^{1/3} x \right)^{3/2}$$

in the region $x > 0$ assuming that a balance between the buoyancy-driven dispersion and the background flow becomes established where D is the coefficient of the buoyancy driven dispersion term in eqn 10.52. In this case, find the structure of the vertically averaged buoyancy field downstream of the CO_2 trap at long times, when the buoyancy-driven shear dispersion controls the mixing.

2. Calculate the mechanical dispersion of a slug of tracer which is released at time τ after the start of the injection in the case that a gravity current with a constant flux of fluid spreads through a deep horizontal porous layer from a linear well. Assume that the permeability varies with height as $k = k_1 y$. Repeat the calculation for the case of a sloping aquifer, and compare and contrast the result with the case of a horizontal aquifer.
3. In the case that a plume of buoyant fluid rises through a series of horizontal layers of baffles, as discussed in Section 10.3, calculate the volume of fluid trapped on each baffle and hence determine how the trapped volume of fluid varies from layer to layer. Consider the implications for estimates of the storage capacity of such an aquifer in the context of CO_2 sequestration.

11 Geothermal power and heat storage

Over many centuries, the extraction of thermal energy from the ground has been of considerable importance, including applications in which warm subsurface water has been used for heating and agriculture. In the 20th century, higher temperature geothermal systems began to be used for power generation, and today there is of order 10 000 MW of installed power generating capacity. For power generation, ideally high temperature vapour is passed through a turbine which thereby generates power. Important examples of high temperature systems include the Geysers in northern California and Larderello in Tuscany, Italy. Presently there is over 3300 MW installed power-generating capacity in the United States, 1800 MW in the Philippines, 1300 MW in Indonesia and nearly 1000 MW in Mexico. Iceland has about 660 MW. The Geysers in northern California are a very substantial geothermal system which mainly produces dry steam from a sandstone reservoir which is heated from below by a large magmatic intrusion over 13 km in diameter. The field has about 1500 MW of installed power-generating capacity and produces a fraction of about 0.6 of this on an average annual basis. The pressure of the steam is in part maintained by injection of treated wastewater designed to boil in the subsurface. In Iceland, geothermal power accounts for over 25% of its electricity generation, and also provides over 85% of the heating and hot water requirements for the buildings.

The basic process in geothermal power generation is the extraction of thermal energy from a high temperature permeable reservoir by production of steam from the reservoir. In the Geysers for example, the reservoir is permeable and this enables close contact of the water with the rock, thereby facilitating thermal energy removal by circulation of fluids. In other ‘hot-dry rock’ systems, there are fractures through which water is circulated, but this requires a sufficiently pervasive network of fractures to ensure good thermal contact and efficient heat transfer.

One of the challenges for geothermal power is the maintenance of pressure in the permeable strata as fluids are extracted. To resolve this challenge, fluid is often injected into the system, as indicated in Figure 11.1. This leads to the migration of a fluid–fluid front and also a thermal front, with the possibility of boiling, scale formation and also changes in density as the injected fluid invades the reservoir.

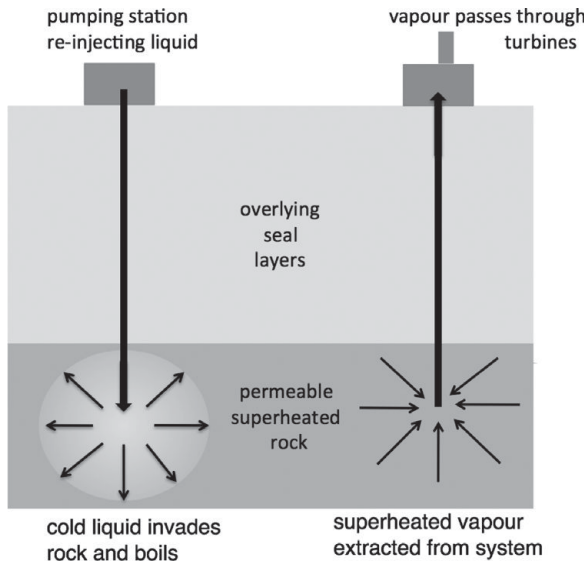


Figure 11.1 Schematic of the injection of water and extraction of vapour from a geothermal power system.

In order to build a picture of the different processes involved, in this chapter we develop a series of simplified models of the flow and heat transfer in the permeable reservoir. We mainly focus on the migration of the injected fluid and the associated thermal fronts. We first consider the evolution of thermal fronts associated with the injection of cold water, and then build in the complexity of boiling in high temperature systems. We also describe how the motion of the injected water may be strongly controlled by gravity, with both compositional and thermal contrasts leading to density differences with the formation fluid. We explore how the thermal inertia of the injected fluid can lead to changes in the buoyancy of the injected liquid producing a dramatic range of flow patterns, some involving reversing buoyancy. We explore the potential for the injected fluid to react with minerals in the reservoir which may lead to scale precipitation or dissolution, and an associated change in the buoyancy and flow pattern of the injected liquid, again with important implications for the efficiency of the heat recovery from the system. We investigate how heterogeneities in the geological strata can lead to dispersion of the thermal fronts, and we consider the role of heat exchange with lower permeability regions of the reservoir adjacent to high permeability pathways in heating up the injected fluid. Finally, we turn to the somewhat related problem of interseasonal thermal energy storage in aquifers, whereby waste heat, produced by power stations or buildings in the summer, may be stored and then recovered in the winter. This has many features in common with geothermal processes, although there are some interesting differences in that for such systems the ground is in essence being used as a thermal battery.

11.1 Thermal fronts

In Chapter 8, we discussed the propagation of thermal fronts in porous rocks, and introduced the idea of thermal inertia. This was shown to be important in the context of reactions and also polymer floods in the case that the polymers are sensitive to temperature. Since thermal fronts typically travel more slowly than fluid fronts, we expect there to be a spatial separation of the leading edge of the injected fluid and the cold thermal front associated with the injected fluid. The injected fluid ahead of the cold front convects the thermal energy which was originally in the rock behind the thermal front. In the case of injection into a warm rock, with no boiling, the location of this boundary layer can be modelled by solving the advection–diffusion equations and calculating how the cooled zone around the injection well grows in time.

If we consider the radial spreading of the fluid from a well into a reservoir of vertical extent H , and if we assume the injection occurs at a rate $2\pi Q$ per unit distance along the well, then the conservation of thermal energy takes the form

$$\frac{\partial T}{\partial t} + \frac{\lambda_l Q}{r} \frac{\partial T}{\partial r} = \frac{\kappa}{r} \frac{\partial}{\partial r} \left(r \frac{\partial T}{\partial r} \right) \quad (11.1)$$

where T is temperature, κ is the average thermal diffusivity of the rock and matrix, $\kappa = \phi\kappa_l + (1 - \phi)\kappa_m$, and λ_l is the ratio of the specific heat of the liquid to the volume averaged specific heat of the matrix and liquid, $C_{pl}/(\phi C_{pl} + (1 - \phi)C_{pm})$, where subscripts l and m denote liquid and matrix. This equation is valid in the limit that the cross-layer conduction is small so that there is no significant heat exchange with the overlying or underlying geological strata; this limit applies for times t such that $H \gg (\kappa t)^{1/2}$, where κ is the thermal diffusivity and H the layer thickness.

Using the similarity variable

$$\eta = \frac{r}{(2\kappa t)^{1/2}} \quad (11.2)$$

we find the problem has solution

$$T(\eta) = T_o + \Delta T \int_0^\eta \eta^{\lambda_l \beta - 1} \exp\left(-\frac{\eta^2}{2}\right) d\eta \quad (11.3a)$$

where $\beta = \frac{Q}{\kappa}$ and

$$\Delta T = \frac{T_1 - T_o}{\int_0^\infty \eta^{\lambda_l \beta - 1} \exp\left(-\frac{\eta^2}{2}\right) d\eta} \quad (11.3b)$$

As expected, owing to the difference in speed of the thermal and fluid fronts, this solution has an internal thermal boundary layer which in this radial geometry is fully resolved, since the front speed decays with time with exactly the same

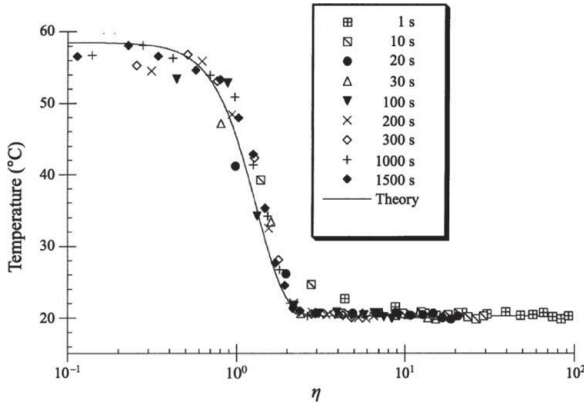


Figure 11.2 Temperature profile as a function of the radius shown in similarity variables for comparison with the theoretical solution Eq. (11.3). After Woods (1999).

time-dependence as the thermal diffusion acts across the front. The model has been tested with a series of experiments in which water is injected into a pack of sand, and the radial temperature profile measured, as shown in Figure 11.2.

11.2 Boiling fronts

In the more complex case of a superheated rock, the injection of liquid leads to boiling of the liquid and production of vapour. Boiling occurs at a prescribed pressure for each temperature, as given by the Clausius–Clapeyron relation (Figure 11.3), and so part of the solution to the problem is the determination of which boiling temperature and pressure the interface selects. This is controlled by the rate of heat and mass transfer across the interface. We note that since there is a mass flux across the boiling front, it travels more slowly than the interstitial speed of the fluid.

To proceed we now model the flow of both the liquid and the vapour, and find the pressure distribution in the formation around the boiling front. The liquid flow follows Darcy’s law and solution of the liquid flow problem from the injection well to the boiling front determines the relationship between the pressure at the injection well and the pressure at the boiling front. This may then be combined with the vapour flow equations, to develop a model for the pressure of the boiling front, relative to that in the far field, in order that the newly formed vapour can migrate ahead of the interface. Since the gas is compressible, we build a model of the gas dynamics using Darcy’s law and an equation of state for the gas to account for the compressibility.

In general, the gas density ρ is a function of pressure p and temperature, T and provided the gas pressure is not too large, we may assume it varies as

$$p = \rho RT \quad (11.4)$$

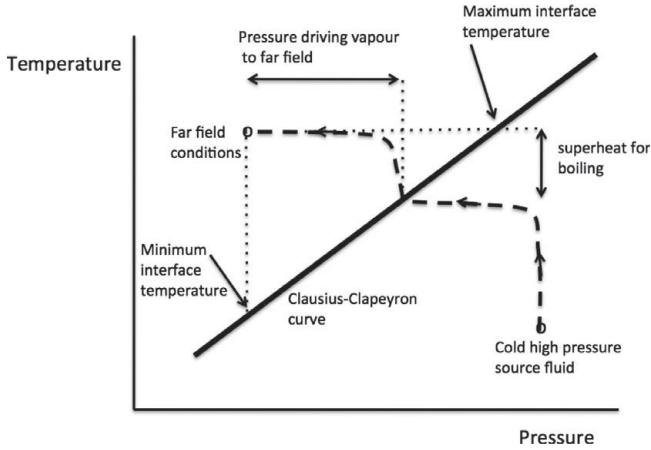


Figure 11.3 Clausius–Clapeyron boiling curve, illustrating the path of the injected liquid in P – T space, as it is heated, boils and then adjusts to the far-field superheated steam conditions.

We now combine this with Darcy’s law for the flow

$$u = -\frac{k}{\mu} \nabla p \quad (11.5)$$

and the equation for the conservation of mass, which gives

$$\phi \frac{d\rho}{dp} \frac{\partial p}{\partial t} = -\frac{k}{\mu} \nabla [\rho \nabla p] \quad (11.6)$$

If we scale the pressure with the far-field pressure, it is seen that the propagation of a pressure disturbance through the formation is diffusive in nature, and that the effective diffusion coefficient is

$$D_{eff} = \frac{kp_o}{\phi \mu RT} \left(\frac{d\rho}{dp} \right)^{-1} \quad (11.7)$$

In a typical geothermal system, with reasonably good permeability rock, of order 0.01–1.0 Darcy, and filled with vapour, this has value of order 10^{-3} – $1.0 \text{ m}^2/\text{s}$ which is much larger than the thermal diffusion scale, $\kappa \sim 10^{-7} \text{ m}^2/\text{s}$. For reasonable injection rates, the vapour flow produced by boiling may be of order 10^{-5} – $10^{-2} \text{ m}^2/\text{s}$ per unit length of an injection well. At the higher end of this range in a low permeability rock $Q > D_{eff}$ and there may be a dynamic pressure signal in the vapour ahead of the boiling front and this will extend over a much longer scale than the temperature field provided $D_{eff} > \kappa$. However, if the injection rate is small compared to the pressure diffusivity, $Q \ll D_{eff}$ then there is negligible dynamic pressure in the vapour, and the interface temperature is governed by the Clausius–Clapeyron temperature associated with the far-field pressure.

11.3 Slow boiling

In the case of slow injection and hence slow generation of vapour compared to the pressure diffusion scale, the temperature field in the vapour follows the relation

$$\frac{\partial T}{\partial t} + \frac{f\lambda_v Q}{r} \frac{\partial T}{\partial r} = \frac{\kappa_b}{r} \frac{\partial}{\partial r} \left(r \frac{\partial T}{\partial r} \right) \quad (11.8)$$

where f is the fraction of the liquid which boils,

$$\lambda_v = \frac{\rho_v C_{pv}}{\phi \rho_v C_{pv} + (1 - \phi) \rho_m C_{pm}} \quad (11.9)$$

with subscript v for vapour, m for matrix and $\kappa_b = \phi \kappa_v + (1 - \phi) \kappa_m$ is the effective thermal diffusivity in the vapour zone.

Also, the change in diffusive heat flux across the interface accounts for the boiling according to the relation

$$\kappa_b \rho C_p \frac{\partial T}{\partial r} \Big|_{+} - \kappa_b \rho C_p \frac{\partial T}{\partial r} \Big|_{-} = \frac{f \rho_l L Q}{r} \quad (11.10)$$

Since the boiling occurs at fixed temperature, the latent heat term on the right-hand side of this equation accounts for the difference between (i) the advective heat flux of the vapour produced by the boiling and (ii) the advective heat flux of the liquid supplied to the interface minus that advected with the moving boiling front. Since there is no external lengthscale in this problem, we expect that the boiling dynamics are governed by a similarity solution for the temperature field, and we explore solutions of the advection–diffusion problem with the objective of determining the boiling rate. We again use the similarity variable

$$\eta = \frac{r}{(2\kappa t)^{1/2}} \quad (11.11)$$

and we define the boiling interface to be located at $\eta = \omega$ and to have temperature T_s . In this case, assuming for simplicity that $\kappa_b = \kappa$, then the temperature in the vapour region is given by

$$T(\eta) = T_s + A \int_{\omega}^{\eta} \eta^{\lambda_v f Q / \kappa_b - 1} \exp\left(-\frac{\eta^2}{2}\right) d\eta \quad \text{for } \eta > \omega \quad (11.12)$$

where A is chosen so that $T(\infty) = T_{\infty}$ the far-field temperature. The temperature in the liquid region is given by

$$T(\eta) = T_s + B \int_{\omega}^{\eta} \eta^{\lambda_l Q / \kappa - 1} \exp\left(-\frac{\eta^2}{2}\right) d\eta \quad \text{for } \eta < \omega \quad (11.13)$$

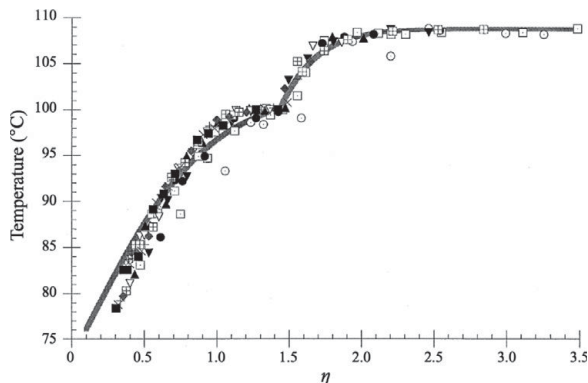


Figure 11.4 Illustration of the temperature distribution through a boiling front, Eqs. (11.12) and (11.13), as measured in an experimental sand pack and compared to the similarity solution shown with the line. After Woods (1999).

where T_s is the boiling temperature based on the far-field reservoir pressure and the Clausius–Clapeyron curve. B is chosen so that $T(0) = T_o$ the injection temperature. The interfacial mass conservation condition across the boiling front, $\eta = \omega$ requires that

$$\omega = \left[\frac{Q(1-f)}{\phi\kappa} \right]^{1/2} \quad (11.14)$$

where f denotes the fraction of liquid which boils, as determined by the Stefan condition (11.10).

This solution has been tested with a laboratory experiment in which a cylindrical sand pack, bound between two relatively low conductivity Perspex plates was heated above the boiling temperature of the injected liquid. The evolving temperature distribution through the sand pack can be scaled to η space, as shown, and is well described by Eqs. (11.10–11.14) (see Figure 11.4).

11.4 Fast boiling

With a faster injection rate, comparable to or larger than the vapour diffusion scale $Q \geq D_{eff}$, the pressure gradient in the vapour region becomes significant, and this can lead to a larger injection pressure, and can lead to a higher interface pressure and temperature. If the boiling temperature increases, there is less thermal energy which can be released from the permeable rock to drive the boiling, and so the fraction of the liquid which boils decreases, in response to the elevated dynamic pressure gradient in the vapour zone. We can model this situation by noting that since the vapour pressure diffusivity, of order $10^{-1} - 10^{-3} \text{ m}^2/\text{s}$, is much larger than the thermal diffusivity, the

thermal boundary layers are much thinner than the pressure transition zones, and so any regions of temperature adjustment occur at nearly constant pressure. We can also observe that if the boiling front advances at a rate larger than the speed of the thermal front in the liquid, $\lambda_l Q/r$, then the water injected into the system will heat up to the boiling temperature prior to reaching the boiling interface. There is then a nearly isothermal region of water, as it advances to the boiling front, where it boils. Steam produced by the boiling then heats up to the far-field temperature across a thermal boundary layer and, over a longer pressure adjustment zone, the pressure adjusts to the far-field value (see Figure 11.3). The key to model this process quantitatively lies in the description of heat and mass conservation across the boiling front, and on the dynamics of the migration of the vapour ahead of the front. This latter process controls the pressure of the interface relative to the far-field pressure for a given flux of vapour.

At the boiling front, we can write down expressions for the conservation of thermal energy by integrating across the thermal boundary layer ahead of the front, and this leads to a balance between the heat released by the rock as it is invaded with the water behind the boiling front, and the latent heat required to vaporise the water and increase the temperature of the newly formed vapour to that of the far field,

$$f\phi(\rho_l L + \rho_v C_{pv} \Delta T) = (1-f)(1-\phi)\rho_m C_{pm} \Delta T \quad (11.15)$$

The conservation of mass across the interface requires the fraction of the liquid which boils to migrate ahead of the front as vapour

$$(\rho_l f + \rho_v(1-f))u = -\rho_v \frac{k}{\mu_v} \frac{\partial p}{\partial x} \quad (11.16)$$

where f is the fraction of the liquid which boils and u is the liquid Darcy velocity. In the energy relation, L denotes the latent heat of boiling and ΔT is the jump in temperature from the interface temperature to the far-field temperature of the vapour. The pressure gradient in the vapour is calculated from the equation for the pressure variation in the vapour phase Eq. (11.6). The final condition we apply at the interface is the Clausius–Clapeyron equation which relates the boiling temperature to the boiling pressure (Figure 11.3).

With radial injection, $2\pi Q$ per unit distance along the well, we expect a self-similar profile in which the position of the boiling front increases with time according to

$$r_b = \left(\frac{2Q(1-f)t}{\phi} \right)^{1/2} \quad (11.17)$$

so that a constant fraction of the injected liquid vaporises. As a result, the pressure gradient in the vapour zone ahead of the front, which spreads in a non-linear diffusive fashion, as given by Eq. (11.6), is always in balance with the oncoming liquid front. Details of the structure of the similarity solutions for the vapour pressure may be found numerically from Eq. (11.6), using the conditions for heat and mass flux conservation

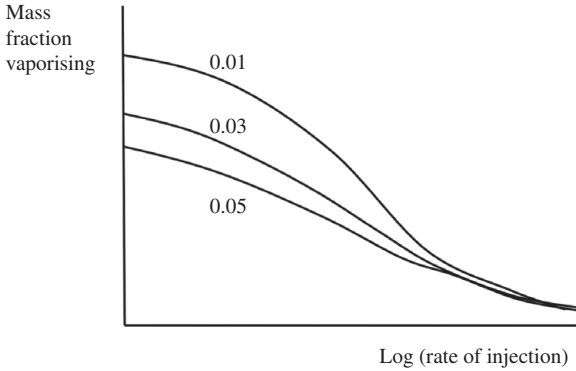


Figure 11.5 Rate of vaporisation of a liquid front illustrated in terms of the fraction which boils, f , as the fluid reaches the boiling front. Different curves correspond to different reservoir porosities. After Woods (1999).

across the boiling front (11.15–11.17), and selecting the solution for which the interfacial temperature and pressure are related according to the Clausius–Clapeyron equation. Solutions of the system show that although the total mass of liquid which boils increases with the injection rate, the fraction of the liquid which boils decreases as the liquid flow rate increases. Eventually as the flow rate increases to very large values, the interfacial temperature approaches the temperature of the far field, and so there is very little thermal energy available for boiling Eq. (11.15); the reservoir then primarily becomes flooded with warm water (Figures 11.3 and 11.5; see Woods, 1999, for more details).

An interesting feature of such boiling problems is that the boiling can lead to the precipitation of salt, since salt may be soluble in the liquid state, but not in the vapour. Typskin and Woods (2005) have explored the precipitation problem driven by such boiling, and shown that this may lead to the cementing or calcification of permeable strata and ultimately suppression of flow.

Another curious feature of boiling fronts in porous media is that the front can become unstable, in a fashion similar to the Saffman–Taylor instability. To see the mechanism for this instability, we note that upstream of the boiling front, the pressure gradient in the liquid zone is $\frac{-\mu_l u}{k}$, where μ_l is the liquid viscosity and k the permeability of the porous layer while in the vapour zone directly ahead of the interface, the mass flux of vapour is $f \rho_l u$, when a fraction f boils. This leads to a Darcy speed of the vapour $f \rho_l u / \rho_v$, and hence a pressure gradient $\frac{-\mu_v \rho_l f u}{\rho_v k}$. The ratio of the pressure gradients downstream to that upstream is therefore given by $f \nu_v / \nu_w$ where ν is the kinematic viscosity. In practice, the kinematic viscosity of vapour is higher than that of liquid and so the pressure gradient across the boiling front increases if a sufficient fraction of the liquid boils, $f > \nu_w / \nu_v$. In this case, there will be instability of the boiling front.

11.5 Boiling gravity-driven flows

In some situations, the water injected into a geothermal reservoir will only be available on a seasonal basis, perhaps associated with melt-water in spring. As a result, the injected liquid may initially be controlled by the pressure-driven injection regime modelled above, but then becomes controlled by gravity once the injection ceases and it spreads beneath the vapour in the system. For this gravity-driven flow, the leading edge of the water will advance into the hot rock and tend to boil off, while the trailing edge of the system where the front descends, will not involve any boiling. This situation is somewhat analogous to the case discussed in the Chapter 9, Section 9.6, of a mound of fluid slumping under gravity, in which case the trailing edge leaves behind a capillary wake. The similarity between the two problems is that the mass of liquid decreases in a power law fashion following a similarity solution of the second kind. In general, there may be an elevated pressure at the boiling front in order to displace the vapour produced by the boiling. However, in order to gain insight into the process, if we assume that the fraction of the liquid which boils off is a constant, f , and that the pressure in the advancing front matches the pressure in the vapour region of the reservoir at that depth, then the governing equations for the associated gravity-driven flow of liquid, of depth $h(x, t)$, have the form

$$\frac{\partial h}{\partial t} = \frac{k\Delta\rho g}{\phi\mu} \nabla[h\nabla h] \quad \text{for} \quad \frac{\partial h}{\partial t} < 0 \quad (11.18a)$$

$$\frac{\partial h}{\partial t} = (1-f) \frac{k\Delta\rho g}{\phi\mu} \nabla[h\nabla h] \quad \text{for} \quad \frac{\partial h}{\partial t} > 0 \quad (11.18b)$$

We now consider a two-dimensional flow, as would arise from a horizontal line source, for which the global conservation of mass, including the boiling, now takes the form,

$$\gamma Q_0 t^{\gamma-1} = \phi \frac{d}{dt} \int_0^{L_2(t)} h dx + \phi \frac{f}{1-f} \int_{L_1(t)}^{L_2(t)} \frac{\partial h}{\partial t} dx \quad (11.19)$$

where $Q_0 t^\gamma$ is the total mass of injected liquid at time t .

This relation is combined with the boundary conditions that there is zero flux at $x = 0$ following a finite injection and that the current depth $h(L_2) = 0$ at the leading edge $x = L_2(t)$. We also impose conservation of depth and flux at the point $x = L_1(t)$ where $\frac{\partial h}{\partial t} = 0$, so that for $x > L_1$ the current boils, while for $x < L_1$ there is no boiling.

As for the capillary trapped gravity current in Chapter 9, Section 9.6, we can seek solutions in terms of the similarity variable $\eta = \frac{x}{H(Dt)^\beta}$ of the form $h = H(Dt)^\alpha f_f(\eta)$ where f_f satisfies the governing equations

$$\phi \left(\alpha f_f - \beta \eta \frac{df_f}{d\eta} \right) = \frac{d}{d\eta} \left(f_f \frac{df_f}{d\eta} \right) \quad \text{for } 0 < \eta < \lambda_1 \quad (11.20a)$$

$$\phi \left(\alpha f_f - \beta \eta \frac{df_f}{d\eta} \right) = (1-f) \frac{d}{d\eta} \left(f_f \frac{df_f}{d\eta} \right) \quad \text{for } \lambda_2 > \eta > \lambda_1 \quad (11.20b)$$

together with the integral equation for mass conservation

$$\gamma = \phi \int_0^{\lambda_1} (\alpha f_f - \beta \eta f_f) d\eta + \frac{\phi f}{1-f} \int_{\lambda_1}^{\lambda_2} (\alpha f_f - \beta \eta f_f) d\eta \quad (11.21)$$

along with the matching conditions at $\eta = \lambda$ (i.e. $x = L_1$) that the interface is continuous and has continuous derivative. Finally we require that

$$f_f(\lambda_2) = 0 \quad \text{and} \quad f_f \frac{df_f}{d\eta} \Big|_{\eta=0} = 0 \quad (11.22)$$

where $\eta = \lambda_2$ corresponds to the nose $x = L_2$.

To solve the problem, we determine the value of the exponent γ for which the solution of the governing equations and the boundary conditions (11.20, 11.22) also satisfies this integral condition (11.21). An illustrative solution is shown in Figure 11.6. Here we see the evolution of the current, along with the locus of the region of rock which has been invaded with liquid, and hence cooled. The region of cooled rock only represents a fraction of the total rock volume, and illustrates the difficulty of injecting water in order to mine the thermal energy from the rock through boiling of this water (see Woods, 1998, for more details).

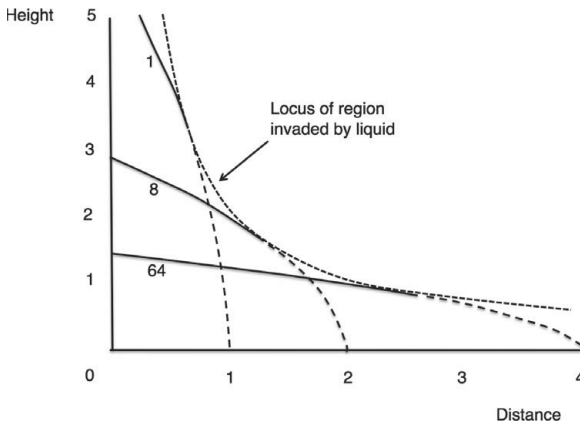


Figure 11.6 Evolution of the shape of a vaporising gravity current with time, shown at dimensionless times 1, 8 and 64. The dashed leading zone of the current represents the part of the current which ascends and vaporises. The locus of the region invaded by the current is shown by the dotted line.

11.6 Double-advective plumes with reversing buoyancy

We have seen that when liquid is injected into a porous rock, the thermal signature of the fluid lags behind the leading edge of the fluid owing to the local heat exchange between the fluid and the solid. As a result, the density and viscosity of the injected fluid will then differ between the leading region of the injected fluid, where the temperature matches the far field, and near well-bore region of the flow where the temperature remains close to the injection value. The changes in the fluid density and viscosity associated with the change in temperature can have a profound influence on the flow, especially in high permeability systems where the gravitational forces are important. We illustrate some of these effects in a two-dimensional model system, observing that the model applies for times short compared to the cross-layer diffusion distance. Later in the chapter we explore the effect of heterogeneities within the formation, which can lead to thermal dispersion, and of heat loss to the boundaries of the system which ultimately changes the rate of propagation of the thermal front.

We first note that if a layer of hot but salty water overlies a layer of cold and fresh water within a porous layer, then the system may be statically stable if the upper layer is sufficiently hot; however, if there is a disturbance to the interface of this system, such that cold fluid rises into the hot pores or hot fluid sinks into the cold pores, the thermal inertia will result in the leading part of the disturbed region of fluid adjusting to the local ambient temperature, while the composition remains unchanged. As a result, the buoyancy of the leading part of the parcels of fluid displaced across the interface changes sign, and they may continue to ascend or descend, leading to convective exchange of fluid. Phillips (1991) called this process the double-advective instability. There is a very broad range of flow problems for which the double-advective instability can control the evolution of the flow, and we present some examples below. In particular, plume or gravity current flows which may develop from a localised source can have very different structure when double-advective effects are present. Indeed, an internal front may develop across which the buoyancy changes in magnitude or even in sign. Some of the different possible transitions in the density of the injected fluid are illustrated in the temperature–composition plane shown in Figure 11.7. In this figure, the tilted lines correspond to lines of constant density, and the origin corresponds to the conditions in the reservoir. If the fluid composition increases, the fluid becomes denser and if the fluid temperature increases it becomes less dense.

In Figure 11.7, the tilted line through the origin represents the (T, C) values in the solution for which the density matches that of the reservoir fluid, which corresponds to the conditions at the origin. This figure is useful for the interpretation of a series of flow patterns which may develop in two-dimensional plumes involving the effects of thermal inertia, and we now consider these. In case a, fluid of lower salinity is injected,

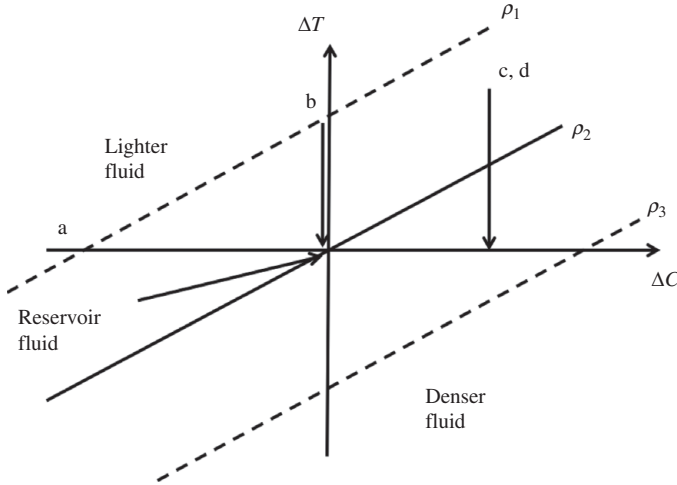


Figure 11.7 Composition–temperature diagram illustrating lines of constant density, ρ_1 , ρ_2 and ρ_3 . Different flow regimes develop for the migration of fluid of one temperature and composition through a second fluid. The cases a–d are shown in Figures 11.8 and 11.9.

and this forms a plume of buoyant fluid rising from the source (Figure 11.8a). For this flow regime, the two-dimensional plume has a steady width, w , behind the head given by the ratio of the volume flux (in this case per unit width of the thin cell), Q , and the uniform upward buoyancy-driven flow (cf. Chapter 10)

$$w = \frac{Q\mu}{k\Delta\rho g} \quad (11.23)$$

In case b, fluid which is hotter and of the same composition is injected, and this forms a buoyant plume within which the fluid temperature adjusts to equal the background temperature once it has passed through the thermal front (Figure 11.8b). As a result the plume develops in a very different fashion, more resembling a moving source of fluid of neutral buoyancy, as the location of the surface across which the temperature changes migrates forward in the cell. As a result of this loss of buoyancy across the thermal front, the fluid spreads outwards. During the experiment, the colour of the dye was changed to help visualise the flow pattern. It is seen that the continuing plume of hot fluid migrates upwards and displaces the thermal front upwards past fluid which was injected earlier but which now has cooled. A curious feature in the photograph in Figure 11.8b is the development of a small streak of clear ambient fluid which appears to follow the boundary between the hot continuing plume and the cooler region where the temperature has adjusted to that of far field. This clear fluid rises up with the plume as a result of heat conduction in the cross-flow direction just above the source. Eventually this will lead to a steady-state plume structure in which the cross-layer thermal diffusion of heat matches the upward advection, as described by Wooding (1963).

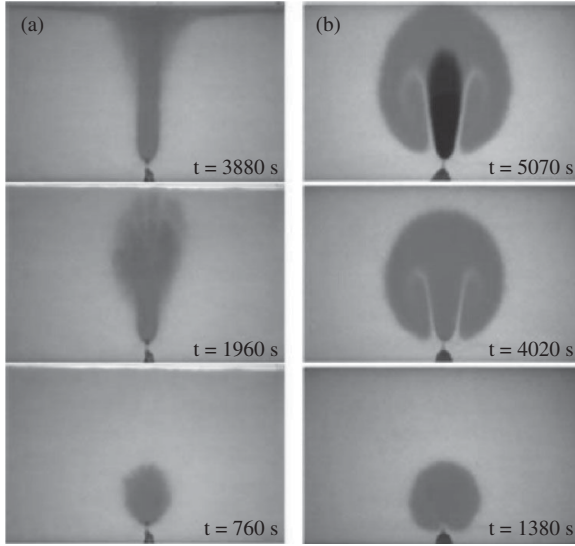


Figure 11.8 Three frames, at successive times illustrating the buoyancy-driven flow in a porous medium driven by (a) a fresh plume migrating through an initially saline solution of the same temperature, and (b) a hot plume migrating through an initially cold fluid of the same composition. During the experiment, the colour of the injected fluid is changed from red to blue to help visualise the flow pattern. After Menand *et al.* (2003). A black and white version of this figure will appear in some formats. For the colour version, please refer to the plate section.

This steady thermal plume is expected to be of relatively small horizontal extent compared to the vertical extent, and so involves a balance of the cross-flow diffusion of heat with the advection by the velocity field (u, v) , leading to the relations for conservation of heat

$$u \frac{\partial T}{\partial x} + v \frac{\partial T}{\partial y} = \kappa \frac{\partial^2 T}{\partial x^2} \quad (11.24)$$

together with Darcy's law

$$v = -\frac{k}{\mu} \alpha g T \quad (11.25)$$

where T is the temperature and the streamfunction ψ is given by

$$\text{relative to the far-field } u = \frac{\partial \psi}{\partial y} \quad \text{and} \quad v = -\frac{\partial \psi}{\partial x} \quad (11.26)$$

where x is the horizontal and y the vertical coordinate. For a steady plume, the vertical heat flux, Q_H , is conserved and so

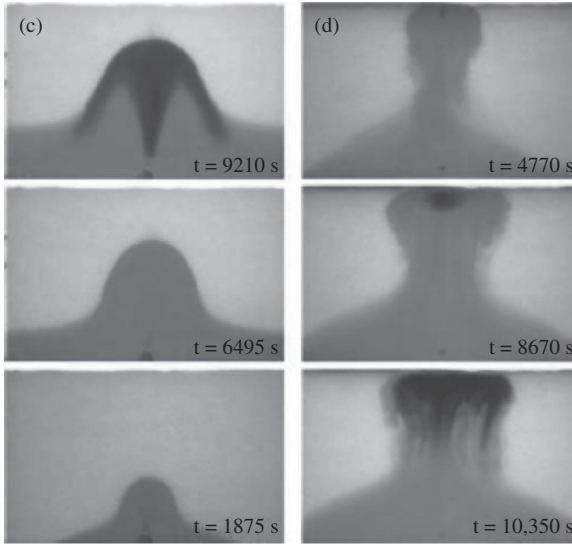


Figure 11.9 Three frames at successive times illustrating the buoyancy-driven flow of a hot, compositionally enriched injection fluid through a porous layer, in the case that the injection fluid is initially less dense than the original fluid in the porous layer. The fluid is injected from (c), the base (left-hand panels) and (d), the top of the layer (right-hand panels). During the experiment the colour of the dye in the injected fluid is changed from red to blue to help visualise the flow pattern. After Menand *et al.* (2003). A black and white version of this figure will appear in some formats. For the colour version, please refer to the plate section.

$$\rho C \int_{-\infty}^{\infty} vTdx = Q_H \quad (11.27)$$

By combining Eqs. (11.24–11.27) with the conservation of heat flux (11.27), it may be shown that these equations have similarity solution of the form

$$\psi(x, y) = -\kappa \left(\frac{y}{\beta}\right)^{1/3} f(\eta) \quad \text{and} \quad T = (Q_H/\rho C\kappa) \left(\frac{\beta}{y}\right)^{1/3} f'(\eta) \quad (11.28)$$

where

$$\beta = \frac{v\kappa^2\rho C}{g\alpha k Q_H} \quad \text{and} \quad \eta = \frac{x}{(\beta y^2)^{1/3}} \quad (11.29a)$$

On substitution into (11.24), it can be shown that the shape function has solution (Wooding, 1963)

$$f(\eta) = \frac{9}{2} \tanh\left(\frac{3\eta}{4}\right) \quad (11.29b)$$

This solution illustrates how the lateral diffusion of heat causes the plume volume flux to increase as it rises. An analogous effect can be seen in the lowest part of the plume in

Figure 11.8b, where the ambient fluid is drawn up around the central core of dyed source fluid.

There are also cases in which the injected fluid is of greater composition than the reservoir fluid, but in which the fluid is initially hotter, so that on entering the porous medium, an upward propagating plume initially develops. However, as the flow migrates through the porous layer and cools across the thermal front, the greater composition of the injected fluid compared to the source fluid leads to a reversal of the buoyancy, and formation of a dense, spreading gravity current, as shown in Figure 11.9c corresponding to case c in Figure 11.7. In Figure 11.9c, the colour of the dyed fluid is changed part way through the experiment from red to blue to help visualise the flow trajectories. It is seen that the continuing flow rises to the top of the red zone, where it encounters the colder original bead pack, cools and then spreads laterally.

If the injected fluid is relatively saline, but initially so hot that the flow is less dense than the original reservoir fluid (case d, Figure 11.7) then if the fluid is supplied to the top of the porous layer, rather than the base, the flow will initially migrate along the upper boundary of the porous layer. However, on migrating through the porous layer, the fluid will eventually pass through the thermal front and cool to the temperature of the surroundings. The greater salinity of the injected fluid then causes this to be denser than the surrounding flow, and the current sinks through the porous layer. The injected fluid then spreads as a relatively dense current on the lower boundary of the domain (Figure 11.9d).

For this latter case, the gravity-driven flow along the upper boundary has an effectively smaller mass flux, in the sense that only that fraction of the flow within the advancing thermal front is buoyant and spreads along the upper boundary. This current therefore only grows at the rate of advance of the thermal front. In contrast, the flux supplied to the lower current is given by that fraction of the fluid which passes through the thermal front. The lateral extent of the two currents, however, depends on the relative magnitudes of the positive and negative buoyancy as well as the respective supply volume fluxes, as may be inferred from the solutions for simple gravity currents presented earlier (Chapter 9). In this case with reversing buoyancy, the descending flow leads to considerable mixing with the ambient fluid, which increases the flux in the lower current.

The development of these more complex flow patterns in cases where both the thermal and compositional fields influence the flow may be critical for optimisation of the heat transfer within a geothermal system. Indeed, the objective of injecting fluid into geothermal systems is to warm up the injected fluid and then recover that thermal energy at the production well downstream. If the flow arranges itself so that there is a significant, laterally spreading plume of cold fluid, which is not localised near the injection point, as occurs in the case of reversing buoyancy (Figure 11.9d), then the production well may extract some of this cold fluid, reducing the effectiveness of the

overall system. Indeed, many higher temperature geothermal systems rely on the temperature of the produced fluid being sufficiently high that the thermal energy can be converted into useful work.

Some of the examples above relate to the case in which the buoyancy changes sign on passing through the thermal front. However, in many systems, the compositional and thermal influence on buoyancy may not be exactly matched in magnitude; the effect of the thermal front may then be to change the magnitude of the buoyancy and in some cases the change in mobility of the fluid may also be significant. We now examine some of these effects, primarily in the context of gravity currents, illustrating how the change in buoyancy on passing through the thermal front can have a profound impact on the spatial distribution of thermal energy within the current.

11.7 Gravity currents with thermal and compositional buoyancy

In the previous section, we examined the dynamics of plumes controlled by both thermal and compositional differences, and focused in particular on the case of reversing buoyancy in which the density of the injected fluid relative to the ambient changes sign on passing through the thermal front. In this section, we explore flows which arise when the density relative to the background changes in magnitude but not in sign on passing through the thermal front. Again, for simplicity, we focus on two-dimensional gravity currents. If the injected fluid initially has temperature ΔT in excess of the ambient and has salinity ΔS smaller than the original fluid, then the initial upslope buoyancy speed will be

$$u_o = \frac{k\rho_o(\alpha\Delta T + \beta\Delta S)g \sin \theta}{\mu} \quad (11.30)$$

where ρ_o is a reference density and α and β are the thermal and solutal expansion coefficients and θ is the angle of inclination of the slope to the horizontal. This will evolve to

$$u_1 = \frac{k\rho_o\beta\Delta Sg \sin \theta}{\mu} \quad (11.31)$$

once the thermal field has adjusted to that of the reservoir.

Assuming the flow continues upslope, the change in depth across the thermal front can be found using a simple mass flux balance, relating the depth upstream, H_o and downstream, H_1 , according to

$$u_o H_o = u_1 H_1 - \Gamma \phi u_o (H_1 - H_o) \quad (11.32)$$

where the final term denotes the upslope migration of the thermal front, with speed Γu_o . This identifies the depth downstream of the thermally adjusted zone as

$$H_1 = H_o \left[\frac{1 - \Gamma \phi}{\frac{u_1}{u_o} - \Gamma \phi} \right] \quad (11.33)$$

There are two different situations possible. If the flow is initially cold, $\Delta T < 0$ the buoyancy will increase on heating up to the formation temperature, leading to an increase in speed, $u_1 > u_o$ and so (11.28) shows there is a thinning of the current (Figure 11.10a).

If the flow is initially hot, then on cooling to the reservoir temperature, the buoyancy of the flow will decrease, causing a deceleration $u_1 < u_o$. In this case, Eq. (11.33) suggests that either there is a deepening of the flow if the interstitial flow speed beyond the thermal front, u_1/ϕ , is greater than the speed of the thermal front, Γu_o , so that

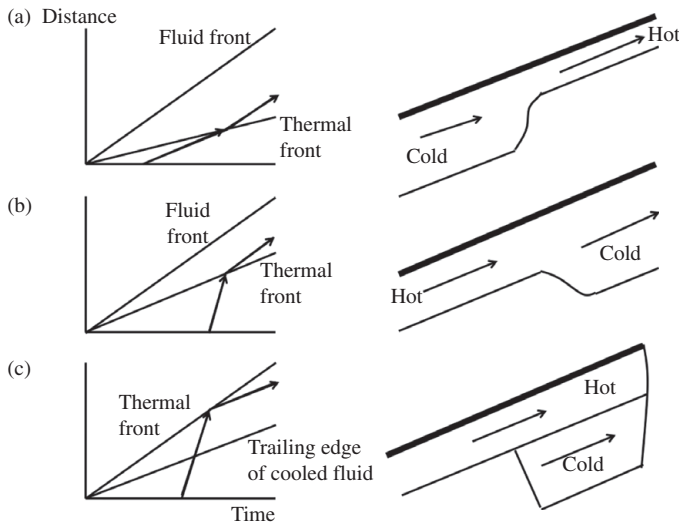


Figure 11.10 Characteristic diagrams in distance–time coordinates and the structure of a buoyancy-driven flow in the case that there is an internal thermal boundary layer in the flow as it runs upslope. (a) Corresponds to the case in which the current buoyancy increases as it heats up, leading to an acceleration of the flow downstream of the thermal front, as shown by the arrow in the characteristic diagram, leading to the thinning and increase of the speed of the current downstream. (b) Corresponds to the case of injection of relatively hot fluid in which, on passing through the thermal front, the current cools and becomes less buoyant than near the source. In this case the buoyancy-driven flow downstream of the thermal front is faster than the speed of the thermal front and the current continues propagating ahead of the thermal front. (c) Situation in which a hot current cools on passing through the thermal front, but in which the speed of the thermally adjusted flow is less than that of the thermal front, as seen in the characteristic diagram. In this case the cooled fluid is overtaken by the thermal front, and hence the continuing cold fluid is displaced downwards by the oncoming hot fluid, and thereby forms a layered gravity-driven flow.

$$u_1 > u_o \Gamma \phi \quad (11.34)$$

(Figure 11.10b). In contrast, if the buoyancy decreases so much across the thermal front that the interstitial speed of the fluid downstream of the front is less than the speed of the thermal front,

$$u_1 < u_o \Gamma \phi \quad (11.35)$$

then the thermally adjusted fluid will form a new layer below the original buoyant current, and this new layer lags behind the original buoyant current. As a result, the thermal front will be at the leading edge of the flow (Figure 11.10c).

In order to describe such flow structures, we can use the method of characteristics to track the evolution of the flow and the thermal front, in a fashion analogous to the presentation in Chapter 9. In the left-hand panels in Figure 11.10 we have included a characteristic diagram to illustrate how the fluid and the thermal fronts advance along the boundary both upstream and downstream of the thermal front.

Case a provides an effective means of recovering the thermal energy from a system while maintaining a relatively deep cooling front by injection of compositionally light fluid. In the case in which a compositionally heavy and cold fluid is injected, we can learn from cases b and c. Now the current will run downslope, along the lower boundary, but as it heats up to the reservoir temperature, its buoyancy is reduced; this will lead to a current which is analogous in structure to one of case b or c in Figure 11.10. If the warmed current advances more rapidly than the thermal front, then the flow will consist of a relatively thin cold current upstream of the front: in this region, the thermal energy has been extracted from the formation. Downstream of the front there will be a thicker heated region in which the fluid carries this thermal energy. This will lead to a less effective spatial pattern of cooling of the formation with thermal energy only being extracted from the thin upstream region analogous to case b, Figure 11.10. If the warmed fluid travels less rapidly than the thermal front then cold fluid will in fact arrive at the production well along with the warm fluid, since the thermal front outruns the warm fluid which has passed through the thermal front (analogously to case C, Figure 11.10). In the engineering context, this has several drawbacks; in particular, the production well is now likely to extract mixed hot and cold fluid, so that the thermal energy mined from the formation by the advancing thermal front is compromised by the direct production of the cold injectate.

The above discussion has focused on models of two-dimensional gravity-driven flow in porous aquifers. One can also examine the flow pattern associated with source-sink flows. In this case, we might contrast the flows generated with a source updip or downdip of the injector well, when a compositionally light but cold fluid is injected, and then warms up to reduce its buoyancy, and the case in which a compositionally heavy but cold fluid is injected and becomes warm, thereby decreasing the buoyancy.

Figure 11.11 shows two example calculations of the flow at an early time and after one reservoir volume of fluid has been injected for the case in which (a) the injector

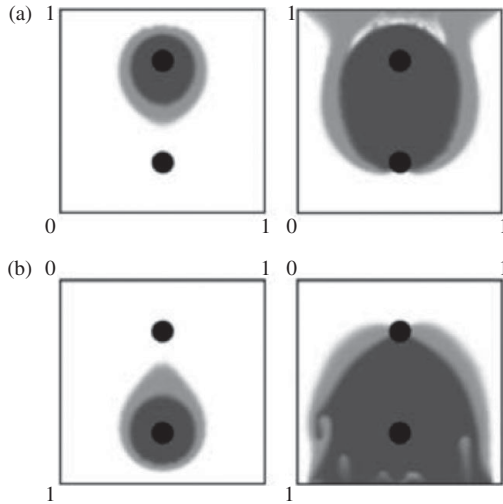


Figure 11.11 Example of a source–sink flow in a porous medium in which the injected fluid is initially buoyant but becomes dense on passing through the thermal front. The initial injection fluid is shaded black, and the thermally adjusted injection fluid is shaded grey. In panel a, the fluid is injected from the upper well, while in panel b the fluid is injected from the lower well. The gravitational acceleration acts downwards in this figure. After Nigam and Woods (2006).

well is updip of the producer well, and the buoyancy of the injected fluid increases across the thermal front owing to the heat transfer from the formation, and (b) the injector well is downdip of the producer well and the buoyancy of the injected fluid again increases owing to heat transfer from the formation. The light grey region indicates the injected fluid which has passed through the thermal front, while the black region corresponds to injected fluid which has not reached the thermal front. The white fluid corresponds to the original reservoir fluid. In the former case (a), the light grey region of thermally adjusted injection fluid is buoyant and so tends to rise to the top of the reservoir rather than flowing into the producer well and this leads to the production of the cold injection fluid, shown as the darker fluid. In the latter case (b), the grey fluid is again less dense than the dark fluid, and so this tends to rise upwards and is drawn into the producer well. As the fluid which spreads downwards away from the producer well passes the thermal front and becomes buoyant, this fluid then mixes back into the colder injected fluid, as seen by the plumes at the base of the system. This latter configuration (b) will recover more of the thermal energy from the system and indicates the key role of thermal changes on the pattern of water flooding (See Nigam and Woods, 2006).

11.8 Scale precipitation and its impact on buoyancy-driven flow

A significant problem in geothermal systems concerns the formation of scale deposits which can fill pore spaces and change the permeability. In Chapter 8 we reviewed some

of the reactions which may arise when fluid of one temperature floods a rock at a different temperature, leading to dissolution or precipitation reactions. We also demonstrated that such reactions may be unstable to a viscous fingering-type instability (Chapter 6) and that with gravity, the reactions may lead to formation of a dominant dissolution channel (Chapter 9). However, the double-advective plumes we have described in this chapter, associated with the change of fluid properties across the thermal front, can also develop in a reacting flow. In particular, since the speed of the reaction front is smaller than the fluid front, then the properties of the injected fluid may change across the reaction front. Since the composition of the injected liquid is likely to be different from the original formation water, the solubility of the water to minerals in the formation may also be different. As the fluid dissolves or precipitates to reach equilibrium with the matrix, the density of the fluid may then also change. This can alter the pattern of flow of the fluids within a system and the associated recovery of thermal energy. With dissolution, it may also lead to formation of channels of high permeability which can control the subsequent flows.

In order to illustrate some of the possible buoyancy-driven flow effects which may arise either with a chemically driven reaction (Chapter 8) associated with differences in composition of the injected fluid, or perhaps slaved to the thermal front, the use of sugar-salt solutions with solid salt powder in a bead pack provides an interesting experimental model system. As the concentration of sugar in a solution changes, the solubility of salt in that solution, for a given temperature, also changes. The density of a sugar-salt solution in equilibrium with salt powder at a given temperature depends on the sugar concentration. As a result, if a sugar solution of one sugar concentration and hence density is injected into a porous layer containing a sugar-salt solution in equilibrium with salt powder, with a different sugar composition, then the injected sugar solution may have a different density from the reservoir fluid. As it dissolves salt to reach equilibrium, the injected fluid may then evolve to a third density.

Rayward-Smith and Woods (2014) developed this experimental system to explore the possible influence of reactions on the buoyancy-driven flow of a liquid injected into a geothermal system. They have shown that a range of flow patterns, all at a uniform temperature, can develop through the injection of one such sugar-salt solution into a bead pack saturated with a second solution and also containing salt powder: in particular, it is possible to generate flows in which the buoyancy of the injected liquid evolves in different ways. Four examples include: (a) the case of constant buoyancy: this regime develops when there is no salt powder in the cell and we have a constant compositionally buoyant plume (see Figure 11.12a). (b) The buoyancy reverts to zero on reaction: this may be achieved by injecting a fluid with the same sugar composition as the original fluid in the porous layer but initially no salt (Figure 11.12b). As the flow advances and dissolves salt, the porous layer becomes depleted in salt near the source. This leads to a growing dissolution channel, along which the continuing supply of unsaturated solution advances until reaching the salt powder where

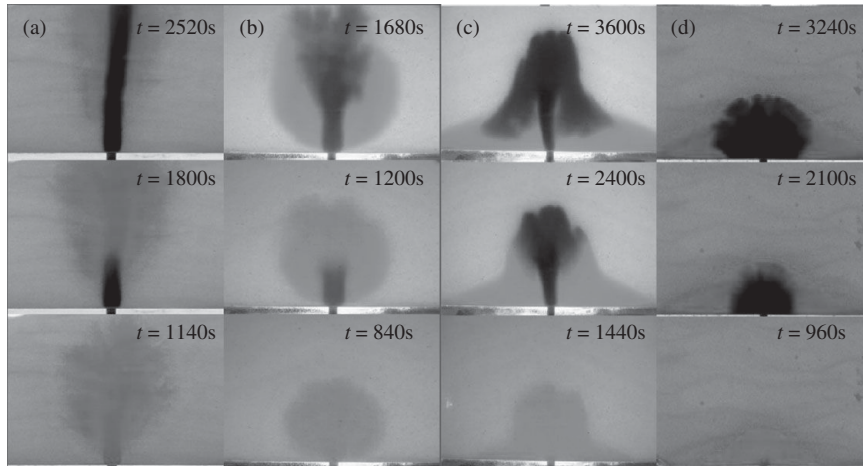


Figure 11.12 Figure illustrating the pattern of flow when a sugar–salt solution is injected into a bead pack saturated with a sugar–salt solution of different sugar content. The bead pack includes a small fraction of salt powder, and as the injected fluid enters the system it dissolves some of this salt, leading to a change in density. The different patterns of flow are illustrated by the sequence of three photographs in each of cases a–d. In a the injected fluid is less dense than the original solution in the bead pack both before and after dissolving the salt, and thereby forms a compositional plume; the halo around the centre of the plume denotes the earlier plume fluid once it has dissolved some of the salt and become of intermediate density between the formation fluid and the injected fluid. This rises more slowly than the more recent injection fluid which rises along the dissolution channel in the centre of the bead pack, until eventually reaching some salt higher in the bead pack. The flow pattern is visualised by changing the colour of the injected fluid from red to black during the experiment. In b the injected fluid is initially more buoyant but becomes neutral on reacting with the salt, and this is analogous to the thermal plume shown in Figure 11.8b. In case c, the injected fluid is initially buoyant but becomes dense on reacting with the salt powder, this leads to a dissolution channel which rises directly above the source, and then a collapsing fountain of dense fluid around the channel which feeds a laterally spreading gravity current on the base of the system. In d the injected fluid is initially dense, but becomes even more dense on reacting with the salt powder, therefore forming a dense laterally spreading gravity current. Photographs courtesy of Will Rayward-Smith. A black and white version of this figure will appear in some formats. For the colour version, please refer to the plate section.

the reaction occurs and reduces the buoyancy of the advancing fluid to zero relative to the original formation fluid. The fluid then spreads out to the side of the advancing reaction channel while the continuing plume grows in the channel. In the photograph the injected fluid is initially dyed red, but then changed to dark blue in order to help visualise the flow pattern. (c) The flow is initially buoyant and rises up through the layer since it contains no salt, although having a greater sugar content than the fluid originally in the bead pack. As the vertical channel of salt is dissolved by the supply fluid, this fluid becomes denser than the original fluid in the formation. The flow then falls back and spreads out on the base of the cell. The fluid is initially dyed red,

but this is changed to dark blue part way through the experiment to help visualise the flow. (d) The injected fluid is initially dense but as it dissolves salt it becomes even denser.

There are numerous other cases one can envisage, and as seen, such effects can be critical for the successful modelling of the flow pattern in geothermal systems, since the change in density with composition may dominate the change associated with temperature, depending on the temperature contrast between the injected fluid and the formation, and the capacity to dissolve minerals. If a reaction-driven flow develops a large-scale plume structure of the form shown in Figure 11.12a, for example, and this plume involves a change in permeability of the formation, then this may control subsequent flows within the system, limiting the potential for cold fluid to sweep through the zones outside the dissolution channels.

11.9 Aquifer thermal energy storage

One of the challenges for renewable energy systems is associated with the storage of energy owing to the intermittent generation, for example as occurs with wind power. In addition, there are large seasonal fluctuations in the external temperature and this leads to the availability of excess thermal energy during the warmer seasons, for example at power stations. For both of these intermittent energy sources, storage of the energy in the form of thermal energy may represent an effective means of conserving the use of primary energy for power and/or heating applications. However, it is key that the energy losses associated with storage are small. One strategy for such storage is known as aquifer thermal energy storage, and has been proposed and indeed implemented in several cases, mainly in Scandinavia and the Netherlands. Some of the fluid mechanical principles have significant overlap with the geothermal flows we have been considering in this chapter. We now outline some of the distinguishing processes specific to or very important in aquifer thermal energy storage systems, which relate to (i) the loss of thermal energy through conduction into the surrounding strata and its impact on the heat recovery temperature and (ii) the recovery of the injected liquid, and potential mixing with the groundwater, which may lead to reactions and scale formation in the system.

With interseasonal heat storage, fluid is injected at one temperature and displaces the formation fluid for a period of order 6 months, and then the fluid is pumped out of the system, perhaps at the same well, for about 6 months (Figure 11.13). There is a gradual loss of thermal energy from the system by diffusion into the surrounding rock. It is of considerable interest to understand the heat-transfer processes in the subsurface in order to assess the potential to recover the thermal energy and also the temperature of this recovered thermal energy, since this may limit its use. If the temperature of the water recovered from the system is too cold, apart for direct use for low-grade heating, it may not be useful without passing through a heat pump. A heat

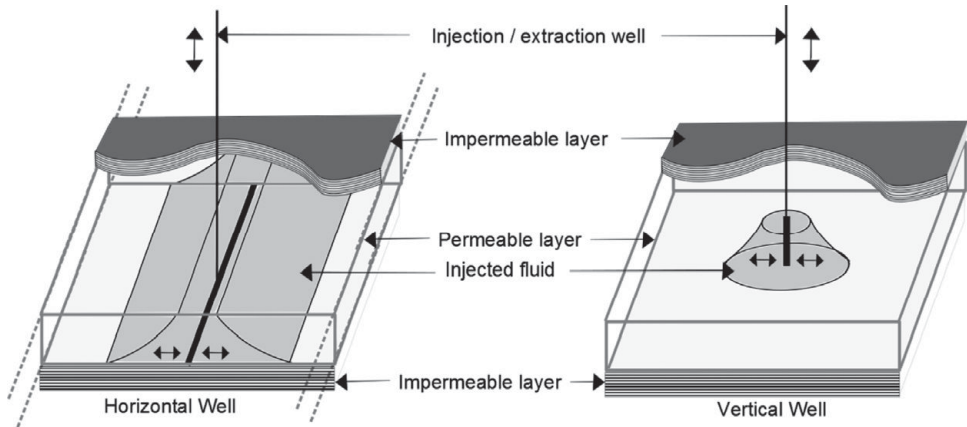


Figure 11.13 A schematic of an aquifer thermal energy storage system in the case of injection from (a) a horizontal line well and (b) a vertical well.

pump is a machine which raises the temperature at which a heat flux is being transferred, essentially by operating as a fridge in reverse. In the present context, thermal energy would be removed from the water by a heat exchanger containing a cold refrigerant which is heated up by the water. The refrigerant is then compressed by an engine which performs work on the refrigerant. This raises the temperature of the refrigerant which then passes through a second heat exchanger at higher temperature. Thermal energy is removed from the refrigerant at this higher temperature into a second fluid which then carries the thermal energy away for use in a heating system or for use in a heat engine. Meanwhile the refrigerant expands and cools, and passes through the primary heat exchanger again to collect more thermal energy from the water which has been extracted from the ground system. The mechanical work required to drive the refrigerant through the system, causing the compression and expansion phases of the flow, is typically only a fraction of about a quarter to a third of the thermal energy flux passing through the heat pump. However, for a given output temperature, this fraction increases substantially as the temperature of the input fluid decreases. As a result, aquifer thermal energy storage is only useful if the thermal energy can be recovered from the ground at sufficiently high temperature. Otherwise the work done by the heat pump, and in pumping water into the ground, and recovering it from the ground may become a significant part of the overall energetics of the system. (We note that there is a further challenge of such systems if the heat pump engine is powered by electricity generated remotely at a power station. This is because such electricity incurs losses in generation, and transmission, so that typically only a fraction of order 0.2–0.25 of the calorific value of the fuel producing the electricity is supplied to the end-user, in contrast to local heating systems which directly convert fuel into thermal energy on site.)

In order to help assess the potential recovery temperature and hence the fraction of the thermal energy injected into the subsurface which may be recovered from a

heat storage system, we develop a series of simplified models. The purpose of the models is to develop insight into some of the limiting processes rather than provide a full simulation of a specific field location. First, we consider a one-dimensional model of injection and extraction from a single well, including diffusion to the far field, to assess the temperature of the recovered fluid over successive cycles in a permeable layer of large vertical extent. We then extend this modelling approach to examine the effect of heterogeneities in the rock structure. These can have a fundamental influence on the heat flow through dispersion of the thermal signal, in an analogous fashion to the compositional dispersion we examined in Chapter 5. We then consider how the injected and formation water interact, over successive cycles, especially in the case that the injected water is of different composition. In particular, we explore how the fraction of original reservoir fluid which is produced during the extraction cycle varies from cycle to cycle. Such effects are important in the case that one does not want to bring water from the target aquifer to the surface. For example, salts in the formation water may precipitate at low pressure and plug the well.

11.10 One-dimensional injection and production of hot water

We first consider a one-dimensional situation, corresponding to an aquifer of considerable vertical extent, in which there is injection of hot water and subsequent recovery of that water, on an interseasonal basis across the whole depth of the aquifer. As motivation for this one-dimensional problem, one may envisage that to enhance the inflow to the system, the well intersects a fracture, so that the injected water flows into the formation from an effective planar source supplied by the well. The heat loss is then primarily parallel to the direction of motion and the problem requires solution of the one-dimensional advection–diffusion equation for thermal energy of the form

$$\frac{\partial \theta}{\partial t} + u \sin \omega t \frac{\partial \theta}{\partial x} = k \frac{\partial^2 \theta}{\partial x^2} \quad (11.36)$$

$$\theta(0) = 1 \quad \text{for} \quad 0 < t < \frac{\pi}{\omega} \quad (11.37)$$

$$\left. \frac{\partial \theta}{\partial x} \right|_0 = 0 \quad \text{for} \quad \frac{\pi}{\omega} < t < \frac{2\pi}{\omega} \quad (11.38)$$

with the boundary conditions (11.37, 11.38) requiring that during the input cycle the temperature at the input is prescribed and during the outflow cycle, the heat flux at the origin is purely advective. In the far field the temperature is a constant, different from the input fluid temperature. The above equations have been put in dimensionless form, by scaling the temperature so that the input temperature is 1 and the far-field temperature is zero. Numerical solution of these equations illustrates how the temperature field gradually diffuses into the far field beyond the region into which fluid is periodically

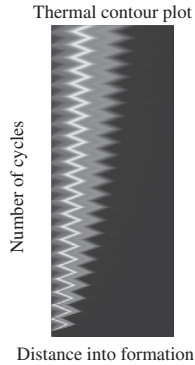


Figure 11.14 Gradual spreading of the injected thermal energy (horizontal axis) to form a region of hot rock over 23 cycles of injection and extraction, with time shown on the vertical axis. The thermal signal gradually diffuses into the far field, ahead of the maximum extent of the injection fluid. For the colour version, please refer to the plate section.

cycled (Figure 11.14). The colours denote different temperature, with red being hot and blue cold. The horizontal axis denotes position and the vertical axis denotes time.

After many injection–extraction cycles, the thermal energy diffusing to the far field becomes a progressively smaller fraction of the injected thermal energy, as its transport becomes rate-limited by diffusion. As a result, the fraction of the thermal energy injected into the system which can then be recovered tends towards unity, and the temperature of the recovered water approaches the injection temperature, neglecting the effects of heat loss through the upper and lower boundaries of the system. Similar calculations can be carried out for other geometries including axisymmetric flow from a line well; for typical injection rates, the outward advective flow will dominate the thermal diffusion (cf. Section 11.1).

11.11 Heat loss to lenses of low permeability

The above one-dimensional picture of heat transfer in permeable rocks is simplified, and does not account for the heat loss in the direction normal to the flow. As described in Chapter 2, rocks may include lenses of low permeability which are bypassed by the flow. However, the thermal diffusivity of rocks is about $5 \times 10^{-7} \text{ m}^2/\text{s}$. This is much larger than the solutal diffusivity, and so the cross-stream diffusion of heat becomes significant much sooner than the cross-stream transfer of solute.

In developing the original model of heat flow through a porous medium in Chapter 8, we identified that the fluid and matrix remain in thermal equilibrium locally owing to the fact that the thermal diffusion time across the grains is much shorter than the typical travel time of the fluid across the grains. However, on larger lengthscales, characteristic of lenses of low permeability rock, the diffusion time is longer and so we expect

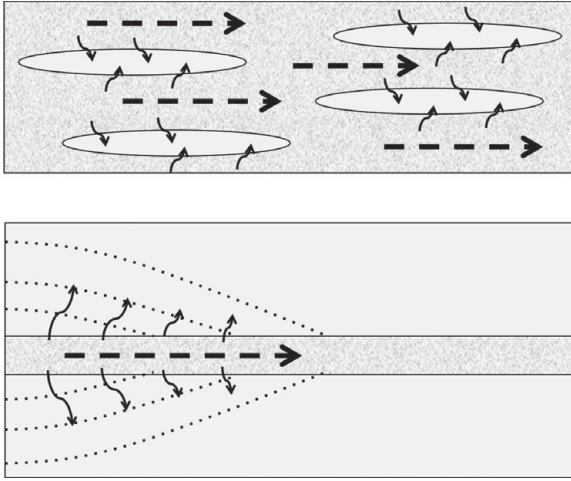


Figure 11.15 (a) Schematic of heat exchange to a series of lenses within a formation, which leads to a reduction in the effective advection speed of the thermal signal through the formation and (b) a schematic of the heat loss to the surrounding impermeable strata in the case of a thin permeable layer embedded within a deeper impermeable region of formation.

that the flowing high permeability zones will change temperature first, and then cross-streamline diffusion will cause the lower permeability zones to adjust. As a result, the mean speed of the thermal front effectively decreases as the fluid now advects the thermal energy originally contained in the matrix of both the high permeability and low permeability zones (cf. Chapter 8); however, the shear in the velocity profile leads to an effective dispersion of the thermal front about this mean.

For example, if there is a lens of low permeability, of thickness H and lengthscale $L \gg H$, then the cross-lens diffusion time scales as H^2/κ . If we assume that a particular layered formation consists of alternating high, h , and low, l , permeability layers, with scale h_h and h_l in the cross-flow direction, we can then follow the model for Taylor dispersion in this system (Chapter 5) to establish the long-time advection–diffusion equation for the temperature. Assuming the flow speed in the low permeability layer is a fraction $\frac{k_l}{k_h}$ of the flow in the high permeability layer, where k_L and k_h are the permeabilities of the two layers, then the mean flow speed is

$$\bar{u} = u_h h_h \frac{\left(1 + \frac{k_l h_l}{k_h h_h}\right)}{(h_h + h_l)} \quad (11.39)$$

In the limit that there is negligible flow in the low permeability layer, $k_l h_l \ll k_h h_h$, the mean Darcy speed averaged across both layers is then

$$\bar{u} = \left(\frac{h_h}{h_h + h_L}\right) u_h \quad (11.40)$$

The mean advection speed for the temperature field is then given by $\Gamma \bar{u}$ where $\Gamma = \rho_l C_{pl} / (\phi \rho_l C_{pl} + (1 - \phi) \rho_m C_{pm})$ is assumed to take the same value in each layer.

We now estimate the effective dispersion of the thermal signal. Our approach is to define the cross-layer averaged temperature,

$$\bar{T}(x, t) = \int_0^{h_h+h_L} \frac{T(x, y, t)}{(h_h + h_L)} dy \quad (11.41)$$

and the difference between the actual temperature and this cross-layer averaged temperature, $\hat{T}(x, y, t) = T - \bar{T}$. We then aim to develop an equation for the evolution of the heat flux through the system, noting that the cross-layer average of the thermal advection–diffusion equation across the layers has the form (cf. Chapter 5)

$$\frac{\partial \bar{T}}{\partial t} + \Gamma \bar{u} \frac{\partial \bar{x}}{\partial x} = \kappa \frac{\partial^2 \bar{T}}{\partial x^2} - \Gamma \hat{u} \frac{\partial \hat{T}}{\partial x} \quad (11.42)$$

As in Chapter 5, the dispersion is quantified by the second term on the right-hand side of (11.42) and to estimate this we require an estimate for \hat{T} . Again, we expect that \hat{T} is controlled by the balance between the shearing of the longitudinal temperature gradient and the cross-layer diffusion of heat, leading to the relation (cf. Chapter 5)

$$\Gamma \hat{u} \frac{\partial \bar{T}}{\partial x} = \kappa \frac{\partial^2 \hat{T}}{\partial y^2} \quad (11.43)$$

The flow speeds in the two layers relative to the mean are given by

$$\hat{u} = \frac{h_L(u_h - u_L)}{h_h + h_L} = f \Delta u \quad \text{for } 0 < y < h_h \quad (11.44a)$$

and

$$\hat{u} = \frac{h_h(u_L - u_h)}{h_h + h_L} = -(1 - f) \Delta u \quad \text{for } h_h < y < h_h + h_L \quad (11.44b)$$

where $\Delta u = u_u - u_L$ and $f = h_L / (h_h + h_L)$. Combining these expressions with equation (11.42), we can find a general expression for the perturbation temperature field as a function of position across the channel, subject to the simplifying assumption of zero normal heat flux on the boundaries $y = 0$ and $y = h_u + h_L$. This would correspond, for example, to a multiply layered system with alternating high and low permeability layers, where h_u and h_L correspond to the half-thickness of the layers. Combining this with the perturbation velocity, we can evaluate the dispersive flux given by the last term on the right-hand side of (11.41),

$$F_{disp} \approx \frac{\Gamma^2 \Delta u^2 H^2}{6\kappa} \frac{\partial^2 \bar{T}}{\partial x^2} A(f) \quad (11.45)$$

where

$$A(f) = 2f^2(1 - f)^2 \quad (11.46)$$

In the special case $f = 0.5$, we find $A(f, h_h, h_L) = 1/2$ and the effective transport equation has the form

$$\frac{\partial \bar{T}}{\partial t} + \Gamma \bar{u} \frac{\partial \bar{T}}{\partial x} = \left(\kappa + \frac{\Gamma^2 \Delta u^2 H^2}{48\kappa} \right) \frac{\partial^2 \bar{T}}{\partial x^2} \quad (11.47)$$

For $u \sim 10^{-5} - 10^{-6}$ m/s, $h_h \sim 1 - 10$ m, and $\kappa \sim 10^{-7}$ m²/s we find D_e has values in the range $10^{-3} - 10^{-5}$ m²/s and so there may be significant dispersal of the thermal front owing to the presence of low permeability layers within the formation. With much thinner layers, < 0.1 m wide, the longitudinal dispersion is smaller than the molecular diffusivity, and with wider layers the dispersion becomes larger. This simplified modelling establishes that provided the lenses are embedded within the flowing zone, then, on longer timescales, they have the effect of changing the mean advection speed of the thermal front as well as producing enhanced longitudinal dispersion.

However, if the formation is of limited extent in the cross-flow direction and is surrounded by impermeable strata, then the evolution of the temperature may be different as we explore below.

11.12 Heat loss to the surrounding formation

In the previous example, we illustrated the change in the effective heat transport speed and dispersion in the case that there is a series of impermeable layers of finite thickness, embedded within the porous layer. We can also envisage situations in which the aquifer is of finite vertical extent, and loses heat to a much thicker impermeable layer of cap-rock above and below the aquifer. In this situation, we are interested in finding the distance beyond which the thermal signal of the injected fluid becomes depleted by heat exchange with the surrounding formation. We consider flow in a laterally extensive permeable layer of thickness $2H$, $-H < y < H$, with flow in the along-layer direction x of speed u . We assume there is a seal rock in the regions $y > H$ and $y < -H$, with thermal diffusivity κ , density ρ_m and specific heat C_p everywhere in the formation.

First, we develop an estimate for the distance $x_d(t)$ over which the thermal energy in the supply fluid will diffuse from the formation into the seal rock. We suppose that at distance x from the source, after a time t , the thermal energy has diffused into the formation above and below the permeable layer a distance of order

$$y_d \sim (\kappa [t - t_t(x)])^{1/2} \quad (11.48)$$

where $t_t(x)$ represents the time since the thermal front reached the point x , given that the injection commenced at $t = 0$ at the point $x = 0$. If the source supplies fluid with speed u and temperature ΔT relative to the formation, to a layer of thickness $2H$ then the thermal energy supplied after time t is $2\rho_l C_{pl} \Delta T H u t$. With the above scaling y_d for

the extent of the region of cross-layer heat loss in the surrounding impermeable rock, we conclude that the thermal signal in the advancing fluid can only extend a distance of order $x_d \sim uH(t/\kappa)^{1/2}$ along the layer, in order to conserve heat.

By comparison with the one-dimensional model presented in Section 11.1, in which we neglected heat loss from the upper and lower boundaries of the flow domain, we infer that the heat loss becomes important once the advection distance of the thermal front Γut becomes comparable to the distance $x_d \sim uH(t/\kappa)^{1/2}$. This occurs at the time $t_a \sim H^2/\Gamma\kappa$. Subsequently the advection of the thermal energy becomes limited by the heat loss to the neighbouring formation. In a layer of 1–10 m thickness, this time ranges from several months to tens of years.

In order to develop an expression for the temperature profile around the permeable layer, it is convenient to examine the typical limit, $uH \gg \kappa$, for which the cross-flow diffusion distance at time t_a , which scales as $H/\Gamma^{1/2}$ is small compared to the distance the thermal signal has advanced along the layer, which scales as $uH^2/\kappa\Gamma$. In this case, for times in excess of t_a , we can neglect the along-layer diffusion of heat and approximate the heat transfer in the surrounding layers, $y > H$ and $y < -H$, with the one-dimensional diffusion equation

$$\frac{\partial T}{\partial t} = \kappa \frac{\partial^2 T}{\partial y^2} \quad (11.49)$$

while in the permeable layer, $-H < y < H$, the temperature satisfies

$$\frac{\partial T}{\partial t} + \Gamma u \frac{\partial T}{\partial x} = \kappa \frac{\partial^2 T}{\partial y^2} \quad (11.50)$$

If we average across the flowing layer, in the direction normal to the flow and denote the mean by the overline notation, then the mean temperature in the flowing layer $\bar{T}(x, t)$ is given by

$$\frac{\partial \bar{T}}{\partial t} + \Gamma u \frac{\partial \bar{T}}{\partial x} = \frac{\kappa}{H} \left(\frac{\partial T}{\partial y} \Big|_{y=H} - \frac{\partial T}{\partial y} \Big|_{y=-H} \right) \quad (11.51)$$

where the term on the right-hand side denotes the heat exchange with the non-flowing layers. The boundary conditions are that at $t = 0$ the temperature in the region $x > 0$ is constant, $T = T_o$, while for $t > 0$, fluid of temperature $T_o + \Delta T$ is supplied with uniform speed u from a well located at $x = 0$ in the region $-H < y < H$. At $y = H$ the temperature and heat flux in the direction normal to the interface are conserved. For times $t \gg t_a$, we expect the temperature variations across the flowing layer to be small, and so we make the approximation $\bar{T} = T(y = H) = T(y = -H)$ (cf. Lauwerier, 1955). Using Laplace transforms, he showed that this problem has solution

$$T(x, y, t) = T_o + \Delta T \operatorname{erfc} \left(\frac{\kappa x / Hu + y}{(\kappa [t - x / \Gamma u])^{1/2}} \right) \quad \text{for } x \leq \Gamma ut \quad \text{and} \quad |y| > H \quad (11.52)$$

while $T = T_o$ for $x > \Gamma ut$. This solution is consistent with the above scalings function becomes of order unity when $y \leq (\kappa t)^{1/2}$ or $x \leq H\Gamma u(\tau/\kappa)^{1/2}$ provided $t \gg t_a$.

The consequences of heat loss to the surroundings, which become important on timescales of years if the layer is of order 10 m deep, can be very significant for the evolution of the flow. Since the injected fluid only retains the injection temperature in a zone close to the source then reaction fronts, buoyancy transitions and other phenomena occur closer to the source, and this can change the overall distribution of the fluids within the system. However, the principles we described earlier in the chapter in the simplified limit of relatively deep layers still obtain, albeit on different lengthscales. Full exploration of reacting flows in such heterogeneous rocks is a rich area for further research.

11.13 Mixing of the injected and formation fluids on extraction

When fluid is injected into an aquifer and then recovered from the same well, there may be some mixing of the injected fluid with the original fluid in the reservoir. As a result some of the reservoir fluid may also be recovered from the well. In the case of a pressure-driven flow, such mixing will be controlled by the longitudinal dispersion, in a similar fashion to that described in Chapter 5, Section 5.7. However, in many cases, it is likely that the composition of the liquid will differ from that naturally occurring in the aquifer, and in that case the injected liquid may be subject to buoyancy forces as well as the pressure-driven flow. In the case that the thermal buoyancy is comparable to the buoyancy associated with the compositional differences, then the structure of the current may evolve across the thermal front, in a fashion analogous to that described earlier in this chapter (Section 11.7). However, in general, the compositional density differences may dominate the buoyancy, and in this case we expect the injected fluid to spread as a gravity current. In this case, the buoyancy contrast may suppress the dispersive mixing. However, the gravitational spreading of the injected fluid is not reversible, as it depends on the local gradient of the depth of the flow. Therefore, during the extraction cycle, some of the formation fluid may be extracted from the well rather than fluid in the leading edge of the spreading injected fluid.

In order to model the problem, it is convenient to consider the case of a two-dimensional horizontal aquifer, $0 < y < H$, with the current depth satisfying the equations for a confined gravity current (cf. Chapter 9)

$$\frac{\partial h}{\partial t} + \frac{Q(t)}{H\phi} \frac{\partial h}{\partial x} = S \frac{\partial}{\partial x} \left(h \left(1 - \frac{h}{H} \right) \frac{\partial h}{\partial x} \right) \quad (11.53)$$

where h is the depth of the dense injected fluid, S is the gravitational speed of the fluid, $S = k\Delta\rho g/\phi\mu$ and ϕ is the porosity. We now solve these equations subject to

the time-dependent boundary conditions at the injection/extraction well, which relate to the injection periods, $2n\tau < t < (2n + 1)\tau$ for which

$$-\phi Sh \frac{\partial h}{\partial x} = Q(t) \quad \text{if } 0 < h < H \tag{11.54}$$

and

$$-\phi SH \frac{\partial h}{\partial x} = Q(t) \quad \text{at } x = x_s(t) \quad \text{where } h = H \quad \text{for } x < x_s \tag{11.55}$$

and the extraction periods, $(2n + 1)\tau < t < (2n + 2)\tau$, for which

$$\phi Sh \frac{\partial h}{\partial x} = Q \quad \text{if } 0 < h < H \tag{11.56}$$

and

$$\frac{\partial h}{\partial t} = 0 \quad h = 0 \tag{11.57}$$

Numerical solution of the system of Eqs. (11.53–11.57) and laboratory experiments using a Hele–Shaw analogue system (Figure 11.17) show that, at long times, the flow establishes a quasi-steady oscillating regime near the well with the flow deepening during injection and thinning during extraction (Figure 11.16). The shapes of the current after 1, 2 and 3 injection and also extraction cycles are shown in Figure 11.17. It is seen that during the injection phase, the dense red injected fluid spreads out under gravity and, during the subsequent extraction cycle, once the depth of the injected red fluid near the source falls off, some of the original aquifer fluid is also produced at the well.

Analysis of the numerical solutions shows that the speed at which the current slowly advances into the far field is given by the scaling $(SH/t)^{1/2}$. This is in fact equivalent to the exchange flow that would develop if there were a reservoir of dense fluid of depth

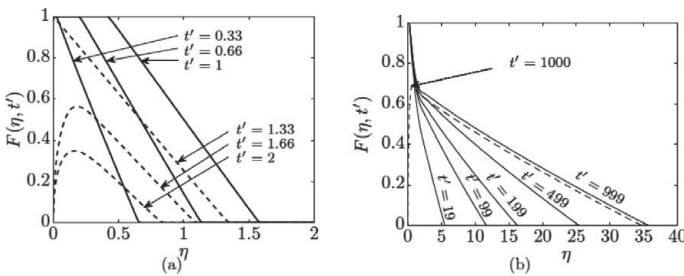


Figure 11.16 Shape of the region of injected liquid (a) during the initial injection and extraction cycle, which runs from time 0 to time 2, and (b) after a number of episodes of cyclic injection and extraction of fluid, illustrating the location of the injected liquid at the end of the injection cycle. The number of injection plus extraction episodes is shown on the individual lines. After Dudfield and Woods (2014).

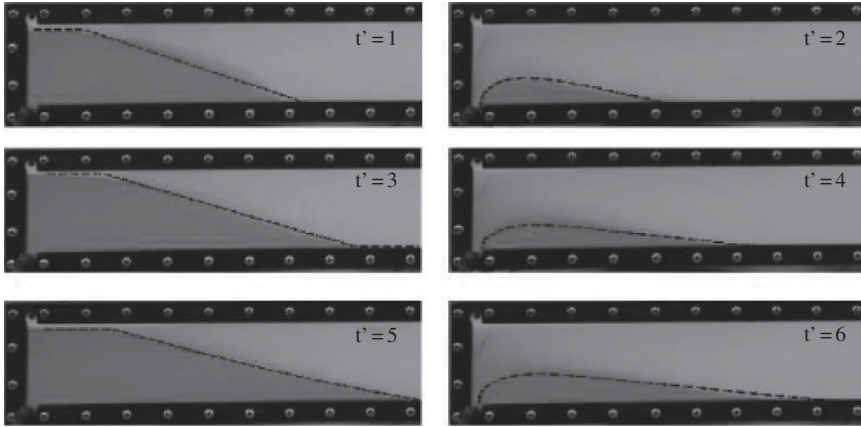


Figure 11.17 Experimental measurement of the current at the end of the injection and extraction phases of the first 3 cycles; the experiment was carried out using a Hele–Shaw cell with two layers of glycerol, the lower of which was more dense and dyed red. This lower fluid was periodically injected into the cell. After Dudfield and Woods (2014). A black and white version of this figure will appear in some formats. For the colour version, please refer to the plate section.

$F_o H < H$ at $x = 0$. In that case, the far-field flow spreads as a self-similar current in which the depth has the form

$$F = F_{af} \left(\zeta = \zeta_o \frac{x}{(SHt)^{1/2}} \right) \quad (11.58)$$

where $S = k\Delta\rho g/\mu\phi$, and for which f satisfies the dimensionless governing equation (cf. Eq. 11.53 with $Q = 0$)

$$-\frac{\zeta}{2} \frac{df}{d\zeta} = \frac{d}{d\zeta} \left(f \frac{df(1-f)}{d\zeta} \right) \quad (11.59)$$

with boundary conditions

$$f = 1 \text{ at } \zeta = 0 \text{ and } f = 0 \text{ at } \zeta = \zeta_{nose} \quad (11.60)$$

The solution to this problem is then determined by applying the global mass balance

$$f \frac{df}{d\zeta} \Big|_0 = \int_0^{\zeta_{nose}} f d\zeta \quad (11.61)$$

For each period of injection τ , and flux Q , there is a value of F_o for which the exchange flow is directly equivalent to the leakage flux from the oscillatory flow (see Dudfield and Woods, 2014).

As a consequence of this continuing but waning flow of injected fluid to the far field, there is a corresponding return flow of original formation water to the production well, which is produced during each extraction cycle. The concentration of this formation

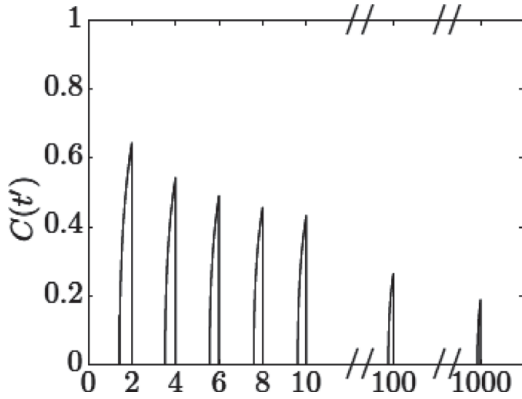


Figure 11.18 Variation of the concentration of original formation fluid which is produced at the well during each of the first five extraction cycles and also during the 50th and 500th extraction cycles.

fluid may be calculated by evaluating the quantity

$$C = \frac{Q - Q_I}{Q} \quad (11.62)$$

from the above solutions, where $Q_I = -uh$ is the flux of injected fluid which is then extracted at the source. Since the flow from the far field gradually decreases from cycle to cycle, the flux of formation fluid produced also decreases with time. As a result, the instantaneous concentration decreases with time as shown in Figure 11.18.

11.14 Exercises

1. Show that if water of temperature T_o is injected into a hot rock of temperature $T_o + \Delta T$, at a slowly decaying rate $Q/t^{1/2}$ then in one dimension, the temperature in the injected fluid may be described by a similarity solution $T(x/(2\kappa t)^{1/2})$ in the case with no boiling. If ΔT is sufficient that $T_o + \Delta T$ exceeds the boiling temperature, $T_B > T_o$, find an implicit expression for the fraction of the injected liquid which boils.
2. Develop a model system of equations for a gravity current supplied by a constant flux of fluid spreading through a porous medium on a horizontal plane in which the relatively dense injected fluid is hotter but more saline than the fluid in the formation. You may assume that the density of the injected fluid increases as it cools. Solution of these equations requires numerical methods.
3. A current of CO_2 is injected with flux Q per unit length along the well into a hot subsurface reservoir, with a sloping upper boundary. If the CO_2 is initially of temperature $T_o - \Delta T$ relative to the reservoir, of temperature T_o , as would typically be the case following injection from the surface, describe the overall structure of

the gravity current, including the depth of the hot and cold regions of the current and the location of the head and of the thermal front within the current. You may assume the buoyancy of the hot CO_2 is $\Delta\rho_h g/\rho_o$ and of the cold CO_2 is $\Delta\rho_c g/\rho$. If the upper boundary of the reservoir has a capillary entry pressure Δp , find the critical conditions on the injection rate that the CO_2 can break through the seal near the well, in the cold region of the flow, but not in the distal region beyond the thermal front.

12 Compressibility and gas flows

In most of the analysis to this point, we have assumed the system remains incompressible. In considering flows between injector and producer wells this is appropriate, provided the injected volume matches the extraction volume; similarly, in our analysis of buoyancy-driven flows, we have considered both confined and unconfined flows, but assumed that there is a drainage radius or outflow well to accommodate the volume of fluid injected into the system. In a laterally extensive aquifer, the finite volume flux which is injected into the field may be accommodated by the compressibility of the rock and the fluid. Owing to the highly incompressible nature of both the rock and also the fluids in the system, the lengthscale over which compressibility effects occur is typically much greater than that of the flow, and this leads to the concept of a drainage radius, far from a well, at which the pressure is nearly constant.

In order to understand the evolution of the pressure field, we can model the rock and fluid as being compressible, with

$$c_r = \frac{1}{\phi} \frac{d\phi}{dp} \quad \text{and} \quad c_l = \frac{1}{\rho_l} \frac{d\rho_l}{dp} \quad (12.1)$$

representing the compressibility of the rock matrix and the fluid, where the effective porosity of the formation changes as the grains compress or expand. The conservation of mass then takes the form

$$\phi_o \rho_l (c_r + c_l) \frac{\partial p}{\partial t} = -\nabla \cdot (\rho_l u) \quad (12.2)$$

and combining this with Darcy's law for the flow, we obtain

$$\phi_o \bar{c} \rho_l \frac{\partial p}{\partial t} = \nabla \cdot \left(\frac{\rho_l k}{\mu} \nabla p \right) \quad (12.3a)$$

for a single phase flow where $\bar{c} = c_r + c_l$. If the pressure changes are small compared to the background pressure, we can linearise the right-hand side of the equation and find

$$\frac{\partial p}{\partial t} = \frac{k}{\bar{c} \phi \mu} \nabla^2 p \quad (12.3b)$$

This is a diffusion equation with diffusivity $D = \frac{k}{c\phi\mu}$. For permeability $k \sim 0.01 - 1.0$ Darcy, viscosity 0.001 Pa s, density $\sim 10^3$ kg/m³, and compressibility $\bar{c} \sim 10^{-9}$ Pa⁻¹, the pressure diffusivity $D \sim 0.1 - 10.0$ m²/s. This suggests pressure signals diffuse a distance of 100 m in times of a few hours to a day.

For the problem in which fluid is injected into a laterally extensive reservoir, of finite vertical extent, at a constant rate, from a central well, if we assume there are no production wells, we can change variables to the similarity variable,

$$\eta = r \left(\frac{\phi\mu\bar{c}}{4kt} \right)^{(1/2)} \quad (12.4)$$

and explore the evolution of the axisymmetric pressure field with time, where r is the distance from the well. At the well we impose the boundary condition that

$$\frac{2\pi kr_w}{\mu} \left. \frac{\partial p}{\partial r} \right|_{r_w} = q \quad (12.5)$$

where q is the volume flux per unit length of a vertical well through the formation, and r_w is the well radius. We find that $\hat{p} = p(r, t) - p(\infty, t)$, the pressure, relative to the far-field pressure, follows the solution

$$\hat{p}(r, t) = \frac{\mu q}{4\pi k} \int_{\frac{\phi\mu\bar{c}r^2}{4kt}}^{\infty} \frac{1}{s} \exp(-s) ds \quad (12.6a)$$

where the flow rate per unit depth is q and r_w is the well radius in the limit $r^2 \gg 4\kappa t / \phi\mu\bar{c}$. With pressure diffusivity of $0.1 - 10$ m²/s and a typical flow rate of 10^{-5} m²/s per metre of well-bore, the pressure signal spreads at a rate which is two to three orders of magnitude faster than the fluid speed, so the pressure front far outruns the fluid front and near the well the flow is essentially incompressible. With a gravity-driven flow, the effective non-linear diffusivity of the buoyancy-driven flow (Chapter 9), which is given by $\frac{k\Delta\rho gH}{\phi\mu}$, has typical value of order $10^{-5} - 10^{-7}$ m²/s, which is again much smaller, confirming the picture that the pressure fronts propagate far beyond the injected fluid. We infer that the near-well flow is essentially given by the confined aquifer gravity current solutions of Chapter 9, while the far-field pressure follows the classic axisymmetric pressure solution (12.4) (see Mathias *et al.*, 2010, for more details). In the limit $r^2 \gg 4\kappa t / \phi\mu\bar{c}$, the pressure at the well (12.6) has the asymptotic form

$$\hat{p}(r_w, t) = \frac{\mu q}{4\pi k} \left[\ln(t) + \ln \left(\frac{4k}{\phi\mu\bar{c}r_w^2} \right) - 0.5772 \right] \quad (12.6b)$$

so that the pressure at the well increases with $\ln(t)$.

In many oil reservoirs, the pressure is maintained close to the original pressure in order to maintain the flow. If the pore pressure of the fluids decreases, the permeability of the formation can decrease as more of the overburden is supported by the matrix,

and this in turn reduces the flow rate. In addition, as the reservoir pressure decreases, it becomes progressively harder to lift the produced fluids to the surface from the base of the well. As a result, primary production from oil fields associated with decompression drive may only lead to production in the order of 10% of the resource. However, with the production of natural gas, which is much more mobile, reservoirs are often drawn down to much lower pressures. In that case, it is often necessary to account for the effects of compressibility. This leads to a different family of compressible flow problems in the reservoir which we now consider. These flow regimes have relevance for gas production from depleting gas fields, as well as production from lower permeability rocks containing so-called ‘tight’ gas and also shale-gas formations. Analysis of some of these compressible problems forms the main thrust of this chapter.

12.1 Idealised one-dimensional gas production

The equation of state for natural gas includes a compressibility factor Z , and is given by the form $p = \rho R Z T$ where Z slowly varies with pressure. In general, the gas is much more compressible than the formation, and so if we combine the equation of state with Darcy’s law, and assume that $Z\mu$ is approximately constant over the range of pressures within the field, then we obtain the mass conservation relation in approximate form (cf. Eq. (12.3))

$$\frac{\partial p}{\partial t} = \frac{k}{\phi\mu} \nabla \cdot (p \nabla p) \quad (12.7)$$

This non-linear diffusion equation for the pressure has effective diffusivity given by

$$\alpha = \frac{k p_o}{\phi\mu} \quad (12.8)$$

in terms of the permeability and porosity of the formation, k and ϕ , and the viscosity of the gas, μ , with p_o a scale for the pressure. We now explore solutions corresponding to pressure-driven production of the gas as it flows into a production well. This has two phases. Initially, there is a phase of depletion during which time the far boundary of the system cannot be felt by the flow, and subsequently there is a phase in which the decompression front has reached the far boundary of the reservoir and the pressure in the overall system then falls. The former regime may be modelled by noting that the lengthscale of the decompression grows in time, leading to a self-similar behaviour. For one-dimensional flow into a line well, we can seek a similarity solution of the form $p = p_o f(\eta)$, where f is dimensionless, p_o is the initial reservoir pressure,

and $f(0) = 1 - \Delta p/p_o$ where Δp is the drawdown (i.e. the reduction) of pressure at the well. If we introduce the similarity variable

$$\eta = \frac{x}{(2\alpha t)^{1/2}} \tag{12.9}$$

then the dimensionless pressure satisfies the shape equation

$$f \frac{d^2f}{d\eta^2} + \left(\frac{df}{d\eta}\right)^2 + \eta \frac{df}{d\eta} = 0 \quad \text{for } \eta \geq 0 \tag{12.10}$$

with the boundary conditions that $f(0) = 1 - \Delta p/p_o$ and $f \rightarrow 1$ as $\eta \rightarrow \infty$. In this solution, we impose the condition that the reservoir pressure at the initial time $t = 0$ has value $f = 1$. The similarity solution applies until such time that the pressure signal reaches the far boundary of the reservoir, at $x = L$ say. In this self-similar phase, the flux at the origin, $q = q_{sim}$, decreases with time as

$$q_{sim}(t) = \frac{kp_o\rho_o}{\mu} f(0) \left. \frac{df}{d\eta} \right|_o \frac{1}{(2\alpha t)^{1/2}} \tag{12.11}$$

where, numerical solution shows that, in the limit $p(0, t) = 0$,

$$\lim_{\eta \rightarrow 0} \left[f(\eta) \frac{df}{d\eta} \right] \approx 0.47 \tag{12.12}$$

This solution is shown in Figure 12.1 with the long-dashed lines. Once the pressure signal has reached the far boundary of the system, $x = L$, at a time of about $0.15L^2/\alpha$, the far-field pressure begins to fall below the initial value. There is now a fixed lengthscale over which the diffusion occurs and the flow follows a separable solution in which the pressure retains a particular spatial profile, but the amplitude decreases in time. To find this solution, we seek a separable solution of the form

$$p(x, t) = p_o h(t) g(x) \tag{12.13}$$

by substituting into the governing equation, Eq. (12.7), we find that

$$h(t) = \left(1 + \frac{c\alpha}{L^2} t\right)^{-1} \tag{12.14}$$

and $g(x)$ is given implicitly by the integral relation

$$x = \frac{L}{a} \int_0^{g(x)} \frac{\tau d\tau}{(1 - \tau^3)^{1/2}} ; x \leq L ; g(x) \leq 1 ; g(1) = 1 \tag{12.15}$$

where

$$c = \frac{3a^2}{2} ; a = \int_0^1 \frac{\tau d\tau}{(1 - \tau^3)^{1/2}} = \frac{1}{3} B\left(\frac{1}{2}, \frac{2}{3}\right) \approx 0.862 \tag{12.16}$$

where $B(a, b)$ is the β function.

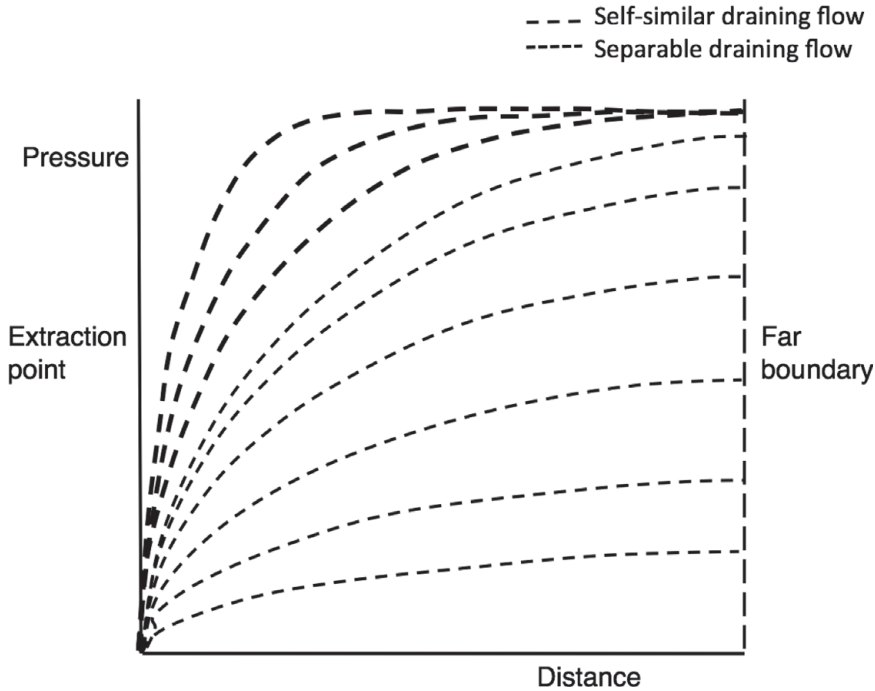


Figure 12.1 Profile of gas pressure with time in a decompression-driven flow. Successive curves denote the pressure of the reservoir, with the long-dashed lines denoting the early time asymptotic behaviour and the short-dashed lines denoting the long-time asymptotic behaviour.

This solution shows that during this phase the flux decays in time as

$$q_{sep}(t) = a \frac{kp_o\rho_o}{L\mu} \left[\frac{1}{1 + \frac{c\alpha t}{L^2}} \right]^2 \quad (12.17)$$

This solution corresponds to the short-dashed lines shown in Figure 12.1, as the pressure at the far field begins to fall off.

The above solutions for the separable flow regime, in the full non-linear problem, can be tested using an analogue Hele–Shaw experiment, in which a layer of syrup is allowed to drain from the cell under gravity by removing the endplate of the Hele–Shaw cell (Figure 12.2). Although this is an analogue system, it confirms the mathematical analysis of the draining flow, and helps visualise the flow pattern. In the Hele–Shaw model the depth of the flow corresponds to the pressure (after Farcas and Woods, 2007).

The relevance of these solutions for interpreting field data can be shown by comparing the evolution of the well pressure with time from field data with the solution for $h(t)$, Eq. (12.14). In the second phase of flow once the boundaries of the domain influence the flow and the separable solution applies, then Eq. (12.14) shows that the slope of the rate of change of the inverse well pressure reflects the effective diffusivity



Figure 12.2 Analogue experiment of gas draining from a porous layer using syrup draining from a Hele–Shaw cell, with an initial constant depth in the cell. A black and white version of this figure will appear in some formats. After Farcas and Woods (2007). For the colour version, please refer to the plate section.

of pressure within the formation. As an example of this, in Figure 12.3, we present a graph showing the variation with time of the inverse of the pressure in a North Sea gas well. One might argue that these data shows a trend which varies linearly with time as predicted by the model. With the model one can then quantify the long-time average flow properties of the reservoir by matching the rate of change of the inverse pressure with time. In making such comparisons, there are differences between the coefficients for one-dimensional flow (presented above) and the analogous radial flow solutions which have a similar time-dependence to (12.14), and this should be included in the uncertainty analysis of the inversion.

Mindful of the approximations in modelling the gas as an ideal gas, with constant viscosity, this is a non-linear solution, corresponding to the case in which the pressure at the well falls to zero. It is interesting to note that in the case that the pressure at the well is only a small value less than the pressure in the far field, ϵp_o where $\epsilon \ll 1$, the governing equations can be linearised to the form

$$\frac{\partial \Delta}{\partial t} = \alpha \frac{\partial^2 \Delta}{\partial x^2} \quad \text{where } p = p_o(1 + \epsilon(\Delta - 1)) \quad \text{with } \epsilon \ll 1 \tag{12.18}$$

Now, the most slowly decaying mode of the power series solution

$$\sum_{n=1}^{\infty} a_n \exp\left(-\frac{(2n+1)^2 \pi^2 \alpha t}{4L^2}\right) \sin\left(\frac{(2n+1)\pi x}{2L}\right)$$

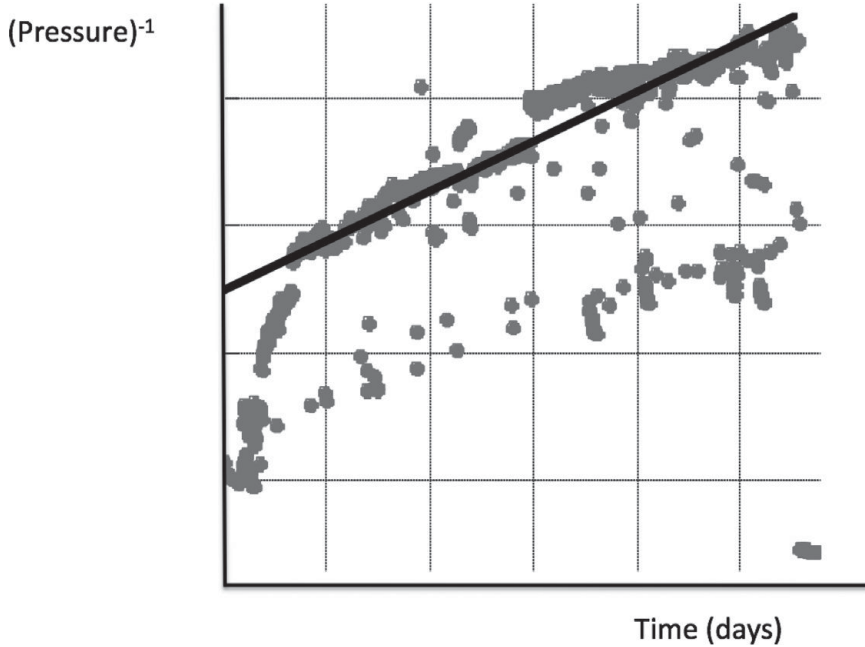


Figure 12.3 Comparison of the time-dependence of the gas production from a North Sea gas field with the simplified model, obtained by plotting inverse pressure as a function of time. The data appear to follow an approximate linear trend as suggested by the line. The intermittent series of lower values in the data may correspond to well shut in events, which are events when the flow is stopped, and the well closed during which time the well pressure increases.

for the problem for which the boundary conditions have the form

$$\Delta(0, t) = 0 \quad \text{and} \quad \left. \frac{\partial \Delta}{\partial x} \right|_{x=L} = 0 \quad \text{for} \quad t > 0 \quad \text{and} \quad \Delta = 1 \quad \text{at} \quad t = 0 \quad (12.19)$$

is given by

$$\Delta_1(x, t) = \frac{4}{\pi} \exp\left(-\frac{\pi^2 \alpha t}{4L^2}\right) \sin\left(\frac{\pi x}{2L}\right) \quad (12.20)$$

12.2 Well selection

Although the above solutions are simple, they have sufficient structure to provide some insight into the selection of well spacing to maximise the economic value of a gas field. To do this, we can observe that the value of the gas decays exponentially with time, with a decay rate λ which depends on the interest rate, so that the total mass produced, Pr , and the value of this production, V , can be approximated in terms of the sum of the early time self-similar solution for the production and the late time separable solution for the production, once the flow has reached the far boundary, in the following form

$$Pr = \frac{kp_o\rho_o}{\mu} \left[\int_0^{0.15\frac{L^2}{\alpha}} \frac{0.47}{(2\alpha t)^{1/2}} dt + \int_{0.15\frac{L^2}{\alpha}}^{\infty} \alpha \left[1 + \frac{c\alpha t}{L^2} \right]^{-2} dt \right] \tag{12.21}$$

$$V = \frac{kp_o\rho_o}{\mu} \left[\int_0^{0.15\frac{L^2}{\alpha}} \frac{0.47 \exp(-\lambda t)}{(2\alpha t)^{1/2}} dt + \int_{0.15\frac{L^2}{\alpha}}^{\infty} \exp(-\lambda t) \left[1 + \frac{c\alpha t}{L^2} \right]^{-2} dt \right] \tag{12.22}$$

By rescaling time, the latter integral can be shown to be a function of the parameter

$$Y = \frac{0.15\lambda L^2}{\alpha} \tag{12.23}$$

which compares the pressure diffusion time across the reservoir with the decay time-scale for the value of money. The parameter Y allows us to recognise how the value of the produced gas decays rapidly as the time to produce, which scales as L^2/α , decreases below the economic time, $\frac{1}{\lambda}$, over which the gas has value, as seen in Figure 12.4.

Such calculations are valuable in helping to design well spacings and well numbers in a gas field, since the value of the produced gas can be compared with the cost of the wells. As the number of wells increases, the cost increases but the production rate also increases. The cost is typically expended in the early part of a project, and then the gas is produced, leading to an optimal number of wells to maximise value. As an extension of the model (12.21–12.22), one can add the cost for each well, so that the model selects an optimal number of wells based on the time-weighted value of the production from each well combined with the cost (Figure 12.5).

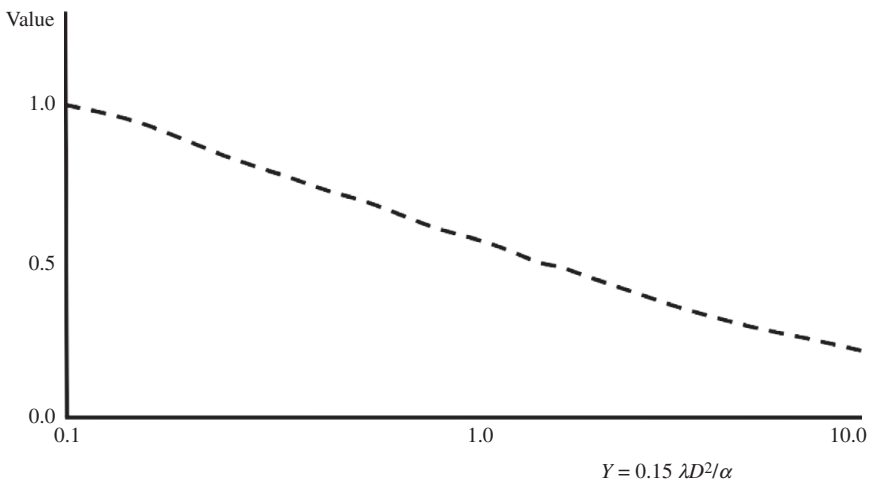


Figure 12.4 Illustration of the ‘value’ of the gas in a field, scaled relative to the value of the total volume of gas if produced today, as a function of the control parameter Y which represents the ratio of the production time to the decay time of the value of money. If Y is large the value of the future production is very small, and the development project becomes much less valuable.

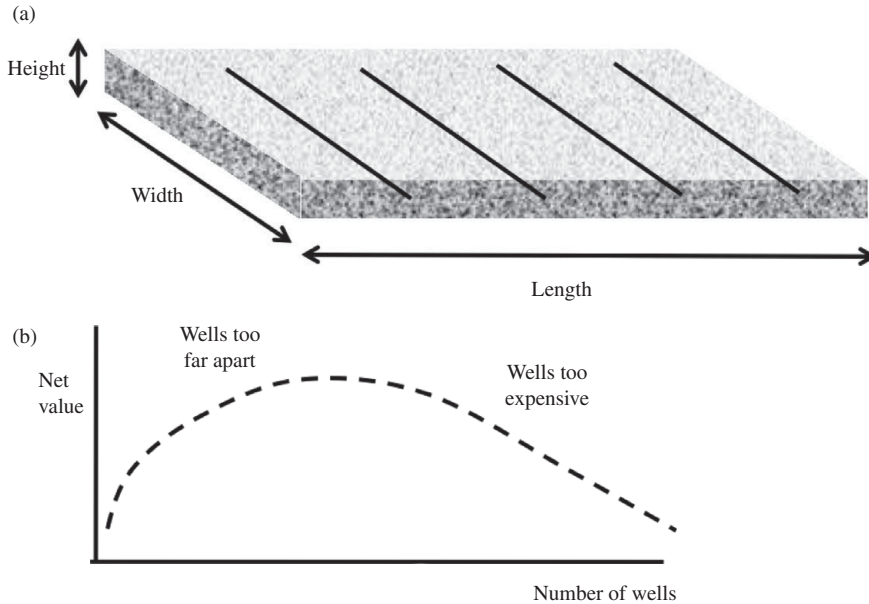


Figure 12.5 (a) Typical array of wells in a low permeability gas field, each designed to drain the gas from the permeable layer, and (b) a calculation of the value of each well spacing in terms of the production rate, the well cost and the economic discount rate. This leads to prediction of an optimal well spacing.

Furthermore, one could introduce a time delay in the production from successive wells, to account for the finite time of development of each well compared to the production life of the wells; this is becoming an increasingly important factor in less permeable rocks presently being developed. If the wells are drilled in sequence, and the time between drilling successive wells is much shorter than the diffusion time $0.15\alpha/L^2$, where L is the well spacing, then the solutions described above apply to leading order. As a result, the sum of n wells, which are drilled in order, would have value $\sum_{i=1}^n \exp(-i\lambda\tau)V(1)$ where $V(1)$ is the value of the first well, and τ is the time delay between wells. This may be approximated as $V(1)/(1 - \exp(-\lambda\tau))$, with $\lambda\tau \ll 1$ provided $n > 1/\lambda\tau$.

12.3 Radial flow and fracking

The above calculation illustrates the flow with a series of linear wells, assuming there is one-dimensional flow into each well. The models can also be used to illustrate the benefits of fracking in order to help produce a greater flux into the well. Fracking is the process by which a fracture is generated around a well through the pressurisation

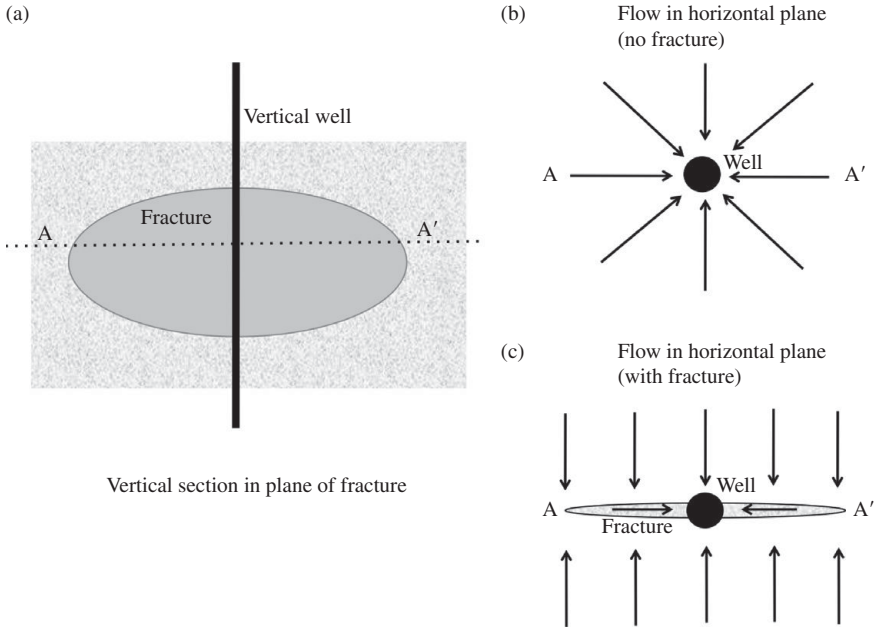


Figure 12.6 (a) Illustration of the vertical plane through a fracture intersecting a vertical well; (b) horizontal plane, including the vertical well, showing radial inflow in the case with no fracture; (c) horizontal plane, including the fracture, showing the inflow to the fracture and then into the well. Section A–A' is common to panels (a) and (c).

of the well above the fracture strength of the surrounding rock. Typically the fractures propagate in the direction of the maximum principal stress, thereby forcing the rock apart in the direction of minimum principal stress. If a horizontal well is drilled and a fracture is produced as shown in Figure 12.6c, then the flow from the formation will travel directly into the fracture and then to the well. This leads to an approximately one-dimensional flow around the fractures as indicated in the schematic, rather than the radial inflow if the well has no fracture (Figure 12.6b). The resistance in the fracture will typically be much smaller than in the formation.

If we assume that the fracture extends a distance R from the well, and that it drains a zone of width R normal to the direction of the fracture (in the case that there are multiple vertical wells spaced $2R$ apart and hence each has drainage scale R (Figure 12.7), then, from Eq. (2.20), the flow from one side of the fracture has a long-time flux

$$Q_H = 2 \frac{k \Delta p}{\mu} \exp\left(\frac{-\alpha \pi^2 t}{4R^2}\right) \tag{12.24}$$

per unit length along the fracture in the direction normal to A–A'. In contrast, if this region of the reservoir was flowing directly into the well with no fracture then the flow would be axisymmetric (Figure 12.6b) governed by the axisymmetric radial flow equation

$$r \frac{\partial p}{\partial t} = \frac{k}{\mu \phi \bar{c}} \frac{\partial}{\partial r} \left(r \frac{\partial p}{\partial r} \right) \quad (12.25)$$

where \bar{c} is the compressibility. At long-times we seek a power series solution of the form

$$p_o - p(r, t) = \Delta p \left(1 - \sum_{n=1}^{\infty} a_n f_n(r/R, \lambda_n) \exp \left(-\frac{\lambda_n \alpha t}{R^2} \right) \right) \quad (12.26)$$

where the initial condition requires that $\sum_{n=1}^{\infty} a_n f_n(r/R, \lambda_n) = 1$. The boundary condition that the pressure is drawn down at the well requires $f_n(r_o/R, \lambda_n) = 0$ where r_o is the well radius, while the condition of zero flux across the drainage radius at $r = R$ requires $\frac{d}{d\hat{r}} f_n(1, \lambda_n) = 0$. The solution to this problem may be written in terms of the variable $\hat{r} = r/R$, as a combination of Bessel functions

$$f_n(\hat{r}, \lambda_n) = Y_o(\lambda_n^{1/2} \hat{r}_o) J_o(\lambda_n^{1/2} \hat{r}) - J_o(\lambda_n^{1/2} \hat{r}_o) Y_o(\lambda_n^{1/2} \hat{r}) \quad (12.27)$$

where λ_n is the solution of the equality

$$Y'_o(\lambda_n^{1/2}) J_o(\lambda_n^{1/2} \hat{r}_o) = J'_o(\lambda_n^{1/2}) Y_o(\lambda_n^{1/2} \hat{r}_o) \quad (12.28)$$

In figure 12.7 we compare the magnitude of the most slowly decaying mode, λ_1 , as a function of $\hat{r}_o = r_o/R$, with the most slowly decaying mode of the flow into a fracture (Eqn 12.20), for a fracture of comparable length to R . The figure illustrates the benefit of fracking a well in terms of accelerating the production. It is important to note that this is a simplified picture of the benefits of fracking in that typically, around the well, there is a damaged zone of reduced permeability, produced during the drilling process. This region requires a larger pressure gradient to carry the same flow, and hence further reduces the flux into a radial well.

Radial flow leads to a smaller production rate than the linear flow because of the convergence of all the streamlines in the case of radial flow. As a result, in gas fields with low permeability rock, it is optimal to generate fractures around the wells, so that the gas can flow into a planar fracture, with relatively low resistance, and then flow into the well. This can substantially increase the flow rate. The main control on the production is then given by the linear flow model with flow in the direction normal to the fracture. This is typically the strategy with vertical wells. Horizontal wells offer further opportunity for fracturing in that a series of regularly spaced fractures can be placed normal to the direction of the well. The flow into each of the fractures can substantially enhance the flow compared to the axisymmetric flow directly into the well (Figure 12.8).

In the next section, we also illustrate how in layered formations, cross-flow between high and low permeability layers provides access to a much larger volume of reservoir, in a somewhat similar fashion to fracture–matrix flow.

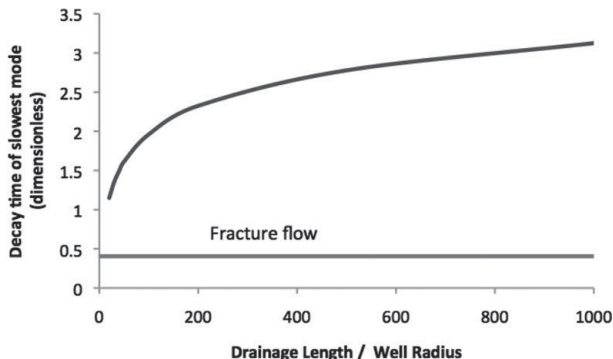


Figure 12.7 Variation of the decay time $1/\lambda_1$ corresponding to the most slowly decaying mode of the radial flow as a function of the drainage radius compared to the well radius. For comparison, the decay time $4/\pi^2$ for the linear fracture is also shown.

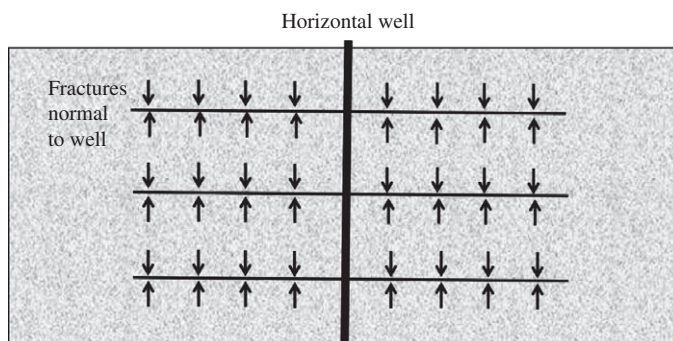


Figure 12.8 Illustration of the flow into a series of fractures which have been produced normal to a horizontal well in order to increase the surface area contacted by the well.

12.4 Multiple-layer formations

As shown in Chapter 2, many sedimentary reservoirs have two or more parallel layers of different permeability, each of which may intersect a well. In some cases there may be a thin layer of seal rock between the layers, while in other cases, the layers may be directly in contact. If we consider the case in which a fracture from a well cuts across the layers (Figure 12.9), then initially, the flow in each layer will migrate directly to the fracture and hence the well. However, since the high permeability layers decompress more rapidly, cross-layer pressure gradients will build up in the reservoir, and this will lead to cross-layer flow. The time for the cross-layer flow from the low to the high permeability strata scales as $\tau_c = H^2/\alpha_v$, where $\alpha_v = k_v p_o / \phi \mu$ refers to the effective cross-layer gas diffusion coefficient in the low permeability layer, of thickness H . The

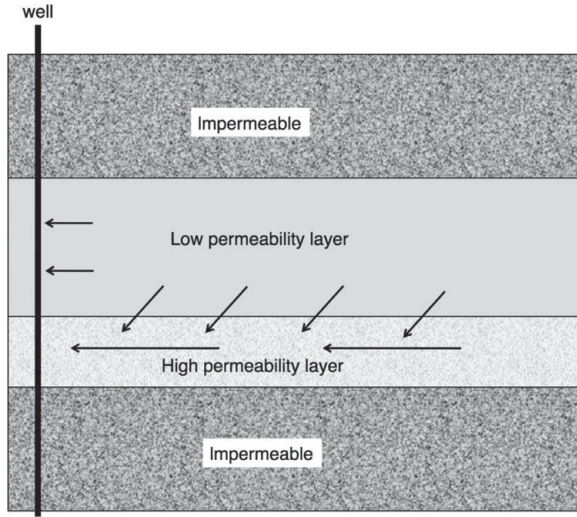


Figure 12.9 Schematic illustrating the flow from the low permeability layer into the high permeability formation and then the well, in addition to directly from the low permeability layer into the well. At early times, the low and high permeability layers behave independently, but once the pressure signal has diffused across the low permeability layer, the flow is dominated by the higher permeability layer and this accesses the gas in both the high and low permeability layers.

timescale for the horizontal drainage flow directly into the well scales as $\tau_d = L^2/\alpha_h$ for gas located a distance L from the well, where $\alpha_h = k_h p_o / \phi \mu$. Once L is sufficient that $(L/H)^2 > \frac{k_h}{k_v}$, the gas tends to migrate cross-layer into the high permeability layer and then flows into the well, rather than flowing directly along the low permeability layer (Figure 12.10).

At early times, since the gas flow is primarily directed to the fracture and hence the production well, the flux is approximately equal to the sum of the fluxes in each of the layers, as given by the similarity solution in each layer. which may be expressed, using Eqs. (12.11) and (12.12), in terms of the flow in one of the layers, layer h , according to the relation

$$Q = \frac{k_h p_o \rho_o H_h}{\mu} \left[1 + \frac{H_l}{H_h} \left(\frac{k_h}{k_l} \right)^{1/2} \right] \frac{0.47}{(2\alpha_h t)^{1/2}} \quad (12.29)$$

where H_h and H_l are the thicknesses of the high and low permeability layers.

At longer times, the pressure in each layer equilibrates owing to the cross-layer flow, and the total flow is then given by

$$q_{equil} = a \frac{p_o \rho_o}{\mu} k_h H_h (1 + KH) \left[1 + \frac{c\bar{\alpha}t}{L^2} \right]^{-2} \quad (12.30)$$

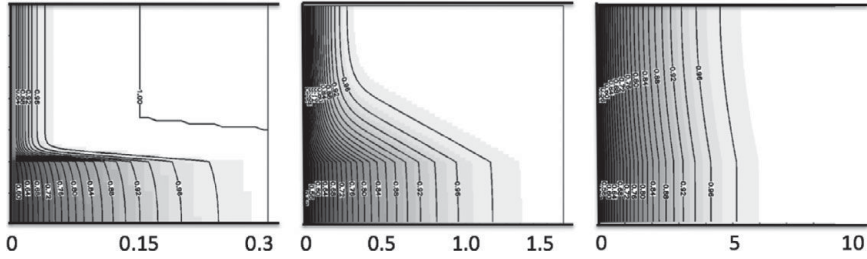


Figure 12.10 Pressure contours within a two-layer flow domain, illustrating the variation of the pressure with position in the formation. Images are shown for three times. The x -axis is rescaled at each time, according to the distance the pressure signal has travelled to allow for comparison of the shape of the pressure profile across the layer. At early times, there is a steep cross-layer gradient between the high and the low permeability zone, as the gas migrates directly to the well from each layer, essentially independently. At the intermediate time, gas has time to diffuse between the layers, with gas from the low permeability layer now being produced directly at the well but also through the high permeability zone. At long times, the pressures are very similar at each position from the well, and the main part of the gas production from the low permeability zone is through the high permeability formation. After Farcas and Woods (2006).

where the effective diffusivity is given by the expression

$$\bar{\alpha} = \frac{k_h p_o \rho_o H_h}{\phi \mu} \left(\frac{1 + KH}{1 + H} \right) \tag{12.31}$$

where $K = k_l/k_h$ and $H = h_l/h_k$. Here the mean permeability is given in terms of the arithmetic average of the two layers, with the same pressure gradient, and the mass of gas being accessed is the mass in both the high and low permeability layers.

12.5 Shale gas

Shale-gas reservoirs are extremely low permeability systems, containing very fine silt particles, organic matter and some pore space containing gas. There is also some adsorbed gas on the solid surfaces and there is likely some gas dissolved within the organic material. As the pressure falls, there will be a release of dissolved and adsorbed gas from the solid material. The release of the gas is controlled by the equilibrium between the free gas pressure and that of the gas adsorbed in the solid material and this is often represented by a Langmuir isotherm which is measured for a particular sample of the material (Figure 12.11). The structure of the shale includes small pores, fractures and very fine solid grains, with the characteristic lengthscales being on the range of microns, as illustrated in Figure 12.12. The transport mechanism for the gas moving through the shale likely involves a combination of diffusion and flow through the micro-pores, at the smallest scales, with Darcy flow becoming established in the

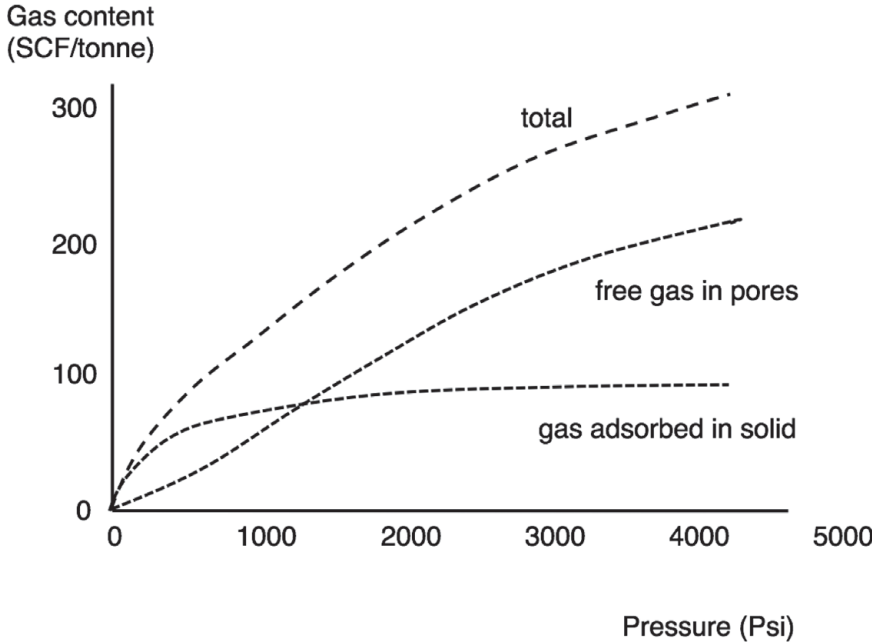


Figure 12.11 Illustration of the form of a Langmuir isotherm for a model shale-gas deposit, indicating how the gas content in the formation is partitioned between the free gas in the pore space and the gas adsorbed in the solid.

larger fractures and pores, although this is presently an area of active research, and the controls on the flow are not fully understood. However, for sufficiently slow flow that the micron-scale processes are not rate limiting, one can envisage a source term in which the rock locally adjusts to the Langmuir isotherm for that pressure, leading to an equation for mass conservation

$$\frac{\partial p}{\partial t} + \frac{dM}{dp} \frac{\partial p}{\partial t} = \frac{k}{\phi\mu} \frac{\partial}{\partial x} \left[p \frac{\partial p}{\partial x} \right] \quad (12.32)$$

where $\alpha = kp_o/\phi\mu$ is the effective diffusivity for the flow through the formation, based on an effective permeability for the macroscopic Darcy-type transport through the material. In many cases the source term is modelled using a Langmuir isotherm, which has the form

$$M = \frac{\alpha p}{p + \beta} \quad (12.33)$$

and leads to a prediction of the gas release with pressure, as illustrated in Figure 12.11.

In the case of small pressure changes in the flow, we can linearise the Langmuir relation, and re-cast the problem using solutions for the problem of gas production

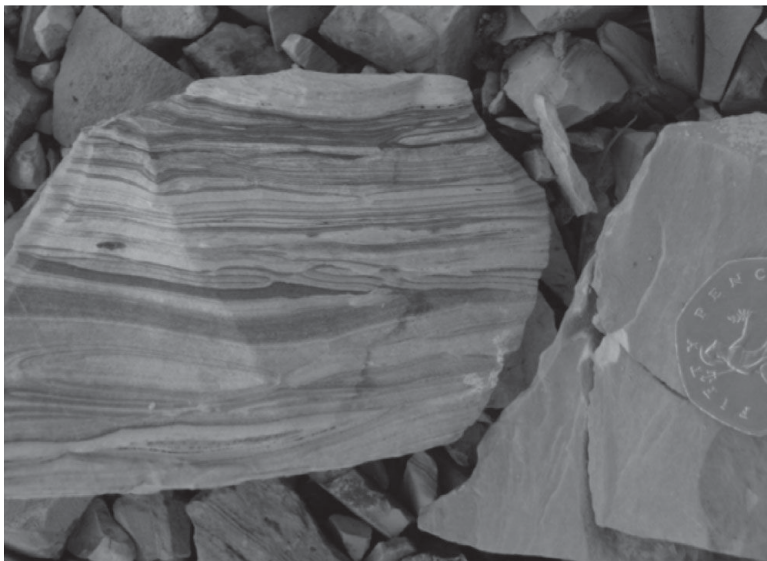


Figure 12.12 Illustration of a shale sample showing the very layered, fine structure of the rock. A black and white version of this figure will appear in some formats. For the colour version, please refer to the plate section.

considered earlier in this chapter, but with a modified value of diffusion coefficient

$$\hat{\alpha} = \frac{\alpha}{1 + \frac{dM(p_o)}{dp_o}} \quad (12.34)$$

However, with non-linear fluctuations in pressure, the full equation (12.32) requires numerical solution. This can be achieved in a large domain using a similarity solution for the initial flow, with the same variable as above, $\eta = x/(\alpha t)^{1/2}$, leading to the ordinary differential equation

$$-\eta \left(1 + \frac{dM}{dp} \right) \frac{dp}{d\eta} = 2\alpha \frac{d}{d\eta} \left[p \frac{dp}{d\eta} \right] \quad (12.35)$$

However, this now requires numerical solution of the ordinary differential equation to calculate the initial phases of the flow using a model for the Langmuir isotherm as measured in the specific formation.

In many shale-gas deposits, the permeability of the formation, as calculated in terms of flow through samples of the formation, is very small, so that with simple decompression flow, the flux is negligible. As a result, the process of fracking has been used to accelerate the release of the gas. The fractures provide a pathway for the gas from the rock immediately around the fractures to the well. Beyond the fractures however, the

flow is controlled by the very slow processes of desorption, diffusion and flow through the very small matrix grains, and this can ultimately limit the accessible mass of gas.

12.6 Exercises

1. If there is a zone of damaged rock around a well-bore of radius $\alpha r_o (> r_o)$, where r_o is the well-bore radius, and with permeability βk where k is the original permeability, calculate the gas flow in a steady-state flow. You may assume the pressure in the well is maintained at a pressure Δp lower than that at a radius $R (> \alpha r_o)$ from the well, where Δp is much smaller than the reservoir pressure. Compare the fractional reduction in the flow as β changes from 1.0 to 0.1.
2. Fluid is injected into a two-layer reservoir, with layers of depth H_1 and H_2 and permeability k_1 and k_2 . Using the model for compressible flow, calculate how the flow is divided between the two layers, assuming the pressure at the well in each layer is the same.

13 Epilogue

In this volume we have explored a series of problems relating to flow in porous rocks with a particular focus on problems of relevance to industry and the environment. Owing to the vast array of processes which can arise with flow in porous rocks, especially with viscosity contrasts between different fluid phases, and applied pressure, capillary pressure and buoyancy forces driving the flow, there are many more problems which could be discussed. However, the present volume serves to introduce the reader to a range of these problems and to the use of different mathematical techniques, especially the development of similarity solutions, to help expose the key physics and in particular the scaling laws which control the time- and lengthscales for specific processes.

In moving forward in the subject, the combination of careful laboratory experiments with simplified mathematical analysis should continue to serve the community in exploring new physical processes, and in developing leading order quantitative descriptions of many flow problems. These approaches also provide an invaluable complement to numerical solution, and provide reference cases with which to test numerical solutions. However, ultimately for engineering application, numerical models will also need to be developed to capture some of the controls associated with specific boundary conditions and shapes, and non-linear evolution of the flows.

Important and emerging areas relate to problems in which the deformation of the porous layer has a dominant influence on the flow, and the continuing challenge of describing flows in complex heterogeneous rocks. In particular, many future hydrocarbon resources lie in heterogeneous rock, and accurate modelling of the flow in these systems needs to account for the heterogeneity and associated dispersion. Given the inevitable lack of detailed quantitative data constraining the flow properties of such systems, models with appropriate levels of parameterisation, capturing the geological correlation scales, which enable complete assessment of the uncertainties will become increasingly relevant. Other important problems include the development of a more complete understanding of the flow processes in both very low permeability rocks host to gas and some oil, and also the flow of very viscous oil in tar-sand deposits. In the

emerging area of carbon sequestration, the acquisition of new field data will be key for continued development of the science and also the development of inverse models to use observations of the evolving spatial distribution of CO₂ and infer the effective flow properties of the host formation (see Dudfield and Woods, 2013). Finally, given the magnitude of the resource, it would be fascinating to develop new insights into the controls on the possible dissociation of methane hydrates within porous layers and the ensuing flow of the methane.

References

- Allen, J. R. L. (2001). *Principles of Physical Sedimentology*. Caldwell, NJ: Blackburn Press.
- Barenblatt, G. (1996). *Dimensional Analysis, Intermediate Asymptotics and Self-similarity*. Cambridge: Cambridge University Press.
- Bear, J. (1972). *Dynamics of Fluids in Porous Media*. New York: Elsevier.
- Bear, J. and Cheng, A. (2010). *Modeling Groundwater Flow and Contaminant Transport*. New York: Springer.
- Behbahani, H., DiDonato, G. and Blunt, M. (2006). Simulation of counter-current imbibition in water wet fractured reservoirs. *J. Petrol. Sci. Eng.*, **50**, 21–39.
- Berkowitz, B. (2010). *Dispersion in Heterogeneous Geological Formations*. New York: Springer.
- Berkowitz, B. and Scher, H. (1997). Anomalous transport in random fracture networks. *Phys. Rev. Lett.*, **79**, 20.
- Berkowitz, B. and Scher, H. (2001). Application of continuous time random walk theory to tracer test measurements in heterogeneous and fractured media. *Ground Water*, **39**, 583–604.
- Bickle, M., Chadwick, A., Huppert, H. E., Hallworth, M. and Lyle, S. (2007). Modelling carbon dioxide accumulation at Sleipnir: implications for underground carbon storage. *Earth Planet. Sc. Lett.*, **255**, 164–176.
- Bijejic, J., Muggerridge, A. and Blunt, M. (2004). Pore scale modeling of longitudinal dispersion. WRR 2004, WR003567.
- Boait, F., White, N., Bickle, M., *et al.* (2012). Spatial and temporal evolution of injected CO₂ at Sleipnir field, North Sea. *J. Geophys. Res.*, **117**, B03309.
- Bodvarsson, G. S., Benson, S. and Witherspoon, P. (2012). Theory of the development of geothermal systems charged by vertical faults. *J. Geophys. Res.*, **87**, 9317–9328.
- BP (2013). *BP Statistical Review of World Energy*. Available at: www.bp.com/statisticalreview.
- Brooks, R. and Corey, A. (1959). Hydraulic properties of porous media. Hydro Paper No. 5, Colorado State University.
- Cardoso, S. and Woods, A. W. (1993). The formation of drops by viscous instability. *J. Fluid Mech.*, **289**, 351–379.
- Chiles, J. P. and Delfiner, P. (1999). *Geostatistics: Modeling Spatial Uncertainty*. New York: Wiley.
- Corey, A. T. (1954). The interrelations between gas and oil permeabilities. *Producers Monthly*, **19**, 38–41.
- Dagan, G. (1989). *Flow and Transport in Porous Formations*. New York: Springer-Verlag.
- Delgado, J. M. P. Q. (2007). Longitudinal and transverse dispersion in porous media. *Trans. I. Chem. E., Supplement 9A*, **85**(9), 1245.
- Del Ioio, G. and Woods, A. W. (2014). Instability of an axisymmetric porous bed through deformation of the boundaries. Manuscript subjudice. BP Institute, University of Cambridge.

- DeLoubens, R. and Ramakrishnan, T. (2011). Analysis and computation of gravity-induced migration in porous media. *J. Fluid Mech.*, **675**, 60–86.
- Dudfield, P. and Woods, A. W. (2014). On the periodic injection of fluid into, and its extraction from, a confined aquifer. *J. Fluid Mech.*, **755**, 111–141.
- Dudfield, P. and Woods, A. W. (2013). On the use of seismic data to monitor the injection of CO₂ into a layered aquifer. *Earth Planet. Sci. Lett.*, **368**, 132–143.
- Dullien, F. A. L. (1991). *Porous Media, Fluid Transport and Pore Structure*. Waltham, MA: Academic Press.
- Eames, I. and Bush, J. (1999). Longitudinal dispersion by bodies fixed in a potential flow. *Proc. Roy. Soc. A*, **455** (1990), 3665–3686.
- Farcas, A. and Woods, A. W. (2007). On the extraction of gas from multilayered rock. *J. Fluid Mech.*, **581**, 79–95.
- Farcas, A. and Woods, A. W. (2009). The effect of drainage on the capillary retention of CO₂ in a layered permeable rock. *J. Fluid Mech.*, **618**, 349–359.
- Farcas, A. and Woods, A. W. (2013). Three dimensional buoyancy driven flow along a fractured boundary. *J. Fluid Mech.*, **728**, 279–305.
- Farcas, A. and Woods, A. W. (2014). Buoyancy driven dispersion in a layered permeable rock. Manuscript subjudice. BP Institute, Cambridge University.
- Freeze, R. A. and Cherry, J. A. (1979). *Groundwater*. Englewood Cliffs, NJ: Prentice Hall.
- Fried, J. J. and Cambarnous, M. A. (1971). Dispersion in porous media. In V. Show (ed.), *Advances in Hydroscience*, 7. New York: Academic Press, pp. 169–282.
- Furtney, J. and Woods, A. W. (2014). On the difference in spatial distribution of mean and variance in well placement problems. Manuscript BPI.
- Gelhar, L. W., Welty, C. and Rehfeldt, K. R. (1992). A critical review of data on field scale dispersion in aquifers. *Water Resour. Res.*, **28**(7), 1955–1974.
- Gerritsen, M. G. and Durlofsky, L. J. (2005). Modeling fluid flow in oil reservoirs. *Annu. Rev. Fluid Mech.*, **37**, 211–238.
- Green, C. and Ennis-King, J. (2013). Residual trapping beneath impermeable barriers during buoyant migration of CO₂. *Transport Porous Med.*, **98**(3), 505–524.
- Gunn, I. and Woods, A. W. (2011). On the flow of buoyant fluid injected into a confined, inclined aquifer. *J. Fluid Mech.*, **672**, 109–129.
- Haward, L. N. (1964). Convection at high Rayleigh number. In H. Gortler (ed.), *Proc. Eleventh Intl. Congress on Applied Mechanics*. Munich: Springer, pp. 1109–1115.
- Hesse, M. and Woods, A. W. (2010). Buoyant dispersal of CO₂ during geological storage.
- Hesse, M., Tchelepi, H. A. and Orr, F. M. (2008). Gravity currents with residual trapping. *J. Fluid Mech.*, **611**, 35–60.
- Hewitt, D. R., Neufeld, J. A. and Lister, J. R. (2013) Convective shutdown in a porous medium at high Rayleigh number. *J. Fluid Mech.*, **719**, 551–586.
- Hinch, E. J. and Bhatt, B. S. (1990). Stability of an acid front moving through a porous rock. *J. Fluid Mech.*, **212**, 279–288.
- Homsy, B. (1987). Viscous fingering in porous media. *Ann. Rev. Fluid Mech.*, **19**, 271–301.
- Huppert, H. E. and Woods, A. W. (1995) The dynamics of gravity driven flow in porous media. *J. Fluid Mech.*, **292**, 55–69.
- Kim, H., Funada, T., Joseph, D. D. and Homsy, G. M. (2009). Viscous potential flow analysis of radial fingering in a Hele–Shaw cell. *Phys. Fluids*, **21**, 074106.
- King, S. E. and Woods, A. W. (2003). Dipole solutions for viscous gravity currents: theory and experiments. *J. Fluid Mech.*, **483**, 91–109.

- Koch, D. and Brady, J. (1985). Dispersion in fixed beds, *J. Fluid Mech.*, 399–427.
- Lajeunesse, E., Martin, J., Rakotomalala, N., Salin, D. and Yortsos, Y. C. (1999). Miscible displacement in a Hele-Shaw cell at high rates. *J. Fluid Mech.*, **398**, 299–319.
- Lake, L. (1991). *Enhanced Oil Recovery*. Upper Saddle River, NJ: Prentice Hall.
- Lauwerier, H. A. (1955). The transport of heat in an oil layer caused by the injection of hot fluid. *Appl. Sci. Res., A*, **5**, 145–151.
- Ma, S., Morrow, N. and Zhang, X. (1997). Generalised scaling for spontaneous imbibition data for strongly water-wet systems, *J. Pet. Sci. Eng.*, **18**, 165–178.
- MacMinn, C., Szulczewski, M. L. and Juanes, R. (2010). CO₂ migration in saline aquifers. Part 1: Capillary trapping under slope and groundwater flow. *J. Fluid Mech.*, **662**, 329–351.
- MacMinn, C., Szulczewski, M. L. and Juanes, R. (2011). CO₂ migration in saline aquifers. Part 2: Capillary and solubility trapping. *J. Fluid Mech.*, **688**, 321–351.
- Mathias, S. A., de Miguel, G. J. G. M., Thatcher, K. and Zimmerman, R. (2011). Pressure build up during CO₂ injection in a closed brine aquifer. *Trans. Porous Media*, **89**, 383–397.
- Maxworthy, T. (1989). Experimental study of interface instability in a Hele Shaw cell. *Phys. Rev. A*, **39**, 5863–5866.
- Menand, T. and Woods, A. W. (2005). Dispersion, scale and time dependence of mixing zones under gravitationally stable and unstable displacements in porous media. *Water Resour. Res.*, **41**, 5.
- Menand, T., Raw, A. and Woods, A. W. (2003). Thermal inertia and reversing buoyancy in flow in porous media. *Geophys. Res. Lett.*, **30**(6), 1291.
- Mitchell, V. and Woods, A. W. (2006). Self-similar dynamics of liquid injected into partially saturated aquifers. *J. Fluid Mech.*, **566**, 345–355.
- Muskat, M. (1937). *The Flow of Homogeneous Fluids through Porous Media*. New York: McGraw Hill.
- Naff, R. L., Haley, D. F. and Sudicky, E. A. (1998). High-resolution Monte Carlo simulation of flow and conservative transport in heterogeneous porous media. *Water Resour. Res.*, **34**(4), 663–697.
- Nichols, G. (2009). *Sedimentology and Stratigraphy*. Chichester, UK: Wiley-Blackwell.
- Nigam, M. and Woods, A. W. (2005). The influence of buoyancy contrasts on miscible source-sink flows in a porous medium with thermal inertia. *J. Fluid Mech.*, **549**, 253–271.
- Otto, C., Lapotre, M. and Woods, A. W. (2014). Transverse and longitudinal mixing across a density interface in a layered porous rock subject to an oscillatory flow. Manuscript sub judice. BP Institute, University of Cambridge.
- Paterson, L. (1985). Fingering with miscible fluids in a Hele Shaw cell. *Phys. Fluids*, **28**, 26–30.
- Pfannkuch, H. D. (1963). Contribution to the study of miscible displacements in a porous medium. *Rev. Inst. Franc. Petrol.*, **18**, 215–231.
- Phillips, O. M. (1991). *Flow and Reaction in Porous Rocks*. Cambridge: Cambridge University Press.
- Phillips, O. M. (2009). *Geological Fluid Mechanics: Subsurface Flow and Reactions*. Cambridge: Cambridge University Press.
- Pritchard, D., Woods, A. W. and Hogg, A. J. (2001). On the slow draining of a gravity current moving through a layered permeable medium. *J. Fluid Mech.*, **444**, 23–47.
- Raw, A. W. V. and Woods, A. W. (2003). On gravity-driven flow through a reacting porous rock. *J. Fluid Mech.*, **474**, 227–243.
- Rayward-Smith, W. and Woods, A. W. (2011). Dispersal of buoyancy-driven flow in porous media with inclined baffles. *J. Fluid Mech.*, **689**, 517–528.
- Rayward-Smith, W. and Woods, A. W. (2014). Experimental analogues for reactions with buoyancy reversal in porous media. Manuscript sub judice.

- Reinhelt, D. (1987). The effect of thin film variations and transverse curvature in the shape of fingers in a Hele Shaw cell. *Phys. Fluids*, **30**, 2617.
- Riolfo, L., Nagatsu, Y., Iwata, S., Maes, R., Trevelyan, P. and DeWit, A. (2012). Experimental evidence of reaction driven miscible viscous fingering. *Phys Rev.*, **E85**, 015394.
- Saffman, P. (1959). A theory of dispersion in a porous medium. *J. Fluid Mech.*, **6**, 321–349.
- Saffman, P. and Taylor, G. (1958). The penetration of a fluid into a porous medium or Hele–Shaw cell containing a more viscous liquid. *Proc. Roy. Soc.*, **245**, 312–329.
- Schwartz, L. (1986). Stability of Hele Shaw flow the wetting layer effect. *Phys. Fluids*, **29**, 3086.
- Sorbie, K. (1991). *Polymer-improved Oil Recovery*. London: Blackie.
- Sudicky, E. and Frind, E. (1982). Contaminant transport in fractured porous media, analytical solutions for a system of parallel fractures. *Water Resour. Res.*, **18**(6), 1634–1642.
- Szulczewski, M. L., Hesse, M. A. and Juanes, R. (2013). Carbon dioxide dissolution in structural and stratigraphic traps. *J. Fluid Mech.*, **736**, 287–315.
- Taylor, G. I. (1953). Dispersion of soluble matter in solvent flowing slowly through a tube. *Proc. Roy. Soc.*, **219**, 186–203.
- Tyspkin, G. and Woods, A. W. (2005). Precipitate formation in a porous rock through evaporation of saline water. *J. Fluid Mech.*, **537**, 35–53.
- van Genuchten, M. and Wierenga, P. (1976). Mass transfer studies in sorbing porous media. I. Analytical solutions. *Soil Sci. Soc. Am. J.*, **40**(4), 473–481.
- van Triet, A., Routh, A. and Woods, A. W. (2014). Control of the permeability of a porous media using a thermally sensitive polymer. *AICHE*, **60**(3), 1193–1201.
- Verdon, J. and Woods, A. W. (2007). Gravity-driven reacting flows in a confined porous aquifer. *J. Fluid Mech.*, **588**, 29–41.
- Verdon, J., Kendall, M., Stork, A., Chadwick, A., White, D. and Bissell, R. (2013). A comparison of geomechanical deformation induced by megatonne scale CO₂ storage at Sleipnir, Weyburn and InSalah. *Proc. Nat. Acad. Sci.*, **110**, E2762–2771.
- Wooding, R. A. (1963). Convection in a saturated porous medium at large Rayleigh number or Péclet number. *J. Fluid Mech.*, **15**, 527.
- Woods, A. W. (1998). Vaporising gravity currents in porous media. *J. Fluid Mech.*, **377**, 151–168.
- Woods, A. W. (1999). Liquid and vapour flow in superheated permeable rock. *Ann. Rev. Fluid Mech.*, **31**, 171–199.
- Woods, A. W. (2002). Gravity driven flow in porous rock. In D. B. Ingham and I. Pop (eds.), *Flow and Transport in Porous Media*. New York: Wiley, pp. 397–423.
- Woods, A. W. and Espie, T. (2012). Controls on the dissolution of CO₂ plumes in structural traps in deep saline aquifers. *Geophys. Res. Lett.*, **39**, L08401.
- Woods, A. W. and Farcas, A. (2009). Capillary entry pressure and the leakage of gravity currents through a sloping layered permeable rock. *J. Fluid Mech.*, **618**, 361–379.
- Woods, A. W. and Mason, R. (2001). The dynamics of two-layer gravity-driven flows in permeable rock. *J. Fluid Mech.*, **421**, 83–114.
- Woods, A. W. and Norrise, S. (2010). On the role of caprock and fracture zones in dispersing gas plumes in the subsurface. *Water Resour. Res.*, **46**, W88522.
- Yih, C.-S. (1966). *Stratified Flows*. Waltham, MA: Academic Press.
- Yortsos, Y. C. and Salin, D. (2006). On the selection principle for viscous fingering in porous media. *J. Fluid Mech.*, **557**, 225–236.
- Young, W. and Jones, S. (1991). Shear dispersion. *Phy. Fluids*, **3**(5), 1087–1101.

Index

- accelerating flow, 244
- acidising front, 103
- acidising reaction, 176
- adsorption, 79
- advection–diffusion equation, 187
- aeolian deposits, 20
- agriculture, 227
- along slope component of gravity, 178
- anisotropy, 51
- anomalous spreading, 76
- aquifer thermal energy storage, 249
- axisymmetric instability, 99
- axisymmetric radial flow, 271

- background flow, 189
- baffles, 45
- Barenblatt, 169, 176
- barium sulfate, 103, 128
- Bear, 116, 195, 199
- Bear and Cheng, 70
- Berkowitz, 70
- Bickle, 198
- Biljivic, 78
- binomial distribution, 209
- Boait *et al.*, 197
- boiling, 230
- boiling front, 230
- boiling front instability, 235
- boiling front stability, 104
- boundary layer, 229
- Bridport sandstone, 15, 217
- Brooks and Corey, 116
- Buckley–Leverett, 118
- buoyancy-driven dispersion, 196, 223, 224
- buoyancy-driven flow, 3, 156, 203
- buoyancy-driven reaction fronts, 174, 247
- buoyancy-driven speed, 157
- buoyancy flows driven by temperature differences, 161
- buoyancy parameter, 199
- buoyancy ratio, 171
- buoyancy reversal, 156, 238, 242
- buoyancy speed, 163

- buoyancy stabilisation, 133
- buoyant plume, 202
- bypass, 38, 188

- capillary entry pressure, 169
- capillary imbibition, 127
- capillary number, Ca , 114
- capillary pressure, 98, 112, 116, 125
- capillary trapped wake of CO_2 , 181
- capillary trapping, 159, 176, 179, 217
- capillary tube, 123
- carbon emissions, 4
- carbon sequestration, 2, 156
- Cardoso and Woods, 102
- channels, 13, 105
- Clausius–Clapeyron equation, 230, 233, 234
- clay barriers, 161
- coal, 6
- compaction, 21
- complex potential, 204
- complex variables, 30
- compositional dispersion, 251
- compositional plume, 238
- compressibility, 3, 262
- compressibility factor, Z , 264
- compressible flow, 183, 230
- compression phase, 250
- confined gravity current, 181
- connate saturation, 114
- conservation of heat, 240
- conservation of mass, 117
- conservation of salt, 133
- constant flux gravity current, 166
- contact angle, 110
- convective flux, high Rayleigh number, 220
- convective mixing, 200
- convective transport, 220
- conventional resource, 7
- convoluted flow, 45
- core experiments, 121
- Corey and Brooks, 121
- correlation, 59, 65

- cost of uncertainty, 62
 cost of wells, 269
 cross-bedding, 18, 49
 cross-layer average, 85
 cross-layer gas diffusion, 273
 cross-slope component of gravity, 178
 curvature of interface, 97
 cycles of injection, 251
 cylindrical lens, 81
- Dagan, 70
 Darcy flow, 105
 Darcy speed, 28
 Darcy's law, 28, 117
 decelerating flow, 244
 decompression drive, 264
 decorrelation, 71
 deformation, 105
 Del Ioio and Woods, 105
 Delgado, 77
 DeLoubens and Ramakrishnan, 192
 deltaic deposits, 13
 density change on reaction, 247
 diffusion time, 76
 diffusion-controlled transport, 129
 dimensionless equations, 42
 Dingle peninsula, 18
 dipole moment, 169
 dipole solutions, 169
 discount rate, 33
 dispersion, 3, 70, 185
 dispersion by lenses, 79
 dispersion coefficient, 77
 dispersion in bead pack, 72
 dispersive flux, 74
 dispersive transport, 88
 dispersive wave, 120
 dissolution, 159, 198, 219
 dissolution channels, 249
 dissolution front, 103
 dissolution rate, 225
 dissolving gravity current, 175
 DNAPL (dense non-aqueous phase liquid), 70, 161
 double advection, 238
 double-advective instability, 238
 drainage, 111, 167
 drainage experiment, 266
 drainage radius, 262
 drainback, 169
 Dudfield and Woods, 182, 198
 Dullien, 122
- Eames and Bush, 80
 economic time, 269
 effective diffusivity, 264
 effective diffusivity, layered reservoir for gas flow, 275
 effective permeability, 33
 effective stress, 104
 effective thermal advection speed, 253
 effective thermal diffusivity, 232
 efficiency of heat recovery, 228
 encapsulant, 143
 encapsulation, 129
 energy sources, 4
 energy storage, 249
 energy supply, 4
 enhanced oil recovery, 157
 Ennis-King, 210
 entry pressure, 112
 equation of state, 230
 error function, 79
 exchange flow, 126, 156, 160, 219, 221, 258
 expansion phase, 250
 expected recovery, 56, 59
 experiment on instability of sand packs, 106
 experiment on macroscopic dispersion, 82
 exponential decay, 126
- Farcas and Woods, 192
 fast boiling, 233
 faults, 47
 fingering, 3
 five-layer gravity current, 215
 flow diversion, 151
 flow in parallel, 33
 flow in series, 32
 flow partitioning, 207
 fluid mixing, 257
 fluid-matrix reactions, 133
 fluvial deposits, 18
 fracking, 7, 270
 fractional flow, 35, 118, 122, 123
 fractional recovery, 60
 fracture width, 106
 fractured reservoir, 126
 fractured rock, 72
 fractures through impermeable rock, 160
 Fried and Combarous, 199
 full dissolution reaction, 141
 Furtney, 60
- gas, 10
 gas cap, 114, 222
 gas drainage, 277
 Gaussian distribution, 209
 Gelhar, 70, 79
 geological waste repository, 4, 160
 geometric controls, 216
 geothermal heat, 2
 geothermal power, 156
 Geysers, northern California, 227
 grain junctions, 74
 grain-grain motion, 105

- gravity and viscous fingering, 95
gravity-driven boiling front, 236
gravity tongue, 188
Green River Basin, 7
growth rate of instability, 100
Gunn and Woods, 185
- heat exchanger, 250
heat loss, 255
heat pump, 250
heat transfer, 128
heating, 227
Hele–Shaw cell, 96, 164, 203, 207, 258
Hesse, 159
Hesse and Woods, 209
heterogeneous rock, 18
Hewitt, 221
high permeability channels, 247
high-temperature vapour, 227
Hinch and Bhatt, 92, 103
Homsy, 92
horizontal baffles, 207
horizontal boundaries, 156
hot dry rock, 227
hydrates, 7
hydrocarbons, 4
hydroelectric power, 4
hydrogen gas, 160, 197
hydrological flow, 161, 197, 226
hydrostatic pressure, 162, 171, 186
hysteresis, 113
- Iceland, 227
image source, 30
imbibition, 111, 125
immiscible displacement, 97
immiscible flow, 92
impermeable boundary, 162
In Salah, Algeria, 159
inclined baffles, 210
inclined porous layer, 178
Indonesia, 227
injection of wastewater, 227
injection temperature, 233
injection well, 230
injection–extraction cycle, 252
interest rate, 268
interface, 171
interfacial tension, 110
intermingling, 70
intermittent generation, 249
interstitial speed, 28
- Juanes, 159
- Kilbaha Bay, 13
- Kim, 97
Kimmeridge Bay, 11
kinematic boundary condition, 103
kinematic viscosity, 235
kinetic delay, 143
King and Woods, 170
Koch and Brady, 70
Kozemy-Carmen relation, 29
- Lajeunesse, 124
Lake, 116, 127, 129
Langmuir isotherm, 275
Laplace’s equation, 99
Larderello, Tuscany, 227
latent heat, 232, 234
lateral diffusion, 241
lateral exchange flows, 221
Lauwerier, 256
layered porous media, 209
layered strata, 10
layered turbidite, 66
layering in sedimentary deposits, 207
leakage, 192
leakage flow, 41
lens of low permeability, 252
lenses, 35
liquid crystal, 131
liquidus, 137
LNAPL (light non-aqueous phase liquid), 70, 161
longitudinal dispersion, 74, 77, 213, 224, 255
long-term dispersion, 88
Loop Head Cliffs, 13
loss of thermal energy, 249
low permeability layers, 207
- Ma, 127
macroscopic dispersion, 80
mass conservation, 28
mass conservation in advancing region, 176
mass conservation in trailing region, 176
Mathias, 263
maximum principle stress, 132, 271
Maxworthy, 97
McKibben and Juanes, 185
mean thermal advection speed, 254
mean buoyancy, 223
mean flow speed, 253
mechanical dispersion, 70
Menand and Woods, 199
method of characteristics, 184, 245
Mexico, 227
miscible fingering experiment, 92
miscible flow, 92
Mitchell and Woods, 184
mixing, 70
molecular dispersion, 71
molecular transport, 220

- Monte Carlo method, 59
multiple states of convection, 221
- natural gas, 264
Netherlands, 249
neutrally buoyant reacting plume, 248
no slip, 75, 116
non-conventional resource, 7
non-linear dispersion, 224
non-linear finger, 106
non-linear wave equation, 108
non-uniform velocity, 212
nuclear energy, 4
- oil shales, 7
onset of convection, 220
optimisation, 59
oscillatory dispersive mixing, 89
oscillatory flow, 89, 258
- partial dissolution reaction, 137
Paterson, 97
Peclet number, 77, 86, 199
permeability, 28
permeability ratio, 153
permeability reduction with polymer, 153
permeable rocks, 1
perturbation concentration, 88
perturbation expansion, 43
Pfannuch, 199
Philippines, 227
Phillips, 70, 74, 128, 238
plume mixing, 202
plume shape near source, 204
plume width, 206
plumes, 156
PNIPAM, 147
point source, 157
Poiseuille flow, 97
polymer, 128, 143
polymer floods, 103
polymer rheology, 129
pore pressure, 104, 263
pore space, 28
pore throats, 111
porosity, 28
potential, 29
power generation, 227
precipitating gravity current, 175
precipitation of salt, 235
precipitation reaction, 104
pressure-adjustment zone, 234
pressure diffusion equation, 263
pressure diffusivity, 231, 233, 263
pressure-driven flow, 71
pressure gradient, 94
pressure wave, 262
- primary production, 264
production well, gas, 264
- radial flow, 99
radioactive contaminants, 70
radioactive material, 160
radius of curvature, 112
random walk, 72
rarefaction wave, 120
Raw and Woods, 176
Rayleigh number, porous, 220
Rayward-Smith and Woods, 179, 211, 247
reaction front, 133, 135, 173, 175
reaction-front speed, 133
reaction time, 129
recovery temperature, 249, 252
refrigerant, 250
Reinelt, 97
relative permeability, 117, 121
reservoir fluid, 238
residual saturation, 111
reversing buoyancy, 228, 242
reversing buoyancy through reaction, 248
Reynolds number, 28
Riolfo, 92
run out distance, 219
- Saffman, 70, 75
Saffman–Taylor instability, 92
salt powder, 247
sand bars, 39
sand pack, 230, 233
saturation, 117
saturation front, 110
scale, 246
scale formation, 103, 227
scaling analysis, 162
Scandinavia, 249
Schmidt number, 77
seal layer, 39
secondary displacement, 158
self-similar solution, 163, 172, 183
self-similar solutions of second kind, 177
sensitivity, 67
sensitivity analysis, 63
sensitivity of model predictions, 52
separable solution, 265, 267
shale gas, 10, 264, 275
shape function, 241
shear dispersion, 84
shear stress, 123
shock, 118, 124
shock front, 3
shock solution, 185
similarity solution, 169, 225, 232, 241, 264
similarity variable, 163, 229, 232, 236, 263
sink, 185

- sink flow, 30
Sleipnir, Norway, 159, 193, 197
sloping boundaries, 156
slow boiling, 232
slug of chemical, 101
Sorbie, 129
source, 30, 185
source–sink flow, 63
specific heat capacity, 229, 255
speed of characteristics, 187
speed of shock, 119
stable density interface, 199
static stability, 238
steady-state plume, 239
Stefan condition, 232, 233
storage capacity, 219
streamfunction, 29, 204, 240
structural trapping, 217
structural traps, 159
sugar–salt solutions, 247
supercritical CO₂, 159
superheated rock, 230
surface tension, 99, 114
sweep efficiency, 53
swept area, 30
swept volume, 54
- tar sands, 7
Taylor, 84
Taylor dispersion, 71, 223, 253
temperature–composition plane, 238
thermal-advection speed, 129, 131
thermal battery, 228
thermal-diffusion scale, 231
thermal diffusivity, 229
thermal dispersion, 251, 253
thermal energy, 227
thermal energy conservation, 130, 251
thermal energy storage, 9, 228
thermal equilibrium, 129, 252
thermal fractures, 132
thermal front, 148, 228
thermal inertia, 132, 228, 238
thermal Peclet number, 131
thermal plume, 203, 239
thermal trigger, 147
thermally driven reactions, 128
three-dimensional gravity current, 190
tight gas, 264
time of flight, 35
topographic trapping, 218
tortuosity, 72
total wetting, 111
tracer tests, 213
transition zone, 115, 125
transverse diffusion, 203
transverse dispersion, 74, 78, 210, 223
transverse mixing, 79
trapped pools, 217
travel time, 80, 215
travelling wave, 133
trigger, 143
Tullig Point, 13
turbidite, 11, 195
turbine, 227
two-fluid gravity currents, 170
two-layer flow, 245
Tyskin and Woods, 235
- uncertainty, 24, 56
unconsolidated media, 92
unconsolidated rock, 104
ungelled polymer, 150
unsaturated formation water, 221
unstable density interface, 199
unstable wavelength, 95
upslope buoyancy speed, 243
utility function, 57
- vadose zone, 161, 162, 213
value, 33
value of production, 268
van Genuchten, 121
van Triet, Routh and Woods, 143, 148
vapour flow, 230
variance, 58, 82
velocity correlation, 74
velocity potential, 204
Verdon, 159
vertical exchange flows, 221
vertically averaged transport, 224
viscosification, 92
viscosifier, 102
viscosity ratio, 171
viscous fingering, 92
volume ratio, 171
- waning flow, 259
water flooding, 7, 23, 157
wavy boundary experiment, 217
wavy horizon, 39
wavy layers, 217
well spacing, 54, 268
West Bay, Bridport, 15
Weyburn, Canada, 159
wind power, 249
Wooding, 203, 239
Woods and Espie, 159, 222
Woods and Farcas, 169
Woods and Mason, 173
Woods and Norris, 160
- Yih, 204
Yortsos and Salin, 195
Young and Jones, 70, 75
Young's law, 110

